Natural Laminar Flow Airfoil Behavior in Cruise Flight through Atmospheric Turbulence

Vom Fachbereich Maschinenbau
an der Technischen Universität Darmstadt
zur
Erlangung des Grades eines Doktor-Ingenieurs (Dr.-Ing.)
genehmigte

D i s s e r t a t i o n

vorgelegt von

Dipl.-Ing. Andreas Daniel Reeh

aus Lich

Berichterstatter:	Prof. Dr.-Ing. C. Tropea
Mitberichterstatter:	Prof. E. B. White
Tag der Einreichung:	05.05.2014
Tag der mündlichen Prüfung:	25.06.2014

Darmstadt 2014
D17

Hiermit versichere ich, die vorliegende Doktorarbeit unter der Betreuung von Prof. Dr.-Ing. C. Tropea nur mit den angegebenen Hilfsmitteln selbständig angefertigt zu haben.

Darmstadt, den 05.05.2014

Abstract

Atmospheric turbulence is encountered frequently in flight. It creates oncoming flow disturbances for aircraft passing through turbulent zones. For natural laminar flow airfoils such conditions are potentially detrimental since their goal of maximizing laminar flow may be counteracted by increased disturbance levels. In this study the flow behavior of a natural laminar flow wing section is investigated in gliding flight experiments under calm and light to moderately turbulent conditions.

A comprehensive measurement platform is integrated into a motorized glider to obtain insights into the flow processes acting on a laminar wing glove in cruise flight. Simultaneous measurements of characteristic airfoil quantities enable important correlations with the oncoming flow disturbances. To develop a comprehensive understanding for flight through turbulence, boundary-layer transition is investigated in detail under calm conditions. Differences of the transition behavior between the upper and the lower side of the airfoil are demonstrated. New insight into the weakly nonlinear transition stage in a low disturbance environment is presented.

Due to the random nature of atmospheric turbulence, characteristic results under moderately turbulent conditions are presented as case studies. This enables a complete examination of the time-varying boundary conditions, the inviscid flow effects and the boundary-layer response to the turbulent forcing. It is shown that all these processes interact with each other. Furthermore, it is demonstrated that the unsteadiness of the oncoming flow assumes an important role in the laminar-turbulent transition process of the airfoil boundary layer. On the lower side of the airfoil significant and rapid upstream fluctuations of transition are verified under moderately turbulent conditions. It is shown that these fluctuations are driven by the time-varying pressure gradient and that transition is initiated by Tollmien-Schlichting waves. Indications for a premature transition behavior under such unsteady conditions are presented, which can only partially be explained by unsteady distortions of the boundary layer. The experimental observations are complemented by numerical investigations employing unsteady panel and boundary-layer methods as well as quasi-steady linear stability theory.

Kurzfassung

Atmosphärische Turbulenz macht sich im Flug als Störung der Anströmung bemerkbar. Solche Bedingungen können die Leistung von Laminarprofilen beeinträchtigen, deren Auslegungsziel eine möglichst weit laminar gehaltene Grenzschicht ist. Dieses Ziel wird potentiell durch das erhöhte Störungsniveau beeinträchtigt. In dieser Arbeit wird daher das Strömungsverhalten eines Laminarprofils im Gleitflug unter ruhigen und leicht bis moderat turbulenten Bedingungen untersucht.

Eine umfangreiche Messplattform, integriert in einen Motorsegler, wird genutzt, um Einblicke in die Strömungsprozesse an einem Flügelhandschuh unter Reiseflugbedingungen zu gewinnen. Simultane Messungen der charakteristischen aerodynamischen Profilgrößen ermöglichen die Korrelation mit den Störungen in der Anströmung. Um ein besseres Verständnis für den Flug durch Turbulenz zu entwickeln, wird die Grenzschichttransition zunächst detailliert unter ruhigen Bedingungen untersucht. Dabei zeigen sich Unterschiede im Transitionsverhalten zwischen der Ober- und der Unterseite des Profils. Neue Erkenntnisse über die schwach nichtlineare Phase der Grenzschichttransition in einer störungsarmen Umgebung werden vorgestellt.

Aufgrund der zufälligen Natur atmosphärischer Turbulenz erfolgt die Betrachtung der Ergebnisse moderat turbulenter Bedingungen als Fallstudien. Dies ermöglicht eine umfassende Untersuchung zeitabhängiger Randbedingungen, reibungsfreier Profileffekte und des Antwortverhaltens der Grenzschicht auf die turbulente Anregung. Die Interaktion all dieser Effekte wird ersichtlich. Die wichtige Rolle der Instationarität der Anströmung im Transitionsprozess der Profilgrenzschicht wird demonstriert. Unter moderat turbulenten Bedingungen werden starke, kurzfristige Fluktuationen der Transition entgegen der Hauptströmungsrichtung auf der Profilunterseite detektiert. Es zeigt sich, dass die Transition durch Tollmien-Schlichting Wellen eingeleitet wird. Daneben werden Anzeichen für eine frühzeitige Transition erfasst, die nur teilweise auf die instationären Veränderungen der Grenzschichtprofile zurückzuführen sind. Die experimentellen Ergebnisse werden ergänzt durch numerische Untersuchungen unter Verwendung instationärer Panel- und Grenzschichtmethoden, sowie der linearen Stabilitätstheorie.

Acknowledgements

This research was supported by the Deutsche Forschungsgemeinschaft (German Research Foundation) under the grant TR 194/48-1.

First of all I would like to acknowledge the support and the guidance of Prof. Dr.-Ing. Cameron Tropea throughout my studies and my employment as a doctoral researcher of the Institute of Fluid Mechanics and Aerodynamics at the Technische Universität Darmstadt. I would also like to thank Prof. Edward B. White from Texas A&M University for his interest in the present work and for refereeing this thesis. I am particularly grateful to Dipl.-Ing. Andreas Güttler, Dipl.-Ing. Lars Opfer, Dr.-Ing. Alexander Duchmann and Dr.-Ing. Jochen Kriegseis. They supported and encouraged me in all phases of the project. I am indebted to Dr. rer. nat Hubert Marschall who taught me a great deal about fluid mechanics.

Furthermore, I would like to acknowledge Dr.-Ing. Wilm Friedrichs, Dr.-Ing. Michael Weismüller and Dipl.-Ing. Martin Stenger for their help and advice related to the flight experiments. I would like to thank Dr. Werner Würz and Dipl.-Ing. Benjamin Plogmann from IAG Stuttgart for the fruitful discussions on laminar-turbulent transition, which further propelled my research interest. Without the help of my students the comprehensive flight experiments would not have been possible. The list is a long one: Daniel Wolfram, Michael Köhler, Thiago Weber Martins, Paul Taubert, Axel Dietrich, Tim Hartmann, Jonas Schulze, Fabian Tenzer, Marcel Bonnert, Rene Cabos, Oxana Ionnikova and Tobias Hofmann. The excellent working atmosphere at the wind-tunnel facilities in Griesheim has always been motivating, foremost due to the presence of my colleagues. The success of the flight tests was in large part due to support of the electronics workshop headed by Martin Weiß and the mechanical workshop headed by Ilona Kaufhold. Klaus Hufnagel, Matthias Quade and Bernd Braun assisted in the solution of problems. Stephanie Lath has always been great help in the project organization. Thanks to Tim Prangemeier and Karl Anton Frank for the proofreading.

Finally, I would like to express my deepest gratitude to the love, encouragement and support I have received over the years from my parents, my grandparents and from Claudia.

Contents

1. Introduction

1.1. Motivation

The forces acting on a fixed-wing aircraft in steady flight can be divided into the components lift, drag, weight and thrust. Aerodynamics considers lift and drag, being the forces exerted on a body by the relative motion of the air. The optimization of the lift-to-drag ratio for a specific design point under ideal, undisturbed flow conditions generally is the primary engineering task for aerodynamicists (Abbas et al, 2013). However, only a fraction of flight operations takes place under ideal conditions. Therefore, several secondary design points and disturbances need to be taken into consideration (Abbot and Von Doenhoff, 1959). Disturbances can significantly affect the efficiency of aircraft operation. One such effect is the influence of atmospheric turbulence on the flight performance of fixed-wing aircraft with natural laminar flow (NLF) airfoil design, which is the subject of the present study.

For conventional subsonic aircraft more than 50 % of the total drag in cruise flight is caused by skin friction (Joslin, 1998) and thereof over 50 % is created on the wing and the empennage surface (Arnal et al, 2008). Using NLF technology, successful drag reduction and lift-to-drag ratio improvement of about 20 % have been achieved under ideal conditions (Holmes and Obara, 1992), in particular by using wings based on NLF airfoils. These airfoils are intended for minimal skin friction drag within a limited angle-of-attack range, which is commonly referred to as the laminar bucket owing to the peculiar shape of the lift-to-drag curve (Somers, 1981). The geometry of the wing is especially shaped to passively delay the transition process of the boundary layer from the laminar to the turbulent state; the latter flow state being associated with significantly higher skin friction. Limiting the instability growth responsible for transition allows for extended streamwise regions of laminar flow. On a smooth, moderately swept wing and for low free-stream disturbance levels, the primary instabilities to be considered are Tollmien-Schlichting (TS) waves (Reed and Saric, 1996). These naturally occur in the form of wave packets (Gaster and Grant, 1975). Cruise flight is usually the primary design point since the lower lift coefficients associated

with cruising airspeeds allow the exploitation of maximum laminar runs on both sides of the airfoil. An efficiency degradation due to turbulence is particularly detrimental in this flight situation. The simultaneous need for a high maximum lift coefficient, a favorable angular momentum balance, uncritical stall characteristics and other requirements further complicate the design process of NLF airfoils. Boermans and Selen (1981), Würz (1995), Selig et al (1995) and Fujino et al (2003) provide details on design philosophy.

Basic questions toward the performance of NLF airfoils, when exposed to atmospheric turbulence, still remain. For instance, Bertolotti (1999) and Fisher et al (2003) report discussions in the glider pilot scene on small-scale turbulence effects degrading the performance of sailplanes, which extensively employ NLF design. However, a verification of such a behavior is pending. Previous research has focussed on individual aspects of the problem but there exists no comprehensive flight investigation which takes into account all the processes interacting simultaneously. It should be noted that such detrimental effects on efficiency are not limited to fixed-wing aircraft. NLF design is also used for wind-turbine blades to increase the energy yield (Somers, 1997). Wind turbines are exposed to considerable levels of turbulence by their operation in the high-shear region of the atmospheric boundary layer. Furthermore, when aligned in wind parks, wake turbulence creates similar disturbances (Vermeer et al, 2003).

1.2. Implications of Atmospheric Turbulence for Airfoil Aerodynamics

Atmospheric turbulence is encountered by aircraft of all categories, especially at boundaries of different atmospheric layers and within the planetary boundary layer (Wippermann et al, 1970). In an aircraft-fixed frame of reference, the consequences of atmospheric turbulence are unsteady fluctuations of the oncoming flow quantities due to the superposition of turbulent eddies of different scales (MacCready, 1962a). Numerous studies have been devoted to the issue of gust loads endangering flight safety in rarely occurring events of severe turbulence, e.g. MacCready (1964); Etkin (1981); Hoblit (1988). As this study focusses on the efficiency of NLF airfoils, only the influence of light to moderate atmospheric turbulence is investigated. Depending on the weather, these conditions can persist for the entire flight time within the atmospheric boundary layer, i.e. the lower part of the troposphere (Wyn-

gaard, 1992). Although the considered turbulence categories do not present any danger to the airframe, larger eddies still affect the aircraft globally causing unsteady forces on the wing (McCroskey, 1973; Staveren, 2003; Mish and Devenport, 2003). Thus, the aircraft itself presents a sensor for turbulence, however, with an imperfect transfer function (MacCready, 1962b). Transient changes in the flow around the wing not only result in lift variations and motions of the aircraft, they also lead to an unsteady development of the wing boundary layer (Patel, 1975; Cebeci et al, 1989) affecting its transition from the laminar to the turbulent state (Obremski and Fejer, 1967; Loehrke et al, 1975; Studer et al, 2006b). Furthermore, small-scale turbulence, which only has a local effect, can potentially excite stronger primary instability waves or entirely different disturbances inside the wing boundary layer in a process known as receptivity (Crouch, 1992a,b; Herbert et al, 1993; Saric et al, 2002). This process has received considerable scientific attention due to its fundamental importance for the explanation of the origin of boundary-layer transition and the explanation of the occurrence of premature transition. Numerous studies have been conducted in order to investigate the consequences of free-stream turbulence in wind tunnels (Westin et al, 1994; Kendall, 1998; Dietz, 1999; Fransson et al, 2005) or in numerical simulations (Buter and Reed, 1994; Bertolotti, 1997; Schrader et al, 2010; Tempelmann, 2011). However, due to the specific composition of atmospheric turbulence, all the effects acting on a wing section can hardly be simulated simultaneously, neither in wind-tunnel experiments nor in elaborate computations (Weismüller, 2011).

Previous in-flight studies concentrated either on the characterisation of atmospheric turbulence, e.g. MacCready (1962a); Sheih et al (1971); Riedel and Sitzmann (1998); Fanning (2012), or investigated boundary-layer transition under perfectly calm conditions, e.g. Nitsche et al (2001); Erb (2002); Peltzer (2008). Horstmann et al (1989) and Runyan and George-Falvy (1979) compared transition positions detected in flight on straight-wing aircraft and in low-turbulence wind tunnels with linear stability analysis. Seitz and Horstmann (2006) investigated the frequency content and spanwise extent of Tollmien-Schlichting (TS) wave packets in a wing boundary layer in flight under calm atmospheric conditions. In a flight experiment with a glider Zanin (1985) reported some comparisons between atmospheric turbulence and boundary-layer disturbances. However, this investigation was limited by the available instrumentation. Inevitable inviscid effects caused by the time-varying oncoming flow which were not considered. Carpenter et al (2010) and Saric et al (2011) conducted in-flight receptivity studies for swept wings.

Yet, the obtained results cannot be transferred to the case of two-dimensional boundary layers. A comprehensive measuring platform for the investigation of the effect of atmospheric turbulence on a straight-wing airplane was developed by Weismüller (2011). His results concentrated on inviscid airfoil effects in gliding flights through turbulence at high angles of attack and associated high lift coefficients.

Due to the various interacting effects, the response of NLF airfoils in real flight have only been studied incompletely. Especially in cruise flight, where nominally the largest portion of laminar flow on NLF airfoils is achieved, a number of fundamental questions remain unanswered for two-dimensional wing sections. In the following section objectives for the present thesis are derived from a summary of these fundamental uncertainties.

1.3. Objectives and Outline of the Thesis

This study is devoted to the investigation of the influence of atmospheric turbulence on the efficiency of a two-dimensional NLF wing section in gliding flight at low lift coefficients. All important aerodynamic effects are to be considered with particular emphasis on the boundary-layer response. The main topics of this thesis can be divided into four categories:

- Characterization of the oncoming flow disturbances imposed by atmospheric turbulence.
- Inviscid airfoil response to turbulent excitation.
- Boundary-layer development with emphasis on the transition development under calm conditions.
- Boundary-layer response with emphasis on the transition development under light to moderately turbulent atmospheric conditions.

When considering the practical application of NLF airfoils in real flight, basic questions remain unanswered in the existing literature in each of the categories. All of the problem categories are interconnected when flying through atmospheric turbulence. In the following, open questions will be identified and they will be reformulated as key questions for the present investigation.

Flight investigations of atmospheric turbulence are not uncommon in meteorology (MacCready, 1962a; Payne and Lumley, 1966; Sheih et al, 1971),

however, the focus is not specifically on the turbulent scales relevant for airfoil aerodynamics. Preceding flight investigations with an aerodynamic background, which are reviewed by Fisher et al (2003), do not present turbulence spectra for various atmospheric conditions. A detailed investigation of oncoming turbulence is not only important for TS wave induced transition but also for swept wings, i.e. three-dimensional boundary layers, where the evolution of cross-flow instabilities is particularly sensitive to free-stream turbulence (Deyhle and Bippes, 1996; Downs and White, 2013). Careful characterization of the oncoming flow is therefore not only helpful to understand the atmospheric physics, it is an indispensable prerequisite for the correlation of the transition process on a wing section with the oncoming flow disturbances (Bushnell, 1990; Saric, 2007).

The extended laminar flow region on two-dimensional NLF airfoils enables gradual TS wave growth and weakly nonlinear interactions of planar and oblique wave modes. Among others, Saric and Levchenko (1984), Kachanov (1994) and Würz et al (2012) describe the occurrence of different types of nonlinear interactions depending on the TS wave spectrum in the linear stage of transition in their wind-tunnel investigations. Although spanwise frequency-wavenumber spectra have been obtained in flight by Peltzer and Nitsche (2004) and Seitz and Horstmann (2006), no evidence of the nonlinear interaction processes has been reported. Recently, de Paula et al (2013) proposed their 'most likely route to laminar-turbulent transition in two-dimensional boundary-layers of airfoils' in a low-disturbance flight environment uniting some of the previous concepts with a theoretical mechanism described by Wu et al (2007).

In a low disturbance wind tunnel Studer et al (2006a) showed that unsteadiness in the laminar boundary-layer development on an airfoil can significantly affect transition. Their results for harmonic variations of the free-stream velocity show the appearance of turbulent bursts which are preceded by a rapid nonlinear development of boundary-layer disturbances. This mechanism was first described by Obremski and Fejer (1967) in an experimental study on a flat-plate boundary layer exposed to oscillating pressure variations. Tani (1969) and Loehrke et al (1975) explain the occurrence of such transition by the rapid quasi-steady growth of TS waves travelling through unsteadily distorted, highly unstable boundary-layer profiles. Although these boundary-layer investigations were probably motivated by gas turbine applications (Walker, 1993), the rapid fluctuations in the pressure distribution observed in the flight investigation of Weismüller (2011) suggest a careful assessment of the unsteady boundary-layer effects.

The question of the instabilities involved in the transition process in flight through atmospheric turbulence and the possibility of premature transition is discussed by Bertolotti (1999). The importance of the free-stream disturbance level on the amplitudes of TS wave packets and their subsequent breakdown had been elucidated since the seminal experiments of Schubauer and Skramstad (1948). About 40 years later, careful wind-tunnel experiments under moderate free-stream turbulence by (Kendall, 1984, 1985) gave rise to the notion that another, essentially linear disturbance growth mechanism must exist besides the two known routes to turbulence, i.e. TS wave initiated transition and the direct nonlinear interaction known as bypass transition (Reshotko, 2008). Basing his analysis on theoretical studies of the Blasius boundary layer (Bertolotti, 1997; Leib et al, 1999) and controlled as well as uncontrolled receptivity experiments on free-stream turbulence (Kendall, 1990; Bertolotti and Kendall, 1997), Bertolotti examined the entrainment of anisotropic turbulence modes into the laminar boundary layer. Such modes are able to 'lift up' (Landahl, 1980) low-speed fluid from direct wall-proximity producing elongated disturbance structures of high and low-speed fluid in a limited spanwise extend which may grow in the streamwise direction proportionally to the boundary-layer thickness (Schmid and Henningson, 2001). The transient growth of these streaks, also named Klebanoff modes (Kendall, 1998), is particularly effective if it originates from streamwise vorticity modes in the low-frequency limit of the free-stream turbulence (Schrader et al, 2010), yielding a similarity to the transient growth caused behind small surface roughness elements (White, 2002). Bertolotti (1999) strongly supports the idea that the Klebanoff modes can trigger premature transition in a two-dimensional wing boundary layer. However, there is no verification for their existence in real flight and it is not necessary that these disturbance modes lead to a premature transition, even if they have reached amplitudes beyond the values at which nonlinear TS wave interaction is observed (Boiko et al, 1994; Cossu and Brandt, 2004). Furthermore, Zanin (1985) observed the participation of TS wave packets in the transition process for all oncoming flow conditions, even when flying through clouds under significantly elevated turbulence intensities. Regarding the fact that the kinetic energy of atmospheric turbulence strongly decays toward the inherent small-scale motions relevant for the excitation of boundary-layer disturbances, it is not clear whether bypass transition on straight wings may occur in flight under common natural conditions.

Based on the preceding literature review a list of key questions is construed for the present investigation:

- What are the implications of the spectral composition of atmospheric turbulence?
- Is it appropriate to consider the inviscid outer flow to be quasi-steady?
- Is there any new insight into the weakly nonlinear stages of transition under calm conditions?
- What is the role of the unsteady boundary-layer development when flying through turbulence?
- Does the transition mechanism change in flight through zones of increased turbulent forcing?
- What are the implications for NLF airfoil design?

It is the objective of the present study to contribute to the existing knowledge and to provide novel insights for these questions. In Chapter 2 the physical background is presented and several problem-specific observations are derived from theoretical considerations. Chapter 3 gives an overview of the experimental and numerical methods employed in this study. The oncoming flow conditions are evaluated in Chapter 4 to examine the peculiarities of the natural excitation. To understand boundary-layer transition in flight through atmospheric turbulence, it is necessary to study the quasi-steady transition behavior. In Chapter 5 the steady angle-of-attack dependence of transition on the airfoil, the involved boundary-layer disturbances under calm conditions and the role of nonlinear TS wave interactions are investigated. The random nature of atmospheric turbulence requires the investigation of boundary-layer transition for selected flight cases. The implications of atmospheric turbulence on the inviscid airfoil aerodynamics are verified in Chapter 6 and the boundary conditions for the boundary-layer development are presented. In Chapter 7 the transition behavior under various turbulent conditions is evaluated with special data reduction procedures and a holistic simulation of the boundary-layer behavior of the NLF airfoil in cruise flight under turbulent conditions is presented. The thesis concludes in Chapter 8 with a summary of the obtained insights, addressing directly the aforementioned key questions.

2. Background and Theoretical Considerations

Investigating the effects of atmospheric turbulence on a NLF airfoil is a multidisciplinary task. Only with solid knowledge of the origin and the characteristics of atmospheric turbulence is it possible to understand the effects on aircraft flight. Since atmospheric turbulence acts in a wide range of scales and intensities, the consideration of different facets of aerodynamics is necessary. The goal of this chapter is the provision of the necessary background. Moreover, this background chapter is not merely intended as a classical introduction to the underlying theory. Several of the presented results are problem-specific and will be used in later chapters.

2.1. Atmospheric Turbulence

Atmospheric turbulence emanates from processes like thermal flow instability (buoyancy driven turbulence), the turbulent velocity boundary layer due to meteorological pressure differences, large-scale orographic interference (wind deflection and separation at large objects), wind shear at inversion layers, energy release through condensation, etc. (Wyngaard, 2010). Besides the synoptical meteorologic conditions, the driving factor for atmospheric turbulence is diurnal changes (Metzger et al, 2007). Especially during daytime, many of the mentioned mechanisms may act simultaneously in the lower layer of the troposphere, the atmospheric boundary layer (ABL), where most of the flight experiments of the present study were conducted. In this layer the dynamic boundary condition on the ground has a strong influence on the motion of the air and thermal convection is a key factor for intense vertical and lateral mixing. Depending on the turbulence production, the ABL can be further subdivided into two parts. In the lower part, the surface layer, turbulence is mainly produced mechanically through high shear extracting energy from the mean wind profile. Only about a hundred meters above ground level, thermal convection driven by solar heating assumes the dominating role in the convective mixed layer (Stull, 1988). Mixing is a ma-

jor effect of turbulence, which strives to homogenize the fluid dynamic and thermodynamic properties in the ABL. Both production processes may be modified to a large extent by surface roughness and other factors. Furthermore, turbulence activity highly depends on the density stratification of the troposphere. At daytime the upper limit of the ABL, ranging between 1 km and 3 km, usually constitutes an inversion layer, i.e. a sign change in the vertical temperature gradient, which caps the buoyancy-induced vertical fluxes. A thin entrainment layer marks the border to the free atmosphere, where the motion of the air is governed by pressure differences and the Coriolis force creating the geostrophic wind. The energy release through condensation at this boundary represents another source creating turbulence from the top of the ABL. At night, when the long-wavelength heat radiation from ground is missing, turbulence is only determined by the wind shear and the ABL subsides to a few hundred meters, leaving a more or less stable residual layer above.

Turbulence is characterized by the irregular superposition of fluctuations of all flow quantities, in which moderately coherent motions over a localized region are perceived as eddies. The coexistence of many of these eddies of different length and energy scales led to the energy cascade concept of Richardson (Batchelor, 1950), stating that the kinetic energy is primarily transferred from larger structures to a multiple of smaller turbulent eddies. The energy-containing eddies relevant for the present study, i.e. those motions involved in the turbulence generation, are generally produced on large length scales of the order of more than a hundred meters (Wyngaard, 1992). Considering the height of the convective mixed layer with $O(1\text{ km})$ and a typical velocity scale of 1 m/s, a Reynolds number $Re \sim O(10^8)$ results for convective turbulence. As the convective updrafts strongly depend on the ground characteristics and have smaller lateral scale than their vertical extent, atmospheric turbulence is intrinsically non-homogeneous and anisotropic in the energy containing range. However, due to the high Reynolds number of the flow, the directional information is lost in the energy cascade toward smaller eddies and the statistics of the motion becomes universal at small scales (universal equilibrium range). Approaching the small-scale end of the process, the dissipative scales, molecular viscosity increases in importance and the kinetic energy is eventually dissipated into heat.

Within the universal equilibrium range, but at substantially larger scales than the dissipative ones, an intermediate range of eddy size exists in which the turbulent kinetic energy is transferred from larger to smaller turbulent structures in an essentially non-dissipative mechanism. This process depends

only on the energy transfer rate from the energy-containing eddies, which is proportional to the energy dissipation rate ϵ (Pope, 2000). In this inertial subrange, which is independent of the kinematic viscosity ν, the law of Kolmogorov for the specific kinetic energy spectrum function holds.

$$E_{\mathrm{kin}} = C_{\mathrm{T}} \epsilon^{\frac{2}{3}} k^{-\frac{5}{3}} \tag{2.1}$$

This power law, which can be derived by dimensional analysis (Wyngaard, 2010), describes the spectral energy distribution as a function of the eddy wave number k. The characteristic length scale is thus $\lambda = 2\pi/k$. The universal constant C_{T} is determined from experiments. A value of $C_{\mathrm{T}} \approx 1.5$ is usually found in the literature (Sheih et al, 1971). Figure 2.1 shows a model

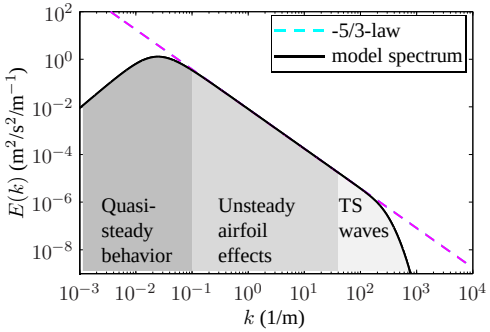

Figure 2.1.: Model of the kinetic energy spectrum of moderate atmospheric turbulence.

spectrum which will be presented mathematically in Chapter 4. The power law decay of the inertial subrange, equation (2.1), is followed by a steeper exponential decay for high wavenumbers corresponding to the dissipation range. In the diagram wavebands of expected airfoil effects are marked in different shades to provide an overview of the turbulent scales relevant for the present investigation.

2.2. Assumptions and Simplifications of the Aerodynamic Problem

Throughout the consideration of the physical background, the presentation of numerical studies and the interpretation of the measurement results in

this thesis, three major assumptions, which need to be justified, simplify the complex problem.

First of all it is assumed that the flow is incompressible, which in mathematical terms signifies

$$\frac{\partial \rho}{\partial t} + \vec{U} \cdot \nabla \rho = 0 \quad \longleftrightarrow \quad \underbrace{\nabla \cdot \vec{U}}_{\mathrm{I}} = 0. \tag{2.2}$$

Since in aerodynamic flow problems the local derivative $\partial\rho/\partial t$ is usually zero, the density ρ must be homogeneous. This signifies that the density change of a fluid element passing an aerodynamic body is negligible. A characteristic pressure for the problem is found at the stagnation point, where the air is decelerated to zero in an isentropic process. Employing compressible stream filament theory along the stagnation streamline, the ratio between the stagnation density ρ_t and the free-stream density ρ_∞ reads (Spurk and Aksel, 2006):

$$\frac{\rho_t}{\rho_\infty} = \left(\frac{\gamma - 1}{2} Ma^2 + 1 \right)^{1/(\gamma-1)}. \tag{2.3}$$

In the flight experiments of this study the Mach number Ma is always less than 0.2 and the heat capacity ratio is constant ($\gamma = 1.4$). The resulting density change of only 2 % justifies the assumption of an incompressible flow.

Limiting the investigation to cruise flight ensures small angles of attack ($-3° \leq \alpha \leq 5°$) and high Reynolds numbers based on the chord length ($2 \cdot 10^6 < Re < 4 \cdot 10^6$). Massive flow separation on the wing can thus be ruled out for the investigated wing section, although the possibility of the existence of a tiny separation bubble will be discussed. This leads to the second assumption; the flow on the considered wing section practically remains attached under all circumstances and the boundary-layer concept is always valid.

The third major assumption concerns the three-dimensionality of the flow on the considered wing section and it is closely connected to the previous statement. Flying a high aspect ratio, straight-wing aircraft at zero side slip, the flow on a wing section at mid-span is indeed almost parallel to the chord, supporting the consideration of a two-dimensional basic flow. Furthermore, low angles of attack imply low lift coefficients minimizing the circulation of the spanwise wake vorticity and thus the induced cross-flow velocity. The second and the third assumption will be substantiated with results in Chapter 3.1.2.

Having presented and reinforced these elementary simplifications, it is possible to introduce the underlying aerodynamic framework of the investigation.

2.3. Airfoil Response to Unsteady Flow Fields

In flight transient loads may occur either through rapid aircraft maneuvers, aeroelastic motions of the wing or external excitation when flying through gust fields. In all these cases rapid changes in the boundary conditions can lead to an unsteady airfoil behavior. The unsteady response of an airfoil moving through a field of atmospheric turbulence can be interpreted as a mechanical impedance (Fung, 2008). The unsteady forcing results in an impeded and phase-shifted response of the airfoil flow compared with the quasi-steady expectation, which is mathematically expressed by using complex quantities.

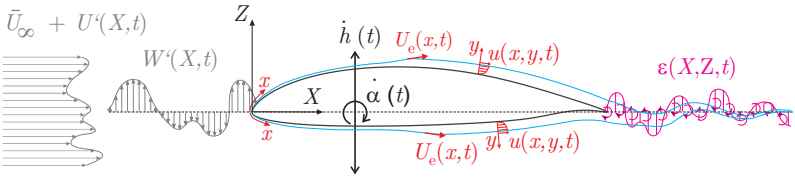

Figure 2.2.: Inviscid and viscous unsteady airfoil effects.

For high Reynolds number airfoil flows the response is twofold, as illustrated schematically in Figure 2.2. Inviscid unsteady effects affect the resulting loads and the boundary conditions for the development of the boundary layer. The unsteady development of the boundary layer constitutes a second, although physically different, impedance. In the boundary-layer concept introduced by Prandtl (1904), viscous flow effects are considered only in a thin shear region close to the airfoil surface, which asymptotically converges toward the driving inviscid outer flow. This framework allows the consideration of two separate problems coupled only by an interaction scheme (Cebeci and Cousteix, 2005). Due to its mathematical accessibility the viscous-inviscid interaction concept provides extremely valuable insight into the physical mechanisms acting on wing section in flight through atmospheric turbulence.

2.3.1. Effects of Gusts and Airfoil Motions on the Inviscid Outer Flow

Revealing insight into the inviscid effects of unsteady attached flows about airfoils are obtained by potential flow theory. For an irrotational flow field ($\nabla \times \vec{U} = 0$) with negligible volume forces, the potential flow and the pressure field are described by two equations. The Laplace equation ($\Delta\phi = 0$) is obtained directly from the continuity equation (underbraced part of equation (2.2)) by the introduction of a velocity potential ($\vec{U} = \nabla\Phi$). The Bernoulli equation is derived from a first integral of the Euler equations (Spurk and Aksel, 2006) and it provides the connection to the pressure field P.

$$\underbrace{\frac{\partial\phi}{\partial t}}_{\mathrm{I}} + \frac{1}{2}\vec{U}\cdot\vec{U} + \frac{P}{\rho} = \mathrm{const} \tag{2.4}$$

Several analytical solutions to the Laplace equation exist, among which a set of singular solutions is especially advantageous for describing airfoil flows (Katz and Plotkin, 2001). Source and sink sheets and potential vortex sheets can be distributed to fulfill the kinematic boundary conditions at the airfoil contour and the Kutta condition of finite flow quantities at the trailing edge. The method of singularities is used for efficient numerical schemes describing steady (Drela, 1989) and unsteady (Cebeci et al, 2005) potential flow about arbitrary two-dimensional airfoils, which will be used extensively in this study. If the airfoil thickness as well the camber are small compared with the chord length ($t/L_c, d/L_c \ll 1$), and the angle of attack is small, a single source-sink sheet and a vortex sheet on the chord line suffice to fulfill the aforementioned boundary conditions in a linearized form. Mathematically the problem reduces by one dimension, which introduces an error $O(\max[(t/L_c)^2, (d/L_c)^2])$ and a singularity at the leading edge (Spurk and Aksel, 2006). Despite these shortcomings thin airfoil theory allows modular analytic investigations and therefore represents a very convenient tool for the qualitative investigation of unsteady inviscid effects (McCroskey, 1973).

A thin airfoil model was developed for this study to investigate these effects. It consists of a steady and a superimposed unsteady part. The solution procedure is depicted in Figure 2.3. The steady part is divided into four solutions (S1 to S4). A vortex sheet representing a flat plate models the effects of the mean angle of attack. The flow deflection due to the airfoil camber at zero incidence is included by another vortex distribution. A

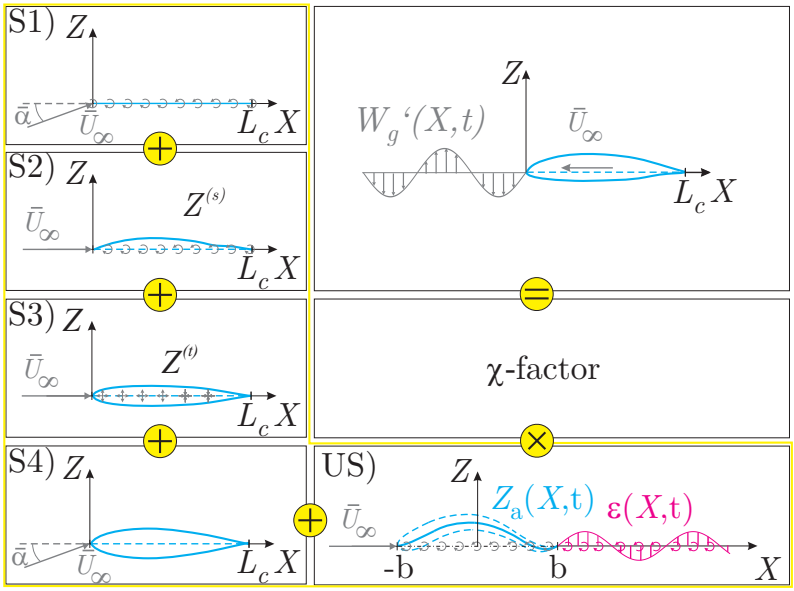

Figure 2.3.: Modular unsteady thin airfoil model.

source-sink sheet incorporates the streamline displacement of the symmetrical airfoil thickness distribution at zero incidence. The fourth contribution is a velocity distribution accounting for the effects of the airfoil thickness, which becomes more important at higher incidence angles (Riegels, 1949). The result of the steady model is the mean velocity distribution $\bar{U}(X)/\bar{U}_\infty$, where the plus and minus signs denote the upper ($\bar{U}_u$) and the lower ($\bar{U}_l$) side of the airfoil.

$$\frac{\bar{U}_{u,l}(X)}{\bar{U}_\infty} = 1 \pm \frac{\bar{U}_{S1}(X)}{\bar{U}_\infty} \pm \frac{\bar{U}_{S2}(X)}{\bar{U}_\infty} + \frac{\bar{U}_{S3}(X)}{\bar{U}_\infty} \pm \frac{\bar{U}_{S4}(X)}{\bar{U}_\infty} \tag{2.5}$$

A summary of the equations of all four components can be found in Appendix A.1. For the steady part, the pressure on the lower and on the upper side of the airfoil is obtained from equation (2.4) by dropping the underbraced term. From the pressure difference $\Delta\bar{P}(x) = \bar{P}_u - \bar{P}_l$ the lift and the angular momentum can subsequently be calculated.

The superimposed unsteady fluctuation of the flow field (US) is described by the vortex sheet approach of Schwarz (1940), which represents the airfoil

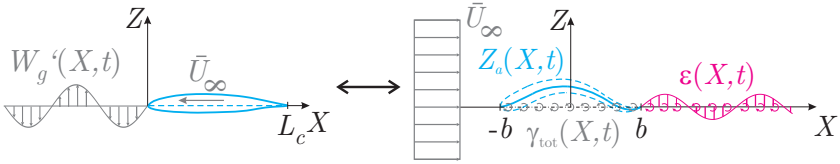

Figure 2.4.: Model of the harmonically deforming thin airfoil.

as a skeleton carrying out small vertical deformations of arbitrary harmonic mode as depicted in Figure 2.4.

$$Z_a(X,t) = \hat{Z}_a(X)\mathrm{e}^{i\omega t} \tag{2.6}$$

The kinematic boundary condition determines the unsteady velocity W_a.

$$W_a(X,t) = \frac{\partial Z_a}{\partial t} + \bar{U}_\infty \frac{\partial Z_a}{\partial X} = \bar{U}_\infty \left(\frac{\mathrm{d}\hat{Z}_a}{\mathrm{d}X} + \frac{i\omega}{\bar{U}_\infty}\hat{Z}_a \right) \mathrm{e}^{i\omega t} = \hat{W}_a(X)\mathrm{e}^{i\omega t} \tag{2.7}$$

According to the assumptions of thin airfoil theory, the unsteady flow effects of the deformable airfoil are described by a harmonically varying vortex sheet on the abscissa ($-b \leq X \leq b, Z = 0$), representing the tangential velocity discontinuity between the upper and the lower side of the airfoil. Note that the ordinate in this derivation is placed at midchord for mathematical convenience. As the boundary conditions vary harmonically, the same functional dependence applies for the vortex sheet representing the airfoil, which causes a jump in the wall-tangential velocity.

$$\gamma_{tot}(X,t) = \hat{\gamma}_{tot}(X)\mathrm{e}^{i\omega t} = \left[\hat{U}_{u,u}(X) - \hat{U}_{u,l}(X)\right] \mathrm{e}^{i\omega t} \tag{2.8}$$

The time-dependent circulation of the airfoil is obtained by the integral

$$\Gamma(t) = \int_{-b}^{b} \gamma_{tot}(X,t)\mathrm{d}X. \tag{2.9}$$

Kelvin's theorem on the conservation of circulation implies that a change of the circulation $\mathrm{d}\Gamma/\mathrm{d}t$ within a time increment $\mathrm{d}t$ requires a vortex shedding of opposite sign at the trailing edge ($X = b = L_c/2$).

$$\bar{U}_\infty \varepsilon(b,t)\mathrm{d}t = -\frac{\mathrm{d}\Gamma}{\mathrm{d}t}\mathrm{d}t = -\int_{-b}^{b} \frac{\partial}{\partial t}\gamma_{tot}(\xi,t)\ \mathrm{d}\xi\mathrm{d}t \tag{2.10}$$

In the thin airfoil approximation the shed vortex distribution ε is convected along the abscissa ($Z = 0$) toward infinity with the free-stream velocity conserving its initial form.

$$\varepsilon(X,t) = \varepsilon\left(b, t - \frac{X-b}{\bar{U}_\infty}\right) \tag{2.11}$$

For $X \geq b$ equation (2.10) can thus be written as

$$\begin{aligned}
\varepsilon(X,t) &= -\frac{1}{\bar{U}_\infty}\int_{-b}^{b}\frac{\partial}{\partial t}\gamma_{tot}\left(\xi, t-\frac{X-b}{\bar{U}_\infty}\right)\,\mathrm{d}\xi \\
&= -\frac{1}{\bar{U}_\infty}\int_{-b}^{b}\hat{\gamma}_{tot}(\xi)\frac{\partial}{\partial t}\left(\mathrm{e}^{i\omega t}\ \mathrm{e}^{-i\omega X/\bar{U}_\infty}\ \mathrm{e}^{i\omega b/\bar{U}_\infty}\right)\,\mathrm{d}\xi \\
&= -\frac{i\omega}{\bar{U}_\infty}\ \mathrm{e}^{i\omega t}\mathrm{e}^{i\omega(b-X)/\bar{U}_\infty}\int_{-b}^{b}\hat{\gamma}_{tot}(\xi)\,\mathrm{d}\xi.
\end{aligned} \tag{2.12}$$

Both, the vortex distribution on the airfoil γ_{tot} and the one in the wake ε induce velocities on the airfoil ($-1 \leq X \leq 1, Z = 0$) described by the law of Biot-Savart. To fulfill the kinematic boundary condition of vanishing vertical velocities on the airfoil skeleton $Z_a(X,t)$, the airfoil velocity $W_a(X,t)$ in equation (2.7) needs to be compensated for.

$$\frac{1}{2\pi}\oint_{-b}^{b}\frac{\gamma_{tot}(\xi,t)}{X-\xi}\,\mathrm{d}\xi + \frac{1}{2\pi}\int_{b}^{\infty}\frac{\varepsilon(\zeta,t)}{X-\zeta}\,\mathrm{d}\zeta = W_a(X,t) \tag{2.13}$$

The first integral of the previous equation constitutes a Cauchy principal value integral. Substituting equations (2.7), (2.8) and (2.12) into equation (2.13) an integro-differential equation for the unknown $\hat{\gamma}_{tot}(X)$ is obtained which can be inverted into an ordinary integral expression (Söhngen, 1939; Bisplinghoff et al, 1996). For some specific boundary conditions analytical solutions for the pressure distribution exist, determining the lift and the angular moment. All intermediate steps are derived in Appendix A.1 since they require considerable mathematical efforts. The airfoil response to vertical harmonic gusts is discussed in detail in the following.

The experimental results of this study will show that NLF airfoils are particularly susceptible to vertical gusts created by atmospheric turbulence. An arbitrary gust shape may be composed of simple harmonic gusts. Therefore, the problem of a harmonic vertical gust is of fundamental importance. Simpler airfoil motions such as heaving and pitching have been computed as well,

but will only be discussed briefly. Note that in the concept of Schwarz (1940) the boundary conditions imposed by a sinusoidal vertical gust can equivalently be expressed as a meandering motion of the airfoil skeleton without any physical inconsistencies in the potential flow field.

$$\begin{aligned} W_a(X,t) &= -W_g'(X,t) = -\hat{W}_g \mathrm{e}^{i\omega\left(t-X/\bar{U}_\infty\right)} = -\hat{W}_g \mathrm{e}^{i\omega t}\mathrm{e}^{-i(\omega b/\bar{U}_\infty)X/b} \\ &= -\hat{W}_g \mathrm{e}^{i\omega t}\mathrm{e}^{i\kappa\cos(\vartheta)} \end{aligned} \tag{2.14}$$

The use of the coordinate transform $X = -b\cos(\vartheta)$, with $0 \leq \vartheta \leq \pi$ and $b = L_c/2$, enables an analytical solution for the amplitude distribution of the pressure difference $\Delta\hat{P}$ between the upper and the lower side. The reduced frequency

$$\kappa = \frac{\omega b}{\bar{U}_\infty} = \; b\; k = \frac{L_c}{2}\; k \tag{2.15}$$

can be related to the wavenumber k in the turbulence spectrum in equation (2.1) by applying the hypothesis of 'frozen turbulence' from Taylor (1938), i.e. the turbulent eddies do not change while the airfoil passes through them.

The following results for the loads in the frequency domain, which are completely derived in Appendix A.1, were obtained for the first time by Sears (1938).

$$\Delta\hat{P}(\vartheta,\kappa) = 2\rho\bar{U}_\infty\hat{W}_g\left(\frac{1+\cos(\vartheta)}{\sin(\vartheta)}\right)\mathrm{S}(\kappa) \tag{2.16}$$

$$\hat{C}_l(\kappa) = \frac{L}{\frac{\rho}{2}\bar{U}_\infty^2 L_c} = \frac{2}{\rho\bar{U}_\infty^2 L_c}\int_0^\pi \Delta\hat{P}\; b\sin(\vartheta)\;\mathrm{d}\vartheta = 2\pi\frac{\hat{W}_g}{\bar{U}_\infty}\mathrm{S}(\kappa) \tag{2.17}$$

$$\begin{aligned} \hat{C}_m(\kappa) &= \frac{M}{\rho\bar{U}_\infty^2 L_c^2} = \int_0^\pi \Delta\hat{P}\;[-b\cos(\vartheta)]\;b\sin(\vartheta)\;\mathrm{d}\vartheta \\ &= -\pi\frac{\hat{W}_g}{\bar{U}_\infty}\mathrm{S}(\kappa) \end{aligned} \tag{2.18}$$

$$\mathrm{S}(\kappa) = \frac{H_1(\kappa)\left(J_0(\kappa)-iJ_1(\kappa)\right)}{H_1(\kappa)+iH_0(\kappa)} + iJ_1(\kappa) \tag{2.19}$$

The function $\mathrm{S}(\kappa)$ named after Sears (1941) is expressed in terms of Bessel and Hankel functions dependent only on the reduced frequency κ. Since it enters linearly into the equations for pressure difference $\Delta\hat{P}$, the lift coefficient $\hat{C}_l$ and the angular moment coefficient $\hat{C}_m$, the function itself describes

the unsteady effects on the airfoil loads. In Figure 2.5 the Sears function is plotted in the complex plane. The modulus $|\mathrm{S}(\kappa)| = \sqrt{\Re(\mathrm{S})^2 + \Im(\mathrm{S})^2}$ describes the amplitude ratio between the unsteady and the quasi-steady solution ($\mathrm{S}(\kappa = 0)$) which attenuates continuously for increasing frequencies κ. The sign variation of the phase angle $\phi = \arctan[\Im(\mathrm{S})/\Re(\mathrm{S})]$ leads to the spiral shape of the Sears function. This can imply positive or negative phase shifts of the airfoil response with respect to the forcing. Also included in the figure, the Theodorsen (1935) function $\mathrm{C}(\kappa)$ represents the complement for heaving and pitching motion due to aeroelastic oscillations or rapid maneuvers, see Appendix A.1 for the definition. The fundamental difference in this excitation is the linear (pitching) or constant (heaving) distribution of the disturbance velocity $W_a(X,t)$ caused by the airfoil motion, whereas multiple wave crests and troughs can be found simultaneously within one chord length for high-frequency sinusoidal gusts. This constrains the response characterized by the Theodorsen function to the lower right quadrant of the complex plane (Bisplinghoff et al, 1996) implying a phase lag and only a limited amplitude attenuation. For reduced frequencies of $\kappa \leq 0.1$ the large gust wavelength almost leads to a correspondence of the two curves.

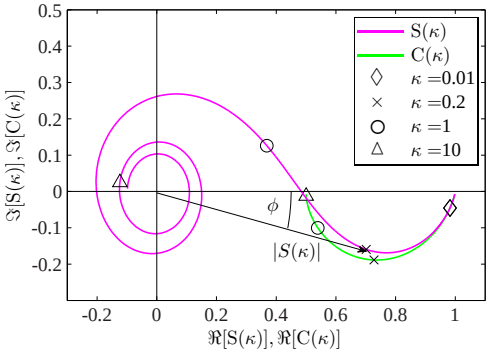

Figure 2.5.: The Sears function in the complex plane.

Although thin airfoil theory is generally rather used for load predictions (Abbot and Von Doenhoff, 1959), the present study focusses primarily on the boundary-layer development of NLF airfoils. For the determination of the unsteady boundary-layer evolution the pressure distribution is not sufficient since unsteady boundary-layer calculations require the prescription of

the outer velocity distribution, as will be shown in Section 2.3.2. Equation (2.8) yields a dependence between the velocity distribution and the vorticity distribution γ_{tot}.

$$\hat{\gamma}_{tot}(\vartheta,\kappa) = 2\hat{W}_g\sqrt{\frac{1-\cos(\vartheta)}{1+\cos(\vartheta)}}\left[-J_0(\kappa) + 2\frac{1-\cos(\vartheta)}{\sin(\vartheta)}\sum_{n=1}^{\infty} i^n J_n(\kappa)\sin(n\vartheta) + \frac{2}{\pi}\frac{\mathrm{S}(\kappa)-iJ_1(\kappa)}{H_1(\kappa)}\int_1^{\infty}\sqrt{\frac{\zeta^+ + 1}{\zeta^+ - 1}}\frac{\mathrm{e}^{-i\kappa\zeta^+}}{\cos(\vartheta)-\zeta^+}\,\mathrm{d}\zeta^+\right] \tag{2.20}$$

Only the semi-infinite integral on the right hand side of equation (2.20), where $\zeta^+ = \zeta/b$, prohibits an analytical solution due to its singularity at the lower integration limit. Historically, this difficulty may be the reason why no solution of γ_{tot} is known from literature, although McCroskey (1973) developed a thin airfoil model for a similar purpose. Despite the mathematical difficulties, the semi-infinite integral can be solved numerically using an adaptive Gauss-Konrod quadrature. Since the integrand only depends on the reduced frequency κ, a look-up table can be computed for every airfoil coordinate ϑ.

The steady part (mean) and the unsteady part (fluctuation) of the model are linearly superposed to obtain a complete solution. All model components including a singularity at the leading edge are multiplied by the Riegels factor χ (Riegels, 1949) enforcing a stagnation point (see Appendix A.1 for the definition). Although this leading-edge correction is rather based on mathematical than on physical considerations, it provides a valuable correction in an engineering sense in the region $X/L_c < 0.15$ (Schlichting and Truckenbrodt, 1967).

Important consequences for airfoil flows become evident when comparing results of the complete unsteady model with its quasi-steady counterpart, which is obtained for the same equations in the limit $\kappa = 0$. Figure 2.6 demonstrates the inviscid airfoil response to a sinusoidal gust with an amplitude of $\hat{W}_g = 3$ m/s, a free-stream velocity of $\bar{U}_\infty = 40$ m/s and a reduced frequency of $\kappa = 0.2$. Considering the Sears function in Figure 2.5, the response of the pressure distribution lags behind the quasi-steady reference for the this case. The attenuation of the unsteady amplitudes can be observed in Figure 2.6(a). Still, the unsteady pressure distribution varies significantly, especially in the leading edge part. The comparison between amplitudes of the quasi-steady and the unsteady velocity distribution calculated with equa-

tion (2.20) qualitatively shows the same trend. Therefore, Figure 2.6(b) is used to demonstrate the influence of the time derivative of the velocity potential in the underbraced term in equation (2.4). Strictly speaking, there is no way to compute the unsteady velocity distribution necessary for boundary-layer computations from an unsteady measurement of the pressure distribution. Using only the steady Bernoulli equation $\sqrt{1 - C_{p,us}}$ introduces a systematic error. From the velocity distribution in Figure 2.6(b) an error of $\Delta U/\bar{U}_\infty = 3$ % on the upper side and 2 % on the lower side is asserted. Although the difference is relatively small for the reduced frequency of $\kappa = 0.2$, it should be kept in mind for the experimental part of this study that the boundary-layer development and its transition from laminar to turbulent are sensitive to changes in the outer flow.

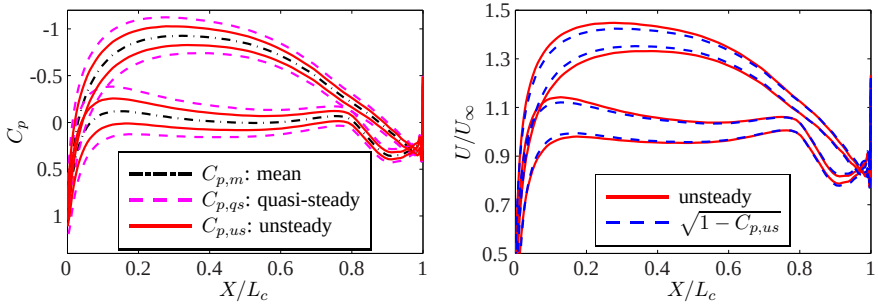

(a) Pressure Distribution

(b) Velocity Distribution

Figure 2.6.: Results of the unsteady thin airfoil model for a mean angle of attack of $\bar{\alpha} = 1$ deg, $\bar{U}_\infty = 40$ m/s, $\rho = 1$ kg/m^3, $W_g = 3$ m/s and $\kappa = 0.2$.

In summary, the inviscid unsteady effects caused by vertical gusts manifest themselves in an attenuation of the amplitudes of both the pressure and the velocity distribution as well as a significant phase shift of the response compared with the quasi-steady expectation. This impedance may of course affect the temporal boundary-layer behavior of an airfoil flying through atmospheric turbulence. Computing a velocity distribution from unsteady pressure measurements with the steady Bernoulli equation leads to systematic errors.

2.3.2. Unsteady Development of the Wing Boundary Layer

For the investigated airfoil flow, strong wall-normal velocity gradients can only be found in the thin boundary layer due to the no-slip condition at the wall. Outside of this region the velocity gradient is small and the effect of viscosity ($\nu \sim O(10^{-5}$ m^2/s) for air) is insignificant. The outer flow can thus be treated by potential flow theory (cf. Section 2.3.1), which is asymptotically matched by the viscous flow at the boundary-layer edge. In the surface-fixed boundary-layer coordinate system (Figure 2.2), characteristic length scales for the wall-tangential direction x and wall-normal direction y are the chord length L_c and the boundary-layer thickness δ ($\delta \ll L_c$), respectively. Choosing the mean free-stream velocity $\bar{U}_\infty$ as a reference, the characteristic time scale $t \sim L_c/\bar{U}_\infty$ is obtained. Furthermore, centrifugal effects are assumed to be negligible and the boundary-layer thickness growth can be shown to be proportional to the square root of the Reynolds number $\sqrt{Re_x} = \sqrt{\bar{U}_\infty x/\nu}$. Using the aforementioned scales and considerations to nondimensionalize the continuity equation and the Navier-Stokes equations, the unsteady boundary-layer equations can be derived from a systematic order-of-magnitude estimate of the individual terms of the conservation equations (Schlichting, 1982). Introducing a stream function ($\vec{U} = (\frac{\partial\psi}{\partial y}, -\frac{\partial\psi}{\partial x})^T$), which fulfills the continuity equation identically, the boundary-layer equations in the dimensional form read:

$$\underbrace{\frac{\partial^2\psi}{\partial y\partial t}}_{\text{I}} + \underbrace{\frac{\partial\psi}{\partial y}\frac{\partial^2\psi}{\partial x\partial y} - \frac{\partial\psi}{\partial x}\frac{\partial^2\psi}{\partial y^2}}_{\text{II}} = \underbrace{-\frac{1}{\rho}\frac{\partial p}{\partial x}}_{\text{III}} + \underbrace{\nu\frac{\partial^3\psi}{\partial y^3}}_{\text{IV}} \tag{2.21}$$

$$0 = \frac{\partial p}{\partial y}. \tag{2.22}$$

The second equation states that the pressure is constant in the wall-normal direction of the boundary layer. The streamwise pressure gradient $\partial p/\partial x$ accounts for the airfoil curvature and it is prescribed by the Euler equation at the boundary-layer edge ($u(x, \delta_e, t) = U_e(x, t)$), which is obtained from a mapping of the inviscid outer flow field onto the edge coordinates of the boundary layer.

$$-\frac{1}{\rho}\frac{\partial p}{\partial x} = \underbrace{\frac{\partial U_e}{\partial t}}_{\text{IIIa}} + \underbrace{U_e\frac{\partial U_e}{\partial x}}_{\text{IIIb}} \tag{2.23}$$

The problem of how a laminar boundary layer responds to fluctuations

of the external flow about a steady mean is of particular importance for the present investigation. Regardless whether the airfoil moves in a uniform stream or whether it is exposed to a convected gust (cf. Section 2.3.1), in the boundary-layer frame of reference the unsteadiness enters from the free-stream boundary (Lighthill, 1954). However, changes in the outer flow will not be uniformly transmitted through the boundary layer toward the wall. Not intuitively at first sight, there are two counteracting mechanisms in unsteady boundary layers. On the one hand momentum diffusion of the free-stream fluctuations lags due to the inertia terms (I and II) in equation (2.21). On the other hand, the constant vertical pressure throughout the boundary layer observed in equation (2.22) leads to a uniform acceleration of the entire boundary-layer profile. Due to the lower inertia in the inner part, the relative effect of this acceleration is stronger on the slowly moving fluid close to the wall. Depending on the unsteadiness of the flow, the inner part of the boundary layer may thus anticipate the free-stream variation while the outer part lags behind. The type of unsteadiness is determined by the relative importance of the two free-stream velocity derivatives (terms IIIa and IIIb) in equation (2.23). As an example consider the case of a flat plate exposed to harmonic stream perturbations of the form

$$U_\infty(t) = \bar{U}_\infty + \hat{U}_\infty \cos\left[\omega\left(t - x/Q\right)\right]. \tag{2.24}$$

Notable differences are observed when comparing a homogeneously varying outer velocity (standing wave, $Q \to \infty$) with the effect of a wave traveling over a flat plate at a finite propagation velocity Q_∞. While the first case is equivalent to a flat plate oscillating laterally in a steady stream, the traveling wave represents the effect of free-stream vortices convected periodically past the plate with their core outside of the boundary layer. The corresponding wavenumber then is $k = \omega/\bar{U}_\infty$, which may be compared with characteristic eddy wavenumbers by considering equation (2.1). The unsteadiness not only increases with the external excitation frequency ω but it is also enhanced by the streamwise growth of the boundary layer (Lighthill, 1954). In both excitation cases it is characterized by the dimensionless frequency parameter κ_δ, which is obtained from the mean free-stream velocity $\bar{U}_\infty$, the angular frequency ω and the streamwise coordinate x.

$$\kappa_\delta = \frac{\omega x}{\bar{U}_\infty} \tag{2.25}$$

Analytical solutions for both cases only exist for specific parts of the frequency range (Lighthill, 1954; Patel, 1975). Complete results require less

restrictive numerical procedures or experiments. Figure 2.7 demonstrates the influence of the frequency parameter κ_δ on the relative amplitude (unsteady to quasi-steady) and the phase of the wall shear stress. The left diagram corresponds to the homogenously varying outer velocity. The right plot represents the effect of a convected gusts with a propagation velocity of $Q = 0.77\ U_\infty$. The numerical results (solid lines) are compared with analytical solutions (dashed lines) from Lighthill (1954) in Figure 2.7(a) and from Patel (1975) in Figure 2.7(b) in the low and the high frequency range. It can be seen that the numerical solution bridges the important intermediate range smoothly. In both cases the wall phase angles ϕ_w approach limiting values with increasing dimensionless frequency. In the standing wave case the phase angle anticipates the free-stream velocity oscillation. A rather strong phase lag is observed in the traveling wave problem. The reason for this behavior can be found in the non-homogeneous pressure gradient in the latter case. For the oscillating flat plate case, the pressure gradient consists only of the term IIIa in equation (2.23) which leads the stream fluctuation by 90°. It creates a strong acceleration in the inner part of the boundary layer which is countered to some extent by inertia. For the convecting gust problem the term IIIb, which lags behind by 90°, assumes a dominating role. This is reinforced by the nonlinear inertia terms II increasing the phase lag toward the wall (Patel, 1975). In the high frequency range, the fluctuations associated with terms I, III and IV in equation (2.21) mainly determine the fluctuation profile (Schlichting, 1982). For the oscillating plate, the fluctuation profiles assume the form of shear waves, similar to the Stokes solution at zero mean velocity, oscillating only in a very thin layer close to the wall. In the convecting gust problem the boundary-layer response is affected as a whole. This explains the markedly different growth rates of the amplitudes in the high frequency range. It should be outlined that self-similarity does not exist for the instantaneous boundary-layer profiles even in simple unsteady flows.

Deeper insight can be obtained by considering typical amplitude and phase profiles for different frequency parameters. In Figure 2.8 such profiles from the experiments of Hill and Stenning (1960) and Patel (1975) are compared for two different frequencies. The amplitude profiles overshoot the quasi-steady value and the maximum is closer to the wall for the higher frequencies. In the case of homogeneous variations of the pressure gradient (Figure 2.8(a)) a phase lead is clearly observed in the inner part and only for high frequencies a lag occurs in the mid section of the fluctuation profiles. In Figure 2.8(b) a phase lag is observed for the entire wall-normal distance increasing toward

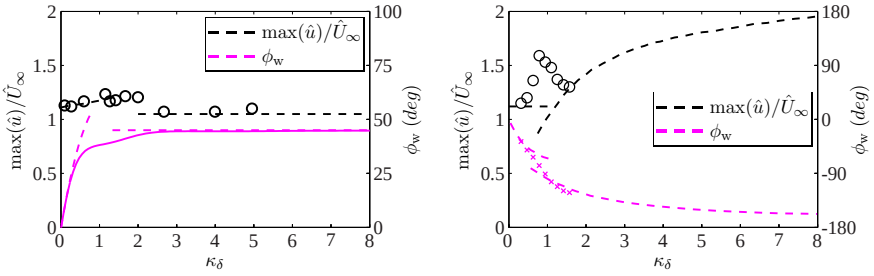

(a) Standing wave

(b) Traveling wave

Figure 2.7.: Variation of the boundary layer with increasing frequency parameter κ_δ. Depicted are the amplitude ratios between the maximum amplitude in the boundary layer and the free stream as well as the phase difference between the free stream and the wall ϕ_w. Dashed lines represent analytical solution from Lighthill (1954) and Patel (1975) and the marker symbols experimental results from Hill and Stenning (1960) and Patel (1975) ($Q = 0.77\ \bar{U}_\infty$). The solid line in 2.7(a) is a reproduction of a numerical solution from Cebeci (1977).

the wall. The amplitude profiles also show a dip besides the overshooting at specific frequencies. In addition to the nonuniform wall-normal phase profile, this further increases the distortion of the instantaneous profiles.

In summary, the unsteady forcing potentially imposed by atmospheric turbulence in the form of convected gusts and airfoil motions can result in considerable distortions of the instantaneous boundary-layer profiles. Fundamental differences in the laminar boundary-layer response may arise from the relative importance of the individual terms in equation (2.23). Whereas term IIIa dominates for rapid airfoil motion, term IIIb assumes the leading role for the convected gust problem. The superimposed mean pressure gradient on an airfoil modifies the unsteady effects (Studer et al, 2006b). Unsteady effects increase with the boundary-layer length which is significant for the investigated airfoil ($L_c = 1.35$ m). The distorted amplitude profiles imply curvature variations instantaneous boundary-layer profiles. This affects the stability characteristics of the boundary layer and can thus lead to unsteady changes of the laminar-turbulent transition process (Obremski and Fejer, 1967; Loehrke et al, 1975; Walker, 1993).

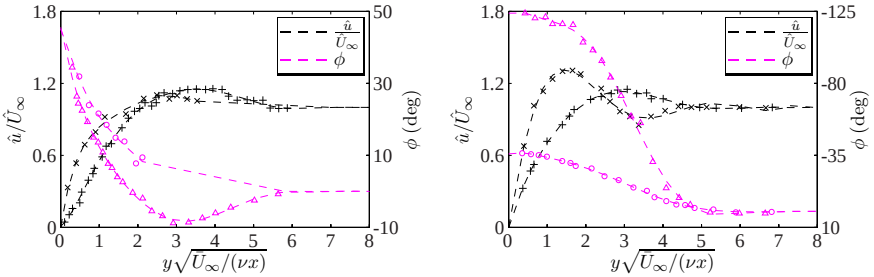

(a) Standing wave: $\kappa_\delta = 0.56$ $(+, \circ)$, $\kappa_\delta = 2.67$ $(\times, \triangle)$.

(b) Traveling wave: $\kappa_\delta = 0.314$ $(+, \circ)$, $\kappa_\delta = 1.570$ $(\times, \triangle)$.

Figure 2.8.: Amplitude and phase profiles of the boundary-layer fluctuations in a flat plate flow for two different forcing cases at two different frequency parameters. Markers represent the experimental results of Hill and Stenning (1960) and Patel (1975). Dashed lines are polynomial fits of the data.

2.4. Boundary-Layer Transition on Natural Laminar Flow Airfoils

Delaying boundary-layer transition passively by shaping the pressure distribution of NLF airfoils requires profound knowledge of the transition process and the underlying physics of the convective instability waves inside the boundary layer.

Laminar-turbulent transition on a NLF airfoil can be divided into different stages as depicted in Figure 2.9: the introduction of external disturbances into the laminar boundary layer creating convective instabilities (the receptivity process), the amplitude-independent downstream evolution of these deterministic disturbances (the linear stage), their interactions altering the laminar boundary layer profiles (the nonlinear stage) and, eventually, the disturbance randomization and breakdown to turbulence. The depicted external disturbances, considered more closely in Section 2.4.2, potentially affect the transition process.

When considering boundary-layer transition in flight through atmospheric turbulence, it should be kept in mind that transition can take different 'routes to turbulence' depending on the external forcing. Such observations were

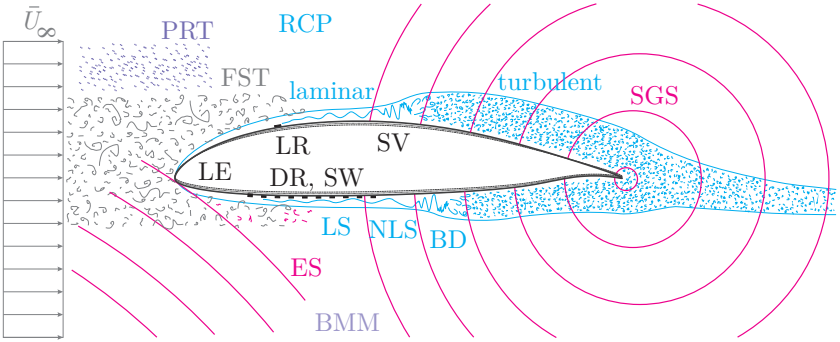

FST	-	free-stream turbulence	LE	-	leading edge	RCP	-	receptivity
ES	-	external sound	LR	-	localized roughness	LS	-	linear stage
SGS	-	self-generated sound	DR	-	distributed roughness	NLS	-	nonlinear stage
PRT	-	liquid or solid particulates	SW	-	surface waviness	BD	-	breakdown
BMM	-	Brownian molecule motion	SV	-	surface vibration			

Figure 2.9.: Boundary-layer receptivity and transition on a NLF airfoil: Forcing disturbance sources, catalysts and transition stages.

structured by Nishioka and Morkovin (1986) and Saric et al (2002) and are reproduced in the schematic Figure 2.10. For low environmental disturbances slow exponential growth of small traveling wavelike flow disturbances (TS waves) is observed. When reaching a certain amplitude, different TS wave modes interact with each other and extract energy from the mean flow. This triggers secondary, nonlinear instability processes which enhance the disturbance level rapidly and eventually cause breakdown to turbulence. With increasing external forcing, combinations of linear modes from an essentially different waveband than the TS waves become important. These modes would not contribute in path A since each one of them decays slowly. How-

ever, depending on the initial disturbance spectrum, non-orthogonal combinations of these modes can induce a transient (non-modal) disturbance growth despite their individual exponential decay. This in turn may lead to spanwise modulations of the boundary-layer flow triggering earlier and different types of secondary mechanisms (path B). Under certain optimal conditions and sufficient forcing these combinations of linear modes introduce perturbations large enough to excite secondary instabilities directly (path C) or to even bypass the classical transition scenario completely (path D). Direct nonlinear interactions leading to immediate breakdown are represented by path E. Whether or not these paths are of importance for NLF airfoils in real flight can only be identified experimentally.

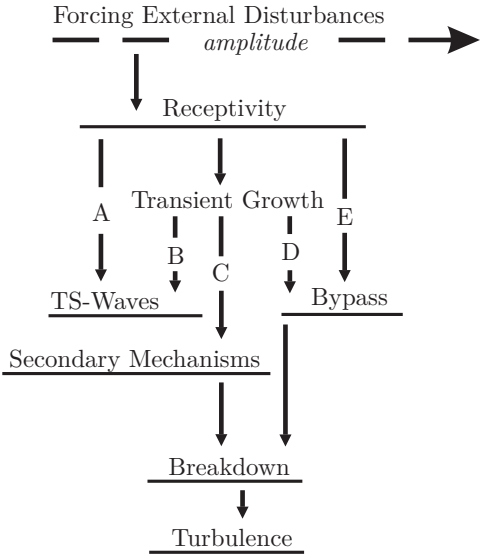

Figure 2.10.: Paths to turbulence, adopted from Saric et al (2002).

2.4.1. Linear Stability Theory

Linear stability theory (LST) is based on a perturbation approach of the Navier-Stokes equations and it describes the evolution of wave modes in the linear, amplitude-independent stage of transition. Therefore, the flow is de-

composed into a quasi-steady base flow and a superimposed disturbance part ($\vec{u} = \vec{\mathcal{U}} + \vec{u}'$ and $p = \mathcal{P} + p'$). By introducing this ansatz into the continuity and the momentum equations, which in this case are nondimensionalized by the quantities $U_\mathrm{e}(x)$ and $\delta_1(x)$ obtained from the boundary-layer solution, the nonlinear disturbance equations are obtained.

$$\nabla \cdot \vec{u}' = 0 \tag{2.26}$$

$$\frac{\partial \vec{u}'}{\partial t} + \vec{u}' \cdot \nabla \vec{\mathcal{U}} + \vec{\mathcal{U}} \cdot \nabla \vec{u}' + \underbrace{\vec{u}' \cdot \nabla \vec{u}'}_{\mathrm{I}} = -\nabla p' + \frac{1}{Re} \triangle \vec{u}' \tag{2.27}$$

Considering only small velocity $\vec{u}'$ and pressure p' disturbances, the underbraced term in equation (2.27) can be neglected and the linear disturbance equations are obtained. The system of equations can be further simplified by the parallel flow assumption $\vec{\mathcal{U}} = \mathcal{U}(y)\vec{e}_x$. This assumption is only fulfilled approximately for the considered two-dimensional boundary layer growing gradually in the streamwise direction.

The set of four partial differential equations (2.26) and (2.27) in four variables can be reduced to a system of two linear differential equations in only two unknowns. Therefore, the flow field decomposition is applied to the curl of the velocity field ($\vec{\Omega}' = \nabla \times \vec{u}'$). The wall-normal disturbance vorticity component is used as an auxiliary variable to describe the spanwise disturbance propagation.

$$\Omega' \equiv \vec{\Omega}' \cdot \vec{e}_y = \frac{\partial u'}{\partial z} - \frac{\partial w'}{\partial x} \tag{2.28}$$

After substantial mathematical conversions, which are presented by Reeh (2008), a set of two linear differential equations in the variables v' and Ω' results.

$$\left[\left(\frac{\partial}{\partial t} + \mathcal{U}\frac{\partial}{\partial x}\right) \triangle - \frac{\mathrm{d}^2\mathcal{U}}{\mathrm{d}y^2}\frac{\partial}{\partial x} - \frac{1}{Re}\nabla^4\right] v' = 0 \tag{2.29}$$

$$\left(\frac{\partial}{\partial t} + \mathcal{U}\frac{\partial}{\partial x} - \frac{1}{Re}\triangle\right)\Omega' = -\frac{\mathrm{d}\mathcal{U}}{\mathrm{d}y}\frac{\partial v'}{\partial z} \tag{2.30}$$

Note that the equations above are of fourth order and equation (2.30) is coupled to (2.29) explicitly by its right-hand side term.

To calculate the linear instability evolution conveniently, a suitable formulation of the disturbances is needed. The linear stage of boundary-layer

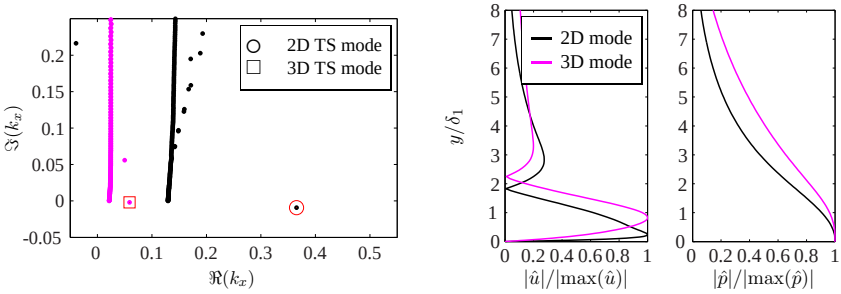

(a) Eigenvalue spectra (b) Wall-normal amplitude functions

Figure 2.11.: Solutions of the eigenvalue problem for the lower-side boundary layer of the investigated airfoil at $X/L_c = 0.3$; $\alpha = -0.92°$, $Re = 3.222 \cdot 10^6$, $U_e = 44.16$ m/s, $\delta_1 = 7.67 \cdot 10^{-3}$ m. 2D TS mode: $f = 1200$ Hz, $k_z = 0$. 3D TS mode: 200 Hz, $k_z = 200$ 1/m.

transition involves small wavelike disturbances of the flow quantities which are described by normal harmonic modes

$$\vec{q}\,'(\vec{x},t) = (\vec{u}', p', \Omega')^T = \hat{\vec{q}}(y)\mathrm{e}^{i(k_x x + k_z z - \omega t)}. \tag{2.31}$$

The complex amplitude function $\hat{\vec{q}}$ is only dependent on the wall-normal coordinate. This implies a local approach to asses the linear stability properties of individual boundary-layer profiles. As the boundary layer is convectively unstable (Drazin and Reid, 1981), the waves are allowed to grow in the streamwise direction x preserving their spanwise wavenumber k_z and their angular frequency ω. In this spatial growth framework, the real part of the complex wavenumber k_x is proportional to the reciprocal of the real wavelength ($\lambda_x = 2\pi/k_{x,r}$) and the imaginary part $k_{x,i}$ is the exponential growth rate of the disturbances.

Substituting the normal mode approach (2.31) into the two disturbance equations (2.29) and (2.30) represents a separation of variables in mathematical terms. It gives rise to the Orr-Sommerfeld (OS) and Squire (SQ)

equations which govern the local linear stability problem

$$\left[(-i\omega + ik_x\mathcal{U})\left(\mathcal{D}^2 - k^2\right) - ik_x\frac{\mathrm{d}^2\mathcal{U}}{\mathrm{d}y^2} - \frac{1}{Re}\left(\mathcal{D}^2 - k^2\right)^2\right]\hat{v} = 0 \tag{2.32}$$

$$\left[-i\omega + ik_x\mathcal{U} - \frac{1}{Re}\left(\mathcal{D}^2 - k^2\right)\right]\hat{\Omega} = -ik_z\frac{\mathrm{d}\mathcal{U}}{\mathrm{d}y}\hat{v}, \tag{2.33}$$

where the differential operator $\mathcal{D}^n = \mathrm{d}^n/\mathrm{d}y^n$ and $k = |\vec{k}| = \sqrt{k_x^2 + k_z^2}$ denotes the modulus of the wave number vector. The system of differential equations constitutes an eigenvalue problem for the eigenvalue k_x and the eigenvectors v' and Ω'. For a boundary-layer base flow the solution yields an eigenvalue spectrum, consisting of a continuous and a discrete part (cf. Figure 2.11(a)). Whereas the TS wave is a discrete mode, eigenmodes of the continuous spectrum are necessary for transient growth (Denissen, 2011), as described in Chapter 1.3. The amplitude functions of the flow quantities u', w' and p' are obtained from the eigenvectors of the solution. Furthermore, the solution of the dispersion relation $k_x = k_x(k_z, \omega, Re)$ governed by equations (2.32) and (2.33) yields the wave propagation angle and the phase velocity of the wave modes.

$$\Psi = \arctan\left(\frac{k_z}{k_{x,r}}\right) \qquad c = \frac{\omega}{k_{x,r}} \tag{2.34}$$

As demonstrated in Figure 2.11 for two-dimensional and oblique wave modes in the studied airfoil boundary layer, LST only provides growth rates and the wall-normal shape of wave modes but it does not give any quantitative information on the amplitudes of the boundary-layer disturbances. Integrating the growth rates $k_{x,i}$, dimensioned with the displacement thickness, from the point of indifferent disturbance amplification (neutral stability, $k_{x,i}(x_0) = 0$) toward some downstream point x, yields the dimensionless N-factor.

$$N = -\int_{x_0}^{x}\frac{k_{x,i}(\xi)}{\delta_1(\xi)}\mathrm{d}\xi = \ln\left(\frac{\hat{A}}{\hat{A}_0}\right) \tag{2.35}$$

The N-factor represents the logarithm of the wave amplitude ratio $\hat{A}/\hat{A}_0$ and it is commonly used for transition prediction methods (Arnal et al, 2008). Still a state-of-the-art airfoil design and analysis tool, the e^N method (Van Ingen, 2008) predicts transition when the envelope of a set N-factor curves resembling two-dimensional wave modes of different frequencies exceeds a specific threshold value. However, this threshold value is purely

determined from some empirical correlation. While the linear growth region is represented correctly, a major deficiency of the e^N-method is the neglect of the mechanism generating the instability waves, i.e. the receptivity process of the boundary layer. As explained by Würz (1995) and Arnal (1992), the semi-empirical method is effective when applied close to the calibration conditions. When employed in slightly different environmental conditions, substantial inaccuracies have been reported (Crouch, 2000). Another deficiency is the complete exclusion of the nonlinear instability development (Reed and Saric, 1996). From an airfoil design perspective this becomes particularly important when transition is not driven by strong adverse pressure gradient but the traveling TS waves develop and interact gradually over a larger streamwise distance. Both omitted stages of transition play a significant role for NLF airfoils in real flight through atmospheric turbulence.

2.4.2. Receptivity to External Disturbances

Receptivity describes the process in which unsteady external disturbances enter the boundary layer and transfer a part of their kinetic energy to excite boundary-layer disturbances, which subsequently amplify or attenuate according to stability properties of the laminar base flow. In the case of small external disturbances, TS waves are formed which evolve according to modal linear stability theory. The receptivity process thus creates the initial conditions for the boundary-layer instability waves in their vital aspects: amplitude, frequency and phase (Saric et al, 2002). Different receptivity mechanisms exist, which should be categorized into forced and natural receptivity for a clear distinction. In the case of forced receptivity an artificial disturbance source such as vibrating ribbon generates a broad disturbance spectrum including the appropriate frequency-wavenumber combination to directly excite instability waves. However, on a NLF airfoil in common flight operation only natural disturbances are present. Figure 2.9 gives an overview of the disturbances, which may be taken into account for natural receptivity mechanisms. The main candidates for the present investigation in gliding flight free of clouds, in which surface vibrations are avoided, are free-stream disturbances, such as self-generated sound and vorticity. These disturbances may entrain into the boundary layer as unsteady fluctuations of the basic state. However, they typically possess longer wavelengths and different phase speeds than the primary instability of the boundary layer, i.e. the TS-waves in the two-dimensional case. Whereas TS waves travel with a fraction of the free-stream velocity, vortical disturbances are convected with

the free stream velocity and acoustic waves travel at the speed of sound. A numerical comparison of the order of magnitude of these quantities is given in Table 2.1. Although the wavelength ranges are overlapping, the kinetic energy of turbulence and sound is usually low within the TS wavenumber range and there is the discrepancy in the phase velocity. However, a wavenumber conversion may enable the transfer of fluctuation energy of larger external disturbances into the eigenmodes of the boundary layer. This mechanism, termed receptivity process, provides the necessary condition

$$k_{\mathrm{TS}} = k_{\mathrm{FD}} + k_{\mathrm{C}}. \tag{2.36}$$

It resembles the coupling of a free-stream disturbance with the wavenumber k_{FD} to the wavenumber of a TS mode k_{TS}. The conversion wavenumber k_{C} is provided by a local or distributed, two or three-dimensional inhomogeneity of the boundary-layer flow. Examples for such heterogeneities are given in Figure 2.9. These short-scale, essentially nonparallel heterogeneities of the base flow (Crouch, 1992a) create a modulation such that a part of the kinetic disturbance energy is transferred to eigenmodes (Dietz, 1999). Therefore, the process is also described as a scattering of the free-stream waves in the literature. The efficiency of the energy transfer is quantified in theoretical studies and generic experiments by the complex receptivity coefficient, which for localized receptivity can be written as (Herr, 2003):

$$\hat{C}_{\mathrm{R}}(\omega_{\mathrm{TS}}, k_z, Re) = \frac{\hat{U}_{\mathrm{TS}}(\omega_{\mathrm{TS}}, k_z)}{\hat{U}_{\mathrm{FD}}(\omega_{\mathrm{FD}})\ \hat{F}(\omega_{\mathrm{TS}}, k_z, k_{\mathrm{C}})}. \tag{2.37}$$

This spectral representation of the receptivity coefficient $\hat{C}_{\mathrm{R}}$ can be interpreted as a transfer function of resulting TS wave spectrum $\hat{U}_{TS}$ and the product between the incoming disturbance spectrum and the spatial Fourier transform of the localized receptivity site.

Although most receptivity investigation have been conducted for two-dimensional configurations, the importance of the three-dimensional aspects of the TS wave generation should not be underestimated since it predetermines the nonlinear disturbance evolution inside the boundary layer (Kachanov, 2000). In the absence of other disturbance sources, the Brownian molecule motion presents a lower bound for instability excitation (Bushnell, 1990; Luchini, 2009).

Table 2.1.: Characteristic properties of disturbances and TS waves in a Blasius boundary layer ($\bar{U}_\infty = 40$ m/s).

	propagation velocity (m/s)	frequency (Hz)	wavenumber (1/m)	wavelength (m)
Acoustic waves	343	50 - 10000	0.916 - 183	0.034 - 6.86
Vorticity (turbulence)	40	12 - 2000	2 - 300	0.02 - 3.14
TS-waves (Blasius flow)	11 - 17	400 - 2400	160 - 900	0.007 - 0.039

2.4.3. Nonlinear Wave Interactions and Breakdown to Turbulence

The onset and the type of nonlinear wave interactions is predetermined by the initial amplitude and the spectral characteristics of the TS waves in the receptivity process. In their subsequent downstream evolution within the linear stage the base flow profiles remain unchanged and the wave modes grow independently. Nonlinearity starts when primary instabilities reach a certain amplitude to modify the base-flow profile such that it becomes unstable toward three-dimensional disturbances and an energy transfer between wave modes of different bands is enabled (Herbert, 1988). This stage of transition is essentially of a resonant nature (Kachanov, 1994) with particular importance of the oblique wave content present in the boundary layer. The first wave modes to amplify and to experience the largest growth rates in the linear stage, the two-dimensional TS waves described as fundamental modes in the following, mainly play the role of an activator and a catalyst in the nonlinear disturbance development to turbulence (Würz et al, 2012). The interactions of wave modes and their rapidly increasing growth lead to the formation of high-shear layers.

In generic experiments differences in the appearance of Λ-shaped high shear patterns have been traced back to the initial amplitude level and the spectral composition of the primary instability waves (Saric and Levchenko, 1984). For flight investigations on a straight wing there are basically two mechanisms to be considered. At low enough initial amplitude levels the primary TS waves are a catalyst creating double-exponential (i.e. exponent in exponent) growth rates for subharmonic instability waves in a parametric

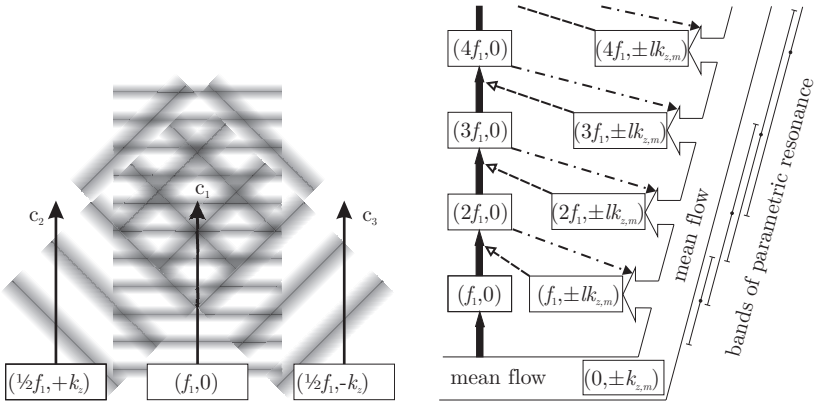

(a) N-regime, simplified illustration of a resonant wave triad

(b) Resonance cascade in the K-regime (Kachanov, 1994)

Figure 2.12.: Nonlinear regimes of boundary-layer transition.

resonance. In this resonance the subharmonic waves extract energy from the base flow without substantial influence on the growth of the fundamental waves. A simplified illustration is provided in Figure 2.12(a). As the subharmonic activity has also been observed in controlled experiments of developing wave packets (Gaster and Grant, 1975; Cohen et al, 1991; Breuer et al, 1997; Medeiros and Gaster, 1999), the subharmonic resonance or N-regime is more probable for low disturbance environments usually associated with gliding flight under ideal conditions (Boiko et al, 2002). The necessary frequency and spanwise wavenumber combination (f,k_z) produces a staggered formation of the Λ-structures in the downstream direction in controlled experiments. At higher initial disturbance levels subharmonics may not have the time to operate since oblique modes at the fundamental frequency activated by weak higher harmonics dominate the nonlinear process. This K-type scenario, named after its discoverer Klebanoff et al (1962), produces streamwise aligned Λ-patterns under controlled conditions.

The N-type of transition is the result of parametric resonance between the fundamental waves at frequencies f_1 and oblique waves at frequencies $f_2 = f_3 = 1/2f_1$. A resonant triad (Craik, 1971) is therefore composed of the modes

$$(f_1, 0), \quad (f_1/2, k_z), \quad (f_1/2, -k_z). \tag{2.38}$$

The phase synchronism condition for parametric resonance requires equal phase speeds and determines the streamwise wavenumber.

$$c_1 = c_2 = c_3 = 2\pi f/k_x, \quad k_{x,2} = k_{x,3} = \frac{1}{2}k_{x,1} \tag{2.39}$$

This mechanism is quite restrictive considering the fact that the TS wave disperse in their downstream evolution and the base flow is usually not self-similar in an airfoil boundary layer. However, Kachanov and Levchenko (1984) showed that the double-exponential growth associated with subharmonic resonance exists for considerable frequency detunings Δf. Even for $\Delta f \approx \pm f_1/4$ substantial growth was observed and the mechanism works for a rather broad band of frequencies, which cannot solely be explained by Craik's triad (2.38). Borodulin et al (2002) further show that moderate detunings in the spanwise wavenumber Δk_z do not jeopardise the amplification of the quasi-subharmonics. Wu et al (2007) present a theoretical explanation for these parametric resonances.

An intrinsic prerequisite for the K-regime is a very weak spanwise modulation of base flow ($f = 0, k_{z,m}$), which in a real flow may also be created by transient effects associated with the entraining of streamwise vorticity of free-stream turbulence (cf. path B in Figure 2.10). The four-wave resonance concept introduced by Kachanov (1994) describes the role of the first overtone $2f_1$ of a high amplitude two-dimensional fundamental wave f_1. The weaker higher harmonic modifies the base flow profile such that it becomes susceptive towards oblique waves at the fundamental frequency with a spanwise modulation wavenumber $k_{z,m}$ closing the four-wave feedback loop

$$(f_1, 0), \quad (2f_1, 0), \quad (f_1, k_{z,1}), \quad (f_1, -k_{z,m}). \tag{2.40}$$

Furthermore, Kachanov found out that the mechanism is not restricted to a single feedback loop but continues in the same manner for the overtones in a resonance cascade. The process depicted in Figure 2.12(b) produces multiple wave resonance which may be characterized by the combinations

$$(nf_1, 0), \quad (mf_1, \pm lk_{z,m}), \tag{2.41}$$

where $n = 2, 3, ...$, $m \approx n/2$ and $lk_{z,m} \approx k_{z,m}$ is the initial spanwise modulation of the base flow. The multiple superposed higher-harmonics can explain the spikes observed in experimental investigations of K-type transition. When decomposed in Fourier space, the spikes reveal the overtones of

the cascade and thus prove their deterministic nature which creates the high shear formations.

The features of the K- and the N-regime only describe the initial nonlinear wave interactions. The development of high-shear layers, their interactions, vortex roll-up and the formation of turbulent spots represent further substages in the breakdown process. Due to their very short streamwise extent, they are of minor importance for transition prediction on airfoils and they are therefore not described in more detail.

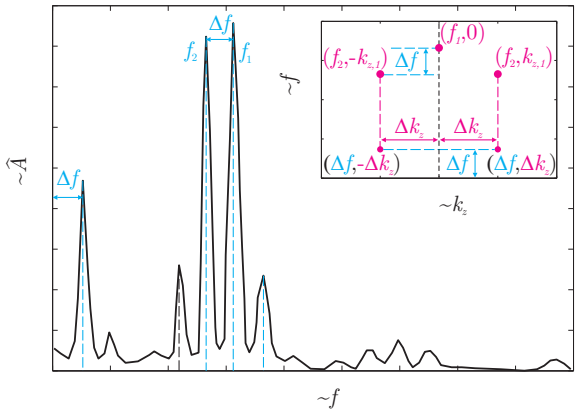

Figure 2.13.: Illustration of the generation of combination modes, partly adopted from Boiko et al (2002).

Another interesting nonlinear phenomenon for the present investigation is the generation of 'difference modes' through nonlinear combinations of primary modes. The mechanism was demonstrated by Kachanov and Levchenko (1984). Two fundamental wave modes with a frequency difference $\Delta f = f_1 - f_2$ at sufficient amplitude produce a difference mode at the frequency $f_\Delta = \Delta f$ in an unstable laminar boundary layer. This effect is explained by the weakly nonlinear effects associated with the underbraced term in the nonlinear disturbance equations (2.27). The mechanism is not limited to a single difference mode but it initiates a whole cascade of possible 'combination modes' as depicted in Figure 2.13. It is shown by de Paula et al (2013) that the combination principle also applies for the spanwise wavenumbers of

the resulting modes.

$$\begin{aligned} f_{\Delta(m,n)} &= |mf_1 \pm nf_2| \qquad m,n = 1,2,... \\ k_{z,\Delta(r,s)} &= rk_{z,1} \pm sk_{z,2} \qquad r,s = 1,2,... \end{aligned} \tag{2.42}$$

Combinations between fundamental and difference modes may create further modes redistributing fluctuation energy into different wavebands. Although initially small in amplitude, self-generated difference modes with specific frequency-wavenumber combinations may be the seeds for subsequent resonant amplification. Due to the double-exponential growth rates common to the subharmonic regime, such modes can assume a transition-dominating role (de Paula et al, 2013).

The question which nonlinear mechanism dominates on a NLF airfoil in real flight under different environmental conditions and whether the presented concepts are interconnected is one of the topics in this study.

3. Methods and Facilities

The simultaneous investigation of all interacting aerodynamic effects described in the previous chapter can only be conducted in a flight experiment since the spectral composition of atmospheric turbulence cannot be simulated in ordinary wind tunnels. The need for a simultaneous measurement of the oncoming flow quantities, the resulting unsteady airfoil effects and the boundary-layer transition development on a NLF airfoil require a comprehensive measurement platform. In this chapter all the components of the measuring system relevant for the present investigation will be introduced, including a detailed uncertainty estimation. Since flight testing requires special procedures, these are explained and the role of the pilot in flight through turbulence is critically reviewed. To shed further light into the aerodynamic mechanisms, it is highly desirable to complement the experimental results with numerical computations. Therefore, the employed numerical methods are described and their accuracy is verified in this chapter.

3.1. Experimental Setup

3.1.1. Research Aircraft

The flight test aircraft is a Grob G109b motorized glider sufficiently powered to enable viable climb rates for the experiments. The aircraft has a simple trapezoidal wing with a span of 17.4 m and an aspect ratio of 15.9. Modifications for the in-flight experiments are summarized in Figure 3.1. The most significant modification is a wing glove on the starboard side (position 3) mantling the original wing between the aileron and the airbrake. On the port wing the probes of an air data system are boom-mounted. It serves as a reference, measuring the flow quantities static pressure (Setra 270, accuracy 3.25 Pa), dynamic pressure (Setra 239HP, accuracy 6.94 Pa), temperature (PT1000, accuracy 0.2 K), relative humidity (Hygrosens CON-HYTEMOD-I2C, accuracy 3 %), angle of attack and side slip angle (both obtained from a Dornier wind vane probe, accuracy 0.1°). The flow angle information from the wind vane is also used for a pilot guidance display.

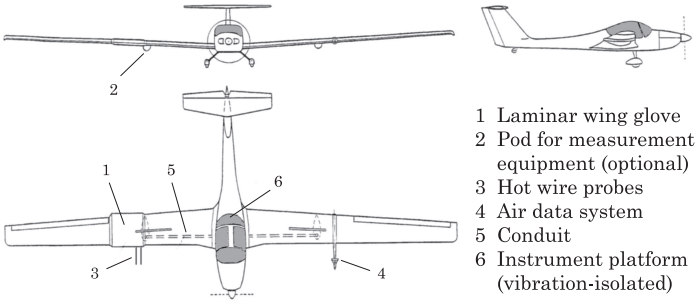

Figure 3.1.: Research aircraft Grob G109b and modifications.

The motorized glider concept enables measurements in powerless flight. This avoids disturbances of the flow, especially noise and vibrations (cf. Chapter 2.4.2), due to the engine and electromagnetic interference with measurement instrumentation. All modifications of the aircraft are certified by the aviation authorities, including a permit to increase the maximum take-off weight from 850 kg to 950 kg. Calibrated airspeeds in the experimental configuration range from 25 m/s to 50 m/s. Further information on the aircraft and the wing glove is given by Weismüller (2011).

3.1.2. Laminar Wing Glove

The simple wing planform with only slight forward sweep and dihedral is convenient for two-dimensional flow investigations. The laminar wing glove was designed to meet all requirements on the desired flow quality and to house the principal measurement instrumentation. Based on a modified version of the AH 93-157 NLF airfoil for sailplanes (Althaus, 1996) shown in Figure 3.2(a), the glove is rectangular in planform with a chord of length $L_c = 1.35$ m and a width of 1.55 m including two 0.1 m wide fillets to the aircraft wing. Weismüller (2011) modified the thickness, the leading-edge radius and the camber of the airfoil such that the lift and drag characteristics of the wing glove compensate for the additional weight and the enlarged thickness of the wing section. The modifications lead to balanced flying qualities, similar to those of the unmodified aircraft for the experimental flight envelope, despite the asymmetric configuration. Furthermore, special attention was paid to an advantageous pressure distribution for the transition investigations. On the lower side of the wing glove positive or negative streamwise pressure

gradients can be adjusted depending on the angle of attack. Specific care was taken on the surface finish through wet sanding and repeated polishing, resulting in a surface roughness of the order of 1 μm. The airfoil geometry data for the wing glove and the aircraft wing can be found in Appendix A.2. Wind-tunnel and flight measured airfoil polar diagrams are presented by Weismüller (2011).

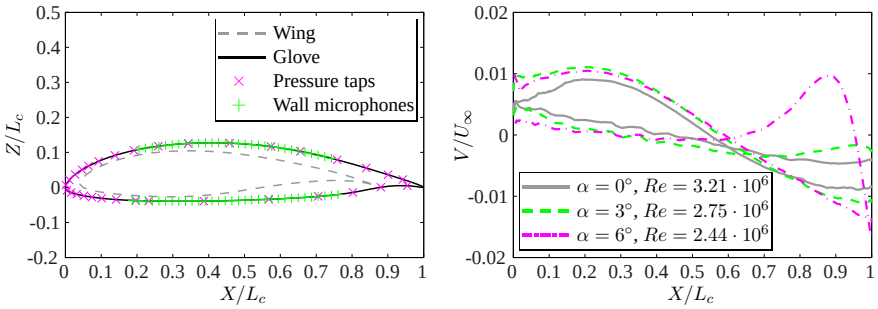

(a) (b)

Figure 3.2.: The laminar wing glove. Left: geometry and the sensor distribution (configuration 1). Right: CFD results for the spanwise velocity along the centerline in a 5mm distance normal to the wall.

For the detection of oncoming flow disturbances hot-wire and pressure probes are mounted on two booms which extend 0.9 m from the leading edge of the wing glove into the free stream. In a storage pod on the lower side, at the edge toward the fuselage, most of the measurement instrumentation is installed to reduce cable lengths. The wing glove covers the spanwise wing section from 3.1 m to 4.65 m, measured from the symmetry axis of the aircraft, such that there is no sweep angle. To substantiate the assumption of two-dimensional flow in Chapter 2.2, three-dimensional RANS-simulations of the starboard wing were conducted by Schulze (2010) for three typical flight conditions. As can be seen in Figure 3.2(b) cross-flow components $\bar{V}/\bar{U}_\infty$ along the centerline of the wing glove, where transition is investigated, amount to less than 2 % for angles of attack below 6° at a 5 mm distance normal to the surface (inviscid outer region, the cross-flow Reynolds number is less than $5 \cdot 10^4$). For the investigated flow conditions the lift coefficient is relatively low and the induced angle of attack is small ($< 1°$ assuming an

elliptical circulation distribution). The effects of the instrument storage pod and the two probe booms on the flow are also insignificant at the centerline. Flow visualizations with tufts from Weismüller (2011) confirm this flow behavior. Comparisons of the experimental results with two-dimensional boundary-layer computations are therefore justified.

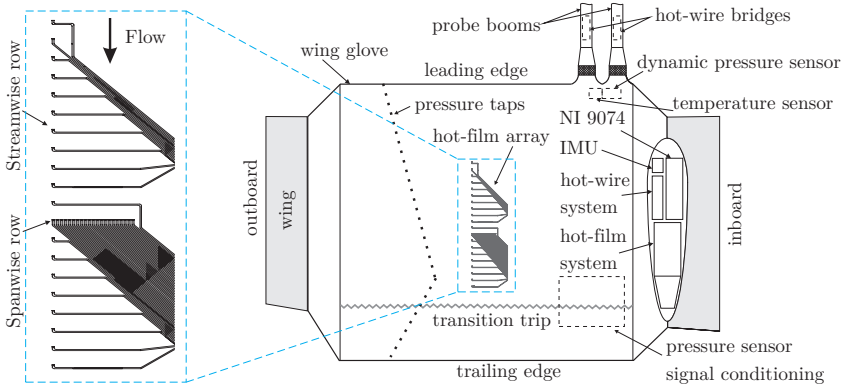

Figure 3.3.: Measuring system components on the wing glove (configuration 2). View on the lower side.

3.1.3. Measuring Instrumentation, Calibration and Data Acquisition

A variety of sensors has been installed on the wing glove. For the present investigation four types of sensors are of particular importance. In the course of the project increased resolution requirements lead to a second generation of the principal measuring system, which enabled additional investigations. Since results of both configurations will be presented in the following chapters, Table 3.1 gives an overview of the changes.

Detection of the Oncoming Flow Fluctuations

The oncoming flow fluctuations are detected with hot-wires and constant temperature anemometers (CTAs). Cross-wire probes (also named X-wire probes, Dantec Dynamics 55P61, probe support 55H24) are used to measure velocity fluctuations in two components. Using two probes mounted on the

Table 3.1.: Changes in the measuring system components and the sampling rates.

Configuration	1	2
Flight campaigns	2011 and 2012	2013
Hot-wire anemometry	4 Dantec mini CTAs	2 Low noise CTAs
f_s (kHz)	20	16/25
Pressure sensors	32 transducers	48 transducers
f_s (kHz)	0.5	1
Transition detection	64 wall microphones	64 surface hotfilms
f_s (kHz)	6.4	16 or 20
Inertial measurements	3 accelerometers	1 INS and 1 AHRS
f_s (kHz)	0.5	0.1

probe booms of the wing glove all three components, as well as fluctuations of the angle of attack and the angle of side slip can be obtained. For simplicity an effective velocity scheme is used to determine the directional sensitivity of the X-wire probes. The effective angle calibration (Bradshaw, 1971) provides sufficient accuracy for the investigated flow angles in the range of $\pm 10°$. The effective cooling velocity $U_{\text{eff}} = f(\Upsilon)U_\infty$ is a velocity equivalent to express the directional dependence of the convective heat transfer of a finite length hot-wire to the dominating normal flow component and the influence of the tangential flow. If the wire is placed normal to the flow, the effective cooling velocity is equal to the free-stream velocity. A modified King's law (Bruun, 1995), relating the anemometer bridge voltage E_b with the convective heat transfer, is given as

$$E_{\text{b}}^2 = A + BU_{\text{eff}}^n = A + Bf^n(\Upsilon)U_\infty^n = A + \tilde{B}(\Upsilon)U_\infty^n. \tag{3.1}$$

The functional dependence of the effective velocity on the probe inclination θ is assumed to follow a simple cosine law for an infinite wire $f(\Upsilon) = \cos(\Upsilon) = \cos(\overline{\Upsilon} + \theta)$, neglecting to first order the tangential contribution to the convective heat transfer. Since the actual geometric slant angle of the wire with respect to probe axis $\overline{\Upsilon}$ is not known a priori (wires are inclined at approximately 45°), an effective value $\overline{\Upsilon}_{\text{eff}}$ for the directional sensitivity is determined in an angle calibration. The empirical correlation $f(\Upsilon_{\text{eff}}) = \cos(\Upsilon_{\text{eff}}) = \cos(\overline{\Upsilon}_{\text{eff}} + \theta)$, where Υ_{eff} is called the effective yaw angle, takes account of the finite wire length and prong interference effects. For moderate probe yaw angles the calibration parameter B in equation (3.1) is

constant and can be eliminated by using the ratio for the yaw dependence:

$$\frac{f(\Upsilon)}{f(\overline{\Upsilon})} = \left[\frac{E\mathrm{b}^2(\Upsilon) - A}{E\mathrm{b}^2(\overline{\Upsilon}) - A}\right]^{\frac{1}{n}} = \frac{\cos(\overline{\Upsilon}_{\mathrm{eff}} + \theta)}{\cos(\overline{\Upsilon}_{\mathrm{eff}})} = \cos(\theta) - \underbrace{\tan(\overline{\Upsilon}_{\mathrm{eff}})}_{\mathrm{I}} \sin(\theta). \quad (3.2)$$

When the $\cos(\theta)$ term is converted to the left-hand side, equation (3.2) constitutes a linear equation for the only unknown $\tan(\overline{\Upsilon}_{\mathrm{eff}})$ as illustrated in Figure 3.4.

The pre-flight calibration on the ground consists of two steps. First a velocity calibration is carried out with the probe support aligned parallel to the flow ($\theta = 0$, hot-wires conversely yawed) to determine the constants A, $\tilde{B}(\overline{\Upsilon})$ and n. Second, an angular traverse at constant velocity is carried out. A linear least square fit is applied to the calibration data in order to determine the parameter $\overline{\Upsilon}_{\mathrm{eff}}$ from equation (3.2). Consequently, the constant $B = \hat{B}(\overline{\Upsilon}_{\mathrm{eff}})/\cos(\overline{\Upsilon}_{\mathrm{eff}})$ and the effective velocity from equation (3.1) are obtained. Note that $\overline{\Upsilon}_{\mathrm{eff}}$ is not equal to the actual geometric slant angle $\overline{\Upsilon}$, since it is a parameter of the directional sensitivity assumption $f(\Upsilon)$.

The effective velocities of the two wires of an X-wire probe are evaluated by using the corresponding anemometer outputs. A sum and difference procedure yields a system of equations for the determination of the two velocity components detectable with a X-wire probe.

$$U_{\mathrm{eff1}} = U\cos(\overline{\Upsilon}_{\mathrm{eff1}}) - W\sin(\overline{\Upsilon}_{\mathrm{eff1}}) \quad (3.3)$$

$$U_{\mathrm{eff2}} = U\cos(\overline{\Upsilon}_{\mathrm{eff2}}) + W\sin(\overline{\Upsilon}_{\mathrm{eff2}}) \quad (3.4)$$

The velocity components U and W are found by Gaussian elimination and the corresponding oncoming flow angle is calculated from $\alpha = \arctan(W/U)$.

The high frequency content of the oncoming flow determines the excitation of boundary-layer disturbances as described in Chapter 2.4.2. Furthermore, gaining insights into the spectral composition of small-scale atmospheric turbulence requires a high sensitivity over a large bandwidth (> 10 kHz) as a consequence of the power-law decay of energy spectrum in equation (2.1). Thus, a small hot-wire diameter of only 2.5 μm is used in order to reduce the thermal inertia of the sensors. The four Dantec Dynamics 54T30 Miniature CTAs used in configuration 1 were not able to resolve the dissipative range of the turbulence. Therefore, a customized CTA system designed by Baumann (2013) was used in configuration 2 including low noise anemometers and elaborate signal conditioning. The measuring bridge circuits and

the feedback controllers are installed directly in the two probe booms, reducing probe cable length to a minimum (<0.8 m). The signal conditioning unit is installed in the storage pod (cf. Figure 3.3). The anemometers are directly battery supplied to avoid high frequency disturbances from DC/DC-converters. Signals are conditioned in two parts, a DC and an AC coupling. The DC part with a low-pass bandwidth of 3.8 kHz (sampling frequency 16 kHz) allows correlations of the oncoming flow quantities with other flow quantities and the motion of the wing glove. The AC part is coupled with a band-pass filter (edge frequencies 50 Hz and 8 kHz) and a low noise amplifier (amplification between 200 and 1000) to detect the dissipation range in the atmospheric turbulence spectra (cf. Figure 2.1). A Delta-Sigma A/D-converter (logging data rate 25 kHz) is used to avoid aliasing of self-induced electronic anemometer noise at high frequencies (Freymuth and Fingerson, 1997).

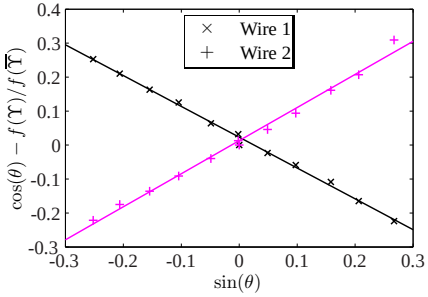

Figure 3.4.: Linear relation for determining the effective angle in a X-wire probe calibration.

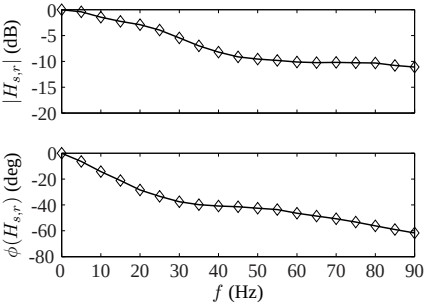

Figure 3.5.: Typical Bode diagram for a in-situ dynamic pressure calibration (line length 0.15 m).

Measurement of the Unsteady Pressure Distribution

The instantaneous pressure distribution on the wing section is important for the evaluation of airfoil lift and the investigation of unsteady flow phenomena. Furthermore, it is a prerequisite for boundary-layer and transition investigations to measure the pressure evolution accurately and provide smooth boundary conditions for the accompanying numerical computations.

The pressure distribution is measured with temperature compensated piezo-resistive miniature pressure transducers (Sensortechnics HCL12XP5, static accuracy 3.1 Pa). The nonuniform distribution of the pressure taps shown in Figure 3.2(a) accounts for high pressure gradient regions. The signals are amplified and the offsets are adjusted to exploit the measurement range of the AD-converters increasing the signal-to-noise ratio. Static calibrations were carried out in situ with a Mensor CPC 6000 (accuracy 1.8 Pa) calibration device before every flight test campaign.

To detect fast pressure changes resulting from turbulent gusts, the sensors are installed beneath the wing glove surface close to the taps minimizing pneumatic line length effects (tubes shorter than 0.1 m). However, even short pressure lines affect the frequency response considerably, as can be seen in Figure 3.5. In order to measure accurately with a bandwidth of at least 45 Hz, a dynamic in-situ calibration (ISA, 2002; Damion, 1994; Perls et al, 1960) was carried out. A calibration device developed by Wolfram (2012) generated sinusoidal pressure signals in steps of 5 Hz up to frequencies of 90 Hz. Whereas one signal line connected to a pressure tap on the wing glove (opening diameter 0.3 mm), the same signal was simultaneous applied to a calibration reference tap with minimum dead volume, feeding a reference sensor. The Kulite XCQ-93 reference sensor (accuray 7 Pa) has a very flat frequency response far beyond the targeted frequency. The obtained amplitude and phase difference between each sensor of the wing glove pressure system and the reference sensor is used to correct the pressure measurements. The frequency response function $H_{s,r}$ (Bendat and Piersol, 2010; Mish and Devenport, 2003) is defined as the dimensionless ratio between the cross-spectral density $G_{s,r}(f)$ of the sensor (subscript s) and the reference sensor (subscript r) and the auto-spectral density $G_{r,r}(f)$ of the reference sensor

$$H_{s,r}(f) = \frac{G_{s,r}(f)}{G_{r,r}(f)} = \frac{E\left[P_s(f) \cdot P_r^*(f)\right]}{E\left[P_r(f) \cdot P_r^*(f)\right]}, \tag{3.5}$$

where f is the frequency, P_s is the complex Fourier coefficient of the sensor signal and P_r is the coefficient of the reference sensor. $E[\,]$ is the expectation and the asterisk denotes the complex conjugate. The pressure signal p_{cor} is corrected by multiplying the Fourier transform of the measured signal P_m with the reciprocal of the transfer function $H_{s,r}$ and applying the inverse

Fourier transform $\mathcal{F}^{-1}$.

$$p_{\mathrm{cor}}(t) = \mathcal{F}^{-1}\{P_{\mathrm{cor}}(f)\} = \mathcal{F}^{-1}\left\{P_m(f)\cdot\frac{1}{H_{s,r}(f)}\right\} = \mathcal{F}^{-1}\left\{\frac{|P_m(f)|}{|H_{s,r}(f)|}\cdot\exp[-i\arg(H_{s,r}(f))]\right\} \tag{3.6}$$

Transition Investigation

Transition detection and investigation is accomplished with arrays of wall sensors in order to minimize disturbances in the boundary layer and to avoid any undesirable receptivity due to their installation. Since one primary interest of this study is the evolution of boundary-layer disturbances, the two transition measurement techniques presented in the following exploit the characteristic TS wave properties. As shown in Figure 2.11(b), the amplitude profiles exhibit maxima directly at the wall for both quantities to be measured, the pressure fluctuation $\hat{p}$ and the wall-shear stress fluctuations ($\propto \partial\hat{u}/\partial y$).

In configuration 1 miniature back-electret microphones (PMO 4015), included in the wing-glove structure with openings to the flow of 0.2 mm in diameter, are used to measure the pressure fluctuations in the boundary layer. The microphones with a diameter of 4 mm are mounted in vibration-cushioned casings sealed with hot glue. The minimal dead volume optimizes the frequency response and is insensitive for Helmholtz resonance. Due to the small opening no additional receptivity is expected from the sensor installation. A signal-to-noise ratio of 58 dB and a sensitivity variation of less than 3 dB in the frequency range between 200 Hz and 4 kHz are specified by the manufacturer. The microphone signals are filtered and amplified in a custom unit. In the experiments 32 microphones were distributed equidistantly (25 mm spacing) in the streamwise direction on the lower side and 32 on the upper side of the airfoil. The microphone arrays were calibrated with a white noise source at a distance of 4 m in a sound-absorbing environment. Equations (3.5) and (3.7) were again applied using the reference signals of a Roga Instruments RG50 microphone with a frequency response better than 1 dB of the sound pressure level in the range from 30 Hz to 4 kHz. This in-situ array matching and calibration scheme yields reasonable results for the transition investigation. An important advantage of wall microphones is the linear sensor characteristic.

In configuration 2 the relation between the wall shear stress and the con-

vective heat transfer is exploited with surface hot-films to obtain insights into the transition process. Details on the physical principle of surface hot-film measurements will be given in Section 3.3.2. A compact 64-channel constant temperature hotfilm system was custom-designed for in-flight experiments by Klähn (2013). It fits in the small storage pod, resulting in short cable lengths to the sensors ($\approx$ 1.3 m). Using FPGA technology, the hotfilm system operates with an internal sampling frequency of 400 kHz per channel. To increase the signal-to-noise ratio a real-time moving average a 25-fold oversampling of the signals is applied internally providing an output data rate of 16 kHz for logging. Depending on the measurement task, a DC- or an AC-coupling of the amplified signal can be acquired. For the study of boundary-layer disturbances the utilization of the full measurement range in the AC-mode is convenient. A special flight-testing feature of the device is a control circuit which automatically measures the cold resistance as well as the ambient temperature before the measurement sequence of 20 s and adjusts all sensor elements to the predefined overheat ratio of typically 1.4.

Customized arrays of Senflex hot-films are used for the experiments. The arrays are manufactured such that the hotfilm sensors and the leads shown in Figure 3.3 are deposited on a polyimide substrate, leading to a maximum thickness of $r = 8$ μm. The typical roughness Reynolds number $Re_r = U_e r/\nu$ of $O(10)$ is one order of magnitude smaller than the level relevant for vortex receptivity, which was estimated with scaled flat plate results from Dietz (1999). The array sheets were bonded on the wing section resulting in a thickness of 51 μm. Filler was carefully applied at the upstream edges to provide a smooth and flush ramp to the array. Seitz (2007) shows that such a slight and gradual change of the airfoil contour is insignificant for the boundary-layer development. An array comprises a hotfilm sensor row in the streamwise direction (20 sensors equidistantly distributed every 28 mm) and a spanwise sensor row consisting of 21 elements in a equidistance of 5 mm. The streamwise row captures the disturbance amplification, the streamwise changes in the transition process and the breakdown to the turbulent boundary layer. The row normal to the base flow detects the spanwise bandwidth of the TS wave packets, i.e the spanwise wavenumber distribution of the waves. On the upper side of the wing glove a mirrored version of the array on the lower side is positioned although only the streamwise row was used for the present experiments. The dynamic sensor response is matched by tripping the boundary layer close to the leading edge in a calibration flight. The resulting disturbance spectrum of the turbulent boundary layer best resembles a white noise source for an in-situ matching of the whole array.

The slight weakening of the fluctuation intensity in the streamwise direction (Cebeci and Bradshaw, 1977) in a fully turbulent boundary layer is not accounted for. It will be seen in Chapter 5 that this effect is insignificant for the interpretation of the results of the present investigation.

Inertial Measurements

The question whether the aerodynamic forces directly translate into motions of the airfoil and whether the elasticity of the wing plays an important role in the process can be partially answered by the integration of inertial measurement units into the research aircraft. Since the three accelerometers distributed on the wing glove structure in configuration 1 could not obtain all the details of the airfoil motion, a SBG Systems I500A attitude and heading reference system (AHRS) was included in the wing glove structure in configuration 2 and an IG-500N inertial navigation system (INS) was installed in the fuselage of the aircraft in proximity to its center of gravity. The AHRS and the INS both include three accelerometers (accuracy 0.5 mg) and three gyros (accuracy 0.5° at 300°/s), providing information on the actual accelerations and angular velocities of the airfoil and the fuselage at an output rate of 100 Hz. Of particular interest is the minimum magnitude of oncoming flow disturbances that leads to a motion of the wing section and, at larger oncoming flow disturbance levels, the response of the airframe to unsteady aerodynamic behavior. The integration of the difference in acceleration and angular velocities of the two inertial measurement units yields the relative motion between the wing section and the fuselage.

Data Acquisition and System Synchronization

The analogue signals of the hot-wires, the pressure sensor and the microphones were acquired using a National Instruments cRIO 9074 system with NI 9205 A/D-converter modules. All the other system components were triggered with the edges of TTL-signals provided by a NI 9401 module. The synchronization of the system components and high sampling rates are indispensable prerequisites for investigations under turbulent conditions. The digitized data was sent via Ethernet or Universal Serial Bus from the system components to a small PC installed behind the cockpit seats. A specific control interface for the experiments was developed using the software LabVIEW.

3.1.4. Avoidance of Systematic Inaccuracies, Experimental Uncertainty and Error Propagation

The accuracy of experimental results is affected by static and dynamic uncertainties. Static errors are subdivided into systematic and random errors. Systematic errors are reproducible and they can be eliminated by a proper correction if they are known. The variance of the random error is a measure of the precision of the experiment. Dynamic errors arise in unsteady measurements from a nonuniform transfer function of the measurement chain in the frequency domain.

The instrument accuracies presented in Sections 3.1.1 and 3.1.3 refer to unknown systematic uncertainties such as nonlinearity and hysteresis as well as random errors of the entire measurement chain. The uncertainty of combined quantities $\Phi_\mathrm{c} = \Phi_c(\Phi_1, \Phi_2, \ldots, \Phi_n)$ is estimated by an error propagation law based on the assumption of independent individual quantities Φ_n. The absolute error $G_\mathrm{max}(\Phi_\mathrm{c})$ is expressed by the absolute values of a truncated Taylor series

$$G_\mathrm{max} = \sum_{n=1}^{N} \left| \frac{\partial \Phi}{\partial x_n} \right| \Delta\Phi_n, \tag{3.7}$$

where $\Delta\Phi_n$ is the specified error of the individual components. Systematic calculations of this type for the flow quantities of interest are given in Table 3.2. These figures, which are given as percentages for convenience wherever possible, represent the most pessimistic case evaluated from the complete flight envelope (25 m/s $\leq U_\mathrm{CAS} \leq$ 50 m/s, $0 \leq H \leq$ 3000 m) of the aircraft. Reference values for this estimate with the subscript '0' are obtained from the ISA standard atmosphere and by assuming a maximum relative humidity $r_h = 0.99$. The saturation pressure and the dynamic viscosity are obtained from the Magnus formula and the Sutherland model with empirical constants given by Etling (2008) and White (1974). Note that errors are typically much smaller in practice. In the following, known systematic errors in the present flight experiments are specified. Their compensation is described and, if necessary, the remaining uncertainty is estimated.

Two procedures were employed to eliminate the known systematic error of the boom-mounted probes positioned in the disturbed flow field of the aircraft. Weismüller (2011) conducted a careful GPS-based in-flight calibration of the pitot-static system proposed by Kimberlin (2003). The position error of the wind vane is corrected by second order polynomials determined by Erb (2002) in inviscid flow simulations of the entire aircraft. It should

Table 3.2.: Derived quantities and associated measurement uncertainty.

Quantity	Formula	Uncertainty
Saturation pressure	$p_{\mathrm{sat}} = 611 \cdot 10^{\left(7.45 \frac{T-273.15}{T-38}\right)}$	1.59 %
Humid air constant	$R_{\mathrm{h}} = R_{\mathrm{d}} \left[1 - r_h \frac{p_{\mathrm{sat}}}{p} \left(1 - \frac{R_{\mathrm{d}}}{R_{\mathrm{v}}}\right)\right]^{-1}$	0.02 %
Density	$\rho = \frac{p}{R_{\mathrm{h}} T}$	0.06 %
Dynamic viscosity	$\mu = \mu_{\mathrm{ref}} \frac{T_{\mathrm{ref}}+K}{T+K} \left(T/T_{\mathrm{ref}}\right)^{3/2}$	0.08 %
Kinematic viscosity	$\nu = \frac{\mu}{\rho}$	0.14 %
Calibrated airspeed	$U_{\mathrm{CAS}} = \sqrt{\frac{2p_{\mathrm{dyn}}}{\rho_0}}$	0.30 %
True airspeed	$U_\infty = \sqrt{\frac{2p_{\mathrm{dyn}}}{\rho}}$	0.46 %
Reynolds number	$Re = \frac{U L_c}{\nu}$	0.70 %
Pressure altitude	$H = \frac{\gamma}{\gamma-1} \frac{R_{\mathrm{h}} T_0}{g} \left[1 - \left(p/p_0\right)^{\frac{\gamma-1}{\gamma}}\right]$	1.68 m
Pressure coefficient	$C_p = \frac{2(p-p_\infty)}{\rho U_\infty^2}$	0.0082

be noted that there is a distance of about 8 m between the wind vane on the port wing and the wing glove on the starboard wing. This distance particularly becomes an issue in the determination of the mean angle of attack when flying through atmospheric turbulence. Therefore, an independent angle determination procedure based on the pressure distribution of the wing glove will be introduced Section 3.3 after the presentation of all necessary methods.

A small cross-flow component was shown to exist on the wing glove in Section 3.1.2 resulting from a slight spanwise pressure gradient. The pressure variations between the positions of the pressure taps and the centerline, where the transition detection sensors are installed (cf. Figure 3.3), is less than $\Delta C_p = 0.0075$ depending on the streamwise position. This difference is added to the instrument uncertainty evaluated in Table 3.2 to obtain the total uncertainty of the surface pressure coefficient of $\Delta C_p = 0.0157$.

The normal and tangential force coefficients with respect to the chord length L_c of the airfoil are obtained experimentally by an integration of the

pressure distribution neglecting shear stress effects.

$$\begin{aligned} C_n &= \int_0^{L_c} (C_{\mathrm{p,l}} - C_{\mathrm{p,u}}) \mathrm{d}(X/L_c) \\ C_t &= \int_0^{L_c} (C_{\mathrm{p,l}} - C_{\mathrm{p,u}}) \mathrm{d}(Z/L_c) \end{aligned} \tag{3.8}$$

$C_{\mathrm{p,l}}$ and $C_{\mathrm{p,u}}$ are the pressure coefficient on the lower and on the upper side of the airfoil. The lift coefficient C_l is obtained by a combination of the force coefficients C_n and C_t in dependence of the (effective) angle of attack α.

$$C_l = C_n \cos(\alpha) - C_t \sin(\alpha) \tag{3.9}$$

The accumulated uncertainty of the normal force coefficient is obtained by integrating twice the uncertainty along the chord ($\Delta C_n = 0.031$). The experimental uncertainty due to the limited number of pressure taps was evaluated with the program XFOIL (Drela, 1989). Distributing panel nodes at the midpoints between the pressure tap positions (32 or 48 taps depending on the configuration) and comparing the results with a solution obtained with 280 panels, the integrated instrument uncertainty of the pressure sensors yields a deficit of the two configurations of $\Delta C_n = 0.0233$ and $\Delta C_n = 0.0164$, respectively. The totals of this case scenario are $\Delta C_{n,1} = 0.0547$ and $\Delta C_{n,2} = 0.0478$ for the entire flight envelope of the aircraft. Since the C_t component is of the order of ΔC_n, only the latter error is included in the error propagation for the lift coefficient. With an effective angle of attack error of $\Delta\alpha = 0.15°$ the uncertainties $\Delta C_{l,1} = 0.0548$ and $\Delta C_{l,2} = 0.0479$ result for the lift coefficient.

In flight, the most significant systematic error associated with constant temperature hot-wire anemometry is caused by the temperature difference between flight conditions and the ground calibration. Several analytical correction formulas proposed by Abdel-Rahman et al (1987) were tested for atmospheric temperature differences of up to 20 K observed in a typical glide from 3300 m to 650 m. None of these formulas provided completely satisfying results, leaving differences of up to 8 % compared to the pitot-static measurements. Fanning (2012) used an in-flight calibration procedure originally proposed by White (2000), which is based on a unit Reynolds number instead of the free-stream velocity. The procedure is convenient for single normal hot-wires. However, for X-wire probes the complexity and the error increase significantly. Therefore, it was decided to evaluate the uncertainty of a simpler approach, relying only on a ground calibration prior to take-off.

To retain precision, an integrated sensor concept is employed. In Table 3.2 and in Section 3.1.1 the accuracy of the mean velocity and the mean flow angle measurements was demonstrated. For the characterization of the oncoming flow disturbances there is no need to reproduce the mean values exactly with hot-wire anemometry. It is sufficient to determine only the fluctuations of the velocity and the flow angles with the desired accuracy.

The CTA principle is based on the convective heat transfer of a wire heated to a constant temperature T_w above the static flow temperature T. Since the heated wire is very thin, the Reynolds number based on the wire diameter d is only $O(1)$ in the present case. Thus, a heat transfer relation can be derived from the Nusselt relation of the laminar flow around an infinite cylinder ($n = 0.5$) and Joule's first law:

$$E_\mathrm{w}^2 = \underbrace{\pi A_0 L_\mathrm{w} R_\mathrm{w} \Lambda(T)\,(T_\mathrm{w} - T)}_{A(T)} + \underbrace{\pi B_0 L_\mathrm{w} R_\mathrm{w} \Lambda(T)\,(T_\mathrm{w} - T) \left[\frac{\rho(T) d}{\mu(T)}\right]^n}_{B(T)} U_\infty^n. \tag{3.10}$$

Note the equivalence to the modified King's law in equation 3.1. The density ρ, the dynamic viscosity μ and the thermal conductivity of the air Λ are temperature-dependent quantities. These quantities are evaluated at the film temperature $T_\mathrm{f} = 0.5(T_\mathrm{w} - T)$ using the corresponding formulas in Table 3.2 and an empirical equation for thermal conductivity Λ given by Bruun et al (1990). The empirical constants A_0 and B_0, the length L_w and the constant resistance R_w of the heated wire as well as the exponent n are independent quantities. From this observation it can be concluded that only the temperature dependency $B(T)$ affects the sensitivity $\partial E_\mathrm{w}/\partial U$ of the anemometer outputs ($E_\mathrm{b}^2 \propto E_\mathrm{w}^2$). Figure 3.6 demonstrates this behavior with exaggerated values of $\Delta T = 50$ K, allowing velocity fluctuations up to $U' = 10$ m/s. Collapsing the two curves for different flow temperatures T at the considered mean velocity $\bar{U}_\infty$, the voltage difference

$$\delta E_\mathrm{w} = E_\mathrm{w}(U_\infty, T_\mathrm{C}) - (E_\mathrm{w}(U_\infty, T_\mathrm{F}) - \Delta E_\mathrm{w}(\bar{U}_\infty)) \tag{3.11}$$

is very low for moderate velocity fluctuations (see Figure 3.6(a)). The voltage difference translates into a systematic error in the determination of the

velocity fluctuations demonstrated in Figure 3.6(b).

$$\delta U' = \left[\frac{(E_\mathrm{w} + \delta E_\mathrm{w})^2 - A(T)}{B(T)}\right]^{1/n} - U_\infty \tag{3.12}$$

Conducting the same analysis for values of $\max(U'/\bar{U}_\infty) = 0.125$ and $\Delta T = 30$ K, which are still higher than practically encountered, an estimate for the maximum velocity fluctuation uncertainty $\delta U'/U' = 0.03$ % results. This conservative analysis also applies for the modified law in equation (3.1) in the case of X-wire measurements. Moreover, Bradshaw (1971) states that the flow angle determination is not very sensitive to temperature changes since both wires of the X-wire probe are affected equally. In the actual flight experiments the accuracy is further increased by linearly correcting for the factor $(T_\mathrm{w} - T)$ as proposed by Lekakis (1996).

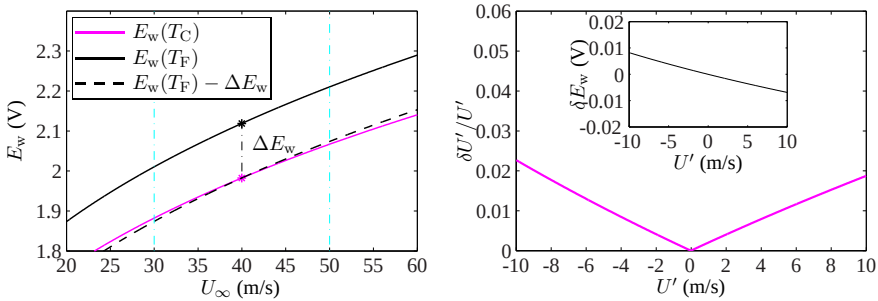

(a) Temperature dependence of King's law

(b) Velocity uncertainty resulting from the voltage difference

Figure 3.6.: Exaggerated example of the influence of the ambient temperature on the heat transfer relation and the resulting uncertainty of the velocity fluctuations for an infinite single normal wire. Calibration: $T_\mathrm{C} = 300$ K. Flight: $T_\mathrm{F} = 250$ K. $\bar{U}_\infty = 40$ m/s and $\max(U'/\bar{U}_\infty) = 0.25$.

The maximum error in the hot-wire measurements of the velocity and the flow angle fluctuations α' and β' is composed of several parts; the temperature error, the signal-to-noise ratio, uncertainty due to binormal cooling and the error of the calibration scheme. The high frequency (> 200 Hz) sensor noise under very calm (flight) conditions translates into less than 0.01° and

0.02 m/s variation of the angle of attack and the velocity. Furthermore, the three-dimensionality of atmospheric turbulence leads to binormal cooling of the wires in a potentially different manner than in the calibration wind tunnel. For turbulent structures larger than the prong separation, both wires of an X-probe are affected equally and the effect on the flow angle measurement is negligible. Nevertheless, binormal cooling is accounted for by assuming a 0.5 % deviation in the effective velocity of each wire based on the results from Zhao and Smits (2006). Bruun et al (1990) show that the effective angle calibration scheme yields an effective-velocity accuracy better than 1 % for probe angles less than 15°. In the present study flow angles remain well below 10°. All mentioned uncertainties sum up to a total error of approximately 1.9 % for the measured angle fluctuations and the velocity fluctuations. Note that these maximum uncertainties correspond to assumed maximum deflections in the flow quantities. For smaller absolute fluctuations the error reduces (cf. Figure 3.6(b)). When composing the total flow angles with the measurement of the mean quantities from the reference system and the determination of the fluctuations with the hot-wires, the independent uncertainties from both measurements may sum up.

The data of all sensors was digitalized with sampling rates (cf. Table 3.1) well above the characteristic frequencies of the investigated processes. Exceeding the Nyquist-Shannon requirement by a multiple enables a reduction of the random error in the postprocessing by employing moving average filters. The dynamic errors in the measurement of rapid fluctuations mainly arise from the attenuation and the phase lag in the transmission of the flow quantities to the sensors and the frequency response of the measurement instruments themselves. An in-situ dynamic calibration and a proper correction of the total frequency response may compensate for these uncertainties. Yet, the uncertainty of the reference signal leads to a possible error in the corrected signals. Typical examples in this study are the dynamic calibrations of the pressure sensors and the microphones, where the uncertainties of the reference instruments were given in Section 3.1.3.

Although the thermal response of a thin hot-wire is much faster than the one of surface hot-film, due to the larger heat capacity of the latter, the thermal lag of both sensors does not allow unsteady measurements directly. In the constant temperature (CT) mode a feedback differential amplifier is employed to compensate for the thermal inertia at the cost of additional complexity and electronic noise (Freymuth and Fingerson, 1997). The resulting frequency response, which may be modeled as a third-order system (Freymuth, 1977), has a velocity-dependent cut-off frequency of $O(10\ \text{kHz})$,

which is tuned by using an electronic square wave signal at the maximum expected flow velocity. The constant part of the frequency response exceeds the frequency band of interest for the free-stream measurements using X-wires by a multiple.

Comparing hot-wire and hot-film measurements in a flight experiment, Seitz (2007) demonstrates that TS wave frequencies of more than 2 kHz can be resolved with a similar hotfilm system of the same manufacturers. Thus, in both applications, the hot-film and the hot-wire measurements, the detection of maximum frequencies in the flow is less an issue than the signal-to-noise ratio, despite the optimization described in Section 3.1.3. In this respect, the major penalty of hotfilms are conduction losses to the wall (Sturzebecher et al, 2001). Furthermore, the nonlinearity of the heat transfer law has much greater significance for surface hot-films than for hot-wires since the time-averaged wall shear stress declines to small values in the transition region of the wing glove as will be demonstrated in Section 3.3.2.

3.2. Numerical Methods

To compare the experimental results of the flight investigation with theoretical predictions, two-dimensional, incompressible flow computations are conducted. Potential flow, boundary-layer and linear stability analysis are employed to gain insights into the investigated processes. Although substantial parts of the boundary-layer and stability methods needed to be developed and implemented throughout the course of the project, a detailed description would exceed the scope of this thesis. Therefore, only a brief summary of the solution procedures will be given in the following and some results of particular interest for the present study, also in later chapters, will be presented verifying these methods. More detailed descriptions can be found in the theses of Köhler (2011), Dietrich (2011), Hartmann (2013), Taubert (2014) and Reeh (2008).

Potential Flow Computations

The boundary conditions for the steady and unsteady boundary-layer computations are prescribed by a solution of the inviscid outer flow field, which is conveniently obtained by a panel method. The airfoil analysis and design tool XFOIL developed by Drela (1989) provides valuable results for steady flows due to its robust and efficient viscous-inviscid interaction scheme. It is based

on piecewise linear vortex distributions on the airfoil panels as well as constant source/sink distributions on the panels representing the airfoil surface and the displacement effect of the wake. After a first iteration consisting of a pure potential flow solution and a subsequent boundary-layer computation, the streamline displacement caused by the boundary layer is incorporated by using an additional wall-normal transpiration velocity (Lighthill, 1958) which modifies the strength of the source/sink panels.

$$V_\mathrm{t} = \frac{\mathrm{d}}{\mathrm{d}x}\left[U_\mathrm{e}(x)\delta_1(x)\right] \tag{3.13}$$

The next boundary-layer iteration is then based on the corrected inviscid flow solution and the procedure is continued until a specified convergence criterion is met. Mathematical justification for the coupling of the two separate flow problems is given by Cebeci and Cousteix (2005). In Section 3.3.1 a very good agreement between XFOIL and the obtained experimental data will be shown.

In unsteady flows another panel method is used. It is based on the simpler formulation of Hess and Smith (1967), which uses only constant vortex sheet panels. The numerical procedure was implemented by Jain (2010), Lambie (2011) and Spiegelberg et al (2014). As explained in Chapter 2.3.1, Kelvin's theorem is obeyed by a vortex shedding into the wake when the bound circulation of the airfoil changes. This is satisfied by an additional panel hinged to the trailing edge, which for each time step adjusts its magnitude as well as the panel length and inclination according to the local flow (Cebeci et al, 2005). It predefines the strength of a free core vortex to be shed in the subsequent time step. Contrary to thin airfoil theory (cf. Figure 2.4), the core vortices convect freely in two spatial dimensions according to the unsteady potential flow field. The additional singularities induce unsteady velocities and lead to larger influence coefficient matrices in the resulting linear system of equations. Due to increased computation time in unsteady flows, the viscous-inviscid interaction scheme developed by Dietrich (2011) was not used in the present investigations. The boundary conditions for the boundary-layer computation in the unsteady case are prescribed directly from the potential flow solution.

Boundary-Layer Method

For the boundary-layer computations the inviscid outer flow field $U_\mathrm{e}(x,t)$ is mapped onto the edge of the boundary-layer domain, where the Euler

equation (2.23) prescribes the necessary boundary conditions at $y = \delta$. The time-dependent boundary-layer equation 2.21 is solved by the finite difference method of Cebeci (1977), which is implemented for laminar and turbulent flow. To increase the efficiency, the procedure is formulated in transformed variables. The Falkner-Skan transformation with the mean velocity distribution $\bar{U}_\mathrm{e}$

$$\eta(x, y) = y\sqrt{\frac{\bar{U}_\mathrm{e}(x)}{\nu x}} \tag{3.14}$$

stretches the wall-normal coordinate and relaxes the spacing requirements compared with the use of physical coordinates. Furthermore, a dimensionless stream function is introduced which reduces the spacing sensitivity in the streamwise direction.

$$F(x, \eta, t) = \psi(x, y, t)\sqrt{\nu x \bar{U}_\mathrm{e}(x)} \tag{3.15}$$

The transformed boundary-layer equation reads

$$\begin{aligned} \frac{\partial}{\partial\eta}\left(b\frac{\partial^2 F}{\partial\eta^2}\right) + \frac{P+1}{2}F\frac{\partial^2 F}{\partial\eta^2} - P\left(\frac{\partial F}{\partial\eta}\right)^2 + P_\mathrm{e} \\ = x\left(\frac{\partial F}{\partial\eta}\frac{\partial^2 F}{\partial x\partial\eta} - \frac{\partial F}{\partial x}\frac{\partial^2 F}{\partial\eta^2} + \frac{1}{\bar{U}_\mathrm{e}}\frac{\partial^2 F}{\partial\eta\partial t}\right), \end{aligned} \tag{3.16}$$

with

$$P = \frac{x}{U_\mathrm{e}}\frac{\partial\bar{U}_\mathrm{e}}{\partial x}, \quad P_\mathrm{e} = \frac{x}{\bar{U}_\mathrm{e}^2}\left(\frac{\partial U_\mathrm{e}}{\partial t} + U_\mathrm{e}\frac{\partial U_\mathrm{e}}{\partial x}\right), \quad b = 1 + \nu_T^+. \tag{3.17}$$

The unsteady boundary conditions of equation (2.23) enter through the term P_e. The dimensionless eddy viscosity ν_T^+ is zero for laminar computations and for the turbulent case it is determined from the algebraic turbulence model of Cebeci and Bradshaw (1977). Since $\partial F/\partial\eta = u/\bar{U}_\mathrm{e}$, the boundary conditions are $F = 0$, $\partial F/\partial\eta = 0$ at the wall ($\eta = 0$) and $\partial F/\partial\eta = U_\mathrm{e}/\bar{U}_\mathrm{e}$ at the boundary-layer edge ($\eta = \delta_\mathrm{e}$). The nonlinear, partial differential equation of the parabolic type (3.16) is discretized into a matrix form by finite differences. For its numerical stability the box scheme of Keller (1978) is employed in the t, x and η-directions. Newton's method is used to iteratively solve the resulting nonlinear system of equations, see also Cebeci and Cousteix (2005) for details. Since the stream function fulfills the continuity equation, the wall-tangential and the wall-normal velocity components are obtained from

the solution. At the stagnation point, which is determined from the discrete inviscid velocity distribution by linear extrapolation, the velocity is zero and a special numerical treatment is needed to initialize the boundary-layer computation. This is accomplished by differentiating the boundary-layer equation (2.21) with respect to x, dropping all negligible terms in the limit of $x \to 0$ and solving the resulting system of equations for the derivative $\partial u/\partial x = \partial^2\psi/(\partial y \partial x)$. This quantity then serves as an input for the general downstream marching scheme at the subsequent station. For unsteady airfoil calculations initial conditions need to be described. To limit the complexity of the procedure, unsteady boundary-layer computations start only at $X/L_c = 0.03$ using quasi-steady results up to that point. Cebeci (1984) proves that the quasi-steady approach in the stagnation point vicinity yields accurate results downstream if unsteady separation in the leading edge region can be excluded. This argument is complemented by the demonstration in Chapter 2.3.2 that unsteady boundary-layer effects are small for low κ_δ and increase with the streamwise coordinate x. Unsteady computations are first carried out for all time steps at each streamwise station before proceeding downstream. To verify the unsteady boundary layer procedure, comparative computations of the two explanatory test cases introduced in Chapter 2 are presented in Figure 3.7. In the case of the standing wave a very good agreement between the experimental and numerical results is obtained for both, the amplitude ratio and the phase profile. In the case of a wave propagating with $Q = 0.77\bar{U}_\infty$ the phase profiles also coincide very closely. However, differences are observed in the amplitude ratio profiles. Whereas the numerical profile for the smaller frequency parameter $\kappa_\delta = 0.314$ agrees reasonably well, the apparent overshooting of the boundary-layer amplitude at $\eta \approx 1.5$ in the experimental data is not reflected in the numerical result for $\kappa_\delta = 1.57$. Several careful recalculations of the discretization and the checking of the code implementation revealed no error. Interestingly, hardly any other numerical simulation of this fundamental test case, especially for turbo-machinery research, is found in the literature. The only direct reference from Evans (1989) examines the low-frequency case with nominally the same numerical procedure and in a technical report (Evans, 1988) the high-frequency case is demonstrated. However, the present implementation represents the experimental results more closely. Decreasing the convection velocity of the traveling wave to $Q = 0.66\bar{U}_\infty$, the amplitude tend closely toward Patel's results with almost identical phase profiles. Besides the unknown experimental uncertainty, Patel (1975) reported a not quantified adverse pressure gradient which may have similar effects. For the unsteady airfoil investigation of this

study the numerical method is deemed to describe the unsteady boundary layer correctly, as the frequency parameter remains below $k_\delta = 0.42$. Since the phase results coincide and the amplitude maximum is lower in the computed results, no artificial instability is expected in applying the quasi-steady stability method to the computed, unsteadily distorted boundary-layer profiles of the airfoil flow. The accuracy of the method for steady flows, and thereby the effect of a mean streamwise pressure gradient in unsteady computations, is verified implicitly in the presentation of the linear stability method in the following section.

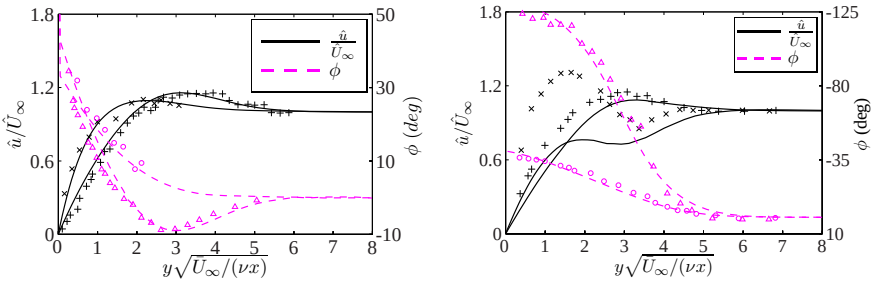

(a) Standing wave: $\kappa_\delta = 0.56$ $(+, \circ)$, $\kappa_\delta = 2.67$ $(\times, \triangle)$

(b) Traveling wave ($Q = 0.77\bar{U}_\infty$): $\kappa_\delta = 0.314$ $(+, \circ)$, $\kappa_\delta = 1.570$ $(\times, \triangle)$

Figure 3.7.: Amplitude and phase profiles of the boundary-layer fluctuations in a flat plate flow for two different forcing cases at two different frequency parameters. Markers represent the experimental results of Hill and Stenning (1960) and Patel (1975), solid lines are the obtained numerical solutions.

Linear Stability Calculations

In order to compare the experimental transition results with theoretical predictions, a linear stability method is used to compute the amplification rates, eigenfunctions and N-factors. In the spatial framework of the linear stability problem (equations (2.32) and (2.33)), the eigenvalue k_x appears up to the fourth order in equation (2.32). To reduce the nonlinear eigenvalue problem to a linear one, two consecutive transformations are necessary. The first transformation is a variable transformation of the independent variable y (Schmid and Henningson, 2001), which eliminates one power of k_x in the

$\left(\mathcal{D}^2 - k^2\right)$ terms by substituting the exponential approach

$$\begin{pmatrix} \hat{v} \\ \hat{\Omega} \end{pmatrix} = \begin{pmatrix} \hat{V} \\ \hat{E} \end{pmatrix} \mathrm{e}^{-k_x y}. \tag{3.18}$$

The second transformation removes the remaining second power of the eigenvalue by the companion matrix method of Danabasoglu and Biringen (1989) at the cost of larger matrices. Eventually, a generalized eigenvalue problem of the form

$$\mathcal{L}_{\text{spatial}}\vec{\hat{e}} = k_x \mathcal{M}_{\text{spatial}}\vec{\hat{e}} \tag{3.19}$$

is obtained, where

$$\vec{\hat{e}} = \begin{pmatrix} k_x\hat{V} \\ \hat{V} \\ \hat{E} \end{pmatrix}. \tag{3.20}$$

A spectral Chebyshev collocation method is used to discretize the boundary-value problem offering an elegant way to compute derivatives by matrix multiplications (Canuto et al, 2007). The dependent variables $\hat{V}$ and $\hat{E}$ are represented by a truncated series of Chebyshev polynomials and a Gauss-Lobatto grid is used for the discrete representation of the independent variable y. Since the Gauss-Lobatto points are only defined on the finite domain $\xi \in [-1, 1]$, the algebraic function $y(\xi) = \frac{\delta}{2}(1 + \xi)$ maps the grid points into the physical boundary-layer domain $y \in [0, \delta_{\mathrm{e}}]$. The solution of the matrix equations results in a complete eigenvalue spectrum. For N-factor computations only the TS mode of the eigenvalue spectrum (cf. Figure 2.11(a)) is needed. To save time computing the N-factors, a shooting procedure for the TS eigenmode is employed after an initial computation of the complete spectrum with the matrix method described before. Therefore, a different set of stability equations is obtained by introducing the normal mode approach (2.31) and the parallel flow assumption directly into the linear disturbance equations ((2.26) and (2.27) without the underbraced term).

$$\left(\mathcal{A} + \mathcal{B}\frac{\partial}{\partial y} + \mathcal{C}\frac{\partial^2}{\partial y^2}\right)\vec{\hat{q}} = 0. \tag{3.21}$$

The definitions of the linear operators $\mathcal{A}$, $\mathcal{B}$ and $\mathcal{C}$ can be found in the works of Duchmann (2012) and Tempelmann et al (2010). The first TS eigenvalue value, initially obtained by the complete matrix method, is extrapolated to the next station serving as an initial guess for the solution. The system

of equations (3.21) is then solved iteratively by a secant method for the eigenvalue until the boundary conditions at the wall are fully enforced. The converged complex wavenumber k_x is used for the extrapolation to the subsequent station in the downstream marching scheme. The dimensional disturbance growth rates $k_{x,i}$ are integrated in order to compute the N-factors according to equation (2.35). Figure 3.8 shows a comparison between N-factor curves calculated with the present procedure and results provided by Würz et al (2003) from IAG Stuttgart. Both computations were based on the same XFOIL pressure distribution. In general a good agreement can be asserted for both sides of the airfoil considering the fact that completely independent boundary-layer and LST programs were employed. Minor deviations result from slight differences in the boundary-layer discretization or truncation errors which become particularly evident when integrating very small growth rates near neutral stability. Three-dimensional TS modes have been verified with values presented by Schmid and Henningson (2001) for the temporal stability problem by applying Gaster's transform (Drazin and Reid, 1981). However, Reed and Saric (1996) point out that the physical errors due to the parallel flow assumption become more important for oblique waves modes.

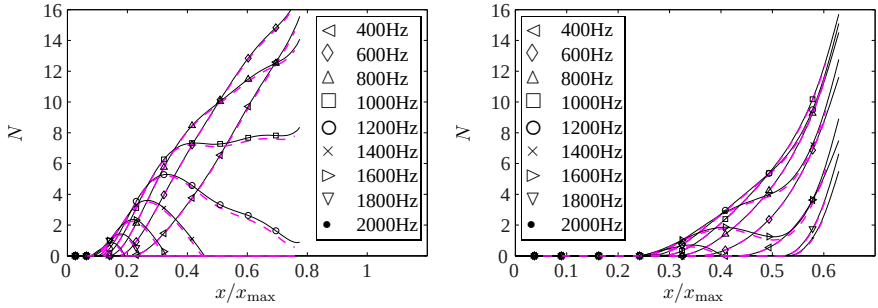

(a) Lower side (b) Upper side

Figure 3.8.: Verification of the boundary-layer and linear stability method by means of N-factor computations on the wing-glove airfoil ($\bar{\alpha} = -0.73°$, $Re = 3.28 \cdot 10^6$). $x_{\max}$ the maximum arc length along the airfoil on each side. Solid lines: present method. Dashed lines: results from IAG Stuttgart.

3.3. Combined Procedures

3.3.1. Boundary-Layer Computations Based on Flight-Measured Pressure Distributions

For the determination of stability properties of the boundary layer, it is important to base the computations of the boundary-layer profiles on accurate boundary conditions. The most realistic boundary conditions are obtained from the pressure measurements, by using Bernoulli's equation (2.4) to derive the necessary velocity distribution. As shown in Chapter 2.3.1, for unsteady flows the use of the steady Bernoulli equation introduces systematic errors, which, however, remain small for the investigated reduced frequencies. The limited number of pressure sensors does not allow direct linear interpolations to obtain a reasonably smooth distribution. Thus, a smooth interpolation or an accurate curve fitting procedure is necessary. Further complication is introduced due the abrupt changes of the pressure distribution in the vicinity of the stagnation point as shown in Figure 3.9(a). Data interpolation with elaborate local procedures such as Akima (1970) polynomials showed an unsuppressible tendency to overshoot in the region of rapidly changing gradients. Therefore, a procedure was developed, which combines the viscous-inviscid method described in Section 3.2 with the experimental results. To obtain a smooth and accurate solution at the leading edge, an XFOIL computation is employed using the specific flight Reynolds number. A MATLAB interface iterates the XFOIL solutions for various angles of attack until the computed distribution matches the experimental mean data of 14 specified pressure gauges in the leading edge region. In this region the boundary-layer is thin and a good coincidence between the panel solution and the measurements is to be expected. The sum of the least squares between the third to the tenth sensor on the lower and the upper side of the wing glove is chosen as an iteration criterion. The angle of attack is varied in increments of $0.01°$. Once convergence is achieved, simple fifth order polynomials, starting from the sixth streamwise sensor position, are used to provide a smooth curve fitting for the laminar boundary layer region. In the overlapping region between the fifth and the tenth sensor, an averaging further smoothes the transition between the numerical solution and the cruve-fitted measurement results. In Figure 3.9(a) a typical result of this robust and reliable method is shown. The differences between the measurements and the XFOIL computation in the aft part of the airfoil may be the result of limitations of the numerical model or slight geometry differences between

the actual wing glove and the airfoil input data. It is possible that the upper side of the wing glove is slightly distorted in flight due to the acting surface pressure. Using the experiment-based results, these differences, which can be expected uniform in the spanwise direction, become irrelevant for the boundary-layer computations. The smooth wall shear stress distributions in Figure 3.9(b) support the effectiveness of the procedure. They are obtained with the method described in Section 3.2 using the boundary conditions obtained from the combined procedure. The wall shear stress on the upper and the lower side declines in the leading edge region and assumes small values in most of the laminar part of the boundary layer. At $X/L_c = 0.575$ and $X/L_c = 0.710$, where transition is experimentally observed, the wall shear stress increases rapidly before descending again in the turbulent part of the boundary layer.

A valuable side effect of this method is the direct determination of the effective angle of attack at the wing glove with an accuracy comparable to the wind vane measurements. In flight through turbulence the spatial distance between the wind vane and the wing glove may introduce inaccuracies in the determination of the mean angle of attack at the wing glove. These uncertainties are avoided by basing the effective angle-of-attack determination on the time-averaged pressure distribution, which for the investigated turbulence agrees well with steady XFOIL computations.

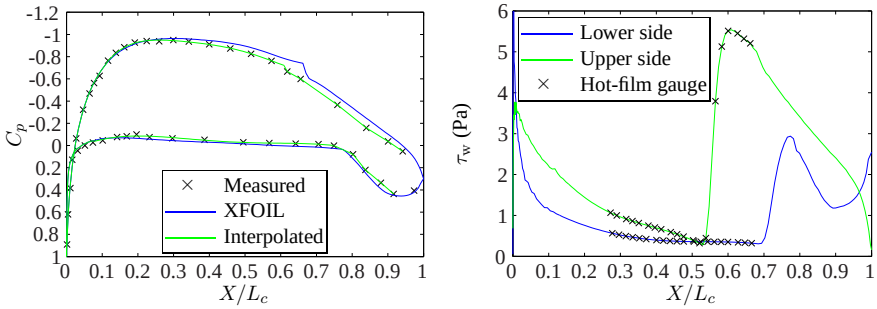

(a) Interpolation of the pressure distribution. Flight case: $\bar{\alpha} = 0.22°$, $Re = 2.95 \cdot 10^6$

(b) Boundary-layer results based on the interpolated boundary conditions

Figure 3.9.: Examples for the combined boundary-layer procedure.

3.3.2. Discussion of In-Flight Calibration Procedures for Surface Hotfilms

The wall shear stress $\tau_\mathrm{w} = \mu(\partial u/\partial y)_\mathrm{w}$ in the streamwise direction determines the convective heat transfer from the thin (0.1 mm) surface hot-film elements, which are aligned perpendicular to the mean flow direction. For incompressible flows, the energy equation and the momentum equation are decoupled (Spurk and Aksel, 2006). In simple laminar flows analytic solutions can be obtained for τ_w and in turbulent flows it can often be assumed that the thermal boundary layer, produced by the small heated element, is thinner than the viscous sublayer. Bruun (1995) therefore proposed a power law commonly used for surface hot-films operated in the constant temperature mode.

$$\frac{E_\mathrm{b}^2}{T_\mathrm{HF} - T} = A_\mathrm{HF}\ \tau_w^{1/3} + B_\mathrm{HF} \tag{3.22}$$

Typical for two-dimensional boundary layers in airfoil flows, the mean wall shear stress changes in the main flow direction and assumes considerably smaller values upstream of laminar-turbulent transition. This behavior of two-dimensional airfoil boundary layers is depicted, for a flight case, in Figure 3.10(a) . As the boundary layer becomes significantly unstable for decelerated flow shortly upstream of transition, which corresponds low laminar skin friction values (cf. Figure 3.9(b)), the nonlinearity of the heat transfer law assumes an important role. A wall-shear stress fluctuation τ'_w at small mean values of $\bar{\tau}_\mathrm{w}$ leads to larger bridge voltage outputs E_b than the same flow fluctuation amplitude at a higher mean level. This behavior is illustrated in Figure 3.10(a). Wall-shear stress fluctuations of the same magnitude at different streamwise positions may thus correspond to different voltage signals. This nonlinear behavior permits the comparison of disturbance growth rates in the streamwise direction when using uncalibrated hotfilms on the upper side of the airfoil, where there is a significant gradient $\partial\tau_\mathrm{w}/\partial x$. The imbedded plot of Figure 3.10(a) demonstrates that even an exaggerated shear stress fluctuation of $\tau'_\mathrm{w} = 0.2$ Pa locally, i.e. at a specific $\bar{\tau}_\mathrm{w}$, yields an almost linear voltage fluctuation. This is of primary importance for investigations in the frequency domain.

In principle a calibration of surface hotfilms can be obtained by using equation (3.22) and an appropriate reference flow. However, the heat transfer also depends on the heat conduction properties of the investigated aerodynamic body. This requires a more difficult in-situ calibration, even if the hotfilms are applied on an insulting material. In-situ calibrations may become inac-

curate for different ambient conditions since not only the heat transfer to the flow changes, but also the component to the substrate is affected (Bruun, 1995). This is a major complication for flight testing practice, in addition to the temperature dependence and the long-term deterioration of the hot-film elements. In previous in-flight investigations special calibration procedures were therefore developed. Carpenter (2009) used a Preston tube to calibrate a spanwise hot-film row in-situ during actual measurements. In this study, with streamwise aligned sensors, a reference measurement would be needed for every sensor position. Seitz (2007) presented a wall shear stress calibration procedure using laminar boundary-layer calculations. The numerical computations were based on pressure distributions obtained experimentally at different airspeeds. The reported experimental uncertainty was 20 %. This specific procedure was tested for the present study. An example of a calibration of eleven sensors in the laminar boundary layer on the upper side of the airfoil at nine different airspeeds is shown in Figure 3.10(b). Since transition on the upper side is fixed within the streamwise section of the hot-film array for all flight test cases, difficulties arise for the downstream sensors as laminar computations cannot be applied. On the lower side, the variation in τ_w is very small (< 0.25 Pa) for different airspeeds complicating reliable calibrations.

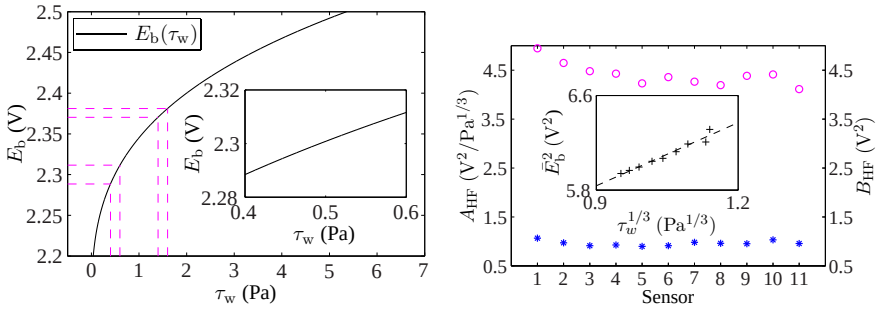

(a) Nonlinear sensor response. Dashed lines: Comparison of output voltages for equal shear stress differences of equal magnitude

(b) Sample calibration. A: $*$. B: $\circ$. $+$: Calibration points

Figure 3.10.: Nonlinearity of the surface hot-film measurement principle and results of an in-flight calibration.

Due to the described complications, it was decided to use the hotfilm ar-

rays only as a means for transition detection and for the investigation of the spectral content of the boundary-layer disturbances, for which they are effective. Direct information on disturbance growth rates can be obtained from the wall-microphone results used in configuration 1. It should be mentioned that there is also an advantage of the nonlinearity of the measurement principle. When the flow decelerates upstream of transition, the CT controller output is amplified by the steeper gradient of the sensor characteristic for low $E_{\mathrm{b}}(\tau_{\mathrm{w}})$. This enables a better signal-to-noise ratio in spectral investigations of the late linear and the weakly nonlinear stage of transition.

3.4. Flight Test Campaigns and Procedures

The flight tests were carried out from the August Euler airfield close to Darmstadt. They were organized in campaigns due to the limited availability of the research aircraft and the comprehensive preparations necessary for the experimental setup. Table 3.3 gives an overview of the conducted in-flight experiments, excluding numerous system check flights in the preparation phase. A flight comprised one or two straight glides from a flight level of almost 3300 m to approximately 650 m, in which data was collected over up to 14 measurement runs of 20 s. While the pilot tried to maintain a predefined flight condition, the flight test engineer operated the measurement system using the LabVIEW interface. At least three different pilots carried out the flights in each campaign to avoid pilot-induced peculiarities in the measurement results.

The targeted angle-of-attack and side-slip-angle as well as the actual flow angles obtained with the wind vane instrument were displayed to the pilot on a special screen. After the pilots had trimmed to an initially stable flight condition with the prescribed angles the recording was started. Atmospheric turbulence inevitably demands control inputs from the pilot in order to maintain a specific flight condition. However, pilots intuitively respond only to larger deflections with balancing control inputs; hence the pilot acts as a high-pass filter. To unify the individual responses, a low-pass filtered flow angle information was displayed to the pilots in the command display to avoid unnatural control inputs. While long wave deviations from the targeted flow angles could be compensated, the effect of inevitable and uncontrollable small gusts was intentionally present. An optical system recording the stick and the pedal motions, which was developed for the last campaign (Ikonnikova, 2013), could not be used due to limitations in the available computer

Table 3.3.: Summary of the conducted in-flight experiments with the complete setup.

Flight campaign	Duration	Number of flights	Total of measurement runs	Percentage of adequate runs
2011	Sep	13	148	33%
2012	Aug - Oct	19	210	41%
2013	Sep - Oct	16	155	35%

power. Nevertheless, the described flight test procedure best resembled a cruising flight situation with emphasis on the particular flow state on the wing glove. Note that the recording interval of 20 s was identified as a compromise between capturing the turbulence effects relevant for airfoil aerodynamics and pilot distraction while flying under visual flight rules. Numerous measurement runs were not deemed adequate for the present investigation as reflected in Table 3.3. This number is explained by insect contamination of the leading edge corrupting transition investigations, unforeseen problems with the measurement instrumentation common in flight testing (radio interference, failure of individual components, etc.) or an exceeding of the strict limits for predefined flow state (most often).

Before the flights, the hot-wire probes were calibrated in-situ with a transportable wind-tunnel. Calibrating in the cold early-morning air assured less ambient temperature differences between the calibration and the flight conditions later in the day. Since a primary goal of the project was the investigation of boundary-layer transition on the wing glove, all flights were conducted in straight gliding flight. The engine was shut down to avoid undesired boundary-layer receptivity and unwanted interferences with the measurement instrumentation. Atmospheric turbulence was mainly encountered due to thermal convection, but orographic wind interference from a mountain ridge close to the airfield was also a possible and predictable source of turbulence. Prior to take-off and after landing photos of the leading edge of the wing glove were taken to exclude any data corruption through bug strikes. Despite the fact that flight research is all but routine work, the efficiency of the flight testing procedures was considerably enhanced by using checklists wherever suitable.

Although most of the experiments took place in the late season of the years and thermals were not as intense as in early summer, considerable turbulence was still encountered. However, this work only investigated the influences

of moderate turbulence on the NLF wing section. Moderately turbulent conditions are found throughout most of the year and they occur frequently in between local zones of strong turbulence, e.g. in strong thermals. These conditions are thus of primary interest for airfoil design regarding efficiency improvements.

4. Characterization of Oncoming Flow Disturbances

In flight through atmospheric turbulence the inviscid as well as the viscous response of the investigated wing section are determined by the oncoming flow disturbances. For any airfoil investigation the characterization of these disturbances is of essential importance. Besides insights into the nature of atmospheric turbulence, the knowledge about typical intensities of the encountered turbulence and its spectral composition yields valuable data beyond the present study. Wind-tunnel investigations as well as numerical computations rely on accurate boundary and initial conditions to simulate realistic processes. Thus, characteristic signals for the oncoming velocity and angle information are presented in Section 4.1. The far-reaching assumption of isotropic turbulence will be substantiated with measurement results in Section 4.2. Characteristic turbulence quantities are obtained for different atmospheric states in Section 4.3 with emphasis on the spectral properties of the energy cascade of atmospheric turbulence.

4.1. Typical Oncoming Flow Conditions

To introduce representative types of oncoming flow conditions for various meteorologic conditions, which were frequently found in the in-flight experiments, four characteristic sample records are described in the following. The records include most of the identified peculiarities of in-flight turbulence. For this specific study, with emphasis on the laminar-turbulent transition process in the wing boundary layer, it is convenient to omit existing standardizations, e.g. from MacCready (1964), and to define specific categories of turbulence. In Section 4.3.1 characteristic quantities will be introduced to uniquely classify the turbulence states. In Figures 4.1 and 4.2 examples of oncoming flow conditions are depicted for the three different turbulence categories which encompass most of the observed effects. For completeness, the quantities characterizing the flow state are listed in Table 4.1. The plots show the temporal angle of attack fluctuations α' and the fluctuations of the

chordwise and the vertical velocity components, U' and W', which were both detected with a single X-hot-wire probe. The velocities are normalized with the mean free-stream velocity and the quantities describing the mean flow state are given in the figure captions and in Table 4.1. Figures 4.1(a) and 4.1(b) depict the data of a flight through calm conditions, which could serve as a reference for the aerodynamic steady-state observations in Chapter 5. The pilot is able to adjust the angle of attack and the airspeed precisely under these conditions. This case also serves as an example for the obtainable pilot accuracy in the adjustment of the flow state under calm conditions. Such conditions are mostly found at high altitudes in the free atmosphere or in the early morning when the ABL has sufficiently subsided due to its nocturnal tranquilization (cf. Chapter 2.1). In the Figures 4.1(b) and 4.1(d), the velocity signals are digitally band-pass filtered by third-order Butterworth transfer functions (5 Hz $\leq f \leq$ 1 kHz) to highlight the small-scale fluctuations in a shorter (3 s) time interval. To obtain a clear view on both velocity components, the origins of the left and the right ordinates are displaced. For the calm case in Figure 4.1(b), however, almost no fluctuations are observed.

Under lightly turbulent conditions, as depicted in Figure 4.1(c), the angle-of-attack fluctuations remain smaller than 1.5°. These conditions are often found within the convective mixed layer when solar heating is rather weak. It is not uncommon to find such conditions continuously for the entire flight time. The depicted case particularly demonstrates the intermittent character of convective turbulence. Whereas the fluctuations are more intense for the first 7 s of the measurement sequence, they decline in the following, until a new spot of higher turbulence is encountered for $t > 18$ s. In between the encounter of the convective plumes, fluctuations of lower intensity are observed in the intermediate part of the filtered signal in Figure 4.1(d) which corresponds to the mixing region between the plumes.

As described in Chapter 2.1, atmospheric turbulence may originate from different weather-dependent mechanisms. Figures 4.2(a) and 4.2(b) present another case of light turbulence, in which the fluctuations appear continuously. The turbulence encountered in this run was created in a layer of wind shear at a flight level of $H \approx 2400$ m with the complete absence of thermal convection. Although the origin of this turbulence is different, its effects on the aircraft are independent of the source.

The third investigated category, i.e. moderate turbulence, in Figure 4.2(c) is also frequently found in flights during daytime, especially during the warmer half of the year when thermal convection is more prominent. These

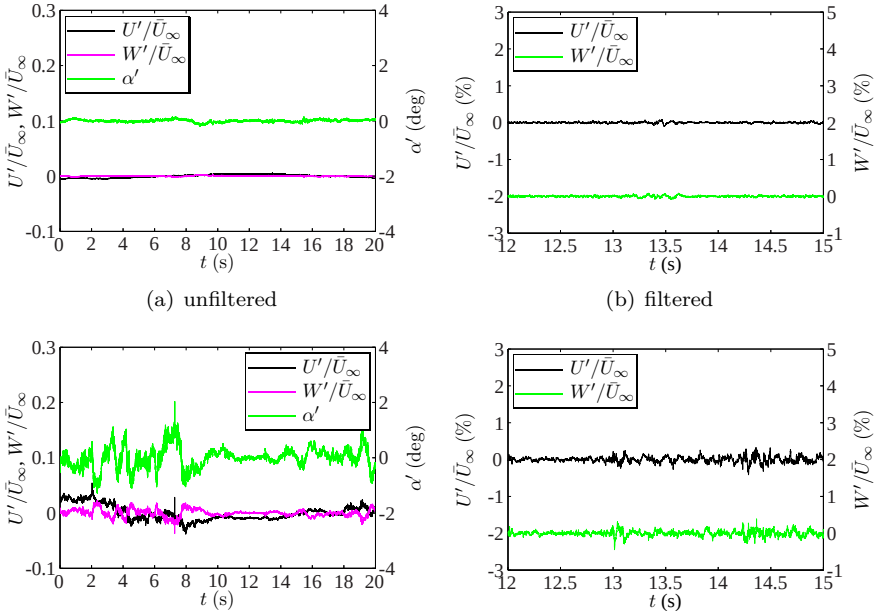

(a) unfiltered (b) filtered

(c) unfiltered (d) filtered

Figure 4.1.: Typical oncoming flow conditions. (a), (b): calm conditions ($\bar{\alpha} = -0.94°$, $\bar{U}_\infty = 43.9$). (c), (d): lightly turbulent conditions ($\bar{\alpha} = -0.95°$, $\bar{U}_\infty = 41.38$).

conditions are felt as slight vibrations inside the cockpit. Under moderately turbulent conditions deviations of up to 2.5° of the mean angle of attack appear as fast and irregular variations. For the pilot it is virtually impossible to control these variations, since there is no intuitive feedback. It can be observed that the angle of attack mainly correlates with the fluctuations of the velocity component $W'/\bar{U}_\infty$ normal to the chord. Thus the fluctuations in the effective angle of attack originate predominantly from vertical gusts imposed by turbulence. They primarily cause lift variations which leads to motions of the aircraft. The long waveform in the longitudinal fluctuation data $U'/\bar{U}_\infty$ is the phugoid motion of the aircraft. This is not a result of turbulence. It is caused by an improper adjustment of the initial flight condition by the pilot at the start of the measurement sequence. Issues of the

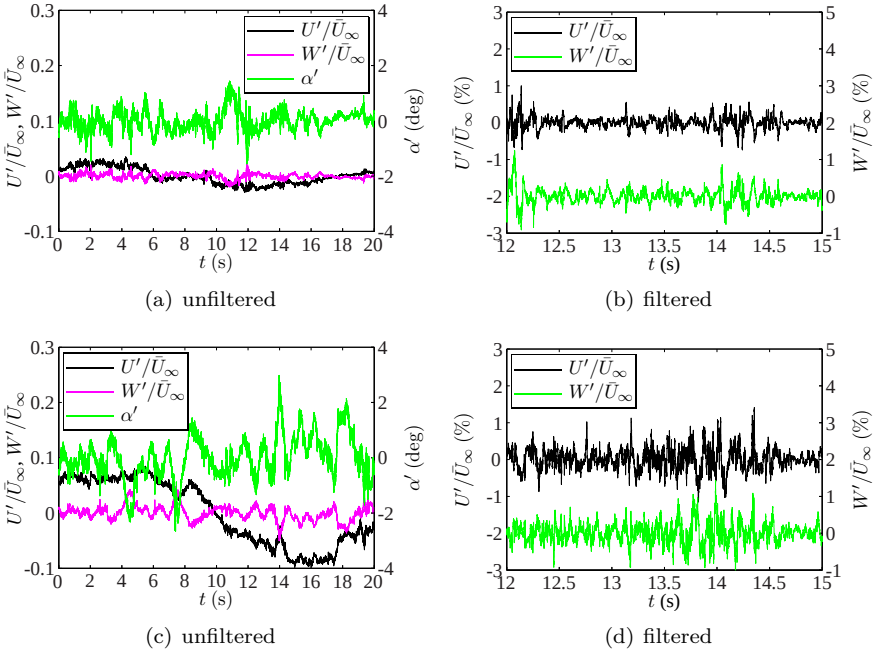

(a) unfiltered (b) filtered

(c) unfiltered (d) filtered

Figure 4.2.: Typical oncoming flow conditions. (a), (b): lightly turbulent conditions in a shear layer ($\bar{\alpha} = -1.3°$, $\bar{U}_\infty = 46.32$ m/s). (c), (d): moderately turbulent conditions in the convective boundary layer ($\bar{\alpha} = -1.16°$, $\bar{U}_\infty = 41.92$ m/s).

flight dynamic eigenmotions of the research aircraft will be addressed in more detail in Chapter 6. Taking a closer look on the details of the fluctuations, the propagation of the turbulent fluctuation intensity toward smaller scales is clearly visible in the filtered signals in Figure 4.2(d). This makes such conditions particularly interesting for boundary-layer transition investigations.

A fourth category of stronger turbulent forcing, relevant for the aerodynamic loads albeit less frequently encountered, was investigated by Weismüller (2011) in flights directly through thermals. These conditions are not investigated here. Stronger turbulence is of less importance for airfoil efficiency considerations since it is not continuously encountered.

The discussed flight cases only give a qualitative picture of the oncoming

Table 4.1.: Comparison of characteristic turbulence quantities for different on-coming flow conditions corresponding to Figures 4.1 and 4.2.

Turbulence intensity (5 / 20 Hz - 1 kHz) Tu_{XZ}	Energy dissipation rate ε (m^2/s^3)	Kolmogorov length scale ℓ_K (m)	True airspeed $\bar{U}_\infty$ (m/s)	Pressure altitude $\bar{H}$ (m)
0.03 % / 0.02 %	$2.97 \cdot 10^{-7}$	$11.84 \cdot 10^{-3}$	43.90	2084.5
0.20 % / 0.12 %	$2.07 \cdot 10^{-5}$	$2.10 \cdot 10^{-3}$	41.38	959.4
0.25 % / 0.15 %	$3.60 \cdot 10^{-4}$	$2.05 \cdot 10^{-3}$	46.32	2409.1
0.30 % / 0.18 %	$7.59 \cdot 10^{-4}$	$1.51 \cdot 10^{-3}$	41.92	800.4

flow disturbances. For a quantitative characterization of the turbulence, the assumption of statistically isotropic fluctuations yields a number of important simplifications. To apply these simplifications for the flight experiments, it is desirable to verify the assumption of isotropy for the encountered turbulence.

4.2. Substantiation of the Assumption of Local Isotropy

Atmospheric turbulence is produced at very large Reynolds numbers ($O(10^7) - O(10^8)$). It is therefore certainly non-homogeneous and non-isotropic at large scales. As explained in Chapter 2.1, the turbulent eddies relevant for the aircraft are more than an order of magnitude smaller than the eddy length scales of the energy containing range. Unsteady airfoil effects and the excitation of boundary-layer disturbances are thus driven only by the small scales contained in the energy cascade process, i.e. the local turbulent motions which are assumed to have lost most of their directional heritage in the decay process. The hypothesis of Kolmogorov (1941) states that the small-scale turbulent motions at very large Reynolds numbers are statistically isotropic. In the following, the isotropy assumption for the scales relevant in the aerodynamic problem will be verified following the approach of Sheih et al (1971), who conducted an in-flight study of atmospheric turbulence at low altitudes.

The investigation of the statistical equality of all three velocity components requires the simultaneous measurement with two X-wire probes. Therefore,

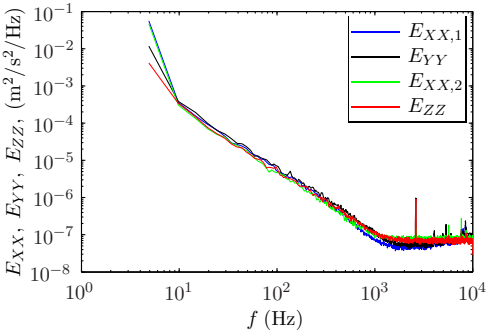

Figure 4.3.: Power spectral density of the three different velocity components.

Figure 4.3 shows the power spectra (PSD, in a signal processing sense) of three velocity components obtained with the commercial CTA system of configuration 1 ($f_s = 20$ kHz). For an estimate of the spectra the method proposed by Welch (1967) was used. The signals are divided into blocks of 4096 samples with 50% overlap yielding a block time of approximately $0.2s$ and 200 blocks for averaging of a typical measurement sequence. The data blocks are Fourier transformed and subsequently averaged, which constitutes a filter. A Hamming window function is applied in order to diminish leakage effects and a compensation factor is used for an accurate estimate of the spectral density (Bendat and Piersol, 2010).

Although the bending into the dissipation range (cf. Figure 2.1) cannot be observed due to the limited sensitivity of the CTA system, the collapsing of all four spectra within the inertial subrange indicates strong similarities in the different velocity fluctuations. To further verify the local isotropy assumption, it is convenient to consider the first derivative of the velocity fluctuation signals since it mainly depends on the small scale motions of interest (Romano et al, 2007). Wyngaard (2010) also shows that anisotropy at small atmospheric scales manifests more clearly in the first derivative than in the pure velocity fluctuations. Furthermore, the first derivative can be used for the determination of the energy dissipation rate, a characteristic turbulence quantity, by transforming it into a spatial derivative. Taylor's hypothesis states that the turbulent patterns do not change while flying through them if the ratio between the mean velocity and the fluctuations is

sufficiently large (Taylor, 1938).

$$\frac{\partial}{\partial t}\vec{U}' = -\frac{1}{\bar{U}_\infty}\frac{\partial}{\partial X}\vec{U}'. \tag{4.1}$$

This assumption of 'frozen turbulence' is only applicable for low turbulence intensities, as demonstrated by Nobach and Tropea (2012). Considering the magnitude of the relative velocity fluctuations in Figures 4.1 and 4.2, the criterion is always fulfilled in the present study. Tennekes and Lumley (1972) demonstrate that the strain rate fluctuations reduce to a simple relation for the energy dissipation rate ϵ in isotropic turbulence, attributing to the fact that most of fluctuation power of the first derivative is contained in the small scale motion.

$$\epsilon = 15\nu\,\overline{\frac{\partial U'^2}{\partial X}} = 7.5\nu\,\overline{\frac{\partial V'^2}{\partial X}} = 7.5\nu\,\overline{\frac{\partial W'^2}{\partial t}}\,. \tag{4.2}$$

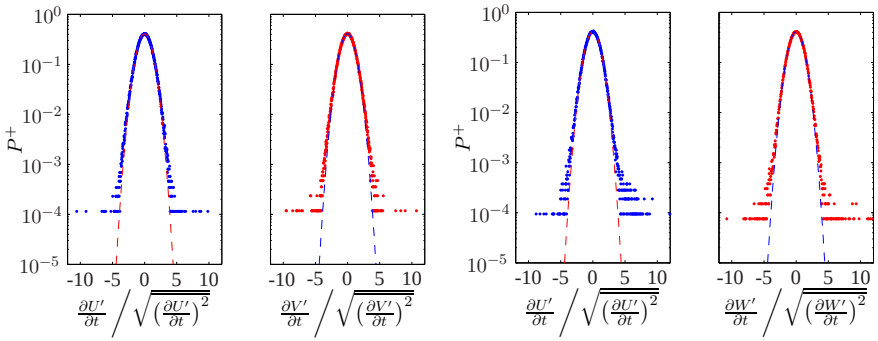

(a) X hot-wire probe 1 (b) X hot-wire probe 2

Figure 4.4.: Normalized frequency distribution (dots) and a comparison with Gaussian probability density function (dashed lines).

To elucidate possible anisotropy in the flight measurements, the probability density distribution P and the joint probability density distribution J (Bendat and Piersol, 2010) of the velocity derivative fluctuations are inves-

tigated.

$$P_X^+ = \sqrt{\overline{\left(\frac{\partial U'}{\partial t}\right)^2}}\, P\left(\frac{\partial U'}{\partial t}\right), \quad P_Z^+ = \sqrt{\overline{\left(\frac{\partial V'^2}{\partial t}\right)}}\, P\left(\frac{\partial V'}{\partial t}\right), \qquad P_Y^+ = \sqrt{\overline{\left(\frac{\partial W'}{\partial t}\right)^2}}\, P\left(\frac{\partial W'}{\partial t}\right) \tag{4.3}$$

In Figure 4.4 the normalized probabilities distributions P^+ are plotted over of the individual random variables normalized with their standard deviation. The distributions corresponding to the spectra of Figure 4.3 are obtained by using 1000 bins and dividing the frequency of events in each bin by the total of measurement points as well as the bin width. For all four components the probability distributions follow closely a Gaussian probability density function (PDF), depicted in dashed lines, up to approximately four standard deviations. The less probable events deviate from the Gaussian PDF and they scatter in exponential tails. The departure from the Gaussian into the exponential tails appears less peculiar than in the investigation of Sheih et al (1971) due to the lower turbulence level and a slight over-damping of the hotwire system due to a conservative adjustment. The important insight for the present investigation is that all the distributions appear similar in the upper part with their peak around zero. As no preferable skewing to the negative or to the positive side is found, this observation supports the isotropy assumption. The statement becomes even more evident when considering the normalized joint probability distributions.

$$J_{XZ}^+ = \sqrt{\overline{\left(\frac{\partial U'}{\partial t}\right)^2}}\sqrt{\overline{\left(\frac{\partial V'}{\partial t}\right)^2}}\, J\left(\frac{\partial U'}{\partial t}, \frac{\partial V'}{\partial t}\right), \qquad J_{XY}^+ = \sqrt{\overline{\left(\frac{\partial U'}{\partial t}\right)^2}}\sqrt{\overline{\left(\frac{\partial W'}{\partial t}\right)^2}}\, J\left(\frac{\partial U'}{\partial t}, \frac{\partial W'}{\partial t}\right) \tag{4.4}$$

In Figure 4.5 the joint probability distributions obtained with both X-wire probes are compared with the fit of a joint Gaussian probability density function (dotted lines). In this case 255 times 255 bins were equidistantly distributed to obtain the two-dimensional information. The contours in both plots are approximately circular with the center at the origin of the coordinate system. The Gaussian density function is closely met in the inner part, whereas increasing deviations are observed in the outer part which resemble

the effect of the tails described in Figure 4.4. The symmetry in these plots substantiates the assumption of local isotropy although a slight skewing in the 45°-direction is visible. Although Sheih et al (1971) observed a slightly more pronounced skewing in a similar plot they also concluded that the small-scale turbulence is isotropic. Their results were obtained with a single cross-wire probe mounted on the wing tip of a low-aspect ratio aircraft. It is possible that the probe position affected the measurements by velocity induction effects. From the present results it can be inferred that the statistics of the turbulent velocity disturbances are invariant toward translation, rotation and reflection of coordinate axis, i.e. that they are locally isotropic in the scales relevant for the present aerodynamic investigation. Contrary to general wind-tunnel experiments, where a certain anisotropy is usually unavoidable, the high Reynolds numbers of atmospheric turbulence ensure an isotropic consideration, at least for the scales relevant for laminar-turbulent transition of the wing boundary layer.

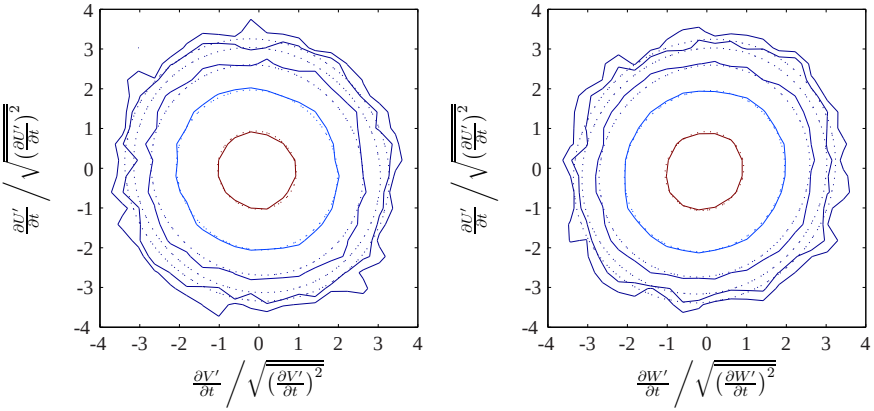

(a) X hot-wire probe 1

(b) X hot-wire probe 2

Figure 4.5.: Contours of the normalized frequency distributions (solid lines) and comparison with the Gaussian joint probability functions J^+_{XZ} and J^+_{XY} (dashed lines). Contour levels from the outer to the inner curves: 0.0005, 0.0010, 0.0036, 0.0182, 0.1004.

4.3. Quantification of In-Flight Turbulence

Different measures may be used to characterize the oncoming turbulence. In wind-tunnel applications employing X-wire measurements, it is common to use the turbulence intensity

$$Tu_{XZ} = \frac{1}{\bar{U}_\infty}\sqrt{\frac{1}{2}(\overline{U'^2} + \overline{W'^2})}, \tag{4.5}$$

which reduces to $Tu \equiv Tu_{XX} = \sqrt{\overline{U'^2}}/\bar{U}_\infty$ in isotropic turbulence. In flight under turbulent conditions, the magnitude of the fluctuation velocities may be affected by flight dynamic eigenmotions as shown in Figure 4.2(c). Thus, a high-pass filter must be applied in order to separate the aircraft motion from smaller-scale turbulence. The question which fluctuations should be included in the analysis, i.e. the choice of the cutoff frequencies, directly affects the measured turbulence intensity. Furthermore, since the turbulent fluctuations in the atmosphere do not depend on the airspeed of the aircraft, the turbulence intensity is reduced for increasing velocities due to the normalization with $\bar{U}_\infty$. It should be noted that a significant portion of the kinetic energy is neglected by the filtering, as it is obvious from Figure 2.1 that most of the fluctuation energy is contained at low frequencies. Decreasing the cutoff frequency of the high-pass filter leads to higher turbulence intensity values as can be seen for the two high-pass frequencies included in Table 4.1. Nevertheless, the turbulence intensities with the properly stated filter enable comparisons with wind-tunnel investigations if the same data reduction is applied. Therefore, Table 4.2 gives an overview of the definitions used in the qualitative description of the flight cases at the beginning of this chapter. The band-pass filter between 5 Hz and 1kHz will be stated with the results of the in-flight investigations. It should be noted that the turbulence intensities stated in Table 4.1 are significantly higher than the ones of low disturbance wind tunnels typically used for the investigation of NLF airfoils. Zanin (1985) reported similar levels in convective turbulence and up to $Tu_{XX} = 1.5$ % (1 Hz - 5 kHz) in cumulus clouds. Fanning (2012) observed values of less than 0.04 % in the still atmosphere (1 Hz - 15 kHz). Riedel and Sitzmann (1998) summarized turbulence intensities measured with different airborne platforms. Although the applied filtering is not quite clear in all cases, they came to similar results including a turbulence intensity of 1 % in an inversion layer. It should be kept in mind that the spectral composition of atmospheric turbulence may be significantly different to the one obtained

Table 4.2.: Definition of characteristic turbulence quantities for the present flight investigation.

	Calm	Lightly turbulent	Moderately turbulent	Turbulent
Turbulence intensity Tu_{XZ} (5 Hz - 1 kHz)	$0 - 0.05$ %	$0.06 - 0.25$ %	$0.26 - 0.4$ %	> 0.4 %

in a wind tunnel, especially at the frequencies relevant for the generation of boundary-layer disturbances.

4.3.1. Spectral Representation of Atmospheric Turbulence

Due to the extensive simplifications in the treatment of isotropic turbulence and the applicability of Taylor's hypothesis, one-dimensional energy spectra reveal a rather comprehensive picture on the small-scale motion of atmospheric turbulence relevant to aircraft. The results shown in the following were obtained with a single X-wire probe using the low-noise CTA system of measurement configuration 2 (cf. Table 3.1). With the justified assumption of local isotropy, the additional small-scale information gathered with these anemometers outweighs the shortcomings of obtaining not all three velocity components.

Figure 4.6 shows the measured one-dimensional, block-averaged power spectral density E_{XX} of four flight cases ranging from calm to moderately turbulent conditions. For higher turbulence levels the kinetic energy density E_{XX} is increased for all scales, shifting the spectra vertically and extending them laterally. All spectra follow a characteristic $-5/3$ power law (dashed lines) for several decades of the frequency axis f. In the high-frequency range, the spectra depict a downward bending indicating the beginning of the dissipation range, which could not be observed when using the commercial CTAs of configuration 1 in the previous flight test campaigns. The disturbance peaks, included in the dissipation range at frequencies $f > 1000$ Hz, are the result of electromagnetic interference. An unknown acoustic source is rather improbable since the peaks did not appear in Figure 4.3. For low turbulence levels these disturbances are particularly evident since the fluctuation energy in the flow is not sufficient to cover their spectral density.

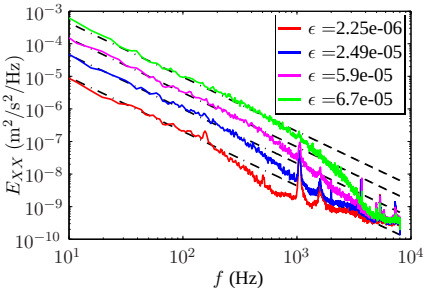

Figure 4.6.: Comparison of longitudinal turbulence spectra measured in a single gliding flight.

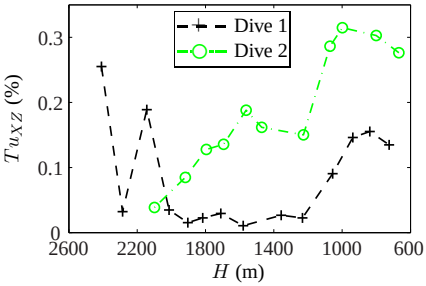

Figure 4.7.: Evolution of the turbulence intensity with the pressure altitude for two different atmospheric states.

To compare the measured spectra with Kolmogorov's power law for the inertial subrange, Taylor's hypothesis is applied to transform the frequency dependence of the measured one-dimensional frequency spectra $E_{XX}(f)$ (based on the chordwise velocity component) into a wavenumber dependence.

$$k = \frac{2\pi f}{\bar{U}_\infty}, \qquad E_{XX}(k) = E_{XX}(f)\frac{\bar{U}_\infty}{2\pi} \tag{4.6}$$

The isotropy of the investigated turbulence enables the relation of the three-dimensional energy spectrum function (2.1) to its one-dimensional counterpart $E_{XX}(k)$ (Pope, 2000).

$$E_{XX}(k_X) = \int_{k_X}^{\infty} \frac{E(k)}{k}\left(1 - \frac{k_X^2}{k^2}\mathrm{d}k\right), \quad E(k) = \frac{k^3}{2}\frac{\mathrm{d}}{\mathrm{d}k}\left(\frac{1}{k}\frac{\mathrm{d}E_{XX}}{\mathrm{d}k}\right) \tag{4.7}$$

The universal constant $C_{\mathrm{T,X}}$ for longitudinal spectrum within the inertial subrange then is given by

$$C_{\mathrm{T,X}} = \frac{2C_{\mathrm{T}}}{(5/3)\,(2+5/3)} = \frac{18}{55}C_{\mathrm{T}}. \tag{4.8}$$

There is quite some variation of the parameter C_{T} in turbulence literature. Saddoughi and Veeravalli (1994) recommend a widely accepted value of 1.5 based on high Reynolds number laboratory measurements. However, in the

presented experiments a better approximation of the inertial subrange law was found with a value of 2, which was also obtained by Sheih et al (1971) in their in-flight study.

Due to the known behavior of atmospheric turbulence in the inertial subrange described in Chapter 2, Section 4.2 and by equation (4.7), a unique way of characterizing the scales in the universal equilibrium range is the calculation of the energy dissipation rate ϵ. This provides an unambiguous quantity for the description of the oncoming flow disturbances independent of the aircraft speed. The energy dissipation rate can be determined either from equation (4.2) or from a least square fit of the one-dimensional form of Kolmogorov's law (equation (2.1) with $C_{T,X} = 0.66$) to the measured spectra E_{XX} within the inertial subrange (Pruis et al, 2013). The latter method is chosen here and this choice will be justified later in this section. Following Kolmogorov's theory for the universal equilibrium range, the length and velocity scales that characterize the dissipation range follow directly from combinations of ϵ and the kinematic viscosity ν:

$$\ell_{\mathrm{K}} = \left(\frac{\nu^3}{\epsilon}\right)^{1/4}, \qquad u_\ell = (\ell_{\mathrm{K}}\nu)^{1/4}, \qquad \tau_\ell = \sqrt{\frac{\nu}{\epsilon}}. \tag{4.9}$$

The energy dissipation rate ϵ and the Kolmogorov length scale ℓ_{K} are two distinct quantities characterizing the oncoming flow disturbances without any need for a high-pass filter as in the case of the turbulence intensity Tu_{XZ}.

Figures 4.7 and 4.8 show the evolution of these quantities for all the measurement runs in two typical gliding flights, denoted as dives in the following. The variation of these quantities with the altitude enables interesting insights into the different sources of atmospheric turbulence encountered in the these experiments. Dive 2 in Figure 4.8(a) shows the typical result for a continuous descent from slightly above the cumulus cloud base into the convective mixed layer of the ABL. While the turbulence intensity Tu_{XZ} (Figure 4.7) and the energy dissipation rate ϵ gradually increase for lower altitudes (Figure 4.8(a)), the length ℓ_{K} declines for increasing turbulence levels to values in the millimeter range (Figure 4.8(b)). The results for dive 1 show a remarkably different behavior. The first and the third measurement run exhibit quite elevated turbulence levels at high altitude of $H > 2000$ m. These remarkably high values for Tu_{XZ} and ϵ were caused by the specific stratification of the atmosphere producing two layers of high wind shear. The convective mixed layer on that day was limited to altitudes of less than

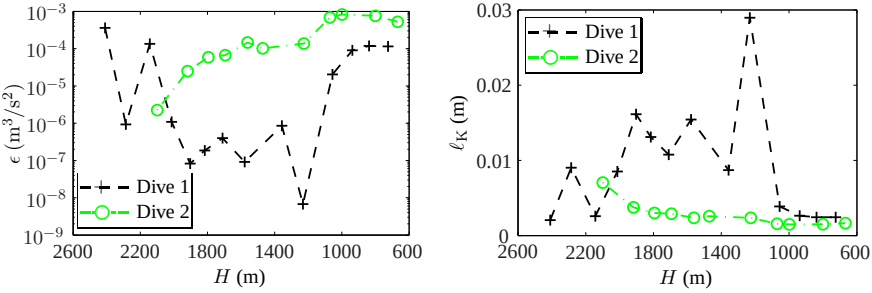

Figure 4.8.: Evolution of the energy dissipation rate ϵ and the Kolmogorov length scale ℓ_K for different pressure altitudes in two different gliding flights. Dive 1: October 18th 2013. Dive 2: October 19th 2013

1100 m due to the stratification and an altostratus overcast prevented efficient solar heating of the ground. Therefore, after the initial wind-shear turbulence, a zone of low fluctuations intensity was found in the intermediate altitudes (1200 m $\leq H \leq$ 1900 m). Only for $H <$ 1000 m was significant convective turbulence found. The order of magnitude of ϵ obtained in these dives, for the different conditions, is in good agreement with the estimates obtained by Pruis et al (2013) using pulsed measurements with a light detection and ranging system for various atmospheric conditions.

To verify the correctness of the shape of the obtained spectra, the model energy spectrum of Pope (2000) is compared with the in-flight data. The model spectrum is a result of theoretical considerations and a series of experimental observations in high Reynolds number turbulence. It is obtained by multiplying the one-dimensional, longitudinal form of equation (2.1) by two dimensionless functions.

$$E = C_T \varepsilon^{\frac{2}{3}} k^{-\frac{5}{3}} f_L(k) f_\ell(k) \tag{4.10}$$

$$f_L = \left(\frac{k L_I}{\sqrt{k^2 L_I^2 + c_L^2}} \right)^{5/3+p_0} \tag{4.11}$$

$$f_\ell = \exp\left[-b \left(k^4 \ell_K^4 + c_\ell^4 \right)^{1/4} - c_\ell \right] \tag{4.12}$$

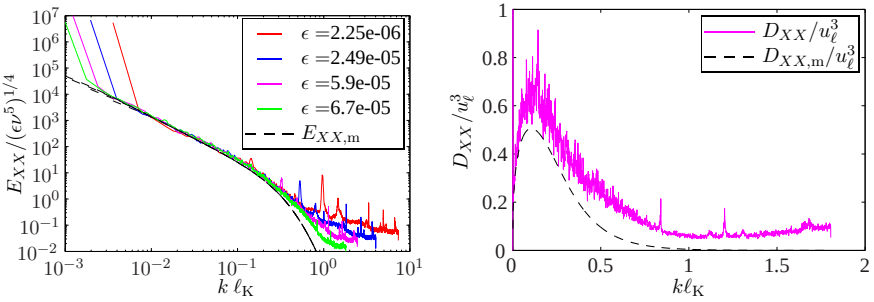

(a) (b)

Figure 4.9.: Spectra with Kolmogorov scalings. (a): Kolmogorov spectrum for different flight cases. (b): Dissipation spectrum corresponding to the case $\epsilon = 7.59 \cdot 10^{-4}$ in Table 4.1.

The multiplicative functions $f_L(k)$ and $f_\ell(k)$ approach a value of one within inertial subrange such that Kolmogrov's law is obeyed. The function f_L, which contains the integral length scale, only diverges from unity for smaller wavenumbers k, which are irrelevant for the aerodynamic considerations. The integral length scale and the intermediate Taylor length scale λ, which are necessary boundary conditions in many numerical simulations, are directly linked via the unfiltered root mean square value of the velocity fluctuations (Pope, 2000).

$$L_\mathrm{I} = \frac{1}{\epsilon}\left(\frac{\pi}{2}\overline{U'^2}\right)^{3/2} = \left(\frac{\lambda}{\sqrt{10}\,\ell_\mathrm{K}^{2/3}}\right)^3 \tag{4.13}$$

The function f_ℓ diverges from unity only for high wavenumbers to model the dissipative range. It depends on the Kolmogorov length scale ℓ_K and is important for the turbulence scales relevant for the excitation of boundary-layer instabilities. The values for the constants $c_L = 6.78$, $p_0 = 4$, $b = 5.2$ and $c_\ell = 0.4$ were chosen as suggested by Pope (2000). Applying Taylor's hypothesis in equation (4.6) and scaling the obtained wavenumber spectra with the Kolmogorov scales of equation (4.9), the curves in Figure 4.9(a) all coincide with the model spectrum $E_{XX,\mathrm{m}}$ in the mid-wavenumber range. The coincidence in the inertial subrange and the beginning of the dissipation range for the significantly different atmospheric turbulence states, indicates

the validity of the employed concepts for the present investigation. Clearly, the energy-containing range is not represented by the measured spectra. Due to the large length scales of the energy containing eddies, unfeasible recording sequences of more than 20 minutes would be necessary (Sheih et al, 1971). Motions of the aircraft caused by turbulence or pilot control inputs would further corrupt small wavenumber measurements, as explained in Chapter 3.4.

At low kinetic energy densities the hot-wire anemometry reaches its resolution limit. As a matter of principle a f^2 increase, or k^2-increase respectively, of the PSD in high-frequency range is caused by the CT controller response to self-generated electronic white noise, see Freymuth and Fingerson (1997). This f^2-increase is not visible in Figure 4.9(a) due to the anti-aliasing filter and the AD-conversion limitation to 16 kHz. Nevertheless, it limits the sensitivity of the hot wires, leading to a rather constant spectral density distribution in the high-frequency end of the measured spectra. In order to quantify this influence for the present investigation, the dissipation spectrum of a typical measurement

$$D_{XX}(K) = 2\nu k^2 E_{XX}(k) \tag{4.14}$$

is compared with the equally scaled model counterpart in Figure 4.9(b). The measurement D_{XX} over-predicts the model dissipation spectrum $D_{XX,\mathrm{m}}$. The peak is also observed at slightly higher $k\ell_{\mathrm{K}}$. This reflects the difficulties involved in the measurement of the small-scale structure of atmospheric turbulence at the airspeeds of the present flight investigation, which become more severe for lower turbulence levels. The deviations in the dissipation range introduce inaccuracies in the determination of the energy dissipation rate ϵ with equation (4.2) since it is directly related to the three-dimensional dissipation spectrum $D(k)$.

$$\epsilon = \int_0^\infty D(k)\mathrm{d}k = 2\nu \int_0^\infty k^2 E(k)\mathrm{d}k \tag{4.15}$$

To obtain the energy dissipation rate more accurately, it was decided to use the power law fit method described above avoiding the use of the dissipation spectrum completely.

While the difficulties in the high wavenumber range are purely technical, the depiction of the energy containing range with an airborne measurement system faces systematic difficulties. It is of course highly desirable to obtain the Taylor scales λ and the integral length scale L_{I} of the turbulence to

describe the spectrum completely, including the part modeled by equation 4.12. However, the determination of these quantities commonly relies on the knowledge of the unfiltered long-term root mean square values (RMS) of the velocity fluctuations in isotropic turbulence or a two point correlation procedure (Bradshaw, 1971). Despite these limitations, the obtained information is more than sufficient to determine the energy density relevant for the airfoil investigations. Since the bending of the energy spectrum E_{XX} can be identified in the measurement results in Figures 4.6 and 4.9(a), the model spectrum in equation (4.11) can be used to obtain improved estimates in the dissipation range. The presented spectra of the oncoming flow disturbances are particularly valuable for boundary-layer transition research, as such in-flight data for different altitudes is indeed rare in the existing literature (Fisher et al, 2003).

In summary, the characterization of the typically encountered oncoming flow disturbances in flight through atmospheric turbulence has been described in this chapter. Flights under various atmospheric conditions were examined which provide an understanding of the origin of atmospheric turbulence. Quantities to describe the turbulent state were presented. The turbulence intensity depends on an arbitrary filtering, whereas the energy dissipation rate, which may be obtained from the measured one-dimensional energy spectra, is a unique quantity for the characterization of atmospheric turbulence. The presentation of the energy spectra is thus necessary for describing atmospheric turbulence. Combining the experimental data with the model of Pope (2000), it is possible to extract information for estimates of the dissipation range, which is important for aerodynamic simulations. Although the notion that the turbulent kinetic energy is only transferred form larger to smaller eddies has been disproved using higher-order statistics (Wyngaard, 2010), Kolmogorov's theory for the equilibrium range of atmospheric turbulence in practice provides a sufficient framework for the present investigation of NLF airfoil effects. The verification of the local isotropy assumption for the relevant fine scales implies that the frequency and statistical moments of the velocity fluctuations of all three components encountered by an aircraft are similar, which is consistent with the observations at low altitudes of Sheih et al (1971). This is an important result for transition experiments, since wind tunnels are mostly exposed to a certain unavoidable level of anisotropy, which affects the boundary-layer receptivity process, especially at higher free-stream turbulence levels (Westin et al, 1994; Kendall, 1998).

5. Investigation of Boundary-Layer Transition under Calm Atmospheric Conditions

The understanding of the boundary-layer transition process on the NLF wing section under ideal conditions is an indispensable prerequisite for the investigation of the more complicated case of flight through atmospheric turbulence. In this chapter the transition behavior on the wing glove will be examined under calm atmospheric conditions. The peculiarities on both sides of the NLF airfoil, implied by the essential differences of the streamwise pressure gradient, will be examined. Results obtained in various flight test campaigns with two different measurement techniques, wall microphones and surface hot-films, will be presented to demonstrate the reproducibility of the experimental results. Fourier transforms will be used to identify the involved boundary-layer disturbances in the transition process. The three-dimensional and nonlinear aspects on the lower side of the airfoil will be highlighted. Wherever helpful, the experimental results will be complemented by boundary-layer and linear stability computations.

For the later investigation of the transition development under turbulent conditions, it is valuable to obtain a reference view of the temporal variation of transition under calm flight conditions. In the following a simple statistical averaging procedure for discrete time windows is employed to illustrate the time-dependent process detected with the streamwise surface hot-film row on the lower side of the airfoil (cf. Figure 3.3). For the measurement sequence of 20 s, the signal of each sensor is divided into overlapping segments (50 %) of 0.1 s which results in 1600 samples for statistics. The result is a statistical value for every 0.05 s. In the present case a time-variable RMS distribution is obtained. Plotting the distribution over the time coordinate and the streamwise sensor positions yields the graphics in Figure 5.1 as a convenient representation of disturbance amplification inside the boundary layer in the time-position domain.

Under the considered calm flight conditions (Tu = 0.04 %, 5 - 2000 Hz), a peak of varying amplitude is found at a chordwise position $X/L_c \approx 0.58$.

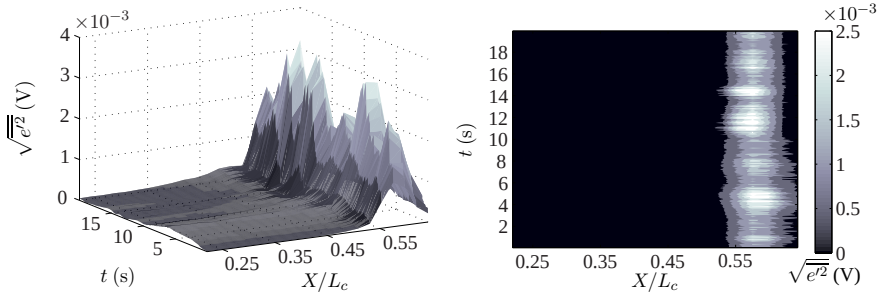

(a) 3D view (b) Top view

Figure 5.1.: Tempo-spatio transition development on the lower side of the airfoil under calm conditions , $\bar{\alpha} = -0.60°$, $Re = 3.142 \cdot 10^6$.

The rapid disturbance amplification between $0.5 \leq X/L_c \leq 0.6$ is explained by the resolution threshold of the hot-film sensors which need a certain shear stress fluctuation level to overcome their sensitivity limitations. The variation in disturbance amplitude reflects the random nature of the actual breakdown process of natural transition. Yet, the constant boundary conditions lead to an almost fixed position of the disturbance maximum. Having obtained this qualitative impression on the steadiness of transition under calm conditions, the physics involved in the process will be investigated closely after the presentation of the following remarks.

Approximately half of the flight measurements stated in Table 3.3 were conducted under calm conditions to verify the steady flow behavior. As demonstrated in Chapter 4 such conditions allow for very precise flying with angle of attack variations of less than 0.1°. Changes of the meteorologic conditions remain small for a measurement run of 20 s. The Reynolds number variation due to the altitude loss is less than 2 %. Thus, transition data averaged over the entire measurement run can be obtained with high precision. When considering the flight test results in the following section, it should be kept in mind that although the angle of attack can be adjusted precisely under calm conditions, the Reynolds number may differ from flight to flight due to meteorologic variations. Furthermore, weight differences of the aircraft affect the fundamental flight mechanical relations of gliding flight (Yechout et al, 2003).

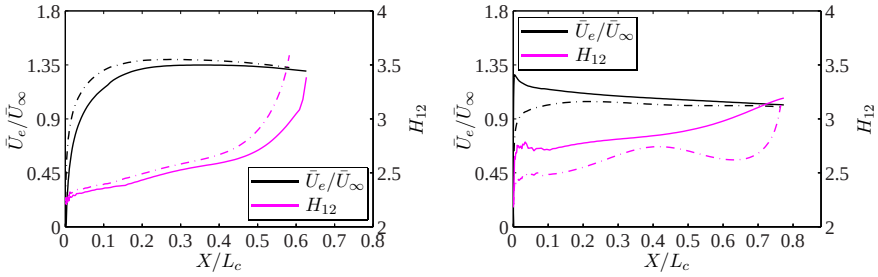

(a) Upper side

(b) Lower side

Figure 5.2.: Boundary conditions for two gliding flights on both sides of the wing glove. Solid lines: $\bar{\alpha} = -2.08°$, $Re = 3.6 \cdot 10^6$. Dashed dotted lines: $\bar{\alpha} = 0.22°$, $Re = 2.951 \cdot 10^6$.

5.1. Steady Dependence of Transition on the Angle of Attack

To examine the behavior of NLF airfoils in flight through atmospheric turbulence, it is necessary to understand the steady angle-of-attack dependency of transition on the investigated wing section. The angle of attack determines the streamwise pressure gradient and thereby the development of the boundary layer and its stability. The goal of maximizing laminar flow is achieved by different strategies on the upper and the lower side of the NLF airfoil, as can already be concluded from the different curvature on both sides of the airfoil in Figure 3.2(a). The upper side is continuously curved, whereas the lower side is almost flat for $0.2 \leq X/L_c \leq 0.7$. Considering the pressure distribution in Figure 3.9(a) and equations (3.8) and (3.9), it can be inferred that the bulk of the lift is created by the pressure deficit on the upper side. Hence, a carefully designed pressure recovery in the aft part of the airfoil is necessary to avoid separation and to yield a smooth trailing edge flow with minimum losses. The lower side does not contribute substantially to the lift and is exposed to lower wall shear stress (cf. Figure 3.9(b)). The major design goal for this side is the minimization of skin friction by a maximization of the laminar part of the boundary layer. Hence, qualitatively different boundary conditions drive the transition process on the two sides of the airfoil due to the specific pressure distribution.

The described airfoil design considerations are reflected in Figure 5.2. It presents the development of the outer velocity $\bar{U}_e(X/L_c)/\bar{U}_\infty$, obtained by the combined procedure of Chapter 3.3.1, for two different angles of attack in gliding flight under calm conditions. The influence of the pressure gradient on the shape of the boundary-layer profiles, which is a first indicator of their stability, is obtained by computing the shape factor $H_{12} = \delta_1/\delta_2$, i.e. the ratio between the displacement thickness δ_1 and the momentum thickness δ_2, with the procedure described in Chapter 3.2. On the upper side, the outer flow is initially accelerated for both angles of attack. At a certain streamwise distance, $X/L_c \approx 0.25$ and $X/L_c \approx 0.35$ respectively, the edge velocity starts to decline. The progressive deceleration corresponds to a continuously increasing adverse pressure gradient. This leads to the sharp rise in the boundary-layer shape factor H_{12} exceeding 3.4 at $X/L_c > 0.5$ in the downstream part for both cases. The shape factor therefore approaches the laminar separation limit of the non-self-similar airfoil boundary layer, which may be lower than the one ($H_{12} = 4$) for Falkner-Skan flow (Schlichting and Gersten, 2000).

The lower side of the airfoil in Figure 5.2(b) exhibits a different behavior. The pressure gradient $\partial\overline{p}/\partial x = -\bar{U}_e(\partial\bar{U}_e/\partial x)$ is constant over a large streamwise distance. For the lower angle of attack, the boundary-layer is strongly decelerated in the region downstream of the leading edge $X/L_c \leq 0.2$ before it is exposed to a constant adverse pressure gradient in the downstream part. For the higher angle of attack, the boundary layer is gradually accelerated tending toward a constant value of the outer velocity. The different pressure gradient in the leading edge region is reflected by the vertical shift of the H_{12} curves. The shape factor for the lower angle of attack increases continuously, whereas H_{12} for the higher angle of attack shows a variation in the downstream part remaining below 2.7 for $X/L_c \leq 0.7$. Both curves remain well below the separation limit upstream of the transition trip at $X/L_c = 0.77$ (cf. Figure 3.3). The tripping of the boundary layer is necessary for the pressure recovery without massive laminar separation in the S-shaped aft part of the airfoil. This peculiarity of the lower side is necessary for the desired trailing-edge angle and it is important for the angular momentum balance of the airfoil.

The consequences of the qualitatively different boundary-layer development become evident when investigating the evolution of transition on the wing section. Figure 5.3 shows the streamwise amplification of the RMS hot-films signals on the two airfoil sides for various angles of attack. In gliding flight the angle of attack is explicitly coupled to the airspeed and thus to the

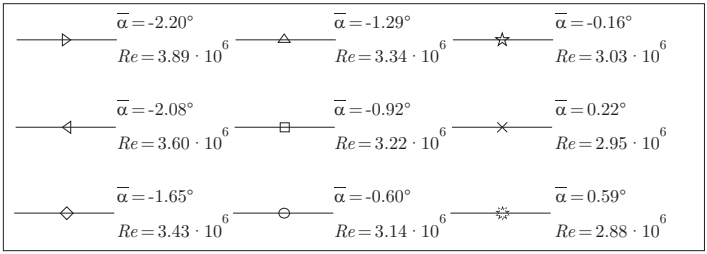

(a) Figure legend

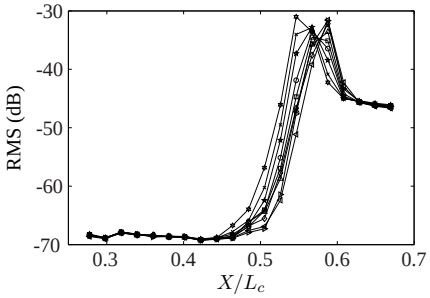

(b) Upper side

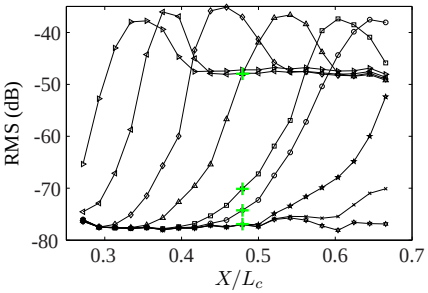

(c) Lower side

Figure 5.3.: Transition development on both sides of the wing glove under calm flight conditions. The larger + marker symbols on the lower side will be referred to in Section 5.2.2.

Reynolds number. All the information shown in Figure 5.3 were obtained in a single dive with 9 measurement runs and they are typical for measurements under calm conditions. The obtained data of each run was averaged over the 20 s recording interval. The logarithmic presentation in decibels reflects the signal-to-noise ratio and it emphasizes potential calibration differences between the sensors. However, the smooth evolution of the curves affirms a good adjustment of the hot-film arrays obtained by the in-flight matching procedure described in Chapter 3.1.3. As discussed in Chapter 3.3, disturbance growth rates cannot directly be derived from the uncalibrated hot-film signals (cf. Chapter 3.3.2). Nevertheless, the unambiguous shape of the RMS distribution undoubtedly marks the transition process.

On the upper side of the wing section in Figure 5.3(b), the streamwise RMS evolution looks remarkably similar for all shown flight cases. As the present experiments focus on cruise flight at low lift coefficients ($0.35 < C_l < 0.85$), transition on the upper side of the wing section is fixed in the region $0.54 < X/L_c < 0.58$. This behavior can be attributed to two counteracting mechanisms. When the angle of attack $\bar{\alpha}$ increases, transition on the upper side is promoted due to an increased adverse pressure gradient. In gliding flight, however, the angle of attack $\bar{\alpha}$ and the chord Reynolds number Re are coupled such that Re decreases for increasing $\bar{\alpha}$ and vice versa. While a higher Re generally promotes transition, a lower Re delays transition. In flight through turbulence, gust induced angle-of-attack variations are inevitable. However, the fluctuations in the incidence flow angle are not necessarily coupled to the Reynolds number as will be demonstrated in Chapters 6 and 7. Therefore, it will be interesting to investigate, whether the fixation of transition on the upper side of the airfoil at low mean angles of attack can persist in flights through elevated levels of atmospheric turbulence.

In contrast to the upper side, transition development on the lower side in Figure 5.3(c) exhibits a very strong dependence on the mean angle of attack. For low $\bar{\alpha}$ the RMS maximum is found in the leading edge part of the hot-film array. It gradually moves downstream for increasing angle of attack. A disturbance fluctuation maximum can no longer be observed for $\bar{\alpha} = 0.22°$. With higher lift coefficients, i.e. higher incidence angles, the flow on the lower side remains completely laminar until encountering the transition trip strip at $X/L_c = 0.77$. Note that the angle-of-attack span between the first and the last peak detection is only 2.8°. Common for state-of-the-art sailplane airfoil design, this makes the lower side severely susceptible to angle-of-attack fluctuations in cruise flight (low $\bar{\alpha}$). Downward directed vertical gusts may

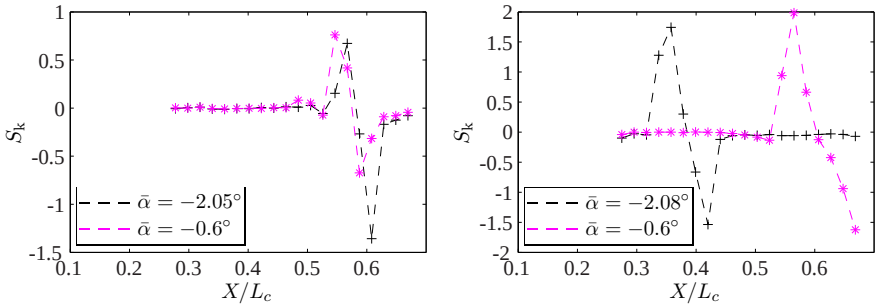

(a) Upper side (b) Lower side

Figure 5.4.: Skewness distribution on both sides of the wing glove for two different angles of attack.

lead to increased boundary-layer instability causing temporarily transition that is not foreseen by considering only the mean oncoming flow. In steady gliding flight, however, the coupling between $\bar{\alpha}$ and Re emphasizes the effect since a lower $\bar{\alpha}$ corresponds to a higher Re.

To verify that the maximum RMS value of the time-averaged hot-film signals is indeed an indicator for transition, the empirical skewness, i.e. the third central statistical moment,

$$S_\mathrm{k} = \frac{1}{N} \sum_{n=1}^{N} \left(\frac{e'_n - \bar{e}}{\sqrt{\overline{e'^2}}} \right)^3 \tag{5.1}$$

is shown in Figure 5.4 for two cases depicted in Figure 5.3. Nitsche (2006) relates the characteristic skewness appearance with a pronounced maximum and a minimum to the intermittency of the flow, i.e. the probability of finding turbulence at a certain position. While the skewness is zero in the laminar part of the boundary layer, it assumes a positive maximum in the transition region. Positive values of S_k correspond to an imbalance of the probability distribution of the wall shear stress fluctuations toward positive values. The negative skewness further downstream indicates that more negative than positive amplitudes are observed in the time trace of the specific sensor. The strong decrease from the global maximum to the minimum is characteristic for the breakdown region. In the developing turbulent boundary layer further downstream S_k tends toward zero again reflecting a symmetric distribution

of the random fluctuations. The qualitative behavior for both sides is similar. The angle-of-attack dependence of the lower side, already observed in Figure 5.3(c), is clearly reflected. As the maximum skewness corresponds to the position of the peak in the RMS distribution, this is a characteristic position for comparisons with N-factor computations.

The preceding results on the intrinsically different angle-of-attack dependence of the two sides of the investigated airfoil are important for flight through atmospheric turbulence. The characteristics of both sides reflect the design philosophy of state-of-the-art sailplane airfoils at the lower edge of the laminar bucket. The implications of the different behavior should be kept in mind for the later investigation of the effects of moderate turbulence.

5.1.1. Disturbance Amplification Factors for Low Turbulence Levels

The disturbance evolution inside a non self-similar two-dimensional boundary layer is highly dependent on the pressure gradient. Moderate deceleration or acceleration has tremendous effects on the linear stability of the boundary layer. This becomes particularly evident when comparing the shape of the N-factor curves on both sides of the airfoil in Figures 5.5 and 5.6, which were computed with the shooting procedure presented in Chapter 3.2. The curves resulting from linear stability theory are compared with the corresponding measurement result of Figure 5.3 to extract transition amplification factors. Frequencies of the TS modes are equidistantly distributed in steps of 100 Hz between 100 and 2000 Hz. As shown in Section 5.1, the location of the maximum RMS yields a characteristic streamwise position in the transition process. It is therefore convenient to compare this maximum with the local N-factor envelope. The highest intersection of a N-curve with the dashed line consequently marks the transition N-factor in Figure 5.5.

The progressive ascent of the two-dimensional N-factor curves on the upper side in Figure 5.5 reflects the continuously increasing deceleration in the narrow streamwise region $0.45 < X/L_c < 0.65$ and the associated strong increase of H_{12} in Figure 5.2. The most amplified frequencies according to LST, at the measured RMS maximum position for both angles of attack, are found in the frequency band $700 \leq f \leq 1300$ Hz. The progressive rise of the N-factor curves for all frequencies is typical for separation bubble proximity (Horstmann et al, 1989). However, the high N-factor values corresponding to the peak in the RMS transition measurements ($N \geq 10$) suggest that natural transition occurs before laminar separation becomes effective (Würz,

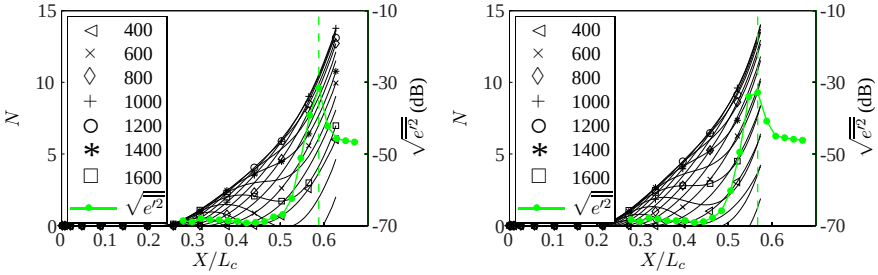

(a) $\bar{\alpha} = -2.08°$, $Re = 3.595 \cdot 10^6$ (b) $\bar{\alpha} = 0.22°$, $Re = 2.95 \cdot 10^6$

Figure 5.5.: Two-dimensional N-factor computations compared with measured transition peaks on the upper side of the airfoil. The numbers in the figure legends denote frequencies of the N-factor curves in Hz.

2014). As mentioned in Section 5.1, the increasing adverse pressure gradient and the decreasing Reynolds number are counteracting. The resulting progressive N-factor evolution in the transition region explains the approximately fixed peak of the disturbance amplification on the upper side for the various flight cases in Figure 5.5. The high amplification provides the grounds for nonlinear interactions in a short streamwise region, promoting the subsequent breakdown to turbulence.

On the lower side, the pressure gradient may be negative or slightly positive depending on the angle of attack (cf. Figure 5.2). It remains moderate and almost constant over the entire streamwise distance up to the transition trip at $X/L_c = 0.77$. Two-dimensional TS waves thus are exposed to a frequency-selective growth and attenuation, which resembles the passing through both branches of the neutral curve, i.e. positions of zero growth rate in a stability diagram. In Figure 5.6 the high frequency N-factor curves are the first to rise and to be damped out before reaching critical levels. The TS modes of lower frequencies evolve over a considerable streamwise distance before initiating breakdown to turbulence. For both considered angles of attack the highest N-factors are found at low frequencies ($400 \leq f \leq 800$ Hz) in the downstream part. Disturbances with different spectral properties thus amplify at different stages. Such a gradual growth of different spectral components promotes weakly nonlinear wave interactions (Würz et al, 2012).

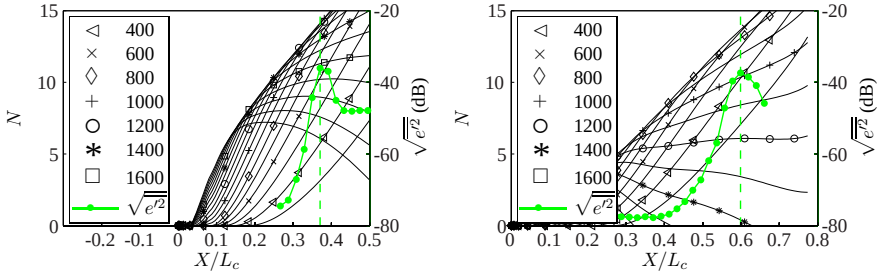

(a) $\bar{\alpha} = -2.08°$, $Re = 3.595 \cdot 10^6$ (b) $\bar{\alpha} = -0.60°$, $Re = 3.142 \cdot 10^6$

Figure 5.6.: Two-dimensional N-factor computations compared with measured disturbance amplification on the lower side of the airfoil. Legend numbers denote frequencies f in Hz.

According to the predictions of LST, Tollmien-Schlichting waves amplify further upstream than the experimentally observed disturbance growth in Figures 5.5 and 5.6. Due to their limited sensitivity, the hot-film system is only able to capture disturbances above a certain amplification threshold. This threshold is found at $N \approx 6$ on both sides of the wing glove. Therefore, a considerable part of the linear growth region cannot be detected. This is a common problem in transition research, especially in flight experiments with multi-sensor arrays (Sturzebecher et al, 2001).

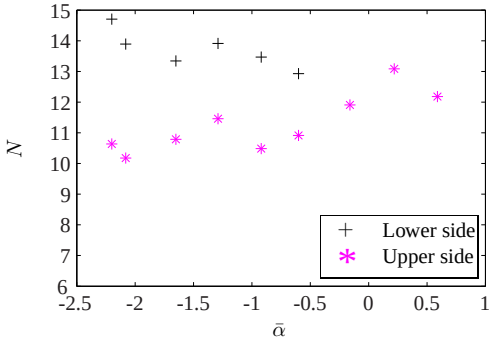

Figure 5.7.: Summary of the transition N-factors determined in nine measurement runs of a single dive.

The peak values in Figures 5.5 and 5.6 correspond to higher amplification factors ($N > 10$) than usually encountered in wind tunnels (Van Ingen, 2008). Figure 5.7 depicts all transition N-factors obtained in the nine measurement runs for both sides. On the lower side RMS peaks are only detected for low $\bar{\alpha}$ and the transition N-factor for these cases exceeds a value of $N = 13$. For low angles of attack the N-factors of the upper side remain below $N = 11$. Only when leaving the laminar separation proximity for $\bar{\alpha} > 0$, N on the upper side assumes similar values to the ones of the lower side.

The reason for the different behaviour of the upper side could not thoroughly be determined. Yet, a conjecture is obtained from the microphone signals of configuration 1 described in Chapter 3.1.3. For low angles of attack under perfectly calm conditions, the microphone signals on the upper side were temporary corrupted by broadband noise. Figure 5.8(a) shows this effect on the time averaged sound pressure level

$$\mathrm{SPL} = \frac{\sqrt{\overline{p'^2}}}{\rho \bar{U}_\infty^2} \tag{5.2}$$

for two different angles of attack of a single gliding flight, where $\bar{\alpha} = -0.54°$ was adjusted prior to $\bar{\alpha} = 0.63°$. For the lower $\bar{\alpha}$ a spurious disturbance amplification is observed far upstream of the disturbance maximum position determined in Figure 5.3(b). For the higher $\bar{\alpha}$ the familiar appearance is retained. The lower side is not affected as can be seen from Figure 5.8(b). The conjecture from this observation is that some flow separation at the probe booms or at the airbrake insert (cf. Figures 3.1 and 3.3) may have produced a broadband acoustic forcing to which the upper side boundary layer was receptive; however, only at low angles of attack. As the position of the Pitot-static probes was changed and even more attention was paid to the fitting of the airbrake cover for the third flight test campaign with the hot-films, the problem was possibly alleviated but the disturbance source may not have been fully eliminated.

Although the coarse distribution of the hot-film elements ($\Delta x = 28$ mm) complicates an exact determination of the peak RMS position, the high amplification factors on the lower side, observed consistently under calm conditions, were surprising at first. Luchini (2009) predicted a thermodynamic upper bound of $N \approx 13$ for a Blasius boundary layer by theoretically investigating the linear receptivity mechanism due to molecular agitation. He determined $\hat{u}/\bar{U}_\infty = 1.5$ % at $N = 13.8$. Considering the low free-stream

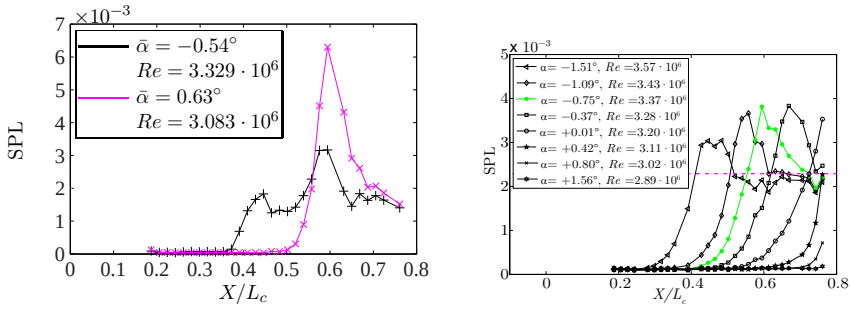

(a) Upper Side (b) Lower side

Figure 5.8.: Transition detection with the wall microphone system. (a): Disturbances of unknown source on the upper side for low $\bar{\alpha}$. (b): Unaffected transition development on the lower side.

turbulence level of $Tu_{XZ} \lesssim 0.04$ % (5 Hz - 2 kHz) and the fact that there was no acoustic noise, except from flow separations on different parts of the airframe, the results of this study indicate that one can approach this limit pretty closely in gliding flight under calm conditions. Yet, Horstmann et al (1989) stated that their N-factors of 13.5 obtained in powered flight 'are rather low values' for flight tests. Runyan and George-Falvy (1979) reported values of $N = 15$ on a straight wing glider, which are deemed plausible by Boiko et al (2002). In this respect, the Brownian molecule motion, which is able to excite any growing modes according to LST due to the uniform spectral distribution, should not be disregarded as a possible receptivity mechanism for two-dimensional boundary layers in gliding flight through the calm atmosphere. Nevertheless, even the slightest vortical and acoustic disturbances or surface vibrations may have an effect on the receptivity process.

The series of transition measurements with the wall microphone array in Figure 5.8(b) supports the previously presented results for the angle-of-attack sensitive lower side. These results were again obtained in a single gliding flight at calm conditions during the second flight test campaign (cf. Table 3.3). Although measured with a completely different transition measurement technique, the microphone results qualitatively resemble the hot-film results presented in Figure 5.3(c). Again, amplification is only observed after the boundary-layer disturbances have overcome a certain signal-to-noise thresh-

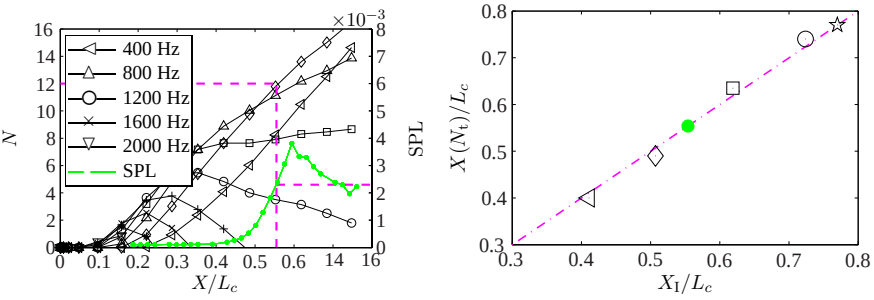

Figure 5.9.: Comparison of characteristic transition positions. (a): Definition of a characteristic disturbance amplification threshold on the lower side. (b): Comparison of characteristic transition positions extracted from the measurements results in Figure 5.8(b) with LST computations using a threshold value of $N_\mathrm{t} = 12$.

old. The growth rate continuously increases, leading to a steep ascent in the nonlinear transition region. The SPL distribution peaks and then falls back to an approximately constant level in the turbulent part of the boundary layer. The microphone results are plotted using a linear ordinate. Since the sensor characteristic is intrinsically linear and the spatial resolution is slightly better ($\Delta X = 25$ mm), a more accurate procedure for N-factor comparisons can be employed. In Figure 5.9(a) the lower horizontal dashed line corresponds to the dashed line in Figure 5.8(b), which represents the mean sound pressure level of the fully turbulent part of the boundary layer for all measurements. Furthermore, the intersection position X_I of this line with rising SPL curve in Figure 5.9(a) corresponds to an N-factor of $N_\mathrm{t} = 12$. In the following the streamwise position of this threshold factor $X(N_\mathrm{t})$ and the intersection positions X_I are compared for various $\bar{\alpha}$. It should be noted that X_I can be determined with more precision than a peak disturbance level since the intersection occurs in the region of high disturbance growth region, where an interpolation improves the accuracy. Furthermore, a possible ambiguity in the determination of a peak position with coarsely distributed sensors is avoided. This enhances the effective accuracy in the characteristic X_I/L_c determination by a factor of four compared to the definitions used in Figure 5.7. Furthermore, as N_t is closer to the linear growth region in the

boundary layer, it is more preferable for comparisons with linear theory than the use of N_{T} (cf. Chapter 2.4.1). Figure 5.9(b) shows the resulting comparison for all the measurement runs in Figure 5.8(b), in which transition was observed. The equal axis in this plot and the 45° slope of the dashed line reveal an approximately linear behavior $X(N_{\mathrm{t}})$ and X_{I} for the lower side of the airfoil. This property makes the lower side of the airfoil specifically interesting for investigations. Under moderately turbulent conditions considerable α-fluctuations were detected, as described in Chapter 4. From the preceding investigation, these can be expected to have a significant influence on the boundary layer. Furthermore, the gradual and selective modal growth of TS waves demonstrated in Figure 5.6 may lead to differences in the boundary-layer disturbance evolution due to increased small-scale turbulence levels. Details on boundary-layer instability under calm conditions are therefore presented in the following section.

5.2. Identification of the Boundary-Layer Disturbances

To obtain information on the boundary-layer disturbances participating in the transition process and their spatial evolution, the hot-film signals are considered in the Fourier domain. A fourth order Butterworth filter with a pass-band between 20 Hz and 4 kHz is employed to separate the part of the signals which contains periodic boundary-layer oscillations. Again, the Welch (1967) method is used to reduce the noise in the power spectral density (PSD) estimation. The signals are therefore block-averaged and a Hamming window function is employed in the Fast Fourier Transforms (FFT) to minimize leakage. The spectra of the hot-film signals included three discrete peaks at 160, 170 and 500 Hz, which were clearly not flow-induced and existed also for zero velocity. These peaks were eliminated by a notch filter. Figure 5.10 depicts the streamwise evolution of the spectra on both sides of the airfoil. The spectra of six streamwise hot-film sensors signals describe conveniently the spectral evolution of the transition process. As expected, the instability amplification on the upper side in Figure 5.10(a) takes place over a short streamwise distance. A distinct band of amplified frequencies can only be observed in a narrow region between $0.45 \leq X/L_c \leq 0.52$ in Figure 5.3(b). The band of amplified frequencies (500 Hz $\leq f \leq$ 1300 Hz), clearly protruding from background noise at $X/L_c = 0.48$, corresponds to

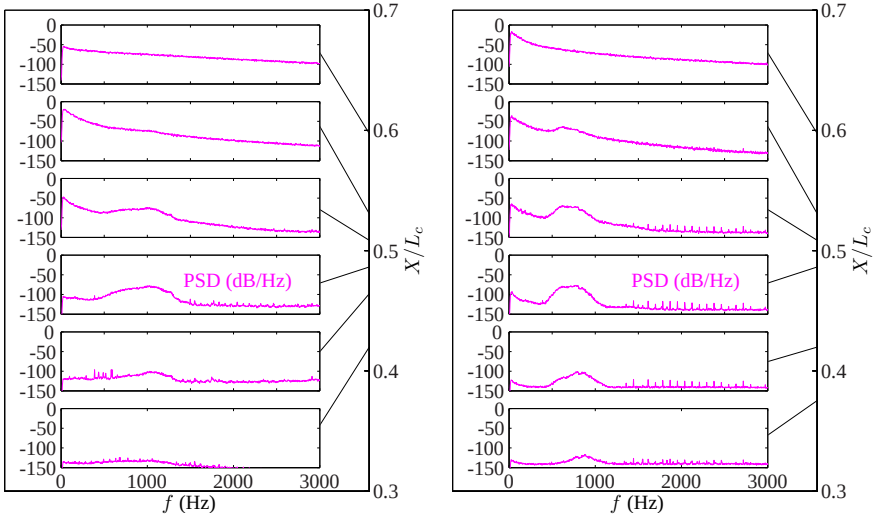

(a) Upper side (b) Lower side

Figure 5.10.: Streamwise evolution of the power spectral density of the hot-film signals ($\bar{\alpha} = -0.92°$, $Re = 3.215 \cdot 10^6$). Note the ordinate on the right hand side of the plots which marks the streamwise sensor position.

the LST observations in Figure 5.6 that a broad band of two-dimensional TS modes amplifies rapidly. The progressive amplification of these modes, centered around 1 kHz, leads to the almost fixed breakdown position in the region of the strong rise of the boundary-layer shape factor observed in Figure 5.2. At the penultimate position in Figure 5.10(a), the spectrum fills up with fluctuation energy from the low-frequency end. No distinct amplification of higher harmonics or sub-harmonics is observed. At the last considered station ($X/L_c \approx 0.6$) the power spectrum is homogenized.

On the lower side, typical features of a transition scenario initiated by two-dimensional Tollmien-Schlichting waves are also found. At a certain streamwise distance ($X/L_c \approx 0.38$) a band of amplified frequencies protrudes from the background noise, appearing as a hump in the subsequent spectra. This hump, initially at frequencies between 800 Hz $\leq f \leq$ 1000 Hz, corresponds to the fundamental TS waves forming the wave packets typical

for natural transition. The broadband disturbance nature points toward a natural receptivity process in which some external broadband forcing produces the necessary initial conditions for all amplifying TS modes according to LST. The TS-hump amplifies downstream and its maximum is slowly displaced toward lower frequencies. Compared with the results of the N-factor computations in Figure 5.6(b), this evolution can be attributed to the changing stability characteristics of the boundary layer, which promote a frequency-selective wave growth depending on streamwise position X/L_c. The fundamental TS waves saturate ($X/L_c \approx 0.54$) and through nonlinear interactions of instability modes, energy is redistributed to lower frequencies. The spectrum fills with spectral density from the strongly amplified low-frequency end and no distinct amplification at the exact sub-harmonic or the higher-harmonic frequencies of the TS-hump are visible in the process. This finding is consistent with the results obtained with wall-microphones in the other two flight test campaigns. The broad-band nonlinear process leads to breakdown to turbulence in the region $X/L_c \approx 0.59$, where no further selective amplification of any frequencies is observed in the spectra.

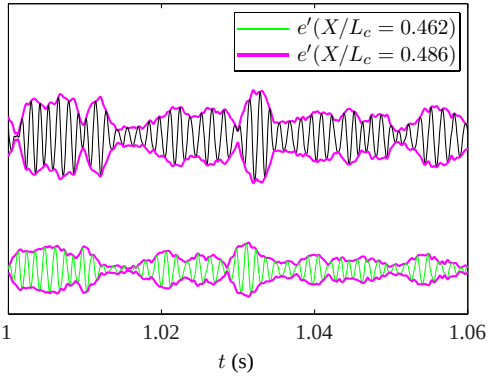

Figure 5.11.: Hot-film signals of two consecutive sensors and their envelope on the lower side of the wing glove ($\bar{\alpha} = -0.92°$, $Re = 3.215 \cdot 10^6$).

5.2.1. Determination of Disturbance Propagation Velocities

To support the statement that the characteristic humps in the power spectra are actually created by a superposition of TS waves of different frequencies, the propagation velocity of the disturbances is determined and compared with LST. The conception of a wave packet is a localized disturbance consisting of partial waves of different frequencies, propagation angles and phase velocities. The phase velocities of the constituent modes can in principle be obtained from the measurements of two sensors closely spaced in the streamwise direction. Calculating the discrete cross-spectrum for the two signals e_1' and e_2'

$$\begin{aligned} G_{12}(f_n) &= \frac{1}{2\pi} \sum_{n=-\infty}^{\infty} \varrho_{12}(t_n)\ \mathrm{e}^{-i(2\pi f t_n)} \\ &= \frac{1}{2\pi} \sum_{n=-\infty}^{\infty} \left[\sum_{m=-\infty}^{\infty} e_1'^{*}(t_n) e_2'(t_n + \tau_m) \right] \mathrm{e}^{-i(2\pi f_n t)}, \end{aligned} \tag{5.3}$$

where ϱ_{12} is the cross-correlation of the signals, the frequency-dependent phase difference of the amplified wave band is identified from the argument of the complex spectrum $G_{12}(f)$. With the known sensor distance and the extracted phase difference, the time difference and, consequently, the phase velocity c is obtained for each mode. However, the Nyquist-Shannon criterion is to be satisfied, i.e. the two sensors need to capture a half of a wavelength simultaneously. In practice a multiple is necessary to obtain low-noise results. The wavelength range of the low-frequency TS waves in the present study, estimated in Table 2.1, exceeds the streamwise sensor distance of $\Delta x = 28$ mm for the hot-films. Thus, the phase velocity cannot be determined directly for all TS frequencies. However, it is possible to identify the propagation velocity of the TS wave packet itself by a similar, extended procedure.

In a process without dissipation, the group velocity describes the velocity of the energy transport of a wave packet in space (Boiko et al, 2002). It is defined as the partial derivative of the angular frequency ω with respect to the modulus of the wavenumber $|\vec{k}| = k$.

$$c_\mathrm{g} = \frac{\partial \omega}{\partial k} = c + k \frac{\partial c}{\partial k} \tag{5.4}$$

The sensor distance in the present case is sufficient to detect the propagation velocity of the wave packets as dispersion needs larger distances in the

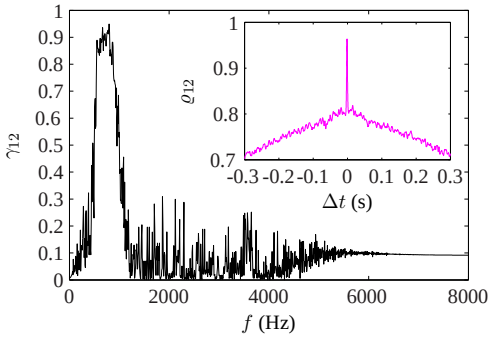

Figure 5.12.: The procedure for determining the group velocity of the TS wave packets (Lower side, $X/L_c = 0.472$, $\bar{\alpha} = -0.92°$, $Re = 3.215 \cdot 10^6$).

airfoil boundary layer to become significant. Yet, the typical shape of a TS wave packet needs to be known to enable a tempo-spatial correlation of the type ϱ_{12} included in equation (5.3). This shape is obtained by applying a discrete Fourier transform to the digitally band-pass filtered (300-2000 Hz, 4th order Butterworth) sensor signals. Following Gaster and Grant (1975), the envelope of a deterministic wave packet can be obtained by using the real and the imaginary part of an inverse Fourier transform of the previously obtained discrete Fourier coefficients $\hat{S}$. As the imaginary part describes a similar wave packet shifted by 90° in phase, the envelope is defined as the absolute value

$$\tilde{s}(t) = \sqrt{\Re\left(\sum_{n=0}^{N/2} \hat{S}_n \mathrm{e}^{i(2\pi f_n t)}\right)^2 + \Im\left(\sum_{n=0}^{N/2} \hat{S}_n \mathrm{e}^{i(2\pi f_n t)}\right)^2}. \qquad (5.5)$$

Figure 5.11 illustrates a result of the procedure for two consecutive sensor positions. Although growing in space and being displaced in time, the general shape of the envelope of the signals is retained and a high correlation between the two envelopes can be expected. Contrary to most laboratory experiments, e.g. Gaster and Grant (1975), Cohen et al (1991) or Medeiros and Gaster (1999), the wave packets observed in flight are not isolated but one wave packet gradually transitions into another. To retrieve the time difference between two consecutive signals, the cross correlation ϱ_{12} is com-

puted. If the envelope shapes of the investigated disturbances are similar, the correlation shows a distinct peak. The displacement of the peak from the abscissa yields the time difference Δt necessary to compute the propagation velocity with the known sensor distance Δx. An example for an investigated flight case is included in Figure 5.12. For deterministic TS waves the proposed procedure is underlined by considering the coherence between the two signals in Figure 5.12

$$\gamma_{12} = \frac{|G_{12}|^2}{G_{11}G_{22}}. \tag{5.6}$$

As the wave packets disperse only gradually, a strong coherence is found for the frequency band of the TS wave hump (see also Figure 5.10).

The comparison of the experimentally obtained disturbance velocity with LST is not straightforward. A 'steepest descent' approach would be formally correct (Schmid and Henningson, 2001), however, a simpler approach is chosen here for convenience. To determine the partial derivative $\partial\omega/\partial k$ in equation (5.4), the two-dimensional TS eigenvalues ($k_x = k_{x,r} + ik_{x,i},\ k_z = 0$) are computed for frequencies ranging from 100 to 2000 Hz in steps of 50 Hz. Hence, only the propagation in the streamwise direction is considered. The frequency distribution enables a rather smooth determination of the derivative $\partial\omega/\partial k_{x,r}$ for all streamwise positions, which is depicted in a contour plot in Figure 5.13. Yet, the group velocity of a TS wave packet is only one value for each streamwise position. Therefore, it is assumed that the bulk of the kinetic energy is transported with the frequency producing the maximum N-factor at each streamwise position. These positions are marked with a solid curve in the position-frequency plane in Figure 5.13. Another characteristic position corresponds to the maximum disturbance growth rate $k_{x,i}$, which is represented by the dashed line.

To compare the LST results with the experimental findings, the procedure described above is used to compute the propagation velocity along the entire streamwise hot-film row on the lower side of the airfoil. Figure 5.14(a) depicts the streamwise evolution of the mean coherence, which has been averaged in the frequency band 700 - 1000 Hz. Only in the region $0.38 \leq X/L_c \leq 0.52$ a significant coherence of $\bar{\gamma}_{12} > 0.5$ is observed. This is exactly the region where the TS humps protrude in the spectra in Figure 5.10, after overcoming the sensor noise and before the flow randomizes completely in the breakdown process of the boundary layer. Moreover, the comparison of the experimentally determined propagation velocities and the LST results show a very good agreement in Figure 5.14(b). The solid line corresponding to the max(N)

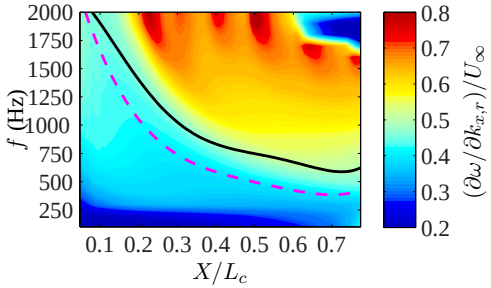

Figure 5.13.: Numerical results for the velocity $\partial\omega/\partial k_{x,r}$ (Lower side, $\bar{\alpha} = -0.92°$, $Re = 3.215 \cdot 10^6$). Solid line: $c_g(\max(N))$. Dashed: line $c_g(\min(k_{x,i}))$.

criterion is closely approached by the experimental values within the coherent region. The curve corresponding to maximum modal growth describes slightly lower velocities. The characteristic propagation velocity on the lower side of the airfoil is found at $c_g/U_\infty \approx 0.47$.

The appeal of this method is its foundation in the time-domain. Therefore, a short signal sequence is sufficient. In the presented results 2.5 s were used for the cross-correlation but in principle smaller time intervals are possible and the test for coherence in the TS wave band is not a necessary prerequisite for the determination of propagation velocities. It was used here to verify the fact that TS waves initiate the transition process on the wing glove under calm conditions. Yet, the determination of the time shift method can in principle be applied to any kind of disturbance which produces a characteristic envelope. It is therefore also useful for the detection of transient disturbances. Under calm conditions, however, the coincidence of the frequency range of unstable modes as well as the good agreement of the propagation velocity compared with LST substantiate the assumption that transition on the wing glove under calm conditions is initiated by the Tollmien-Schlichting type of instability.

5.2.2. Three-Dimensional and Nonlinear Aspects of the Transition Process

Even in a low-disturbance flight environment three-dimensional aspects are important in the transition of a two-dimensional boundary layer. Figure

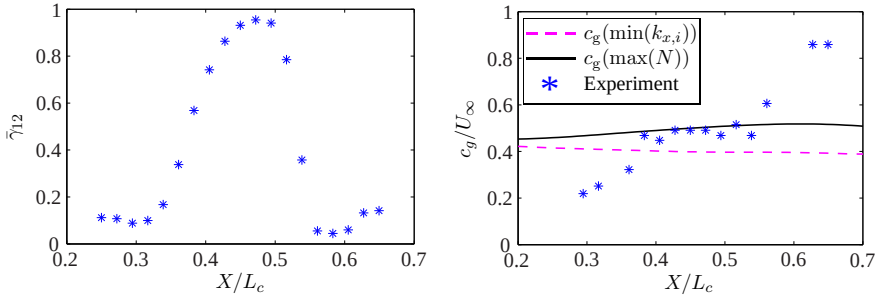

(a) Coherence averaged for $300 \leq f \leq 1000Hz$

(b) Disturbance propagation velocity

Figure 5.14.: Streamwise evolution of mean coherence and comparison of the disturbance propagation velocity with LST results ($\bar{\alpha} = -0.92°$, $Re = 3.215 \cdot 10^6$).

5.15 illustrates the contours of the time traces recorded by the 21 hot-film sensors of the spanwise row on the lower side (cf. Chapter 3.1.3). The signals have been band-pass filtered in the range 300 to 2000 Hz to highlight the wavelike character of the disturbances. The contour plot represents the linear transition stage (cf. Figures 5.3(c)). The disturbances are predominantly two-dimensional, even though oblique disturbance are present. The boundary layer is unstable toward oblique TS modes, although the two dimensional ones have higher amplification rates according to LST (cf Figure 2.11).

The question which TS-wave frequencies and propagation angles are involved in the transition process under calm conditions can be assessed by using frequency-wavenumber spectra. Such spectra are experimentally obtained from the signals of the spanwise hot-film row. They contribute to the understanding of the transition process and yield insights into the later, essentially three-dimensional stages of transition. The hot-film signals $e'_{mn} = e'(t_m, z_n)$ from the spanwise sensor row at $X/L_c = 0.482$ on the lower side can be represented in the spectral domain by applying a discrete Fourier transform twice. It is first applied in the spanwise direction z and then in

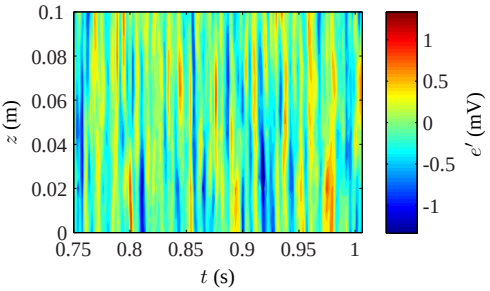

Figure 5.15.: Natural TS wave packets on the lower side of the wing glove ($X/L_c = 0.482$, $\bar{\alpha} = -0.60°$, $Re = 3.142 \cdot 10^6$).

the time domain t.

$$\hat{S}_{kl} = \sum_{m=0}^{M-1} \sum_{n=-\frac{N-1}{2}}^{\frac{N-1}{2}} \frac{2e'(t_m, z_n)}{M(N-1)} \exp\left[-i\left(2\pi f_k t_m + k_{z,l} z_n\right)\right] \quad (5.7)$$

The transformation results in a two-dimensional matrix of Fourier coefficients in the discrete frequency-wave-number plane $\hat{S}_{kl} = \hat{S}(f_k, k_{z,l})$. The resolution of the spatial wavenumber detection is limited to

$$k_{z,\min} = \frac{2\pi}{\Delta z\,(N-1)}. \quad (5.8)$$

According to the Nyquist-Shannon theorem, the largest detectable wavenumber is

$$k_{z,\max} = \frac{\pi}{\Delta z}. \quad (5.9)$$

In the present case with $N = 21$ sensors, equidistantly distributed every 5 mm, values of $k_{z,\min} = 62.8\mathrm{m}^{-1}$ and $k_{z,\max} = 628.3\mathrm{m}^{-1}$ result.

The spanwise sensor row is locally fixed and different boundary-layer states can thus only be observed by carefully changing the angle of attack. Slight changes in the angle of attack result in a deceleration or an acceleration of the lower side boundary layer and lead to the streamwise displacement of the transition process observed in Figure 5.3(c). Figure 5.16 shows frequency-wavenumber spectra measured in flight for four different angles of attack. While the frequency axis in the contour plots scales the temporal periodicity

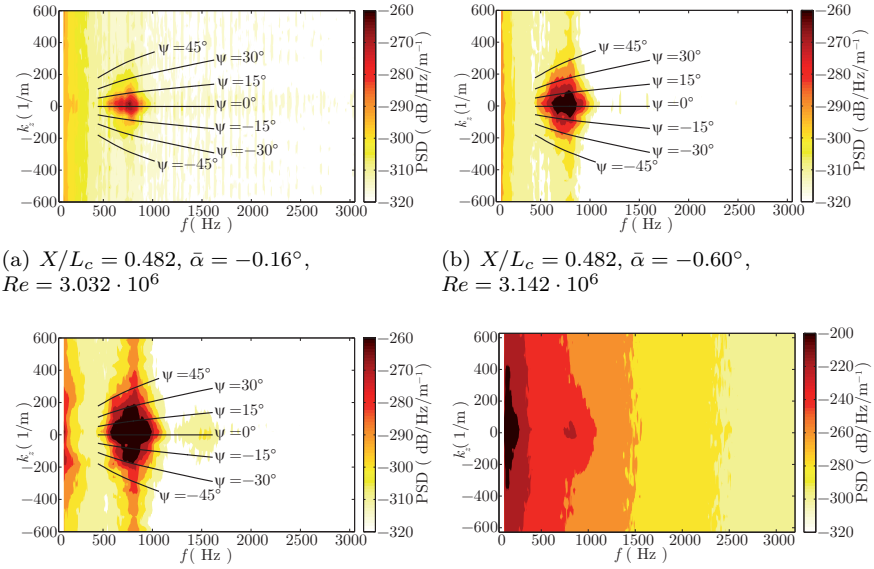

(a) $X/L_c = 0.482$, $\bar{\alpha} = -0.16°$, $Re = 3.032 \cdot 10^6$

(b) $X/L_c = 0.482$, $\bar{\alpha} = -0.60°$, $Re = 3.142 \cdot 10^6$

(c) $X/L_c = 0.482$, $\bar{\alpha} = -0.92°$, $Re = 3.215 \cdot 10^6$

(d) $X/L_c = 0.482$, $\bar{\alpha} = -1.29°$, $Re = 3.325 \cdot 10^6$

Figure 5.16.: Frequency-wavenumber spectra obtained with the spanwise hotfilm row on the lower side.

of the signals, the spanwise wavenumber accounts for the spanwise periodicity contained in the boundary-layer disturbances. The shown results correspond to the four different angles of attack highlighted with plus markers in Figure 5.3(b). The superimposed lines of constant wave angles Ψ of equation (2.34) were calculated using the boundary-layer and the stability method in Chapter 3.2.

For the highest angle of attack, $\bar{\alpha} = -0.16°$ in Figure 5.16(a), a concentrated region of high amplitude appears for frequencies between 500 Hz $< f <$ 900 Hz and spanwise wavenumbers of $|k_z| < 200$ m^{-1}. The deviation of the maximum from the zero propagation angle is due to a slight sideslip angle of the wing glove that is consistently present but is insignificant for the transition development. TS wave packets with a predominant two-dimensional propagation direction are typical for natural transition in a low

disturbance environment, as can be seen in the frequency-wavenumber previously obtained by Peltzer and Nitsche (2004) and Seitz (2007) in similar flight test configurations. The corresponding wave propagation angles remain below 20°at this early transition stage. Nevertheless, the presence of slightly oblique TS waves with different frequencies is the reason for the appearance of the localized wave packets and the three-dimensional character of laminar-turbulent transition in the later stages. In the second case, $\bar{\alpha} = -0.60°$ in Figure 5.16(b), the disturbances are more amplified due to the increased instability of the boundary layer. They have spread toward higher spanwise wavenumbers, signifying an increased amplification of oblique TS waves. For $\bar{\alpha} = -0.92°$ in Figure 5.16(c) the boundary layer has become even more unstable, especially toward three-dimensional modes. Besides the amplification of highly oblique TS waves at the fundamental frequencies, fluctuation energy at very low frequencies can be observed to magnify symmetrically for wavenumbers around $\pm 200\mathrm{m}^{-1}$. Furthermore, a region of higher-harmonic waves can be seen to evolve from the background noise in the frequency band between 1300 Hz and 1700 Hz. This indicates that the nonlinear transition stage has started. For $-0.92° \geq \bar{\alpha} \geq -1.29°$ the disturbance energy grows steeply. The spectrum fills up with fluctuation energy in-between the fundamental wave combinations and the growing low-frequency disturbances with a rich spanwise wavenumber content. To support these observations, analogies can be drawn to the streamwise evolution of the power spectra in Figure 5.10(b) and the disturbance amplification in Figure 5.9(b). For the lowest angle of attack ($\bar{\alpha} = -1.29°$, Figure 5.16(d)), the low frequency content for all spanwise wavenumbers has vastly grown. The flow is highly transitional and the disturbances are randomized.

From these observations it can be concluded that a certain portion of three-dimensional receptivity must be involved in generating the three-dimensional modes (Kachanov, 2000). Furthermore, no significant nonlinear activity at the exact subharmonic wave band was detected in either Figure 5.10 or in Figure 5.16, which is also consistent with the microphone measurements. At a certain amplification levels of the fundamental TS waves, the power spectra fill up with fluctuation energy from the low frequency end. Furthermore, a high amplification of oblique disturbances at $|k_z| \approx 200\ \mathrm{m}^{-1}$ can be identified in the initial nonlinear transition stage. Except for a significantly weaker maximum at the first overtones of the fundamental waves, there are no other wave interactions visible in Figure 5.16(c). The same qualitative appearance of the frequency wavenumber spectra can also be found in an article of Peltzer (2004), although the authors do not discuss this issue. In the absence of

visible signs of N-type or K-type wave interaction, the question arises which nonlinear mechanism eventually leads to breakdown of the two-dimensional boundary layer in a low disturbance flight environment.

Breuer et al (1997) observed oblique low-frequency disturbances in the late transition stage of an isolated wave packet. They attributed the subsequent breakdown of the wave packet to the 'oblique' transition mechanism, which is associated with the lift-up effect and a growth of streaky structures (Henningson et al, 1993). Indeed, the low-frequency part of the spectrum in Figure 5.16(c) exhibits a certain similarity to spectral representation of streaks given by Westin et al (1998). According to Schmid and Henningson (2001) the 'oblique' mechanism is effective at high disturbance levels. However, there is no obvious source for the appearance of the low-frequency fluctuations if they are not self-generated. In a low-disturbance environment, these low-frequency disturbances can, however, be self-generated by weakly nonlinear interactions of a broad band of fundamental TS wave frequencies and wavenumbers. In an experimental wind-tunnel investigation, de Paula et al (2013) demonstrated that the amplitude modulations involved in TS wave packets are able to generate difference modes at significantly distinct frequency bands through a quadratic combination interaction. This mechanism was described schematically in Chapter 2.4.3. The experimentally observed double-exponential downstream growth of the difference modes was explained by a mechanism theoretically proposed by Wu et al (2007) (a similar mechanism for wind-driven surface waves is described by Lee (2012)). The mechanism is much less restrictive than the classical wave triad of Craik (1971), in that it only requires nearly the same phase speed c of a planar and two oblique wave modes to produce super-exponential growth of the three-dimensional modes. If travelling at the same phase speed, the oblique waves can interact resonantly with the fundamental modes. Furthermore, Würz et al (2012) verified large possible detunings in frequency and spanwise wavenumber, which still produce such growth. Thus, natural TS wave packets are able to create their own three-dimensional low frequency modes (see also Medeiros and Gaster (1999)), denoted as seeds, for the later resonant nonlinear interactions with the two-dimensional, fundamental TS waves through the phase-locked mechanism of detuned subharmonic resonance. The broadband frequency and wavenumber distribution of the fundamental modes in natural transition provides a large variety for possible interaction combinations, including the appropriate ones for the resonant growth.

To support the hypothesis that the described mechanism is indeed a candidate for the early nonlinear stage, corresponding to the observations of the

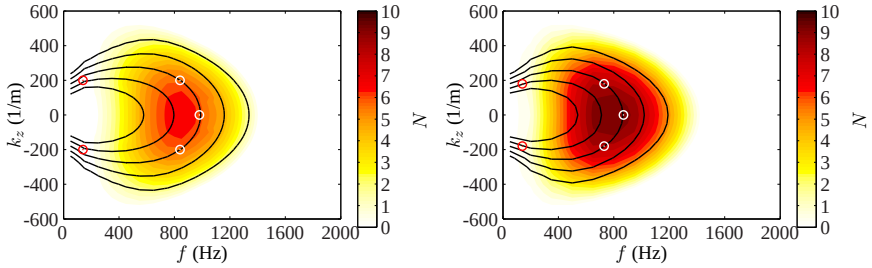

(a) $X/L_c = 0.482$, $\bar{\alpha} = -0.60°$, $Re = 3.142 \cdot 10^6$

(b) $X/L_c = 0.482$, $\bar{\alpha} = -0.92°$, $Re = 3.215 \cdot 10^6$

Figure 5.17.: Frequency-wavenumber spectra obtained with LST. Solid lines represent contours of equal phase speed c. From the inner to the outer curve: $c/\bar{U}_e = 0.31, 0.33, 0.35, 0.37, 0.39$. Marker symbols indicate typical wave combinations for the resonant growth of self-generated difference modes.

flight experiments, LST is employed. The LST calculations yield the disturbance growth rates $k_{x,i}$ and the phase velocity c of all modes in the frequency-wavenumber plane. The growth rates are integrated by using equation (2.35) to obtain a N-factor distribution in the frequency-wavenumber plane for each streamwise position. In Figure 7.15(a) two results corresponding to the flight cases of Figures 5.16(b) and 5.16(c) are depicted. For both cases it is seen that the N-factor maximum corresponds very well to the experimental observation. Furthermore, solid lines are included in the plots. These lines represent contours of equal phase speed c. Strikingly, those phase speed curves closely embracing the N-factor maximum all tend towards a spanwise wavenumber at $|k_z| \approx 200$ m^{-1}, which corresponds to the experimentally observed peculiarity in Figure 5.16(c). In both figures the generation of two exemplary difference modes according to equation (2.43) is highlighted by circles. Even if the difference modes may differ slightly in their phase velocity, compared with the source modes, there are still modal combinations included in the fundamental TS hump that share their phase velocity exactly and enable strong resonant growth. Furthermore, Wu et al (2007) point out that the criterion of equal phase speeds only needs to be fulfilled approximately. An inherent feature of the interaction mechanism is the fact that the fundamental modes need to reach sufficiently high amplitudes to produce dif-

ference modes of significant amplitude. For the angle of attack $\bar{\alpha} = -0.92°$, the resonant growth of the difference modes has already started; otherwise the interaction modes would not have overcome the resolution threshold of the hot-films. Regarding the computed level of $N < 10$ for this case, there still remains a difference $\Delta N > 3$ to the observed transition position. Thus, the high observed N-factors in Section 5.1.1 and the absence of disturbance modes in the wavebands of the N and the K-type nonlinear regime provide the necessary conditions in a low-disturbance flight environment. It should be noted that the low-frequency wave modes are even underestimated in the experimental frequency-wavenumber spectra. The partial derivative included in the definition of the wall shear stress $\tau_w = \mu(\partial u/\partial y)_w$ is lower for oblique TS modes with low frequencies than for plane fundamental ones. This behavior was demonstrated in Figure 2.11(b). Therefore, it can be concluded that self-generated and phase-locked resonance at large sub-harmonic detunings is indeed a candidate for the description of the early nonlinear stage in the present flight experiments under calm conditions.

In summary, the use of two different transition detection systems in three different flight campaigns yielded consistent findings for the streamwise transition evolution on the airfoil. Steady variations of the angle of attack revealed a high sensitivity of the lower side toward the changing pressure gradient, whereas transition remained locally almost fixed on the upper side. High transition N-factors of $N \approx 13.5$ were determined on the lower side of the wing glove. On the upper side transition N-factors were lower for low angles of attack, but at higher incidence angles they approached the same magnitude. The observed initial growth stages match the theoretical predictions obtained by numerical LST investigations. A procedure for determining the propagation velocity of boundary-layer disturbances was introduced and the consideration of frequency-wavenumber spectra on the lower side of the wing glove yielded insights into the route of natural transition in a low-disturbance flight environment. Similarities to the wind-tunnel investigations of de Paula et al (2013) were observed and reinforced. The evolution of oblique low-frequency modes, besides the TS waves at the fundamental frequencies, have been highlighted, which pave the way for detuned subharmonic resonance. Having obtained these necessary insights into the quasi-steady transition mechanism, it is possible to study the behavior of the NLF airfoil in flight through atmospheric turbulence.

6. Flight through Turbulence I: Response of the Inviscid Outer Flow

The random nature of atmospheric turbulence complicates the investigation of airfoil effects in flight tests considerably. The general airfoil response to the oncoming flow disturbances is different to most generic wind tunnel experiments since the boundary conditions change continuously and the aircraft is a free system, reacting with motions to the forcing. The randomness of the changing boundary conditions discussed in Chapters 2.1 and 4.1 prohibits statistically reproducible experiments. It is only possible to study the effects of single events, which, however, are observed frequently enough to justify their relevance for airfoil efficiency considerations. For such investigation, correlations between the oncoming flow and the airfoil response are an indispensable prerequisite. This requires a completely synchronized, integrated measurement platform (cf. Chapter 3.1) and special signal processing techniques. Bendat and Piersol (2010) coined the term 'nonstationary data analysis' for the evaluation of such transient data, where the experiment cannot be repeated under statistically similar conditions. Accurate repeatability requires generic laboratory experiments and numerical analysis. Although wind-tunnel testing is beyond the scope of this in-flight study, an attempt will be made to model the relevant mechanisms. Therefore, the important interacting and competing processes observed in this and the following chapter will be simulated numerically.

The flight cases studied in the following encompass the most important effects observed in the flight test campaigns listed in Table 3.3. Since the experiments are not exactly reproducible under stationary statistical conditions, ensemble averaging techniques cannot be used. Furthermore, the measurement sequences are limited by the high sampling rates required for the transition investigation instrumentation and the pilot accuracy under moderately turbulent conditions. In these limited time periods stronger turbulent gusts are not encountered continuously. It is therefore reasonable to structure the investigation in case studies to demonstrate the most important effects and examine single events in detail. The in-flight experiments thus provide valuable insight into the relevant processes acting on a NLF

wing section and their physical nature. Particularly, they shed light into the question of the importance of the effects discussed in Chapter 2 for the present application. However, they cannot provide statistical evidence on the frequency of such events.

In flight through turbulence all main aerodynamic mechanisms described in Chapter 2 are interdependent. The present chapter focusses on the effects of the inviscid outer flow introduced in flight through light and moderate atmospheric turbulence. As the inviscid outer flow sets up the boundary conditions for the boundary-layer investigation, the results of this chapter are closely connected to the investigation of boundary-layer transition in the subsequent chapter. After some introductory remarks on the turbulent forcing and the flight dynamic eigenmotions of the research aircraft in Section 6.1, two aerodynamic case studies will be presented in Section 6.2. Whereas case study 1 focusses on the general differences between calm and moderately turbulent conditions, case study 2 is intended as a more detailed investigation of the most interesting effects identified in the first study. This chapter focusses on the unsteady forces resulting from temporal variations of the pressure distribution created by turbulence.

6.1. Remarks on Flight Dynamical Motions in Flight through Turbulence

In Chapter 4.1 the significance of angle-of-attack variations caused by vertical gusts was pointed out. To demonstrate that these time-varying oncoming flow conditions indeed create a significant airfoil response, the oncoming flow state is correlated with suitable quantities extracted from the measurement results. The dynamically calibrated pressure transducers, described in Chapter 3.1.3, enable the measurement of the instantaneous pressure distribution in flight through atmospheric turbulence. Using equations (3.8) and (3.9) the normal force C_n coefficient and the lift C_l coefficient of the wing section is determined. The lightly turbulent case in Figure 4.1(c) will serve as a convenient example. Figure 6.1(a) compares the temporal evolution of the angle-of-attack fluctuations α', obtained with the hot-wires, with the two-dimensional normal force coefficient C_n of the wing glove. A high correlation between the two quantities can be expected from the comparison. To determine the time lag between the signals, a cross-correlation of the two quantities is shown in the lower part of the figure. The cross-correlation

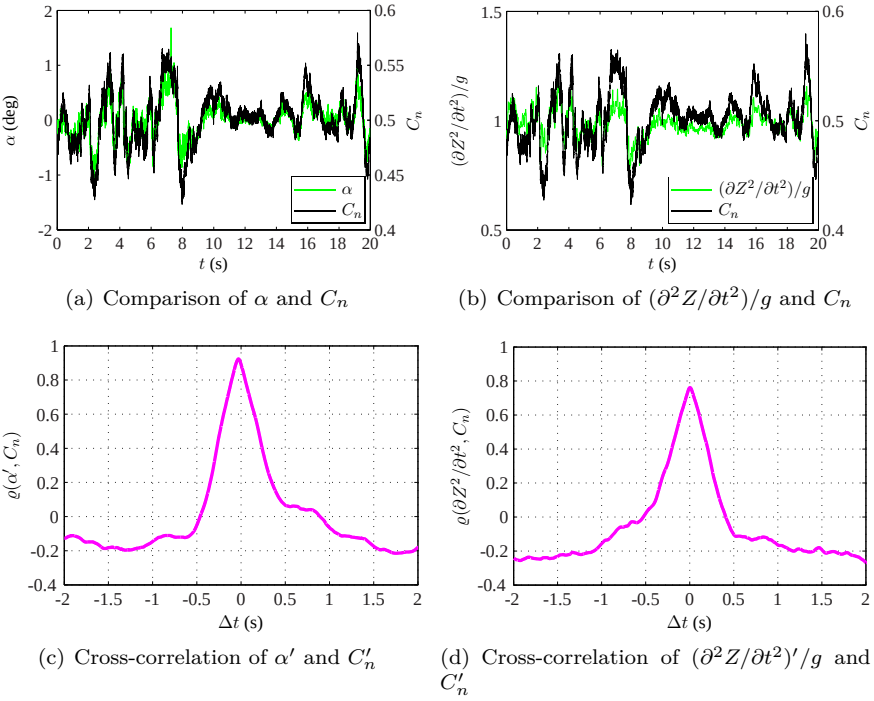

(a) Comparison of α and C_n

(b) Comparison of $(\partial^2 Z/\partial t^2)/g$ and C_n

(c) Cross-correlation of α' and C_n'

(d) Cross-correlation of $(\partial^2 Z/\partial t^2)'/g$ and C_n'

Figure 6.1.: Cross-correlations for lightly turbulent conditions, $\bar{\alpha} = -0.95°$, $\bar{U}_\infty = 41.38$ m/s, $Tu = 0.20$ %, $\epsilon = 2.07 \cdot 10^{-5}$ m^2/s^3.

coefficient ϱ is normalized such that the autocorrelations of the signals equal unity (Bendat and Piersol, 2010). The peak value $\varrho_{\alpha,C_n} \approx 0.9$ is slightly displaced to the left from the ordinate, representing a time lag of 29 ms. Thus, the boom-mounted X-wire probe, 0.9 m ahead of the leading edge, senses gusts earlier than the pressure distribution of the wing glove. A simple estimate using the mean free-stream velocity $\bar{U}_\infty = 41.38$ m/s of the present case and the quarter-chord of the airfoil ($L_c/4 = 0.338$ m) leads to convection time of 30 ms, which is in good agreement with the present measurements. In the theory of thin airfoil aerodynamics, discussed in Chapter 2.3.1, the lift acts at the quarter-chord.

For such lightly turbulent conditions, the inertia of the aircraft wing is

large enough to allow a distinction between the gust excitation and the airfoil response. Under moderately turbulent conditions (cf. Table 4.2 for the definition), the normal force acting on the airfoil is partly due to the disturbance and partly due to the motion of the airfoil itself (Fung, 2008). The gusts in the oncoming flow field create rapid changes of the airfoil pressure distribution, which determines the dominating force component normal to the chord. The resulting forces, in turn, cause airfoil motions. An exact distinction between these contributions is not intended as the present study focusses on the boundary-layer response which is indifferent to the source of unsteady forcing.

To demonstrate the accuracy of the sensor synchronisation, Figure 6.1(d) shows a cross-correlation between the normal force coefficient and the dimensionless normal acceleration, which was obtained by the altitude heading and reference system (AHRS) inside the wing glove described in Chapter 3.1.3. Again a high correlation coefficient results and this time the lag is essentially zero, as it is smaller than the sampling period of the AHRS which obtains the accelerometer data at a rate of 100 Hz. The correlations under light turbulent conditions demonstrate that the loads on the airfoil result from the oncoming flow disturbances and are not pilot induced. In addition, the time scales of the transient disturbances are too small to allow intuitive pilot reactions.

Such accelerations do not exclusively act on the investigated wing section. They affect the wing globally and lead to aircraft motions. This is a major difference to wind-tunnel experiments, where the investigated airfoils are usually stationary fixed. The inevitable motion caused by turbulence may also excite flight mechanical eigenmotions. Such motions need to be assessed in a flight investigation of atmospheric turbulence.

To determine the flight dynamic stability of the aircraft, either experimental system identification procedures can be employed (Jategaonkar, 2006) or stability calculations can be conducted (Yechout et al, 2003). Results of the latter method will be shown here since they are considered more depictive. The aircraft is considered as a rigid model with six degrees of freedom. This results in four ordinary vector differential equations (Brockhaus et al, 2011). Aeroelastic motions as well as unsteady aerodynamic effects are neglected and gliding flight is considered. The problem is linearized about trimmed flight conditions, which are exposed to small disturbances, to obtain a simplified eigenvalue problem. The aerodynamic stability derivatives and the flight dynamical eigenvalues are obtained with the vortex lattice program AVL from Youngren and Drela (2006). Therewith, the lifting surfaces, i.e.

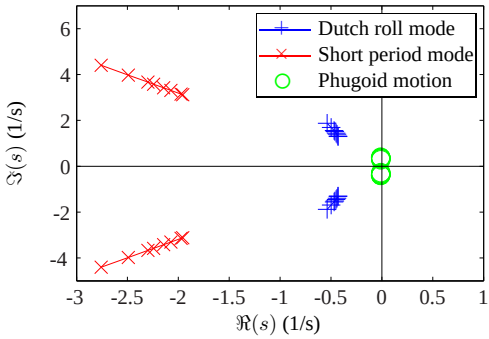

Figure 6.2.: Flight-mechanical eigenmodes of the research aircraft G109b. Velocity variation: $34.9, 35.2, 37, 38.3, 40.1, 41.1, 44.5, 49.3$ m/s. The Dutch roll and the short period mode tend to higher ω for increasing $\bar{U}_\infty$.

the wing, including the wing glove, and the empennage are represented by horseshoe vortex panels. The dynamic system matrix requires realistic input for the mass distribution, the inertia and the center of gravity. This data was obtained from weighing of the aircraft and from a mass allocation in a CAD model available from Erb (2002). The aerodynamic and the inertia stability derivatives determine the root locus of the resulting eigenvalues s. Figure 6.2 shows the root progression of three characteristic eigenmotions of the aircraft for the airspeed variation listed in the figure caption. The ordinate describes the angular frequency ω of the motion, whereas the abscissa is related to the damping coefficient D.

$$\begin{aligned} f &= \frac{\omega}{2\pi} = \Im(s) \\ D &= \sin\left[\arctan\left(\Re(s)/\Im(s)\right)\right] \end{aligned} \tag{6.1}$$

Higher damping coefficients correspond to higher damping. Each periodic mode is described by two poles, one in the upper and one in the lower quadrant. The 'Dutch roll' mode is a lateral motion, which involves sideslip and a combined bank-yaw motion. It is found at low frequencies and it is less damped than the higher-frequency short period mode. The short period mode refers to the longitudinal dynamic stability of the aircraft and it essentially involves pitching motions and angle-of-attack oscillations. Since α

Table 6.1.: Frequency range of the flight dynamic eigenmodes.

Mode	f (Hz)	κ	D
Phugoid motion	0.048 - 0.063	0.01	0.03 - 0.04
Spiral mode	aperiodic		
Dutch roll	0.21 - 0.3	0.025 - 0.026	0.28 - 0.32
Short period mode	0.5 - 0.7	0.06	0.53 - 0.54
Roll mode	aperiodic		

fluctuations are caused by vertical gusts, this mode is of particular importance for the present investigation. For higher airspeeds, the Dutch roll and the short period mode both tend to larger frequencies and higher damping. The third type of period eigenmode is the phugoid motion. Its poles are close to the unstable half-plane ($\Re(s) > 0$). The low damping associated with this position explains the occurrence of such motions in some of the measurement runs (cf. Figure 4.2(c)). The phugoid motion is a periodic oscillation of airspeed and altitude at constant angle-of-attack which varies approximately in inverse proportion to the airspeed. It does not change the airfoil behavior significantly, except for the variation of the chord Reynolds number, which in many cases is negligible. Furthermore, the low eigenfrequencies are far apart from the relevant scales for unsteady airfoil effects.

In Table 6.1 only the short period mode slightly protrudes into the range of unsteady aerodynamic effects ($\kappa > 0.05$, (Leishman et al, 2006)) discussed in Chapter 2.3.1. However, even strong intentional elevator excitations in flight tests under calm conditions have been found to die out within less than one oscillation period. This aperiodic behavior is explained by the high damping ($D > 0.5$) verified in Table 6.1. The oscillation reluctance is a common characteristic for this motorized glider category (Thomas, 1999). Therefore, it can be expected that turbulence inevitably leads to aircraft motions. Yet, it will be shown in the following section that excitation time scale can be significantly smaller than the time scale of the aircraft eigenmotions.

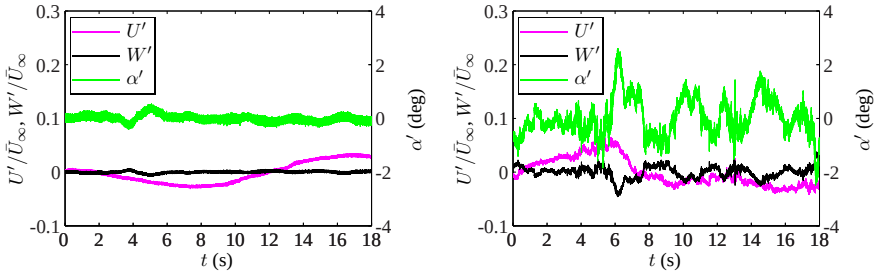

(a) Calm conditions:
$Tu = 0.04$ %, $\epsilon = 1.03 \cdot 10^{-7}$

(b) Moderately turbulent conditions:
$Tu = 0.26$ %, $\epsilon = 2.86 \cdot 10^{-4}$

Figure 6.3.: Oncoming flow disturbances for two measurement runs under different conditions. (a): calm conditions ($\bar{\alpha} = -0.75°$, $Re = 3.368 \cdot 10^6$) (b): moderately turbulent conditions ($\bar{\alpha} = -0.63°$, $Re = 3.488 \cdot 10^6$).

6.2. Effects of the Time-Varying Pressure Distribution

In the following the two case studies are introduced to depict the effects of the time-varying pressure distribution caused by random disturbances in the oncoming flow. In Chapter 7 these variations will play an essential role for the boundary-layer development.

6.2.1. Case Study 1: Comparison of Calm and Moderately Turbulent Conditions

To understand the airfoil behavior under moderately turbulent conditions, it is instructive to compare a typical case directly with a similar measurement under calm atmospheric conditions.

The oncoming flow fluctuations of two such cases are shown in Figure 6.3. The left plot shows a flight through calm air. The pilot is able to adjust the angle of attack precisely and the absolute value of airspeed varies slowly in a long waveform which is identified as the phugoid motion of the aircraft. Figure 6.3(b) shows a flight through moderately turbulent air, which is felt as a slight shaking inside the cockpit. It is obvious that even under these moderately turbulent conditions rapid and irregular deviations from the mean

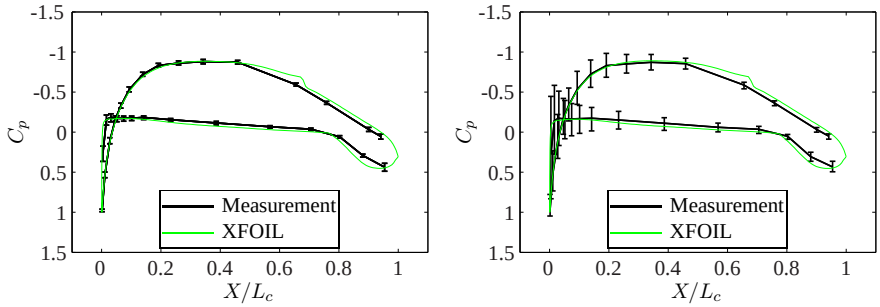

(a) Calm conditions:
$Tu = 0.04$ %, $\epsilon = 1.03 \cdot 10^{-7}$

(b) Moderately turbulent conditions:
$Tu = 0.26$ %, $\epsilon = 2.86 \cdot 10^{-4}$

Figure 6.4.: Mean pressure distribution (lines) and maximum deflections (vertical bars) of the pressure coefficient at the measurement stations for two runs under different conditions. (a): calm conditions ($\bar{\alpha} = -0.75°$, $Re = 3.368 \cdot 10^6$) (b): moderately turbulent conditions ($\bar{\alpha} = -0.63°$, $Re = 3.488 \cdot 10^6$).

angle of attack of up to 2.5° occur. For the pilot it is virtually impossible to control these variations and to keep the airspeed constant since his reaction would be too slow and there is no intuitive feedback. Furthermore, there is an increase in small-scale fluctuation intensity. It can be observed that the angle of attack essentially follows the fluctuations of the velocity component normal to the chord, i.e. the effects of vertical gusts.

The difference between two measurements at similar $\bar{\alpha}$ and Re becomes apparent in a comparison of the pressure distributions in Figure 6.4. The lines depict the mean pressure distributions and a numerical solution of the two-dimensional airfoil analysis program XFOIL, which was matched by using the procedure described in Chapter 3.3.1. The vertical bars in the figure depict the maximum deflections of the pressure coefficient during the measurement sequence. Even for the moderately turbulent conditions, a good agreement between the mean measurement results and the computation is found. In the calm case in Figure 6.4(a), there are almost no fluctuations in the pressure coefficient C_p. For moderately turbulent conditions in Figure 6.4(b), the fluctuations of the oncoming flow disturbances cause strong temporal deflections. The maximum amplitudes intensify in the leading edge region, where $\hat{C}_p \geq 0.2$ is observed. Thus, significant changes of the pressure

gradient result in this region on both sides of the airfoil. On the lower side, even sign changes of $\partial P/\partial X$ occur.

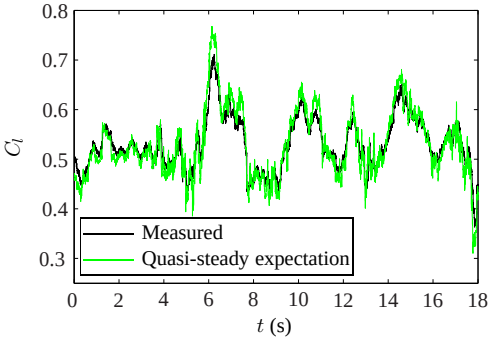

Figure 6.5.: Comparison of lift measurement and quasi-steady expectation computed with equation (6.2).

The changes in the pressure distribution result from the random angle-of-attack fluctuations with amplitudes of $\alpha' > 2°$ observed in Figure 6.3(b). The relevance of unsteady airfoil effects, described in Chapter 2.3.1, in the present flight tests can be assessed by comparing the integral lift response with a quasi-steady expectation in Figure 6.5. The quasi-steady curve is obtained by substituting the measured angle-of-attack signal into a linear fit of the experimental $\bar{C}_l$-$\bar{\alpha}$-curve

$$C_{l,\mathrm{qs}} = 0.0965\ \alpha + 0.589. \tag{6.2}$$

The fit is obtained from the mean $\bar{C}_l$-$\bar{\alpha}$ included in Figure 6.6 and the hot-wire signals of Figure 6.3(b) are smoothed with a zero-lag moving average, using overlapping 25 ms intervals. In Figure 6.5 the resulting $C_{l,\mathrm{qs}}$ signal is compared with the measured lift coefficient C_l obtained with equations (3.8) and (3.9). In general, a notable agreement of the curves is observed. Nevertheless, the quasi-steady solution overshoots in instants of rapid lift changes, e.g. for $t \approx 6$ s. Furthermore, a slight phase lag of the unsteady measurement can be observed in such peaks. Both identified differences between the two curves reflect the theoretical results of the unsteady thin airfoil model discussed in Chapter 2.3.1, which predicts an impeded and phase-shifted inviscid response due to the shedding of potential vortices into

the wake of the airfoil. lift curve. The skewing is characteristic for unsteady airfoils without flow separation (McCroskey, 1982).

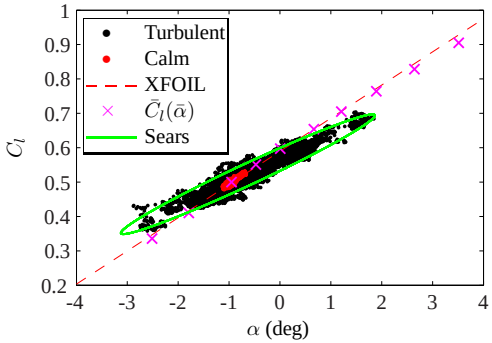

Figure 6.6.: Lift response in flight through calm conditions and through moderate turbulence. The dots correspond to the cases shown in Figure 6.4. The ellipse corresponds to the analytical solution in equation (2.17).

In the C_l-α diagram in Figure 6.6 the unsteadiness of the inviscid airfoil response becomes more apparent. The two flight cases of Figure 6.4 are represented as point clouds of all measured C_l-α combinations. A comparison with the results of a measurement of the mean lift curve obtained for $\bar{\alpha}$ and a steady computation with XFOIL is provided. The point distribution of the calm case accumulates directly on the mean experimental lift curve, which agrees well with the steady numerical solution. The data for moderately turbulent conditions deviate from the steady lift curve and scatter considerably. Deviations from the linear, quasi-steady expectation of $\Delta C_l \geq 0.05$ are visible. The deviations yield a clear indication of unsteady airfoil effects. From the insight obtained with the thin airfoil model in Chapter 2.3.1, the departure from the linear curve in equation (6.2) can be attributed to hysteresis effects caused by the impeded and phase-shifted load response of the airfoil in flight through atmospheric turbulence (cf. Figures 2.6(a) and 2.6(a)). To highlight the hysteresis effects, the analytical solution of Sears (1941) for the harmonic vertical gust problem (equation (2.17)) is included in Figure 6.6, using the parameters $\kappa = 0.3$, $\hat{W}_g = 1.5$ m/s and $\bar{U}_\infty = 41.22$ m/s. The resulting ellipse adequately encloses the measured C_l distribution and shows the skewing from the steady, linear lift curve. The skewing is characteristic

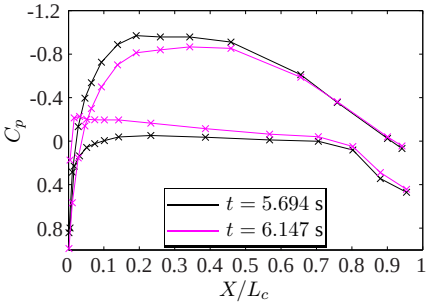

Figure 6.7.: Instantaneous pressure distributions due to an upward directed gust.

for unsteady airfoils without flow separation (McCroskey, 1982).

The rapidness of the unsteady changes of the two aforementioned cases is further demonstrated by the consideration of the instantaneous pressure distributions in Figure 6.7 at two different time instants. In the quick succession of less than 0.5 s, the pressure distribution changes considerably due to the effect of an upward directed gust. In between these instants of time the airfoil travels around 15 chord lengths, which gives a notion of the characteristic forcing time scales observed in the present flight experiments.

It should be noted that lift variations are not the only integral inviscid effects caused by unsteady airfoil excitation. If one considers quasi-steady plunging motion of a symmetrical airfoil in a uniform stream at zero chord incidence, the changes of the effective angle of attack generate a small thrust component. This effect was described by Betz (1912) and it was experimentally investigated by Katzmayer (1922). Furthermore, in an unsteady framework the potential vortex shedding into the wake of the airfoil is generally not limited to only one dimension. The induced velocity can thus generate additional drag or thrust depending on the type of the motion (Birnbaum, 1924; Cebeci et al, 2005).

Considering the low drag coefficients of NLF airfoils, it is deemed possible that viscous drag increase in flight through atmospheric turbulence may partly be compensated by inviscid thrust generation. A comparison of the orders of magnitude of these effects would be valuable for future research. It could provide confirmation or refusal to the notion of some glider pilots that the net performance of sailplanes is improved in flight through turbulent

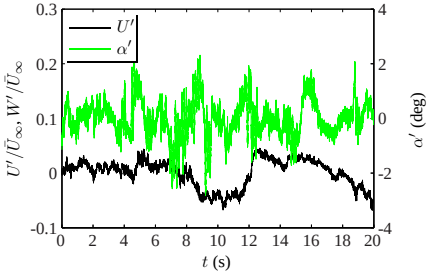

Figure 6.8.: Oncoming flow disturbances for the moderately turbulent conditions of case study 2 ($\bar{\alpha} = -0.63°$, $Re = 3.488 \cdot 10^6$, $Tu = 0.36$ %, $\epsilon = 1.77 \cdot 10^{-3}$).

conditions.

6.2.2. Case Study 2: The Role of the Instantaneous Pressure Gradient

The second case study is intended to shed light into the important role of the time-varying pressure distribution in the boundary-layer development and its influence on laminar-turbulent transition, which will be discussed in detail in Chapter 7. Similar to Section 6.2.1 the boundary conditions for this flight case are presented in the following. In contrast to case study 1, the flight was conducted during the third flight test campaign (cf. Table 3.3). The higher data rates of the measurement instrumentation will be important for the examination of the details of the time-dependent changes in the flow. The oncoming flow conditions for this flight through moderate turbulence is presented in Figure 6.8. It comprises chordwise velocity fluctuation and angle-of-attack fluctuations of less than 3°. The angle-of-attack signal in this flight is obtained by a wind vane on the left wing of the aircraft as no X-wire probe was available. Thus, only the chordwise velocity is based on a hotwire-measurement with a single-wire probe. Despite the visible eigenfrequency ($f \approx 10Hz$) of the wind vane in the α' signal, this case will be particularly depictive for boundary-layer effects investigated in Chapter 7.1.2. Furthermore, the argumentation will mainly base on the fluctuations of the pressure distribution discussed in the following.

Figure 6.9(a) shows a contour plot of the temporal fluctuations of the

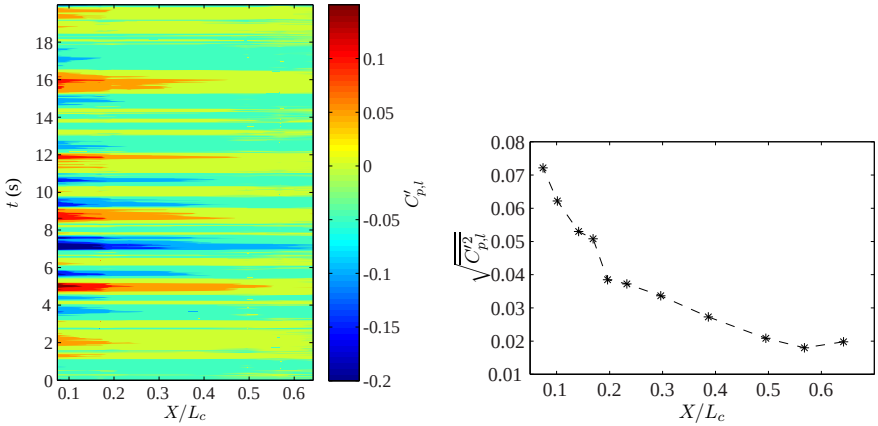

(a) Temporal fluctuations

(b) RMS of C'_p on the lower side

Figure 6.9.: Fluctuations of the pressure coefficient on the lower side.

pressure coefficient $C'_{p,l}$ on the lower side of the wing glove in the streamwise region between $X/L_c = 0.07$ and $X/L_c = 0.64$. Fluctuations of $C'_{p,l}$ are observed continuously, reaching peak values of $C'_{p,l} \geq 0.15$ in several short time periods of the 20 s measurement run. Moreover, changes in the sign of the pressure coefficient become apparent. The $C'_{p,l}$ variations intensify in the leading edge region. To underline this gradual intensification, the RMS values of the pressure fluctuations are shown in Figure 6.9(b). Characteristic instantaneous pressure distributions for one such event at $10.2\ \text{s} \leq t \leq 11.2\ \text{s}$ are depicted in Figure 6.10. In the leading edge part a strong negative deflection of $\Delta C_p \geq 0.2$ is observed at $t = 10.645$ s. The distributions prior to and after this event almost coincide. In contrast to the event in Figure 6.7, where an acceleration of the boundary layer can be expected on the lower side of the airfoil, a significant pressure increase in the chordwise direction is found in the present case. Hence, a strong deceleration of the boundary layer is expected, which generally promotes boundary-layer transition.

The pressure variation undoubtedly plays an outstanding role for the boundary-layer development. Under calm conditions in Chapter 5.1 it was found that transition on the lower side varied significantly for small changes in the angle of attack, whereas the transition position on the upper side was almost insensitive to such changes. Having presented these typical unsteady

boundary conditions in flight through moderate atmospheric turbulence, it will be interesting to examine whether quasi-steady boundary-layer considerations remain valid.

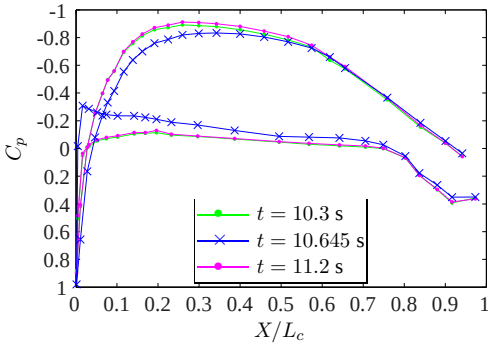

Figure 6.10.: Instantaneous pressure distributions due to a downward directed gust.

In the preceding sections correlations between oncoming flow disturbances and characteristic airfoil quantities were described. It was shown that flight dynamical motions of the aircraft are unavoidable. Yet, they are sufficiently damped and do not compete with the unsteady aerodynamic process. Evidence was provided that steady theory cannot solely describe all the inviscid effects acting on a NLF airfoil in flight through moderate atmospheric turbulence. The fluctuating oncoming flow quantities randomly excite the airfoil and cause a rapidly changing pressure distribution with $\Delta C_p \geq 0.2$ in the leading edge part. Hence, the integral loads and the boundary conditions for the boundary-layer development vary continuously. The lower side of the airfoil is particularly affected by sign changes of the pressure gradient. This leads to accelerations and decelerations of the laminar boundary-layer flow over considerable distances. The boundary conditions described in this chapter determine the boundary-layer development. Yet, the boundary layer itself represents a dynamical system with a characteristic response to unsteady changes. In the following chapter it will be shown that even small changes of the inviscid outer flow lead to considerable variations in the boundary-layer transition process.

7. Flight through Turbulence II: Boundary-Layer Response

The time-varying pressure distribution examined in Chapter 6.2 affects the boundary-layer development and its transition from the laminar to the turbulent state. Furthermore, an increased level of small-scale turbulence is observed for moderately turbulent conditions, as it was pointed out in Chapter 4. In-flight investigations of boundary-layer transition cannot consider one of these effects separately since both act simultaneously. The unavoidable, random changes of the boundary conditions prohibit stationary measurements. In flight through moderate turbulence, time needs to be taken into account as an additional variable of the problem which complicates the investigation tremendously. Only with high sampling rates and special postprocessing procedures is it possible to shed light into the evolution of the boundary-layer disturbances.

In this chapter it will be shown that the changing inviscid flow field leads to an unsteady boundary-layer development. The influence of the time-dependence of transition under moderately turbulent conditions is demonstrated in Section 7.1. The experimental observations are complemented by comprehensive numerical investigations in Section 7.2 by employing unsteady panel and boundary-layer methods as well as quasi-steady linear stability theory. The chapter is concluded in Section 7.3 with a discussion of the importance of small-scale turbulence on the transition process observed in the experiments.

7.1. Time-Dependence of Transition

The case studies of Chapter 6 serve as convenient examples for the observed flow characteristics during the three measurement campaigns. The individual strength of the two different transition measurement systems employed in this study, will be exploited to substantiate the results and to add additional details. Case study 1 again points out the differences between flight through calm and moderately turbulent conditions. Case study 2, for a slightly higher

turbulence level, is used to demonstrate some further peculiarities of the transition process. The important role of the pressure gradient on both sides of the airfoil is substantiated. The results of case study 2 will show that the lower side of the airfoil is the more interesting one for the present investigation. Investigations on this side are carried out in the time-frequency domain to identify the involved boundary-layer disturbances.

7.1.1. Case Study 1: Comparison of Calm and Moderately Turbulent Conditions

In the present experimental setup there is no direct means to determine the boundary layer profiles. Only indirect methods, such as the measurement of the changing boundary conditions and the disturbance evolution inside the boundary layer, can be used to interpret its state. The measurement of these quantities, however, provides important insight into the boundary-layer response to the external excitation. To obtain a general impression of the differences in the temporal transition development for moderately turbulent conditions, the moving statistics procedure, which was introduced in the beginning of Chapter 5, is applied to obtain a time-variable sound pressure level (SPL). The wall microphone system in case study 1 was operated at a sampling rate of 6.4 kHz. Using 1600 samples for the statistics at every considered position in time (50 % overlap) yields a time-variable SPL value for every 0.125 s. The result is the three-dimensional contour plots in Figure 7.1, which illustrate the spatio-temporal disturbance amplification in the boundary layer on the lower side of the airfoil. Strong upstream deflections of the disturbance amplification are seen with displacements $\Delta X/L_c > 0.3$. At several time instants, very rapid changes in the streamwise amplification occur. The time scale of some fluctuations is less than 0.5 s. The rapid streamwise fluctuations of the disturbance onset, and thus boundary-layer transition, raises the question on the nature of these variations. To obtain insight, it is necessary to correlate the fluctuations to the oncoming flow disturbances and to investigate the role of the temporal evolution of the pressure gradient.

The linear sensor response of the wall microphones offers the advantageous possibility to employ the threshold procedure depicted in Figure 5.9(a) for unsteady conditions. The transparent plane in Figure 7.1(a) corresponds to the characteristic SPL of $2.3 \cdot 10^{-3}$ in the fully turbulent part of the boundary layer, which was also used for the determination of N_t in Chapter 5.1. It is again used as the amplification threshold for moderately turbulent

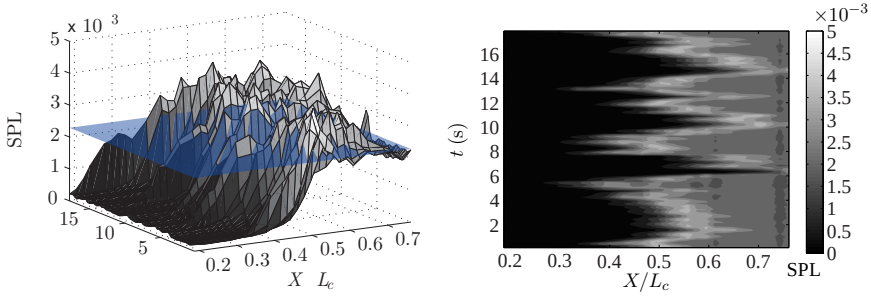

(a) 3D view (b) Top view

Figure 7.1.: Tempo-spatio transition development on the lower side of the airfoil moderately conditions , $\bar{\alpha} = -0.63°$, $Re = 3.488 \cdot 10^6$, $Tu = 0.26$ %, $\epsilon = 2.86 \cdot 10^{-4}$.

conditions. Figure 7.2 compares the zero-lag low-pass filtered (100 Hz) α variations of Figure 6.3 (the mean angle of attack has been added) with the streamwise position, where the time-dependent SPL exceeds specified amplification threshold. For the calm case, the position X_t only varies slightly for $3 \leq t \leq 6$, when a small variation of the angle of attack is observed. For moderately turbulent conditions it is noted that transition is displaced significantly upstream for decreasing angles of attack and vice versa. Qualitatively, a good correlation between angle of attack variations and the position of the exceeding of the amplification threshold is observed. It should be recalled from the investigation in Chapter 5.1 that the boundary layer decelerates for negative angles of attack and promotes the growth of Tollmien-Schlichting waves. For increasing α the TS waves evolution is generally damped on the lower side of the airfoil. Yet, an important peculiarity is found for the considered moderately turbulent flight conditions. The amplification threshold is exceeded even for positive angles of attack. This finding disagrees with the observations in Figure 5.8(b), where the threshold amplification was not reached for positive angles of attack and similar Reynolds numbers under calm conditions.

To obtain first indicative values of the transition modification, it is reasonable to compare the instantaneous SPL distribution with purely quasi-steady N-factor computations based on the actual pressure distribution. In Figure 7.3 the result of a steady computation at time instant $t = 6.15$ s is shown,

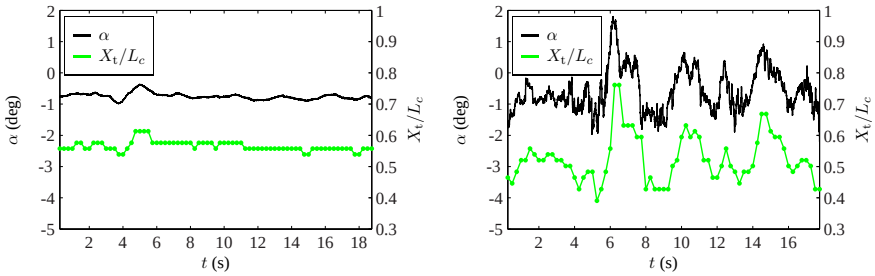

(a) Calm conditions:
$Tu = 0.04$ %, $\epsilon = 1.03 \cdot 10^{-7}$

(b) Moderately turbulent conditions:
$Tu = 0.26$ %, $\epsilon = 2.86 \cdot 10^{-4}$

Figure 7.2.: Comparison between the angle of attack fluctuations and the exceeding of the amplification threshold on the lower side of the wing glove. (a): calm conditions ($\bar{\alpha} = -0.75°$, $Re = 3.368 \cdot 10^6$) (b): moderately turbulent conditions ($\bar{\alpha} = -0.63°$, $Re = 3.488 \cdot 10^6$).

which is based on the pressure distribution shown in Figure 6.7. The N-factors remain well below the value of $N_t = 12$, which was used under calm conditions for the comparison in Figure 5.9(b). Although the instantaneous SPL approaches the threshold level for $X/L_c \geq 0.55$, the curve only intersects at $X/L_c \approx 0.72$. Considering the N-factor of $N \approx 9.5$ at that position, where a difference $\Delta N \approx 2.5$ can be asserted compared with calm conditions. Even though such an N-factor reduction results only in a streamwise transition displacement $\Delta X/L_c \approx 0.1$, such differences were found in various flight test results at similar moderately turbulent conditions.

Investigations in the Time-Frequency Domain

A common way to identify boundary-layer disturbances under steady conditions is the consideration of frequency spectra. Under calm flight conditions in Figure 5.10, the TS wave hump clearly protruded in the power spectra. Under moderately turbulent conditions, however, mean amplitude spectra are corrupted due to the upstream and downstream deflections of transition. If the flow is only turbulent for a fraction of the recording time at a specific sensor position, this information is lost in the spectral averaging. Therefore, it is more convenient to apply a method similar to the moving statistics

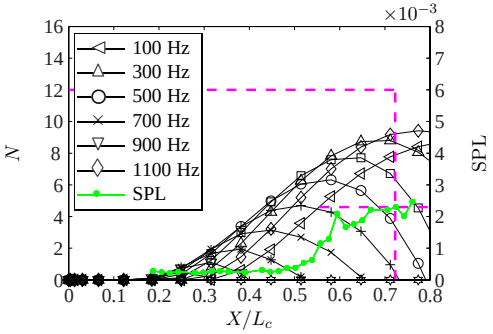

Figure 7.3.: Comparison of the measured instantaneous disturbance amplification and quasi-steady N-factor computations at $t = 6.15$ s.

procedure in Figure 7.1 to compute time-dependent power spectra. The drawback of such short-time Fourier transforms (Bendat and Piersol, 2010) is higher spectral noise due to the limited number of samples used for each computation. The resulting spectrograms are thus a compromise between the desired temporal resolution and the accuracy of the spectral estimation. Nevertheless, the procedure provides important insight when comparing the results for the calm and the moderately turbulent flight case introduced in Figure 6.4 for different streamwise positions.

The short-time Fourier transforms were obtained by using intervals of 0.5 s with 50 % overlap, i.e. 3200 samples for each Fourier transform. To obtain a reasonable estimate of the power spectral density of the ratio between the pressure fluctuations and unit pressure, a Hamming window function is applied. As expected, the temporal evolution of the spectra for calm oncoming flow conditions in the left column of Figure 7.4 exhibit a smooth and constant temporal behavior. The amplification of a distinct frequency band corresponding to the one of the TS wave packets is clearly visible for the first two streamwise positions. Only for the last sensor position, $X/L_c = 0.56$, does the frequency content vary in time. This is associated with the increasing intermittency before breakdown to turbulence and small variations in the angle of attack, which become important in the breakdown region.

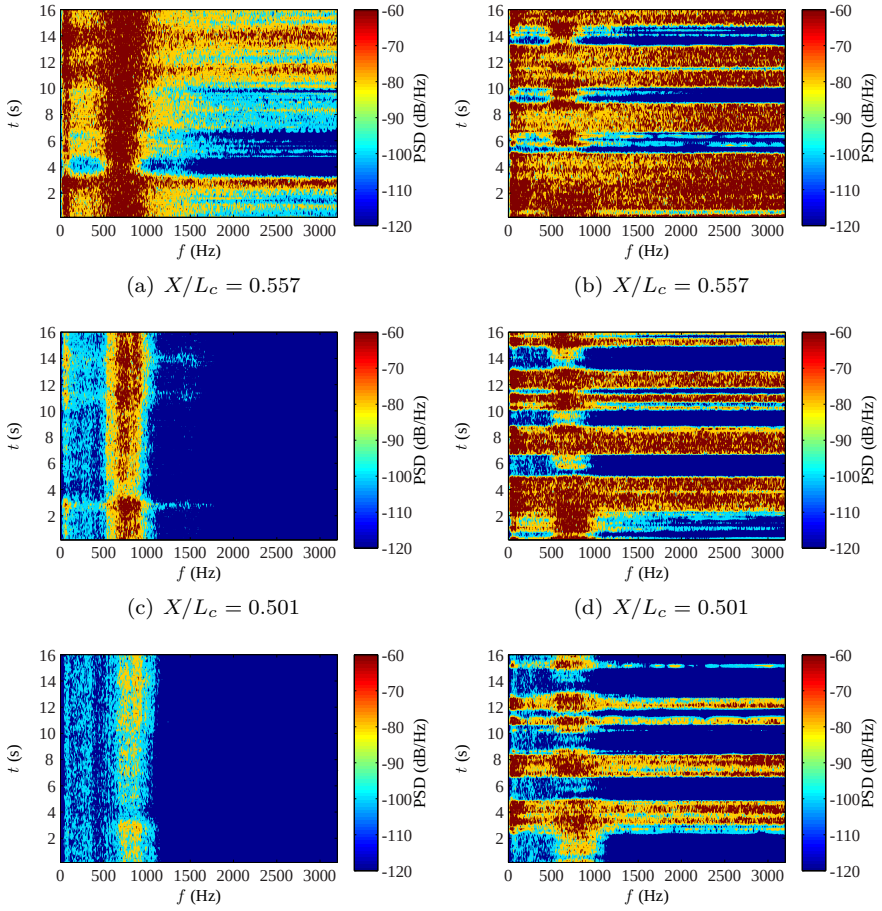

(a) $X/L_c = 0.557$ (b) $X/L_c = 0.557$

(c) $X/L_c = 0.501$ (d) $X/L_c = 0.501$

(e) $X/L_c = 0.446$ (f) $X/L_c = 0.446$

Figure 7.4.: Results of short-time Fourier transforms of the microphone signals corresponding to the oncoming flow disturbances in Figure 6.3. (a, c, e): calm conditions. (b, d, f): moderately turbulent conditions.

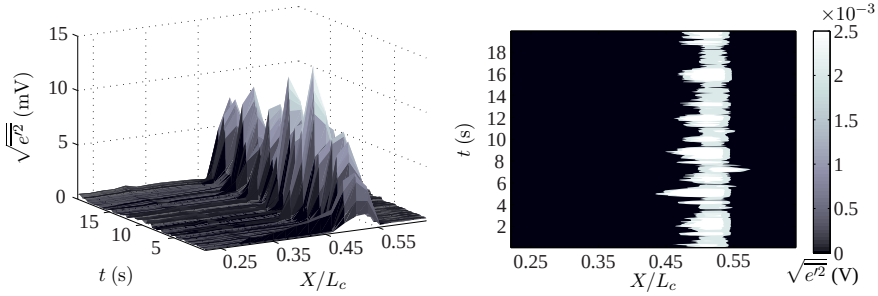

(a) 3D view (b) Top view

Figure 7.5.: Tempo-spatio transition development on the upper side of the airfoil under moderately turbulent conditions , $\bar{\alpha} = -0.63°$, $Re = 3.359 \cdot 10^6$, $Tu = 0.36$ %, $\epsilon = 1.77 \cdot 10^{-3}$.

The spectrograms for flight through moderately turbulent air in the right column appear significantly different. Even at the first considered position, $X/L_c = 0.45$, the amplitude increases significantly over all frequencies for specific time periods. In between these instants, the hump of TS wave packets still protrudes from the elevated disturbance level. For the sensor position $X/L_c = 0.55$,the fractions of time with completely filled spectral density are expanded. Nevertheless, time fractions of completely laminar flow also exist, as can be seen from the low amplification in the TS frequency band. For the last streamwise position, the boundary layer is mostly turbulent. Laminar or transitional behavior can only be observed for a fraction of time.

7.1.2. Case Study 2: The Role of the Instantaneous Pressure Gradient

Case study 2 offers the possibility to consider the transient processes on the lower side more closely due to the higher sampling rate of the hot-film system. Furthermore, simultaneous measurements on the upper side of the airfoil were possible in this configuration, as described in Chapter 5.1. Both sides of the airfoil are depicted for the moderately turbulent oncoming flow conditions in Figure 6.8. The time-dependent RMS values reveal remarkable differences between the upper and the lower side of the airfoil.

On the upper side in Figure 7.5 streamwise variations of the disturbance

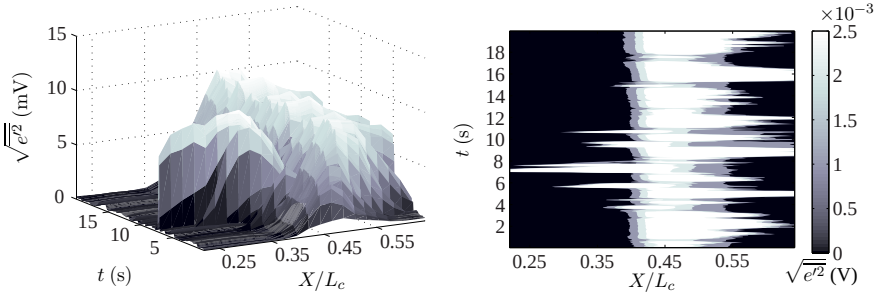

(a) 3D view (b) Top view

Figure 7.6.: Tempo-spatio transition development on the lower side of the airfoil under moderately turbulent conditions. Hot-film measurements at $\bar{\alpha} = -0.63°$ and $Re = 3.359 \cdot 10^6$, $Tu = 0.36$ %, $\epsilon = 1.77 \cdot 10^{-3}$.

amplification onset of are visible for the whole measurement sequence. However, they are limited in their streamwise extent to $\Delta X/L_c \leq 0.1$. Despite the peak-to-peak variation of $\alpha' = 3°$ shown in Figure 6.8, transition is clearly fixed in a narrow region. A reason can be found in the adverse pressure gradient. It leads to a strong deceleration of the boundary layer in the region $0.4 \leq X/L_c \leq 0.6$, which was examined in detail under calm conditions in Chapter 5.1. The streamwise variation of transition is thus constrained by the local pressure gradient. Despite the typical variations observed in Chapter 6.2.2, it only becomes strongly adverse in a narrow streamwise region and causes high disturbance amplification. Only for higher mean angles of attack $\bar{\alpha}$ does this situation change, as the deceleration of the boundary layer moves significantly upstream. However, these cases are beyond the scope of the present investigation. From the observed streamwise fixation of disturbance amplification in the region of highest TS wave growth it can be concluded that no sign of bypass transition was found on the upper side in the present investigation. Bypass transition due to direct entrainment of free-stream turbulence would not depend as strongly on the adverse pressure gradient in the region $0.4 \leq X/L_c \leq 0.6$. The implications of this important finding are discussed in more detail in Section 7.3.

The evaluation of possible premature transition is difficult on the upper side as the transition process under all conditions is confined to a small

streamwise region, where only a few hot-film sensors detect the disturbance amplification. In contrast, the gradual TS wave growth over large streamwise distances on the lower side is expected to be more influenced by free-stream turbulence. Increased disturbance levels may cause higher initial TS wave amplitudes and trigger earlier nonlinear wave interactions. Therefore, this study focusses on the lower side, where a high pressure gradient sensitivity has been asserted in case study 1. The described features are typical for the lower side of state-of-the-art sailplane airfoils, making such an investigation especially interesting.

Figure 7.6 shows the response of the lower side to the turbulent excitation. The disturbance amplification is remarkably different in comparison to the upper side. At several time instants significant and very rapid changes in the streamwise disturbance amplification appear. Upstream and downstream deflections of the disturbance amplification of $\Delta X/L_c > 0.2$ are observed for very narrow time scales ($\Delta t < 0.5$ s). The typical event found for 10.2 s $\leq t \leq$ 11.2 s is of particular interest in the following.

Quasi-steady N-factor calculations are conducted for this event to demonstrate differences in the obtained transition N-factors N_T compared with calm flight conditions. The computations are based on the two significantly different instantaneous pressure distributions in Figure 6.10. The experimental transition curves in Figures 7.7(a) and 7.7(b) are based on 1600 hot-film samples. The transition N-factors corresponding to the peak amplification are found within $10 \leq N_{\mathrm{T}} \leq 11$ and this is well below the values observed for calm conditions ($N_{\mathrm{T}} \approx 13.5$ in Figure 5.7). The reconfirmation of a N-factor reduction compared with the calm air findings substantiates the result of Figure 7.3.

The boundary conditions for the computations in Figure 7.12, i.e. the unsteady edge velocity, were determined from the surface pressure measurements. Under unsteady conditions this leads to a bias as demonstrated in Chapter 2.3.1. Bernoulli's equation (2.4) contains the time derivative of the velocity potential and this term is neglected when using the steady version of the equation with the instantaneous pressure data. Furthermore, the time history of the unsteady boundary-layer development is neglected in these calculations. Therefore, systematic inaccuracies are involved in such purely quasi-steady considerations based on instantaneous measurement results. The relevance and the extent of these inaccuracies is assessed numerically in Section 7.2.

Despite these uncertainties, it is found that the upstream fluctuations of disturbance growth in Figure 7.6 closely correspond to negative deflections

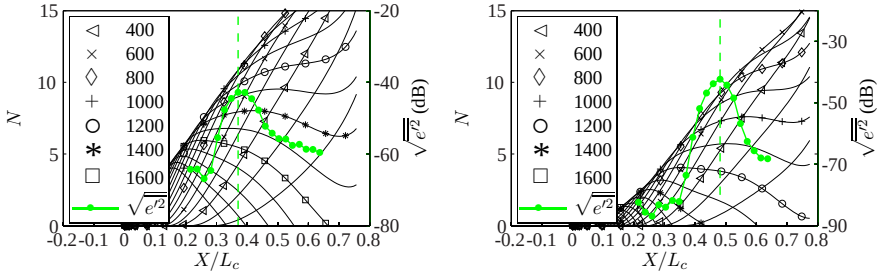

(a) $t = 10.65$ s (b) $t = 11.2$ s

Figure 7.7.: Comparison of transition measurements with quasi-steady N-factor computations, which are based on the instantaneous pressure distribution in Figure 6.10. Legend numbers denote frequencies f in Hz.

of the pressure coefficient $C_{p,l}$ in Figure 6.9 at approximately the same time. A decreasing streamwise pressure gradient generally stabilizes the boundary layer, whereas an increasing gradient has a destabilizing effect. Thus, to some extent the fluctuating transition position can be explained by the quasi-steady considerations in Chapter 5.1. In any case, the question whether the reduction of characteristic transition N-factors can be attributed to an unsteady boundary-layer evolution or to the increased small-scale turbulence level needs to be addressed with a careful examination of the important role of the instantaneous pressure gradient. The next step is the identification of the boundary-layer disturbances involved in the time-varying transition process under moderately turbulent flying conditions.

Wavelet Analysis of the Temporal Transition Fluctuations

As discussed in Chapter 1.3 the intermittent occurrence of transition has also been reported in a generic wind-tunnel experiment from Studer et al (2006a), where the pressure gradient was varied harmonically. They observed the rapid appearance of nonlinear disturbances and turbulent bursts in an airfoil boundary layer due to the unsteadiness of the boundary layer in a low-disturbance wind tunnel. In the present study, however, the variations of the pressure gradient and increased levels of small-scale turbulence are present at the same time. The striking rapidness of some of the tran-

sition fluctuations with durations of less than 0.3 s in Figure 7.6(b) calls for a profound investigation into the spectral details. In particular, it is of interest whether these events are indeed caused by short-time variations of the pressure gradient or if some convective instability promotes a premature breakdown to turbulence.

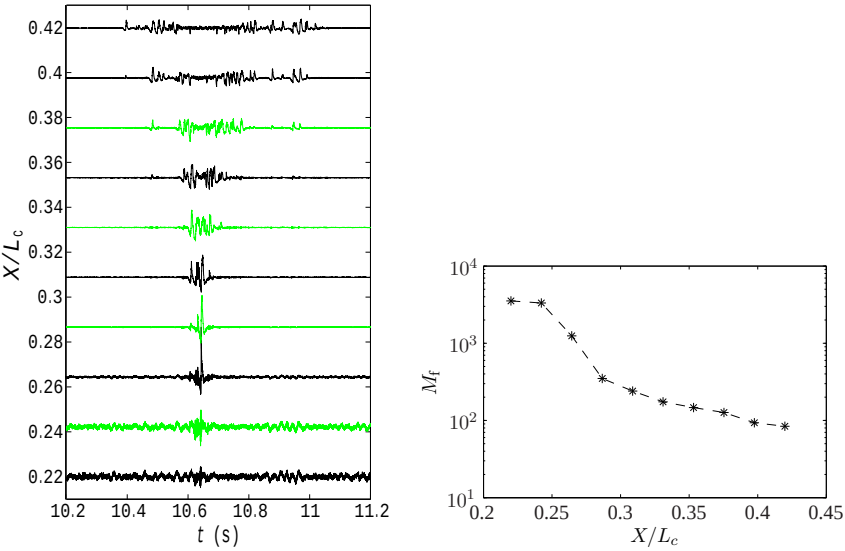

(a) Fluctuation signals

(b) Magnification factor

Figure 7.8.: Magnified hot-film raw signals of ten sensors of the streamwise row on the lower side. The pressure distributions in Figure 7.8 pertain to the same time segment. Marked signals are used for the Wavelet analysis.

To obtain an impression of the transition deflection in the time-position domain, Figure 7.8 shows the hot-film signals at ten streamwise stations for the time period $10.2\,\mathrm{s} < t < 11.2\,\mathrm{s}$. The voltage signals of the considered time sequence have been normalized and magnified depending on the streamwise sensor position

$$s'_n = M_f \frac{e'_n}{\sqrt{\overline{e'^2_n}}}, \qquad \text{with} \qquad M_f = \frac{\Delta x}{L_c} \max_{\forall n} \left(e'_n / \sqrt{\overline{e'^2_n}} \right). \tag{7.1}$$

M_f is an arbitrary scaling constant, which is chosen as the dimensionless sensor distance $\Delta x/L_c$ times the maximum value of all ten dimensionless sensor signals. The scaling only serves for a clearer view on the nonlinear transition evolution at the upstream sensor stations in a single plot. Due to the normalization with RMS values for the considered time period of 1 s, which is depicted in figure 7.8(b), the transition evolution in the upstream part is highlighted and small-scale disturbances appear attenuated in the downstream region.

The nonlinear transition stage appears as sudden bursts of high amplitudes in each of the sensor signals. The occurrence of large amplitudes is shifted in time. A wedge-shaped transition development is immediately apparent. Starting at $t \approx 10.4$ s, $X/L_c = 0.42$ and proceeding in time, transition is displaced upstream until reaching a tip position at $t \approx 10.64$ s. Continuing along the timeline from the tip of the wedge, transition is displaced downstream again and reaches the last depicted sensor in less than 0.1 s. On both sides of the wedge localized waveforms are visible. Yet, only strong low-frequency, nonlinear modulations can be observed in the depicted time interval. The most amplified TS waves are expected at significantly higher frequencies (700 - 1500 Hz) from Figure 7.7(a). Completed breakdown and homogenised turbulence can only be observed inside the transition wedge downstream of the sensor position $X/L_c = 0.353$.

The time period, over which the transition wedge appears, corresponds to the $C_{p,l}$-fluctuations shown in Figure 6.9, which reaches a minimum at the exact time instant, where the wedge tip is observed. A minimum in $C_{p,l}$ leads to a deceleration of the boundary layer in the present flight case. It can be inferred from these considerations that boundary-layer transition is mainly driven by the pressure gradient under these disturbed flow conditions. The wedge-shape of the upstream transition deflections excludes the possibility of a pure bypass transition caused by a convective disturbance generated by free-stream turbulence.

The nonlinearity of the disturbances far upstream of the mean transition region calls for deeper insight into the spectral properties of the process to determine whether it starts it starts with linear instability wave amplification or whether it is intrinsically nonlinear. The appearance of the transition wedge is highly localized in space and time. As discussed in Section 7.1.1, conventional Fourier analysis, which is conceptually delocalized in time, may not shed sufficient light into the details in such short time periods. Therefore, wavelet analysis is employed to investigate the transient process. The use of this method is inspired by the works of Hudgins et al (1993), Studer et al

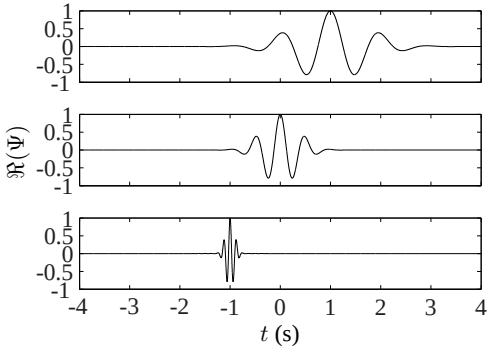

Figure 7.9.: Example for the scaling of a Morlet wavelet.

(2006b) and Bernardini et al (2013). Since the important basics of wavelets are presented in each one of these works and further information can be found in the review of Farge (1992), only a brief summary of the most important aspects of the continuous wavelet transform is given. The transform can be interpreted as an inner product between an analyzing function, i.e. the wavelet, and the signal to be analysed. It is defined by the integral

$$\hat{W}(a,\tau) = \frac{1}{\sqrt{a}} \int_{\infty}^{\infty} e'(t) \Psi^* \left(\frac{t-\tau}{a} \right) \mathrm{d}t. \tag{7.2}$$

The function Ψ^* denotes the complex conjugate of the wavelet which is intrinsically localized in time. It can be compressed or stretched by the scale parameter a and shifted in time by the parameter τ to locally approximate the function $e'(t)$ to be analyzed as it is shown in Figure 7.9. In order to be admissible for the transform, the analyzing function Ψ needs to fulfill certain mathematical requirements (Farge, 1992). The strength of wavelet analysis is that a great variety of analyzing functions exist and a suitable one can be chosen for the particular physical process. Here, a Morlet wavelet is used for its superior representation of sine-like signal parts, as these are expected from determinism involved in boundary-layer transition.

$$\Psi(t) = \sqrt{\pi b} \mathrm{e}^{(i 2\pi f_c t)} \mathrm{e}^{\left(\frac{t^2}{b}\right)} \tag{7.3}$$

The wavelet function constitutes a plane wave modulated by a Gaussian envelope. The scales used in wavelet analysis cannot directly be connected

to frequencies in the Fourier sense. The maximization of a given wavelet with a sine wave yields the center frequency f_c. In equation (7.2), the scale parameter a is connected to the center frequency f_c of the wavelet by the relation $f_p = f_c f_s/a$, where f_p is the pseudo-frequency and f_s is the sampling rate. For a Morlet wavelet, the pseudo-frequency f_p is a good approximation of the real frequency f. In the present case the scales a are prescribed as $1/\log(a)$ to obtain a favorable pseudo-frequency distribution between 1 Hz and 8 kHz, which is the important range for the present investigation. The resulting wavelet coefficients $\hat{W}$ from equation (7.2) yield the energy spectrum $\hat{W}\hat{W}^* = |\hat{W}|^2$, which represents the energy content of the signal in the time-scale domain, i.e. the time-pseudo-frequency domain in the present case.

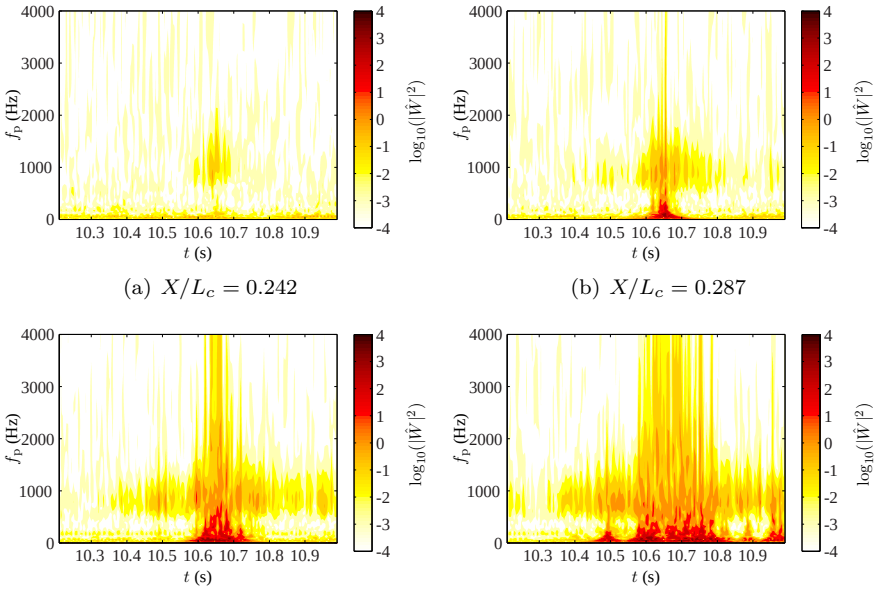

(a) $X/L_c = 0.242$ (b) $X/L_c = 0.287$

(c) $X/L_c = 0.331$ (d) $X/L_c = 0.375$

Figure 7.10.: Disturbance energy in the time-pseudo-frequency domain at different streamwise positions. Contours of the normalized wavelet coefficient are given in logarithmic scale.

In Figure 7.10 the result of the wavelet analysis is demonstrated for four different streamwise positions marked in Figure 7.8, corresponding to the second, the fourth, the sixth and the eighth streamwise station in Figure 7.8. Maybe the most important insight into the transition mechanism can be inferred from the contour plot in Figure 7.10(a) at $X/L_c = 0.242$. Only a small portion of the time-frequency domain contains energy. At $t \approx 10.6$ s and within the frequency band between 500 and 1800 Hz disturbances are amplified. The concentration in a particular frequency band suggests that transition is indeed initiated by a linear amplification of TS waves prior to the subsequent nonlinear evolution. For the second station at $X/L_c = 0.287$, short-time nonlinear processes can already be observed due to the broader frequency distribution approximately at the same time when the transition wedge reaches the tip position upstream. The nonlinearity is inferred from the spreading over the entire frequency range. Yet, the energy transfer occurs on a very short time scale. At earlier and later time instants, amplification of the TS wave frequencies is observed. Further downstream, the nonlinear stage at $X/L_c = 0.331$ and $X/L_c = 0.375$ covers longer time intervals. The last streamwise station in Figure 7.10(d) includes the breakdown to turbulence of the wedge at $t \approx 10.65$ s and another nonlinear amplification can be observed at $t \approx 10.95$ s. The nonlinear stage in Figures 7.10(b), 7.10(c) and 7.10(d) is preceded and followed by amplification in the TS wave band.

From these results it can be concluded that the appearance of the 'transition flashes' is associated with the time-dependent development of the laminar boundary layer which is driven by rapid changes of the flow field along the boundary-layer edge. These changes are mainly caused by vertical gusts and the resulting airfoil motion in flight through moderate turbulence, as it was demonstrated in Chapter 6.

In their generic wind-tunnel experiments, Studer et al (2006a) investigate two frequencies of periodic pressure gradient changes in an airfoil boundary layer. Their lower frequency case has strong similarities to the present results. In their high frequency case, the unsteady boundary-layer effects were strong enough to cause transition by the convection of a turbulent front after formation of an initial turbulent spot. This type of transition, first discovered by Obremski and Fejer (1967), is not observed in the present flight cases.

The spatio-temporal evolution of the observed transition wedges is initiated by linear, modal amplification of TS waves which amplify rapidly and transform into nonlinear disturbances. A pure bypass transition attributed

to an entrainment of free-stream turbulence can be excluded from the wedge shape of the disturbance evolution in Figure 7.8 and the disturbance amplification within the TS wave band. As a conclusion, transition is clearly driven by the time-dependent pressure gradient. In the present flight experiments Tollmien-Schlichting waves are involved in the transition process under all investigated circumstances. Nevertheless, a combined effect of unsteady boundary-layer development and higher small scale free-stream turbulence forcing on transition cannot be excluded and it will be discussed in more detail in Section 7.3. Furthermore, there is no means to measure the unsteady boundary-layer profiles directly in the flight experiments. Thus, unsteady profile distortions and their implications for linear stability need to be investigated numerically.

7.2. Numerical Simulation of the Unsteady Airfoil Behavior

The experimental investigations described in the preceding sections give rise to serious doubts whether a quasi-steady framework is sufficient for the present investigation. These doubts lead to the implementation of the unsteady boundary-layer method described in Chapter 3.2. Together with the unsteady panel program (Chapter 3.2) it enables a completely unsteady prediction of the laminar boundary-layer behavior. Under the premise that Tollmien-Schlichting waves play a vital role in the transition process, which was substantiated in Section 7.1.1, the local LST method (cf. Chapter 3.2) can be employed to compute disturbance growth rates from the instantaneous boundary-layer profiles. The use of a quasi-steady method for transition prediction is justified since the frequencies of the observed TS waves are about two orders of magnitudes higher than the frequencies associated with the inviscid airfoil response (cf. Chapter 6.2.1) which is also pointed out by Obremski and Morkovin (1969). The parallel flow assumption for the stability method greatly alleviates the problem, as the local procedure is completely decoupled from the spatio-temporal boundary-layer evolution. It is only based on the instantaneous shape of the local boundary-layer profiles. From the observations in the preceding sections and the theoretical considerations in Chapter 2.3.2, significant distortions of the boundary-layer profiles are expected. Their influence on boundary-layer stability and on the common N-factor transition prediction scheme is investigated in the following.

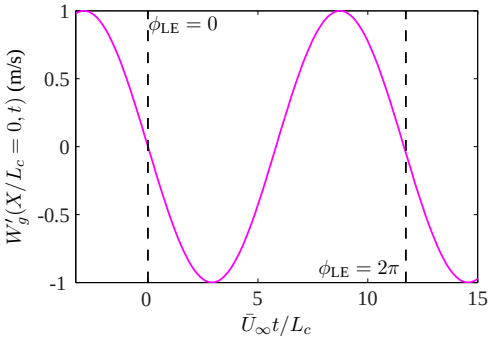

Figure 7.11.: Harmonic gust excitation of the airfoil and definition of the leading edge phase ϕ_{LE}.

A harmonic excitation of the airfoil offers the possibility to obtain more general insight into the unsteady mechanism when comparing the results with quasi-steady computations. Incorporating the findings of Chapter 6.2 and Section 7.1, a sinusoidal vertical gust with an amplitude of $W'_{\mathrm{g}} = 1$ m/s and a reduced frequency of $k = 0.2$ is deemed to be a convenient test case. Figure 2.4 and Figure 7.11 illustrate the inviscid excitation. The mean flow is prescribed as: $\bar{\alpha} = -0.5°$, $\bar{U}_\infty = 40$ m/s and $Re = 3.6 \cdot 10^6$. The unsteady potential flow solution was provided by Spiegelberg et al (2014). To illustrate the unsteady boundary conditions, Figure 7.12(a) shows the maximum amplitudes of the pressure distribution compared with its mean value. The boundary-layer investigation focusses exclusively on the lower side of the airfoil, where a strong influence of the changing pressure gradient and remarkable deflections of boundary-layer transition were observed experimentally. The temporal resolution of the simulation is 3 ms. To economize computation time, stability computations are only conducted for 18 equidistant streamwise stations ($0.04 \leq X/L_c \leq 0.7$) and nine TS wave frequencies of ranging from 300 to 1900 Hz in steps of 200 Hz. Due to the preliminary character of this investigation, only two-dimensional TS modes are considered, although three dimensional wave modes can be computed accordingly.

To demonstrate resulting unsteady boundary-layer effects, Figure 7.12(b) shows an instantaneous boundary-layer profile at $X/L_c = 0.5$ for the time

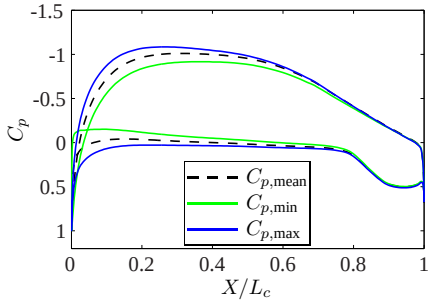

(a) Unsteady variation of the pressure distribution

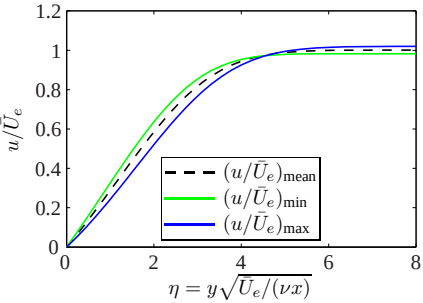

(b) Variations of the boundary-layer profile at $X/L_c = 0.5$ on the lower side

Figure 7.12.: Airfoil response to a sinusoidal gust excitation. $\kappa = 0.2$, $\bar{U}_\infty = 40$ m/s, $W'_\mathrm{g} = 1$ m/s.

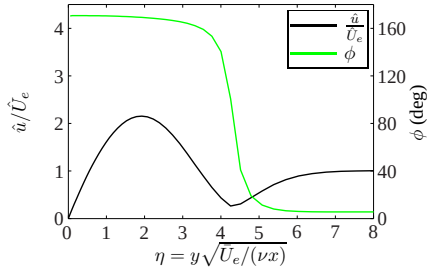

(a) $X/L_c = 0.28$

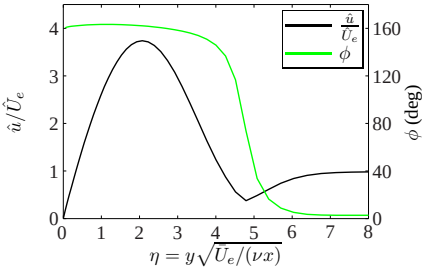

(b) $X/L_c = 0.61$

Figure 7.13.: Amplitude and phase profiles of the laminar boundary-layer oscillation.

instants corresponding to the maximum and minimum amplitudes of the outer flow. The shape of these profiles appears considerably distorted when compared with the mean counterpart. Even small changes in the curvature of the boundary-layer profile may affect linear stability since the profile shape enters directly into the Orr-Sommerfeld equation (2.32). A better view on the streamwise evolution of the boundary-layer oscillation is obtained by considering the relative amplitude and phase profiles for two different streamwise positions. In Figure 7.13, the relative amplitudes depict the ratio between the local velocity amplitude inside the boundary layer and the one of the edge velocity. The phase profile ϕ refers to the harmonic oscillation of the outer flow $U_\mathrm{e}(t)$. From the comparison of the amplitudes of the two streamwise positions it is noticed that unsteady effects increase with the length of the boundary layer. This is a common characteristic (cf. equation (2.25)) of unsteady boundary layers. A distinct amplitude maximum at $\eta \approx 2$ can be observed at both positions. The local boundary-layer velocity amplitude reaches three times the values of the edge amplitude at the downstream position $X/L_c = 0.61$. The phase profile all exhibit a positive phase shift at $\eta \approx 4.5$ and tend toward $\phi \approx 165°$ at the wall for both positions. Obviously excitation of the airfoil with a sinusoidal gust yields a distinct response compared with flat-plate investigations discussed in Chapter 2.3.2, where such strong amplitude maxima were not observed for similar frequency parameters. A major difference in the present case are the inhomogeneous unsteady changes of the streamwise pressure gradient. Hence, the demonstrated variations of the boundary-layer profiles also reflect the non-self-similar development of the mean boundary layer.

The investigation of the role of the unsteady boundary-layer effects in the transition process requires the comparison with a quasi-steady reference. The LST results shown in the following are therefore compared with quasi-steady boundary-layer solutions, which are obtained by neglecting the time-dependent terms in the governing equation 2.21. The boundary conditions provided by the unsteady panel method and all steps in LST computations remain the same. Naturally, the primary interest of this investigation is the influence of the unsteadiness on the disturbance growth rates $k_{x,i}$ of the two-dimensional TS modes. Figure 7.14 shows the evolution of dimensionless growth rates $k_{x,i}(t)/\delta_1(t)$ for two different TS wave frequencies at the same streamwise positions examined in Figure 7.13. Solid lines represent the unsteady computations and dashed lines depict the quasi-steady reference. The abscissa of the plot is the phase ϕ_LE which refers to the actual vertical velocity of the sinusoidal gust at the leading edge. At $\phi_\mathrm{LE} = 0$ the

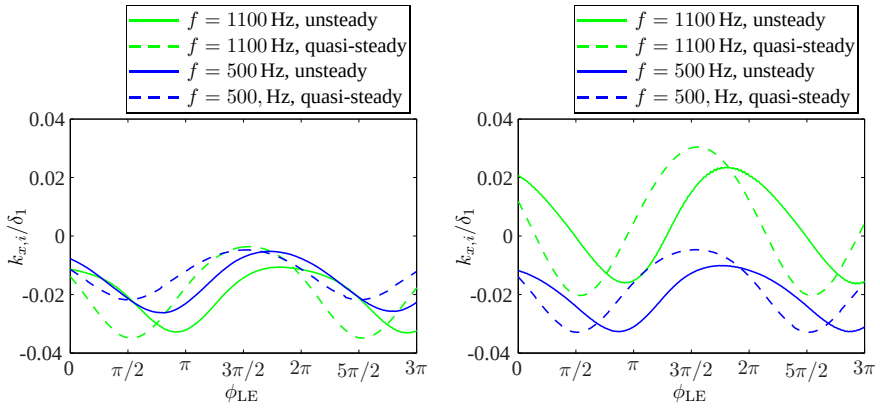

(a) $X/L_c = 0.28$ (b) $X/L_c = 0.61$

Figure 7.14.: Evolution of the dimensionless growth rate $k_{x,i}$ over an oscillation cycle. $k_{x,i} < 0$ leads to TS wave growth, $k_{x,i} > 0$ signifies attenuation.

vertical gust velocity at the leading edge is zero and it has its first minimum at $\phi_{\mathrm{LE}} = \pi/2$ (cf. Figure 7.11). From the reduced frequency $\kappa = 0.2$ and the oscillation period of approximately 0.53 s the time difference can be obtained. In Figures 7.14(a) and 7.14(b) a phase shift between the unsteady $k_{x,i}$ and its quasi-steady counterpart is visible at first sight. The unsteady case lags behind. Furthermore, differences in the amplitude of the growth rate oscillations can be observed. The growth rates for the high-frequency case (1100 Hz) oscillates between the maxima and minimum amplitudes of the quasi-steady reference. The behavior of the lower-frequency TS mode is different. In Figure 7.14(a) the minimum is found at lower values than the quasi-steady curve, signifying higher TS-wave growth. The amplitude maxima are found at approximately the same growth rates. This situation is reversed for the downstream position. At $X/L_c = 0.61$, a 500 Hz TS wave is exposed to approximately the same minimum growth rate, but the maximum is found at lower values. As a result, the net growth of the 500 Hz mode at both positions is larger in the unsteady case than in the quasi-steady one. These peculiarities become evident in the consideration of the time-dependent N-factor evolution. Furthermore, it was shown in Figure

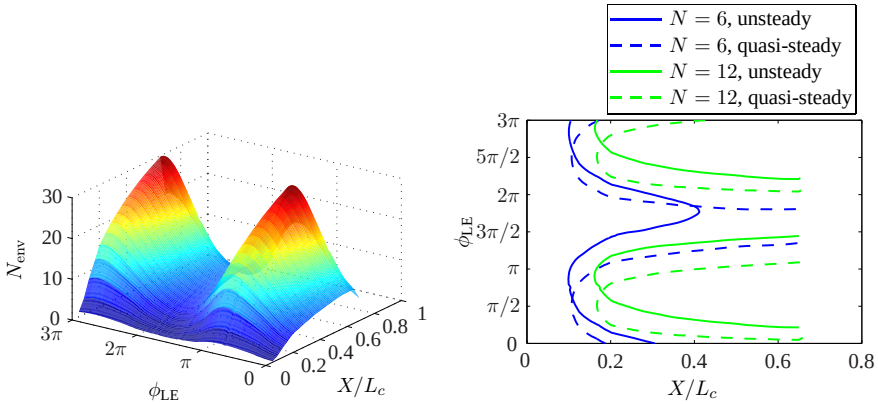

(a) 3D view on the N-factor evolution in the unsteady case

(b) Comparison of the steady and the unsteady N-factor evolution

Figure 7.15.: Results of the unsteady N-factor computations. $\phi_{\mathrm{LE}} = 2\pi$ corresponds to $t = 0.53$ s.

5.6 that two-dimensional TS-waves with $f \approx 500$ Hz are among the most amplified modes on the lower side for $\bar{\alpha} = 0.6°$.

The calculation of N-factors from the obtained matrix of eigenvalues is not straightforward in the unsteady case. It is to be considered that the instability waves travel at a phase velocity $c(x,t)$ which is smaller than the local edge velocity $U_{\mathrm{e}}(x,t)$. Thus, the gradual wave propagation in time and space adds another dimension into the procedure. Furthermore, assumptions on the origin of the waves need to be made to prescribe the starting point of the considered wave propagation. In the present case the point of neutral stability for each of the investigated TS modes is chosen. From that point the individual waves evolve independently in the position-time domain. In the present parameter regime propagation times of 30 ms are common. As the outer flow changes unsteadily, the traveling wave runs through boundary-layer profiles of alternating phases and thus changing stability properties. It is therefore possible that N-factor curves intersect in the time direction depending on the individual dispersion relations. Therefore, only the maximum N-factor at each position at any time instant is considered in the following.

The result of the procedure is demonstrated in the three-dimensional surface plot in Figure 7.15(a). The periodic amplification and attenuation of

the envelope N-factor is apparent. An indication of the transition behavior due to such excitation can be obtained by considering the envelope of the obtained N-factor curves in two dimensions. Figure 7.15(b) compares the result of purely quasi-steady considerations and the unsteady solution for two different N-factor contours, $N_{\text{env}} = 6$ and $N_{\text{env}} = 12$. Again, a considerable phase shift of almost $\pi/2$ ($\Delta t \approx 0.13$ s) between the solutions is asserted. For $N = 12$, the curve of the quasi-steady case appears symmetrical, whereas a slight asymmetry may be recognized for the unsteady case. More important, during the upstream transition deflection, the maximum quasi-steady and unsteady N-factor envelope curves in Figure 7.16(a) only differ by $\Delta N_{\text{env}} \approx 1$. Thus, displacement of transition due to the unsteady distortions of the boundary-layer profiles is small in the case of a downward-directed gust. This situation changes for a downstream transition deflection which is caused by the upward-directed half-period of the gust excitation. In the quasi-steady case, the N-factor of $N_{\text{env}} = 6$ in Figure 7.15(b) is not reached in the vicinity of $\phi_{\text{LE}} = 3\pi/2$ at $X/L_c \leq 0.7$. In the unsteady case $N_{\text{env}} = 6$ is exceeded no further downstream than $X/L_c = 0.4$. This means that boundary-layer disturbance growth is enhanced significantly in the downstream transition deflection, which corresponds to the gust half-period with positive amplitudes W'_{g}. At $X/L_c = 0.7$ the N-factor difference amounts $\Delta N_{\text{env}} \approx 2.5$ in Figure 7.16(b). An explanation for this behavior is found in the simple dimensionless relation (2.25). Unsteady boundary-layer effects increase with the length of the laminar boundary-layer. Thus, significant changes in the transition evolution are only observed when the laminar runs are sufficiently extended.

In summary, the unsteadiness changes the TS wave growth significantly if the laminar boundary layer has a certain length. Moreover, the changes of the modal growth, created by the unsteady boundary-layer development, depend on the TS wave frequencies. The N-factor evolution in the unsteady and the quasi-steady case is similar in the leading edge part of the airfoil, but a significant envelope N-factor increase ($\Delta N_{\text{env}} \approx 2.5$) is observed if the TS wave growth is gradual. This finding may explain the observed N-factor shift in Figure 7.3. The flight case corresponds to a downstream transition deflection caused by an upward directed gust. However, it cannot fully explain the observation for the upstream deflection in Figure 7.7(a), where transition occurs at $X/L_c \approx 0.38$ in the transition wedge in Figure 7.8. This case represents the response to a downward directed gust, where transition is deflected upstream. For such upstream deflections, the influence of the boundary-layer unsteadiness on the N-factor is not as important since

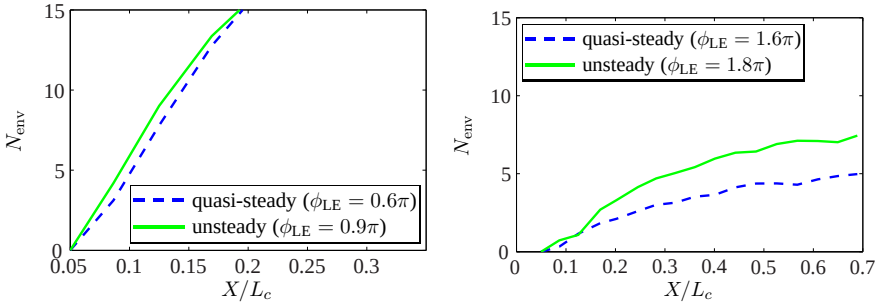

(a) Effect of downward-directed gust

(b) Effect of upward-directed gust

Figure 7.16.: Envelope N-factors based on quasi-steady and unsteady boundary-layer computations. The excitation phase ϕ_{LE} corresponds to the maximum and minimum values found for each computation.

the length of the laminar run is shorter. This conclusion yields an indication that small-scale turbulence also plays a role in the transition process, which will be discussed in more detail in the following section.

In general, TS wave growth and thus transition exhibits a significant phase delay when the unsteadiness of the boundary-layer evolution is taken into account. A time shift is also observed in the experimental data in Figure 7.2, although one additionally has to account for the convection time between the probe boom tip and the leading edge. However, it has to be kept in mind that comparisons between measurements under moderately turbulent conditions and N-factor calculations are biased, if quasi-steady boundary-layer solutions are computed by applying the steady Bernoulli equation to the instantaneous pressure distribution. The recalculation of real flight cases accounting for the complete time history is pending. As this study focussed on the revealing of the general mechanism in harmonic test cases, the recalculation of real flight cases is a valuable starting point for future research. The incorporation of a viscous-inviscid coupling between the panel and the boundary-layer code discussed in conjunction with equation (3.13) is proposed to enhance the accuracy of comparisons with experimental data.

7.3. Effects of Atmospheric Small-Scale Turbulence on Boundary-Layer Disturbances

The question of the influence of small-scale turbulence on the boundary-layer development is probably the most interesting to transition researchers, as it has focussed the attention for decades (Kendall, 1998). Although the present study was not intended as an in-flight receptivity experiment, some valuable indications of the receptivity mechanism, relevant for NLF airfoils in real flight within the atmospheric boundary layer, can be extracted from the previously presented results. These considerations may facilitate future investigations.

As explained in Section 7.1.2, no indication of bypass transition was found in the present flight experiments. On the upper side of the airfoil, transition development was triggered by the increasingly adverse pressure gradient in the region $0.45 \leq X/L_c \leq 0.6$. Disturbance amplification is clearly confined to the region, where TS modes experience the highest growth rates according to LST (cf. Chapter 5.1). On the lower side, amplification in the TS waveband was always found prior to the nonlinear disturbance evolution, even for rapid transition deflections caused by gusts (cf. Figure 7.10). The fluctuations of the pressure gradient were determined as the primary cause of the transition deflections. A penetration of the free-stream turbulence into the boundary layer, which causes a direct excitation of nonlinear boundary-layer disturbances (path D and path E in Figure 2.10), would not depend as much on the pressure gradient (Boiko et al, 2002). Nevertheless, the narrow streamwise region in the experimental setup, which is associated with the rapid disturbance growth of instability waves, makes it difficult to distinguish whether the primary TS modes are more amplified and whether other disturbance modes contribute to the transition process.

Considering the elevated turbulence intensity levels in flight through moderately turbulent conditions ($Tu \leq 0.4$ %), the question if TS waves are the only disturbances inside the airfoil boundary layer, which are able to trigger transition, is of importance. When drawing comparisons with wind-tunnel experiments, it should be recalled that the turbulence encountered in the in-flight experiments is intrinsically different to wind-tunnel turbulence of nominally similar turbulence intensity levels. In Figure 7.17 the one-dimensional energy spectra of a large-scale wind tunnel and the turbulence spectrum of a moderately turbulent flight case, shown in Figures 4.2(c) and 4.2(d), are compared. It is seen that the high-pass filtered wind-tunnel spectrum

exhibits a higher kinetic energy density for frequencies $f > 200$ Hz. For the considered airfoil boundary layer the waveband relevant for TS waves amplification is 300 Hz $\leq f \leq$ 2 kHz. In this waveband the wind-tunnel turbulence creates stronger fluctuations. The increased energy content can excite stronger boundary-layer disturbances. Furthermore, it was shown in Chapter 4.2 that the fluctuations contained in the small-scale part of the inertial subrange and in the dissipation range are locally isotropic. This is a difference to most wind-tunnel investigations, where a certain degree of anisotropy is inevitable (Westin et al, 1994). This anisotropy may influence the boundary-layer disturbance generation (Kendall, 1998). It is therefore deemed plausible that the TS wave dominated transition scenario can persist at nominally higher Tu values in atmospheric flight than under ordinary wind-tunnel conditions.

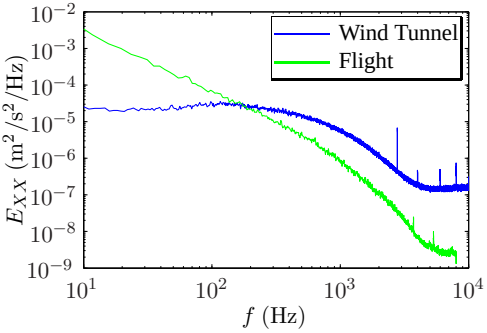

Figure 7.17.: Comparison of one dimensional turbulence spectra in flight and in a large-scale wind tunnel. Flight test: $Tu = 0.3$ % (5 - 1 kHz), cf. Table 4.1. High-pass filtered (1 Hz - 10 kHz) wind-tunnel results spectrum from Weismüller (2011): $Tu = 0.34$ %, $\bar{U}_\infty = 30$ m/s.

The presence of TS waves in all investigated cases, which is also observed by Zanin (1985) in flights at even higher turbulence intensities, is explained by the relatively weak receptivity process found on a typical laminar wing section. In Figure 7.18 the evolution of the two-dimensional N-factor curves upstream of the neutral stability point is depicted for the most amplified TS wave modes. It is seen that the curves decline significantly in the leading edge region. The blunt leading edge of the airfoil leads to a high acceleration

in this region which stabilizes the boundary layer and results in a significant attenuation of any TS waves created in the leading-edge receptivity mechanism. Assuming a transition N-factor of 11 results in difference of at least $\Delta N = 16$ to the leading edge region. Thus, the initial wave amplitude would be approximately 10^7 times smaller than the maximum fluctuation observed at the peak disturbance amplification position. Due to these small values, leading edge receptivity is not considered to significantly alter the disturbances in the airfoil boundary layer, even under increased external disturbance levels. Hence, another receptivity mechanism must be responsible for the energy transfer of the external vorticity into the TS waves, which provides the necessary phase speed and wavenumber matching (cf. Chapter 2.4.2). Local receptivity sites are avoided by the polished airfoil surface. Furthermore, the efficiency of disturbance generation by vorticity at a local site is rather low compared to acoustic forcing (Saric et al, 2002; Herr, 2003). Bertolotti (1999) considers a distributed excitation of TS-waves through turbulence. He also points out that the efficiency is weak since the vorticity does not penetrate as deep into the boundary-layer as acoustic waves, which create a Stokes layer (White et al, 2000). However, the mechanism is continuously present along the laminar boundary layer in flight through atmospheric turbulence. Nevertheless, Bertolotti (1999) deems the generation of low-frequency streaks as much more effective.

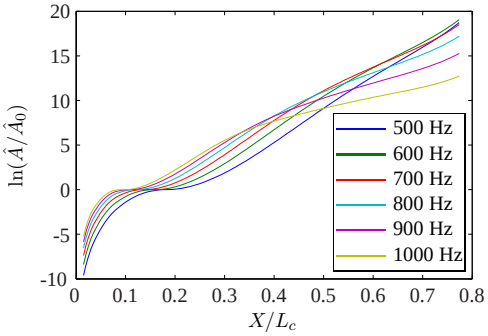

Figure 7.18.: Attenuation of two-dimensional TS waves upstream of the neutral stability point ($N = 0$).

With the considerations above, the finding of the N-factor reduction of $\Delta N \approx 3 - 4$ (compared with calm flying conditions) in Figures 7.7(a) and

7.7(b) in transient gust encounters cannot be fully explained, despite the inaccuracy introduced by the quasi-steady comparison demonstrated in Section 7.2. It has been verified that external turbulence is not able to change the mechanism completely and it has been demonstrated that Tollmien-Schlichting instability certainly plays a vital role in the considered transition process. However, the present experimental setup did not allow a detailed investigation into the topic of the possible generation of low-frequency Klebanoff modes. The conjecture of Bertolotti (1999) that external vorticity couples directly into the airfoil boundary layer and produces low-frequency streaks cannot be excluded. The streaks may modify the evolution TS waves, which were shown to be involved in the transition process under all circumstances. If streaky disturbance structures grow sufficiently, earlier secondary instabilities may be triggered from the interactions with TS waves (Boiko et al, 2002). On the other hand, streaks can also attenuate the TS modes evolution in its linear growth stages (Cossu and Brandt, 2004).

Further clarification of this question remains open for future research. Flight investigations under calm conditions and light turbulence could be conducted with specifically designed two- and three-dimensional roughness elements on the wing glove. With these deterministic receptivity sites it is possible to determine the efficiency of the coupling between atmospheric turbulence and TS waves with a specified receptivity function, such as equation (2.37). Furthermore, a method to distinguish between vortex and acoustic receptivity by using a tapered roughness strip has been developed by Herr (2003). However, care has to be taken that the wave evolution is not modified by varying pressure gradients. For the examination of the possible existence of Klebanoff modes it is suggested to use wall sensor distributions closely spaced in both, the streamwise and the spanwise, directions. At least two such array patterns would be needed in the streamwise direction to exploit the linear growth characteristics of TS waves. This may enable a differentiation between transient disturbances and TS waves via the known dispersion relation of the latter. It would be further helpful to conduct wall-normal measurements in flight (Duchmann et al, 2010), since the amplitude maximum of the Klebanoff modes is usually found at half of the boundary-layer thickness (Westin et al, 1998).

8. Conclusions

The aerodynamic behavior of a NLF airfoil was studied under calm reference conditions and in flight through light and moderate atmospheric turbulence. All flight test results were obtained in gliding flight at low angles of attack corresponding to cruise airspeeds. A theoretical framework was developed and the important flow mechanisms were identified to provide the necessary background for the experimental investigation. The considered two-dimensional boundary-layer framework enabled a separate treatment of the inviscid outer flow and facilitated comparisons of the experimental results with analytical and numerical solutions.

A comprehensive in-flight measurement system was developed to meet the needs of the investigation. The unsteady and random boundary conditions encountered in flight through turbulence required a completely synchronized measurement system and high data rates. Verifications of the experimental results could be obtained by comparisons with advanced two-dimensional airfoil theory. Therefore, numerical procedures were implemented to describe unsteady airfoil effects and to determine the linear stability characteristics of the time-dependent boundary layer. Combined experimental and numerical methods were developed to enable the recalculation of flight cases. Three comprehensive flight test campaigns were conducted with two different experimental setups. The distinct measurement instruments employed in these campaigns complemented one another in their intrinsic strengths. Jointly, they enabled deeper insights into the acting mechanisms.

The flight investigation was split into three parts. A brief summary of each part will be given in the following paragraphs, before referring directly to the key questions of the literature review in Chapter 1.3. The major insight obtained in this study will be presented after a repetition of the corresponding key question.

The oncoming flow disturbances were characterized in an investigation of atmospheric turbulence with emphasis on the eddy length scales relevant for airfoil aerodynamics. Characteristic turbulence categories were defined for the present study. In particular, the small-scale end of the inertial subrange and the dissipation range of atmospheric turbulence were considered. These

turbulent velocity fluctuations potentially influence the transition process of the wing boundary layer. For the subsequent airfoil investigation, characteristic disturbance categories were defined and an unambiguous description of the atmospheric turbulence state in flight experiments was proposed.

The investigation of boundary-layer transition under moderately turbulent conditions required a comprehensive understanding of the transition process under ideal, calm conditions. Approximately half of the test flights were conducted under calm conditions to verify the transition characteristics of both sides of the investigated wing section. On the upper side of the airfoil, strong boundary-layer disturbance growth was observed in a narrow streamwise region for all angles of attack. The constancy of the transition position for the investigated angles is explained by a strongly increasingly adverse pressure gradient in this specific region which drives the rapid amplification of Tollmien-Schlichting (TS) waves. On the lower side an almost constant pressure gradient governs the frequency-selective growth or attenuation of TS waves which enables laminar flow over a major part of the surface. However, the pressure gradient, and hence the transition process, is highly sensitive to angle-of-attack variations. By using Fourier analysis and determining disturbance propagation velocities, the dominant role of TS waves as transition-triggering disturbances was verified under calm conditions. To enable comparisons with other flight experiments and wind-tunnel studies, transition N-factors were determined. For the lower side values of $N_T \geq 13$ were consistently found, whereas they were slightly reduced for the upper side ($N_T \approx 11$). A spanwise row of closely distributed hot-film sensors enabled the investigation of the three-dimensional aspects of the transition process and provided new insight into the weakly nonlinear stage.

In-flight investigations of atmospheric turbulence are complicated by the random nature of the boundary conditions. Turbulent gusts inevitably lead to forces which act on the wing and result in motions of the aircraft. Flight dynamic eigenmotions and unsteady aerodynamic effects need to be considered. High data rates and pilot-accuracy requirements limited the maximum recording time during in-flight measurements to 20 s. Therefore, the important processes observed in the three flight test campaigns were most conveniently discussed by the examination of case studies. These case studies demonstrated the results of typical flight measurements, which encompassed all relevant effects. Case study 1 provided a direct comparison of the differences between flights through calm and moderately turbulent conditions, whereas case study 2 focussed on specific details of the boundary-layer transition process under moderately turbulent conditions. The boundary condi-

tions were presented explicitly to enable comparison with the inviscid and viscous airfoil response. It was verified that the pressure forces on the airfoil, caused by gusts, lead to unsteady airfoil effects. The continuous forcing creates a highly time-variable pressure distribution, which in turn changes the boundary-layer development. The time dependence is transferred to the boundary layer, which itself presents a dynamical system with a characteristic response. Furthermore, the unsteady boundary conditions lead to significant streamwise fluctuations of transition. On the upper side transition occurred within a narrow streamwise region ($\Delta X/L_c \leq 0.15$), whereas upstream transition deflections $\Delta X/L_c \geq 0.3$ for short time periods ($t \leq 0.5$ s) were found on the lower side. The unsteady boundary-layer behavior on the lower side was modeled numerically. Light was shed into the linear stability properties of temporally distorted boundary-layer profiles. The study was completed by a discussion on the implications of increased small-scale turbulence levels on boundary-layer transition in the conducted flight experiments.

- What are the implications of the spectral composition of atmospheric turbulence?

Atmospheric turbulence is intrinsically different to wind-tunnel turbulence. Most of the energy is contained at length scales larger than the chord length of the investigated wing section. Larger eddies act as gusts and create an unsteady forcing of the wing. As the aircraft responds with motions, a detailed investigation of larger scale turbulence is not possible. Yet, the spectral properties of the important small scale turbulence were examined closely. In accordance with the flight investigation of Sheih et al (1971), it was shown that the atmospheric turbulence can be considered isotropic at scales corresponding to the lower end of the inertial subrange and within the dissipation range of the energy spectrum. This range is particularly important for boundary-layer investigations. Kendall (1998) points out that grid-generated turbulence in wind tunnels inevitably contains a residual anisotropy, which can affect the generation of boundary-layer disturbances. In contrast, the high Reynolds numbers of atmospheric turbulence practically ensures isotropic conditions at small scales. Furthermore, it is important to note that the frequency range of TS waves observed in the laminar airfoil boundary layer in large part includes the dissipation range of atmospheric turbulence. The velocity fluctuations of atmospheric turbulence have lost most of their kinetic energy in the cascade process before they become relevant for the laminar-turbulent transition process of the wing boundary layer.

- Is it appropriate to consider the inviscid outer flow to be quasi-steady?

Unsteady effects occur in flight through moderate turbulence when gusts are encountered. Deviations of $\Delta C_l > 0.05$ from the steady lift curve are typical. In case study 1 it was shown that the harmonic gust solution of Sears (1941) with the parameters $\kappa = 0.3$ and $W'_g = 1.5$ m/s tightly enclosed all events in the experimental C_l-α distribution. In terms of the boundary-layer behavior, the inviscid effects influence the boundary conditions. The time-varying pressure gradient dictates the boundary-layer development, which is sensitive to small changes. If accurate calculations of the time dependent boundary-layer evolution are required, the impeded and phase-shifted inviscid outer flow should be taken into account.

- Is there any new insight into the weakly nonlinear stages of transition under calm conditions?

Generally, very high transition N-factors were observed under calm conditions, which even approach or exceed the bound of $N = 13$ predicted by Luchini (2009) for a flat plate. This enables elongated linear and weakly non-linear TS wave evolution. All modal combinations, which are amplified according to linear stability theory (LST), were shown to exist in the experiments as they produced the characteristic TS wave humps in frequency-wavenumber spectra. When reaching a certain amplitude, oblique waves and their nonlinear interactions with the two-dimensional fundamental waves were shown to be particularly important on the two-dimensional wing section. Evidence was provided, that the generation of 'difference modes' from wave modes contained in the fundamental TS wave band is indeed a candidate for providing seeds for subsequent detuned subharmonic resonance. A linear stability computation showed that the experimentally observed low-frequency disturbances, which accumulated at spanwise wavenumbers $k_z \approx \pm 200$ m^{-1}, fulfilled the criterion of equal phase speeds with the most amplified two-dimensional TS modes. According to Wu et al (2007) this is a necessary criterion for resonant growth. Thus, strong similarities of the observed transition process with the wind-tunnel experiments of de Paula et al (2013) were asserted. They considered the described mechanism as the 'most likely route to the laminar-turbulent transition in two-dimensional boundary layers of airfoils with a long extent of laminar flow' under calm flying conditions.

- What is the role of the unsteady boundary-layer development when flying through turbulence?

The time-variable boundary conditions caused by turbulent gusts can lead to an unsteady boundary layer development. Characteristically, the boundary-layer response lags behind these short-time changes. Moreover, significant unsteady distortions of the instantaneous boundary-layer profiles result, especially in the downstream part of the airfoil. The unsteady boundary-layer effects intrinsically depend on the length of the laminar run. The distortions change the linear stability properties of the flow and promote a higher growth of TS waves. The numerical investigation of the airfoil response to a harmonic vertical gust excitation ($\kappa = 0.2$, $W'_{\mathrm{g}} = 1$ m/s) yielded an envelope N-factor difference of $\Delta N_{\mathrm{env}} \approx 2.5$ on the lower side of the airfoil.

- Does the transition mechanism change in flight through zones of increased turbulent forcing?

A direct bypass transition, created by convective boundary-layer disturbances, was not found in the present study. It was demonstrated that the upstream transition deflections were, in all investigated cases, the result of rapid changes in the pressure gradient. These changes promoted strong linear growth or attenuation of TS waves. TS waves were shown to be involved in the transition process under all circumstances by means of short-time Fourier transforms and wavelet analysis. The vital role of TS waves is also highlighted by the pressure gradient sensitivity of the observed transition process, which clearly excludes the possibility of bypass transition. In accordance with the considerations of Bertolotti (1999), it is assumed that the TS waves are created in a distributed vortex receptivity process, which is relatively weak compared with acoustic receptivity (Dietz, 1999; Herr, 2003). Nevertheless, in comparison with the findings under calm conditions, quasi-steady N-factor computation indicated a reduction of the transition N-factor on the lower side of the airfoil. For downstream transition deflections, which are caused by upward directed gusts, this behavior can partially be explained by the described distortions of the unsteady boundary-layer profiles. The distorted profiles are more unstable and promote higher amplification of two-dimensional TS waves. For upstream transition deflections, the distortions are smaller compared with the quasi-steady reference. Thus, the N-factor reduction of $\Delta N \approx 2-3$ can only be explained by an elevated boundary-layer disturbance level created by small-scale turbulence. The question whether this behavior results solely from higher initial amplitudes of TS waves or

whether Klebanoff modes also play a role in the mechanism cannot be answered with the present experimental setup. Further clarification of this question remains open for future research.

- What are the implications for NLF airfoil design?

The unsteadiness of the inviscid outer flow leads to an attenuated response of the pressure distribution compared with a quasi-steady reference. Therefore, an airfoil design based on quasi-steady potential flow calculations of the gust response overemphasizes the variations of the boundary conditions for subsequent boundary-layer computations. The boundary-layer response to time-varying boundary-conditions can depart significantly from quasi-steady expectations, especially if TS waves amplify gradually over large streamwise distances. Characteristic time scales for transition deflections, caused by upward or downward directed gusts, were of the order of $0.2\ \mathrm{s} \leq \Delta t \leq 1\ \mathrm{s}$, in which the airfoil traveled between 6 and 30 chord lengths. The relevance of unsteady airfoil and boundary-layer effects can be assessed by the simple relations for the reduced frequency κ and the boundary-layer frequency parameter $\kappa_\delta(x)$. For modern sailplane airfoils laminar runs of more than 90 % have been achieved on the lower side. In this respect, it is valuable to consider the implications of the observed streamwise transition deflections. For wind-turbine applications these considerations may be even more important, as the unsteady effects generally increase with chord length. The elongated laminar runs can only be achieved by allowing controlled growth and attenuation of TS-waves in the upstream part of the airfoil (Satorius, 2007). Therefore, the growth is limited to a predefined N-factor threshold, which is lower than the expected transition N-factor. Designers should be aware of the findings of the present study, which indicate a transition N-factor reduction in transient events caused by moderate turbulence. Furthermore, it should be assessed in future investigations whether weakly nonlinear wave interactions are promoted by increased atmospheric turbulence levels and may therefore affect design considerations.

In any case, the importance of the lower edge of the laminar bucket in the lift-drag diagram should be reassessed, incorporating the notion that random vertical gusts are continuously present in flight through moderate atmospheric turbulence. It is to be verified for the individual airfoil design if angle-of-attack deviations of $1^\circ \leq \alpha' \leq 3^\circ$ from the design point can be detrimental for the overall performance in cruise flight. Slight efficiency reductions under ideal conditions may be outweighed by a better performance under real operating conditions.

Bibliography

Abbas A, de Vicente J, Valero E (2013) Aerodynamic technologies to improve aircraft performance. Aerospace Science and Technology 28:100–132, DOI 10.1016/j.ast.2012.10.008

Abbot IH, Von Doenhoff AE (1959) Theory of Wing Sections, Dover, Mineola, chap 4 Theory of Thin Wing Sections, pp 65–79

Abdel-Rahman A, Tropea C, Slawson P, Strong A (1987) On temperature compensation in hot-wire anemometry. Measurement Science and Technology 20:315–319, DOI 10.1088/0022-3735/20/3/017

Akima H (1970) A new method of interpolation and smooth curve fitting based on local procedures. Journal of the Association for Computing Machinery 17:589–602, DOI 10.1145/321607.321609

Althaus D (1996) Niedriggeschwindigkeitsprofile, Vieweg Verlag, Braunschweig, chap Gewölbte Profile ohne Klappen, pp 126–128

Arnal D (1992) Boundary-layer transition: Prediction, application to drag reduction. AGARD Report ADP006968(786)

Arnal D, Casalis G, Houdeville R (2008) Practical transition prediction methods: Subsonic and transonic flows. NATO RTO-EN-AVT-151, Paper presented during the AVT-151 RTO AVT/VKI Lecture Series held at the von Karman Institute, Rhode St. Genèse, Belgium, 09-12 June 2008.

Batchelor GK (1950) The application of the similarity theory of turbulence to atmospheric diffusion. Quarterly Journal of the Royal Meteorological Society 76:133–146, DOI 10.1002/qj.49707632804

Baumann M (2013) Manual of the System Low-Noise Miniature CTA System. Ingenieurbüro Dr. Baumann

Bendat J, Piersol A (2010) Random Data Analysis and Measurement Procedures, 4th edn. Wiley, Hoboken, NJ

Bernardini C, Benton S, Chen J, Bons J (2013) Investigation of pulsed blowing control mechanism using wavelet analysis and accoustic excitation. AIAA Paper AIAA-2013-0850

Bertolotti FP (1997) Response of the blasius boundary layer to free-stream vorticity. Physics of Fluids 9:2286–2299, DOI 10.1063/1.869350

Bertolotti FP (1999) Effect of atmospheric turbulence on a laminar boundary layer. Technical Soaring 25(2):154–159, presented at the 26th OSTIV Congress, Bayreuth, Germany

Bertolotti FP, Kendall JM (1997) Response of the blasius boundary layer to controlled free-stream vortices of axial form. AIAA Paper 97-2018

Betz A (1912) Ein Beitrag zur Erklärung des Segelflugs. Zeitschrift für Flugtechnik und Motorluftschiffahrt 21:269–272

Birnbaum W (1924) Das ebene Problem des schlagenden Flügels. Zeitschrift für angewandte Mathematik und Mechanik (ZAMM) 4:277–292, DOI 10.1002/zamm.19240040401

Bisplinghoff RL, Holt A, Halfman RL (1996) Aeroelasticity, Dover, Mineola, chap Chapter 5.6 Thin Airfoils Oscillating in Incompressible Flow, pp 251–281

Boermans LLM, Selen HJW (1981) On the design of some airfoils for sailplane application. Delft University of Technology Report LR-326

Boiko A, Grek G, Dovgal A, Kozlov V (2002) The Origin of Turbulence in Near-Wall Flows. Springer, Berlin

Boiko AV, Westin KJA, Klingmann BGB, Kozlov VV, Alfredsson PH (1994) Experiments in a boundary layer subjected to free stream turbulence. part 2. the role of ts-waves in the transition process. Journal of Fluid Mechanics 281:219–245

Borodulin I V, Kachanov Y, Koptsev DB, Roschektayev AP (2002) Resonant interactions in APG boundary layer: II. Detuned resonances. Journal of Turbulence 3, DOI 10.1088/1468-5248/3/1/063

Bradshaw P (1971) An Introduction to Turbulence and its Measurement. Pergamon Press, Oxford

Breuer KS, Cohen J, Haritonidis JH (1997) The late stages of transition induced by a low-amplitude wavepacket in a laminar boundary layer. Journal of Fluid Mechanics 340:395–411

Brockhaus R, Alles W, Luckner R (2011) Flugregelung. Springer, Berlin

Bronstein I, Semendjajew K, Musiol G, Mühlig H (2005) Taschenbuch der Mathematik. Harri Deutsch Verlag, Frankfurt am Main

Bruun HH (1995) Hot-Wire Anemometry, Principles and Signal Analysis. Oxford University Press, Oxford

Bruun HH, Nabhani N, Fardad AA, Khan MA, Hogarth E (1990) Calibration and analysis of X hot-wire probe signals. Measurement Science and Technology 1:782–785, DOI 10.1088/0957-0233/1/8/019

Bushnell D (1990) Instabilities and Transition, Springer, Berlin, chap Notes on Initial Disturbance Fields for the Transition Problem, pp 217–232. ICASE/NASA LaRC

Buter TA, Reed HL (1994) Boundary layer receptivity to free stream vorticity. Physics of Fluids 6:3368–3379, DOI 10.1063/1.868395

Canuto C, Hussaini MY, Quarteroni A, Zang TA (2007) Spectral Methods, Evolution to Complex Geometries and Applications to Fluid Dynamics. Springer, Berlin

Carpenter AL (2009) In-flight receptivity experiments on a 30-degree swept-wing using micron-sized discrete roughness elements. PhD thesis, Texas A&M University

Carpenter AL, Saric W, Reed HL (2010) Roughness receptivity studies in a 3-D boundary layer - flight tests and computations. In: Schlatter P, Henningson D (eds) 7th IUTAM Symposium on Laminar-Turbulent Transition, IUTAM, Springer, Berlin, IUTAM Bookseries, vol 18, pp 105–110, DOI 10.1007/978-90-481-3723-7_15

Cebeci T (1977) Calculation of unsteady two-dimensional laminar and turbulent boundary layers with fluctuations in external velocity. Proceedings of the Royal Society A 225-238(1681), DOI 10.1098/rspa.1977.0096

Cebeci T (1984) Calculation of boundary layers of oscillating airfoils. NASA TM 85943:1–24

Cebeci T, Bradshaw P (1977) Momentum Transfer in Boundary Layers. McGraw-Hill Higher Education, New York

Cebeci T, Cousteix J (2005) Modeling and Computation of Boundary-Layer Flows. Springer, Berlin

Cebeci T, Carr LW, Jang HM (1989) An interactive boundary-layer procedure for oscillating airfoils including transition effects. AIAA Paper AIAA-89-0020

Cebeci T, Platzer M, Chen H, Chang KC, Shao JP (2005) Analysis of Low-Speed Unsteady Airfoil Flows. Springer, Berlin

Cohen J, Breuer KS, Haritonidis JH (1991) On the evolution of a wave packet in a laminar boundary layer. Journal of Fluid Mechanics 225:575–606

Cossu C, Brandt L (2004) On Tollmien-Schlichting-like waves in streaky boundary layers. European Journal of Mechanics B/Fluids 23:813–833, DOI 10.1016/j.euromechflu.2004.05.001

Craik ADD (1971) Non-linear resonant instability in boundary layers. Journal of Fluid Mechanics 50(2):393–413, DOI 10.1017/S0022112071002635

Crouch JD (1992a) Localized receptivity of boundary layers. Physics of Fluids 4:No. 7

Crouch JD (1992b) Non-localized receptivity of boundary layers. Journal of Fluid Mechanics 244:567–581, DOI 10.1017/S0022112092003197

Crouch JD (2000) Variable N-factor method for transition prediction in three-dimensional boundary layers. AIAA Journal 38(2):211–216

Damion JP (1994) Means of dynamic calibration for pressure transducers. Metrologia 30:743–746

Danabasoglu G, Biringen S (1989) A Chebyshev matrix method for spatial modes of the Orr-Sommerfeld equation. NASA contractor report 4247:1–13

Denissen NA (2011) Roughness-induced transient growth: Continuous-spectrum receptivity and secondary instability analysis. PhD thesis, Texas A&M University

Deyhle H, Bippes H (1996) Disturbance growth in an unstable three-dimensional boundary layer and its dependence on environmental conditions. Jounal of Fluid Mechanics 316:73–113

Dietrich A (2011) Development and implementation of a viscous-inviscid interaction method for unsteady airfoil analysis. Master Thesis, TU Darmstadt

Dietz AJ (1999) Local boundary-layer receptivity to a convected free-stream disturbance. Journal of Fluid Mechanics 378:291–317, DOI 10.1017/S0022112098003243

Downs R, White EB (2013) Free-stream turbulence and the development of cross-flow disturbances. Journal of Fluid Mechanics 735:347,380, DOI 10.1017/jfm.2013.484

Drazin PG, Reid WH (1981) Hydrodynamic Stability. Cambridge University Press, Cambridge

Drela M (1989) Xfoil: An analysis and design system for low Reynolds number airfoils. In: Mueller T (ed) Low Reynolds Number Aerodynamics, Lecture Notes in Engineering, vol 54, pp 1–12, DOI 10.1007/978-3-642-84010-4_1, program version 6.96

Duchmann A (2012) Boundary-layer stabilization with dielectric barrier discharge plasmas for free-flight application. PhD thesis, TU Darmstadt

Duchmann A, Reeh A, Quadros R, Kriegseis J, Tropea C (2010) Linear stability analysis for manipulated boundary-layer flows using plasma actuators. In: Schlatter P, Henningson D (eds) 7th IUTAM Symposium on Laminar-Turbulent Transition, IUTAM, Springer, Berlin, IUTAM Bookseries, vol 18, pp 153–158, DOI 10.1007/978-90-481-3723-7_23

Erb P (2002) Untersuchung der Grenzschichttransition im Flugversuch. PhD thesis, Technische Universität Darmstadt

Etkin B (1981) Turbulent wind and its effect on flight. AIAA Journal 18(5):327–345, DOI 10.2514/3.57498

Etling D (2008) Theoretische Meteorologie. Springer, Berlin

Evans RL (1988) Unsteady laminar boundary layers subject to standing wave or travelling wave freestream fluctuations. Tech. Rep. CUED/A-Turbo/TR 124, Univ. Engineering Dept., Cambridge, England

Evans RL (1989) Computation of unsteady laminar boundary layers subject to traveling-wave freestream fluctuations. AIAA Journal 27:1644–1646, DOI 10.2514/3.10313

Fanning JA (2012) In-flight measurements of freestream atmospheric turbulence intensities. Master Thesis, Texas A&M

Farge M (1992) Wavelet transforms and their applications to turbulence. Annual Review of Fluid Mechanics 24:395–457

Fisher D, Horstmann KH, Riedel H (2003) Flight test measurement techniques for laminar flow. RTO AGARDograph 300

Fransson JHM, Matsubara M, Alfredsson PH (2005) Transition induced by free-stream turbulence. Journal of Fluid Mechanics 527:1–25, DOI 10.1017/S0022112004002770

Freymuth P (1977) Frequency response and electronic testing for constant-temperature hot-wireire anemometers. Journal of Physics E: Scientific Instruments 10(7):705–710, DOI 1088/0022-3735/10/7/012

Freymuth P, Fingerson L (1997) Hot-wire anemometry at very high frequencies: Effect of electronic noise. Measurement Science and Technology 8:115–116, DOI 10.1088/0957-0233/8/2/001

Fujino M, Yoshizaki Y, Kawamura Y (2003) Natural-laminar-flow airfoil development for a lightweight business jet. Journal of Aircraft 40:609–615, DOI 10.2514/2.3145

Fung YC (2008) An Introduction to the Theory of Aeroelasticity, Dover, Mineola, chap 8 Transient Loads, Gusts, pp 272–305

Gaster M, Grant I (1975) A theoretical model for the development of a wave packet in a laminar boundary-layer. Proceedings of the Royal Society A 347:271–289

Hartmann T (2013) Development of a boundary layer method for computing airfoil flows under varying onflow conditions. Master Thesis, TU Darmstadt In German

Henningson DS, Lundbladh A, Johansson AV (1993) A mechanism for bypass transition from localized disturbances in wall-bounded shear flows. Journal of Fluid Mechanics 250:169–207, DOI 10.1017/S0022112093001429

Herbert T (1988) Secondary instability of boundary layers. Annual Review of Fluid Mechanics 20:487–526, DOI 10.1146/annurev.fl.20.010188.002415

Herbert T, Stuckert G, Esfahian V (1993) Effects of free-stream turbulence on boundary-layer transition. AIAA Paper AIAA-93-0488

Herr S (2003) Experimental investigation of airfoil boundary-layer receptivity and a method for the characterization of the relevant free-stream disturbances. PhD thesis, Universität Suttgart

Hess JL, Smith AMO (1967) Calculation of potential flow about arbitrary bodies. Progress in Aerospace Sciences 8:1–138

Hill PG, Stenning AH (1960) Laminar boundary layers in oscillatory flow. Journal of Basic Engineering 82(2):593–607, DOI 10.1115/1.3662672

Hoblit (1988) Gust Loads on Aircraft: Concepts and Applications. AIAA Education Series, AIAA, DOI 10.2514/4.861888

Holmes BJ, Obara CJ (1992) Natural Laminar Flow and Laminar Flow Control, Springer, Berlin, chap Flight Research on Natural Laminar Flow Applications, pp 73–142. ICASE/NASA LaRC Series, DOI 10.1007/978-1-4612-2872-1_3

Horstmann KH, Quast A, Redeker G (1989) Flight and wind-tunnel investigations on boundary-layer transition. Journal of Aircraft 27(2):146–150, DOI 10.2514/3.45910

Hudgins L, Friehe C, Mayer M (1993) Wavelet trransforms and atmospheric turbulence. Physical Review Letters 71:3279–3282

Ikonnikova O (2013) Development of a system for the detection and the analysis of flight control inputs for the research aircraft G109b. Bachelor Thesis, TU Darmstadt . In German

ISA (2002) A guide for the dynamic calibration of pressure transducers. Tech. Rep. ISA-37.16.01-2002., The Instrumentation, Systems, and Automation Society

Jain M (2010) Aeroelastische Modellierung eines Klappenprofils zur passiven Böenlastminderung. Bachelor Thesis, TU Darmstadt

Jategaonkar RV (2006) Flight Vehicle System Identification: A Time Domain Methodology, Progress in Aeronautics and Astronautics, vol 216. AIAA, Reston, VA

Joslin RD (1998) Aircraft laminar flow control. Annual Review of Fluid Mechanics 30:1–29, DOI 10.1146/annurev.fluid.30.1.1

Kachanov Y (1994) Physical mechanisms of laminar-boundary-layer transition. Annual Review of Fluid Mechanics 26:411–482, DOI 10.1146/annurev.fl.26.010194.002211

Kachanov Y (2000) Three-dimensional receptivity of boundary layers. European Journal of Mechanics B/Fluids 19(5):723Ű744, DOI 10.1016/S0997-7546(00)90102-X

Kachanov Y, Levchenko VY (1984) The resonant interaction of disturbances at laminar-turbulent transition in a boundary layer. Jounal of Fluid Mechanics 138:209–247

Katz J, Plotkin A (2001) Low-Speed Aerodynamics, Cambridge University Press, Cambridge, chap 3 General Solution of the Incompressible, Potential Flow Equations, pp 44–74

Katzmayer R (1922) Über das Verhalten der Flügelflächen bei periodischen Änderungen der Geschwindigkeitsrichtung. Zeitschrift für Flugtechnik und Motorluftschiffahrt 13:80–82, translation available (NACA TM-147)

Keller HB (1978) Numerical methods in boundary-layer theory. Annual Review of Fluid Mechanics 10:417–433, DOI 10.1146/annurev.fl.10.010178.002221

Kendall JM (1984) Experiments on the generation of Tollmien-Schlichting waves in a flat plate boundary layer by weak freestream turbulence. AIAA Paper AIAA-84-0011

Kendall JM (1985) Experimental investigation of disturbances produced in a pre-transitional laminar boundary layer. AIAA Paper AIAA-85-1695, DOI 10.2514/619851695

Kendall JM (1990) Boundary layer receptivity to freestream turbulence. AIAA Paper 90-1504

Kendall JM (1998) Experiments on boundary-layer receptivity to free-stream turbulence. AIAA Paper AIAA-98-0530, DOI 10.2514/6.1998-530

Kimberlin RD (2003) Flight Testing of Fixed-Wing Aircraft, AIAA, Reston, chap 3 Airspeed Theory and Calibration, pp 29–38

Klähn J (2013) Manual for the 64-Channel Constant Temperature Hotfilm System. Konstruktionsbüro Joachim Klähn

Klebanoff PS, Tidstrom KD, Sargent LM (1962) The three-dimensional nature of boundary-layer instability. Journal of Fluid Mechanics 12(2):1–34

Köhler M (2011) Development and implementation of a method for solving the laminar boundary-layer equations in airfoil flows. Master Thesis, TU Darmstadt URL `http://tuprints.ulb.tu-darmstadt.de/3173/`, http://tuprints.ulb.tu-darmstadt.de/3173/

Kolmogorov AN (1941) The local structure of turbulence in incompressible viscous fluid for very large reynolds numbers. Proceedings of the USSR Academy of Sciences 30:299–303, DOI 10.1098/rspa.1991.0075, In Russian, translated into English by V. Levin. Proceedings of the Royal Society A 434 (1991): 9-13

Lambie B (2011) Aeroelastic investigation of a wind turbine airfoil with self-adaptive camber. PhD thesis, TU Darmstadt, http://tuprints.ulb.tu-darmstadt.de/2769/

Landahl MT (1980) A note on an algebraic instability of inviscid parallel shear flows. journal of Fluid Mechanics 98:243–251, DOI 10.1017/S0022112080000122

Lee S (2012) Nonlinear interaction of wind-driven oblique surface waves and parametric growth of lower frequency modes. Journal of Fluid Mechanics 707:150–190

Leib SJ, Wundrow DW, Goldstein ME (1999) Effect of free-stream turbulence and other vortical disturbances on a laminar boundary layer. Journal of Fluid Mechanics 380:169–203

Leishman JG, Rycroft, M J Shyy W (2006) Principles Helicopter Aerodynamics, 2nd edn, Cambridge University Press, Cambridge, chap Ch. 8 Unsteady Airfoils, pp 423–523

Lekakis (1996) Calibration and signal interpretation for single and multiple hot-wire/hot-film probes. Measurement Science and Technology 7:1313–1333, DOI 10.1088/0957-0233/7/10/004

Lighthill MJ (1954) The response of laminar skin friction and heat transfer to fluctuations in the stream velocity. Proceedings of the Royal Society A 224(9):1–23, DOI 10.1098/rspa.1954.0137

Lighthill MJ (1958) On displacement thickness. Journal of Fluid Mechanics 4(4):383–392, DOI 10.1017/S0022112058000525

Loehrke R, Morkovin M, Fejer AA (1975) Review - transition in nonreversing oscillating boundary layers. Journal of Fluids Engineering 97:534–548, DOI 10.1115/1.3448111

Luchini P (2009) A thermodynamic lower bound on the level of transition-triggering disturbances. In: Schlatter P, Henningson D (eds) 7th IUTAM Symposium on Laminar-Turbulent Transition, Stockholm, Sweden, IUATAM, Springer, Berlin, IUTAM Bookseries, vol 28, pp 11–18

MacCready PBJ (1962a) The inertial subrange of atmospheric turbulence. Journal of Geophysical Research 67(3):1051–1059, DOI 10.1029/JZ067i003p01051

MacCready PBJ (1962b) Turbulence measurements by sailplanes. Journal of Geophysical Research 67(3):1041–1050, DOI 10.1029/JZ067i003p01041

MacCready PBJ (1964) Standardization of gustiness values from aircraft. Journal of Applied Meteorology 3:439–449, DOI 10.1175/1520-0450(1964)003<0439:SOGVFA>2.0.CO;2

McCroskey WJ (1973) Inviscid flowfield of an unsteady airfoil. AIAA Journal 11(8):1130–1137, DOI 10.2514/3.50558

McCroskey WJ (1982) Unsteady airfoils. Annual Review of Fluid Mechanics 14:285–311, DOI 10.1146/annurev.fl.14.010182.001441

Medeiros MAF, Gaster M (1999) The production of subharmonic waves in the nonlinear evolution of wavepackets in boundary layers. Journal of Fluid Mechanics 399:301–318

Metzger M, McKeon B, Holmes H (2007) The near-neutral atmospheric surface layer: Turbulence and non-stationarity. Philosophical Transactions of the Royal Society A 365(1852):859–876

Mish P, Devenport W (2003) An experimental investigation of unsteady surface pressure on an airfoil in turbulence. Tech. Rep. 20030032963, NASA

Nishioka M, Morkovin M (1986) Boundary-layer receptivity to unsteady pressure gradients: Experiments and overview. Journal of Fluid Mechanics 171:219–261

Nitsche A W; Brunn (2006) Strömungsmesstechnik. Springer, Berlin

Nitsche W, Suttan J, Becker S, Erb P, Kloker M, Stemmer C (2001) Experimental and numerical investigations of controlled transition in low-speed free flight. Aerospace Science and Technology 5:245–255, DOI 10.1016/S1270-9638(01)01105-1

Nobach H, Tropea C (2012) A statistical method for transforming temporal correlation functions from one-point measurements into spatial and spatio-temporal statistics. Experiments in Fluids 53:1815–1821, DOI 10.1007/s00348-012-1392-3

Obremski H, Fejer A (1967) Transition in oscillating boundary layer flows. Journal of Fluid Mechanics 29:93–111

Obremski H, Morkovin M (1969) Application of quasi-steady stability model to periodic boundary-layer flows. AIAA Journal 7(7):1298–1301

Patel MH (1975) On laminar boundary layers in oscillatory flow. Procedings of the Royal Society A 347(1648):99–123, DOI 10.1098/rspa.1975.0200

de Paula IB, Würz W, Krämer E, Borodulin V, Kachanov YS (2013) Weakly nonlinear stages of boundary-layer transition initiated by modulated Tollmien-Schlichting waves. Journal of Fluid Mechanics 792:571–615

Payne FR, Lumley JL (1966) One-dimensional spectra derived from an airborne hot-wire anemometer. Quarterly Journal of the Royal Meteorological Society 92:397–401

Peltzer I (2004) Flug- und windkanalexperimente zur räumlichen entwicklung von tollmien-schlichting-instabilitäten in einer flügelgrenzschicht. PhD thesis, Technische Universität Berlin

Peltzer I (2008) Comparative in-flight and wind tunnel investigation of the development of natural and controlled disturbances in the laminar boundary layer of an airfoil. Experiments in Fluids 44:961–972, DOI 10.1007/s00348-007-0455-3

Peltzer I, Nitsche W (2004) Recent Results in Laminar-Turbulent Transition, Notes on Numerical Fluid Mechanics and Multidisciplinary Design, vol 86, Springer, Berlin, chap Experimental Investigations of Natural and Controlled Transition on a Laminar Flow Airfoil, pp 269–280

Perls TA, Miles DO, Wilner LB (1960) Sinusoidal pressure generator with wide amplitude and frequency ranges. The Journal of the Acoustical Society of America 32:274–281

Pope SB (2000) Turbulent Flows, Cambridge University Press, Cambridge, chap 6 The scales of turbulent motion

Prandtl L (1904) über Flüssigkeitsbewegung bei sehr kleiner Reibung. In: Verhandlungen des III. Internationalen Mathematiker-Kongresses, Teubner, Heidelberg, pp 484–491

Pruis MJ, Delisi P, N AN, H PF (2013) Atmospheric turbulence estimates from estimates from a pulsed lidar. AIAA Paper 2013-0512, DOI 10.2514/6.2013-512

Reed H, Saric W (1996) Linear stability applied to boundary layers. Annual Review of Fluid Mechanics 389-428

Reeh AD (2008) Development and implementation of a method for linear stability analysis of natural and manipulated boundary-layer flows. Bachelor Thesis, TU Darmstadt

Reshotko E (2008) Paths to transition in wall layers. NATO RTO-AVT-151 . Paper presented during the AVT-151 RTO AVT/VKI Lecture Series held at the von Karman Institute, Rhode St. Genèse, Belgium, 09-12 June 2008.

Riedel H, Sitzmann S (1998) In-flight investigation of atmospheric turbulence. Aerospace Science and Technology 5:301–319, DOI 10.1016/S1270-9638(98)80007-2

Riegels F (1949) Das Umströmungsproblem bei inkompressiblen Potentialströmungen. Ingenieur-Archiv 17(2):94–106, DOI 10.1007/BF00571966

Romano GP, Ouellette NT, Xu H, Bodenschatz E, Steinberg V, Meneveau C, Katz J (2007) Springer Handbook of Experimental Fluid Mechanics, Springer, Berlin, chap Measurements of Turbulent Flows, pp 746–789

Runyan LJ, George-Falvy D (1979) Amplification factors corresponding to transition on an unswept wing in free flight and on a swept wing in wind tunnel. AIAA Paper AIAA-79-0267

Saddoughi S, Veeravalli SV (1994) Local isotropy in turbulent boundary layers at high Reynolds number. Journal of Fluid Mechanics 268:333–372, DOI 10.1017/S0022112094001370

Saric W (2007) Handbook of Experimental Fluid Mechanics, Springer, Berlin, chap 12.3 Boundary-Layer Stability and Transition, pp 886–896

Saric W, Levchenko VY (1984) Forced and unforced subharmonic resonance in boundary-layer transition. AIAA Paper AIAA-84-0007:1–9, DOI 10.2514/6.1984-7

Saric W, Reed H, Kerschen E (2002) Boundary-layer receptivity to freestream disturbances. Annual Review of Fluid Mechanics 34:291–319, DOI 10.1146/annurev.fluid.34.082701.161921

Saric W, Carpenter AL, Reed H (2011) Passive control of transition in three-dimensional boundary layers, with emphasis on discrete roughness elements. Proceedings of the Royal Society A 369:1352–1364, DOI 10.1098/rsta.2010.0368

Satorius D (2007) Experimental investigation of weakly nonlinear interactions of instability waves in a non self-similar boundary layer on an airfoil. PhD thesis, Universität Stuttgart

Schlichting H (1982) Grenzschicht-Theorie, Braun Verlag, Karlsruhe, chap 7 Die Grenzschichtgleichung der ebenen Strömung; Plattengrenzschicht, pp 129–150

Schlichting H, Gersten K (2000) Boundary Layer Theory. Springer, Berlin

Schlichting H, Truckenbrodt E (1967) Aerodynamik Des Flugzeuges: Erster Band, vol ., Springer, Berlin, chap 6 Der Tragflügel unendlicher Spannweite bei inkompressibler Strömung (Profiltheorie)

Schmid P, Henningson DS (2001) Stability and Transition in Shear Flows. Springer, Berlin

Schrader LU, Brandt L, C M, Henningson DS (2010) Receptivity to free-stream vorticity of flow past a flat plate with elliptic leading edge. Journal of Fluid Mechanics 653:245–271, DOI 10.1017/S0022112010000376

Schubauer GB, Skramstad HK (1948) Laminar-boundary-layer oscillations and transition on a flat plate. NACA Report 909

Schulze J (2010) Numerische Simulation verschiedener Strömungszustände am Forschungsflugzeug G109b. Bachelor Thesis, TU Darmstadt

Schwarz L (1940) Berechnung der Druckverteilung einer harmonisch sich verformenden Tragfläche in ebener Strömung. Luftfahrtforschung 17:379–386

Sears WR (1938) A systematic presentation of the theory of thin airfoils in non-uniform motion. PhD thesis, California Institute of Technology

Sears WR (1941) Some aspects of non-stationary airfoil theory and its application. Journal of the Aeronautical Sciences 8(8):104–108

Seitz A (2007) Freiflug-Experimente zum Übergang laminar-turbulent in einer Tragflügelgrenzschicht. DLR Forschungsbericht 2007-01

Seitz A, Horstmann KH (2006) In-flight investigation of Tollmien-Schlichting waves. In: Meier G, Sreenivasan K (eds) IUTAM Symposium on One Hundred Years of Boundary Layer Research, IUTAM, Springer, Berlin, Solid Mechanics and Its Applications, vol 129, pp 115–124, DOI 10.1007/978-1-4020-4150-1_11

Selig M, Maughmer M, Somers D (1995) Natural-laminar-flow airfoil for general-aviation applications. Journal of Aircraft 32:710–715, DOI 10.2514/3.46781

Sheih CM, Tennekes H, Lumley JL (1971) Airborne measurement of the small-scale structure of atmospheric turbulence. Physics of Fluids 201(14):201–215, DOI 10.1063/1.1693416

Söhngen H (1939) Die Lösung der Integralgleichung $g(x) = \oint_{-a}^{a} \frac{f(\xi)}{x-\xi} d\xi$ und deren Anwendung in der Tragflügeltheorie. Mathematische Zeitschrift 45(1):245–262

Somers D (1981) Design and experimental results for a natural-laminar-flow airfoil for general aviation applications. NASA Technical Paper 1861

Somers D (1997) Design and experimental results for the s809airfoil. National Renewable Energy Laboratory (NRELlSR-440-6918):1–98

Spiegelberg H, Cordes U, Hagedorn P, Tropea C (2014) Note on a self-adaptive airfoil with kinematically coupled leading and trailing flap. In: Ecker H, Steindl A, Jakubek S (eds) ENOC 2014 - Proceedings of 8th European Nonlinear Dynamics Conference, Institute of Mechanics and Mechatronics, Vienna University of Technology, iSBN: 978-3-200-03433-4

Spurk H, Aksel N (2006) Strömungslehre. Springer, Berlin

Staveren V (2003) Analyses of aircraft responses to atmospheric turbulence. PhD thesis, TU Delft

Studer G, Arnal D, Houdeville R (2006a) Laminar-turbulent transition in oscillating boundary layer: Experimental and numerical analysis using continuous wavelet transform. Experiments in Fluids 41(5):68–698, DOI 10.1007/s00348-006-0190-1

Studer G, Arnal D, Houdeville R, Seraudie A (2006b) Experimental and numerical analysis of unsteady boundary layer transition using continuous wavelet transfrom. In: Schlatter P, Henningson D (eds) 6th IUTAM Symposium on Laminar-Turbulent Transition, IUTAM, Springer, Berlin, IUTAM Bookseries, vol 78, pp 275–280

Stull R (1988) An introduction to boundary layer meteorology. Kluwer DOI 10.1007/978-94-009-3027-8

Sturzebecher D, Anders S, Nitsche W (2001) The surface hot wire as a means of measuring mean and fluctuating wall shear stress. Experiments in Fluids 31:294–301, DOI 10.1007/s003480100284

Tani I (1969) Boundary-layer transition. Annual Review of Fluid Mechanics 1:169–196

Taubert P (2014) Development of a method for computing the unsteady boundary layer in flight through. Master Thesis, TU Darmstadt In German

Taylor GI (1938) The spectrum of turbulence. Procedings of the Royal Society A 164(18):476–490, DOI 10.1098/rspa.1938.0032

Tempelmann D (2011) Stability and receptivity of three-dimensional boundary layers. PhD thesis, KTH Stockholm

Tempelmann D, Hanifi A, Henningson D (2010) Spatial optimal growth in three-dimensional boundary layers. Journal of Fluid Mechanics 646:5–37, DOI 10.1017/jfm.2012.235

Tennekes H, Lumley JL (1972) A First Course in Turbulence. The MIT Press, Cambridge, MA

Theodorsen T (1935) General theory of aerodynamic instability and the mechanisms of flutter. NACA Report 496

Thomas F (1999) Fundamentals of Sailplane Design. College Park Press, Maryland

Van Ingen J (2008) The e^n method for transition prediction. Historical review of work at TU Delft. AIAA paper 3830

Vermeer LJ, Sorensen JN, Crespo A (2003) Wind turbine wake aerodynamics. Progress in Aerospace Sciences 39:467–510, DOI 10.1016/S0376-0421(03)00078-2

Walker GJ (1993) The role of laminar-turbulent transition in gas turbines: A discussion. Journal of Turbomachinery 115(2):207–217, DOI 10.1115/1.2929223

Weismüller M (2011) A new approach to aerodynamic performance of aircraft under turbulent atmospheric conditions. PhD thesis, TU Darmstadt, http://tuprints.ulb.tu-darmstadt.de/2934/

Welch PD (1967) The use of fast Fourier transform for the estimation of power spectra: A method based on time averaging over short, modified periodograms. IEEE Transactions on Audio and Electroacoustics 15(15):70–73, DOI 10.1109/TAU.1967.1161901

Westin KJA, Boiko AV, Klingmann BGB, Kozlov VV, Alfredsson PH (1994) Experiments in a boundary layer subjected to free stream turbulence. Part 1: Boundary layer structure and receptivity. Journal of Fluid Mechanics 281:193–218, DOI 10.1017/S0022112094003083

Westin KJA, Bakchinov AA, Kozlov VV, Alfredsson PH (1998) Experiments on localized disturbances in a flat plate boundary layer. part 1. the receptivity and evolution of a localized free stream disturbance. European Journal of Mechanics B/Fluids 17(6):823–846, DOI 10.1016/S0997-7546(99)80016-8

White EB (2000) Breakdown of crossflow vortices. PhD thesis, Arizona State University

White EB (2002) Transient growth of stationary disturbances in a flat plate boundary layer. Physics of Fluids 14:4429–4439, DOI 10.1063/1.1521124

White EB, Saric WS, Radetzsky RH (2000) Laminar-Turbulent Transition, Springer, Berlin, chap Leading-Edge Acoustic Receptivity Measurements Using a Pulsed-Sound Technique, pp 103–108. IUTAM Symposia, DOI 10.1007/978-3-662-03997-7_13

White FM (1974) Viscous Fluid Flow. McGraw-Hill, New York

Wippermann F, Klug W, Hasse L, Weber F (1970) Promet, meteorologische Fortbildung. Tech. Rep. 70/01, German Weather Forecast Service (DWD)

Wolfram D (2012) Entwicklung von Messtechnik zur dynamischen Kalibration von Drücken und der Erfassung von intationären Flugzeugbewegungen. Bachelor Thesis, TU Darmstadt

Wu X, Steward P, Cowley S (2007) On the catalytic role of the phase-locked interaction of Tollmien-Schlichting waves in boundary-layer transition. Journal of Fluid Mechanics 590:265–294, DOI 10.1017/S002211200700804

Würz W (1995) Hitzdrahtmessungen zum laminar-turbulenten Strömungsumschlag in anliegenden Grenzschichten und Ablöseblasen sowie Vergleich mit der linearen Stabilitätstheorie und empirischen Umschlagskriterien. PhD thesis, Universität Stuttgart

Würz W (2014) Private communication

Würz W, Herr S, Wörner A, Rist U, Wagner S, Kachanov YS (2003) Three-dimensional acoustic-roughness receptivity of a boundary layer on an airfoil: Experiment and direct numerical simulations. Journal of Fluid Mechanics 2003:135–163, DOI 10.1017/S0022112002003348

Würz W, Sartourius D, Kloker M, Borodulin V, Kachanov Y, Smorodsky B (2012) Nonlinear instabilities of a non-self-similar boundary layer on an airfoil: Experiments, DNS, and theory. European Journal of Mechanics B/Fluids 31:102–128, DOI 10.1016/j.euromechflu.2011.07.006

Wyngaard JC (1992) Atmospheric turbulence. Annual Review of Fluid Mechanics 24:205–233, DOI 10.1146/annurev.fl.24.010192.001225

Wyngaard JC (2010) Turbulence in the Atmosphere. Cambridge University Press, Cambridge

Yechout TR, Morris S, Bossert D, Hallgren W (2003) Introduction To Aircraft Flight Mechanics: Performance, Static Stability, Dynamic Stability, And Classical Feedback Control. AIAA

Youngren H, Drela M (2006) AVL 3.27 - User Primer. MIT, http://web.mit.edu/drela/Public/web/avl/

Zanin BY (1985) Laminar-Turbulent Transition, Springer, Berlin, chap Transition at Natural Conditions and Comparison with the Results of Wind-Tunnel Studies, pp 541–546. DOI 10.1007/978-3-642-82462-3_67

Zhao R, Smits AJ (2006) Binormal cooling errors in crossed hot-wire measurements. Experiments in Fluids 40:212–217, DOI 10.1007/s00348-005-0060-2

Nomenclature

Latin Letters

Symbol	Dimension	Description

upper case

A	V^2	hot-wire calibration constant
A_{HF}	$\frac{\mathrm{V}^2}{\mathrm{Pa}^{\frac{1}{3}}}$	hot-film calibration constant
$\hat{A}$	$\frac{\mathrm{m}}{\mathrm{s}}$	wave amplitude
$\hat{A}_0$	$\frac{\mathrm{m}}{\mathrm{s}}$	wave amplitude at the neutral point
B	$\frac{\mathrm{V}^2\ \mathrm{s}^{\mathrm{n}}}{\mathrm{m}^{\mathrm{n}}}$	hot-wire calibration constant
B_{HF}	V^2	hot-film calibration constant
C_l	–	lift coefficient
$C_{l,\mathrm{qs}}$	–	quasi-steady lift coefficient
C_n	–	normal force coefficient
C_p	–	pressure coefficient
$C_{\mathrm{p,l}}$	–	pressure coefficient on lower side of the airfoil
$C_{p,m}$	–	mean pressure coefficient
$C_{p,qs}$	–	quasi-steady pressure coefficient
$C_{\mathrm{p,u}}$	–	pressure coefficient on upper side of the airfoil
$C_{p,us}$	–	unsteady pressure coefficient

C_T	–	universal turbulence constant
C_t	–	tangential force coefficient
$C_m(\kappa)$	–	angular moment coefficient
D	–	damping coefficient
C_R	–	receptivity coefficient
$\mathcal{D}$	–	differential operator
D_{XX}	$\frac{\mathrm{m}^3}{\mathrm{s}^3}$	dissipation spectrum
$E[\,]$	–	expectation value
E_b	V	bridge voltage
E_kin	$\frac{\mathrm{kg\ m}^2}{\mathrm{s}^2}$	kinetic energy
E_w	V	X-wire voltage
E_{XX}	$\frac{\mathrm{m}^2}{\mathrm{s}}$	power spectral density
$F(x,\eta,t)$	–	dimensionless stream function
$\mathcal{F}$	–	Fourier transform
$G(\Phi_\mathrm{c})$	–	absolute error
$G_{12}(f)$	V^2 s	cross spectrum
$G_{r,r}$	–	auto-spectral density of reference sensor
$G_{s,r}$	–	cross-spectral density of sensor to reference sensor
H	m	flight level
H_{12}	–	boundary-layer shape factor
$H_{s,r}$	–	transfer function
J	–	joint probability density distribution
J^+	–	normalized joint probability density distribution
M_f	–	Magnification factor

Ma	–	Mach number
L_I	m	Integral length scale of the turbulence
L_c	m	chord length
L_w	m	X-wire length
N	–	N-factor
N_T	–	transition N-factor
N_t	–	threshold N-factor
N_env	–	envelope N-factor
P	$\frac{\mathrm{kg}}{\mathrm{m\ s^2}}$	pressure
P	–	probability density function
P^+	–	normalized probability density function
P_m	–	Fourier transform of measured signal
P_r	–	Fourier coefficient of the reference sensor signal
P_s	–	Fourier coefficient of the sensor signal
Q	$\frac{\mathrm{m}}{\mathrm{s}}$	propagation velocity
R_d	$\frac{\mathrm{m}}{\mathrm{s^2\ K}}$	dry air constant
R_h	$\frac{\mathrm{m}}{\mathrm{s^2\ K}}$	humid air constant
R_w	$\frac{\mathrm{V}}{\mathrm{A}}$	hot-wire resistance
Re	–	Reynolds number
Re_r	–	roughness Reynolds number
T	K	static flow temperature
T_C	K	calibration temperature
T_F	K	fluid temperature
T_f	K	film temperature
T_HF	K	hot film temperature

Tu_{XX}	–	one-dimensional turbulence intensity
Tu_{XZ}	–	two-dimensional turbulence intensity
T_w	K	hot-wire temperature
$S(\kappa)$	–	Sears function
S_k	–	skewness
$\hat{S}$	–	Fourier coefficient
$\vec{U}$	$\frac{\mathrm{m}}{\mathrm{s}}$	velocity vector
U_CAS	$\frac{\mathrm{m}}{\mathrm{s}}$	calibrated airspeed
U_e	$\frac{\mathrm{m}}{\mathrm{s}}$	edge velocity
U_eff	$\frac{\mathrm{m}}{\mathrm{s}}$	effective cooling velocity
U_∞	$\frac{\mathrm{m}}{\mathrm{s}}$	free-stream velocity
U_TS	m	Tollmien-Schlichting wave spectrum
$\vec{\mathcal{U}}$	$\frac{\mathrm{m}}{\mathrm{s}}$	base flow velocity
V	$\frac{\mathrm{m}}{\mathrm{s}}$	flight velocity
V_t	$\frac{\mathrm{m}}{\mathrm{s}}$	transpiration velocity
$\hat{W}$	–	wavelet coefficient
W_a	$\frac{\mathrm{m}}{\mathrm{s}}$	normal airfoil velocity
W_g	$\frac{\mathrm{m}}{\mathrm{s}}$	gust velocity
Z_a	m	airfoil displacement

lower case

a	$-$	scale parameter
a	$\frac{\mathrm{m}}{\mathrm{s}}$	speed of sound
a_z	$\frac{\mathrm{m}}{\mathrm{s}^2}$	normal acceleration
b	m	half chord length
c	$\frac{\mathrm{m}}{\mathrm{s}}$	phase velocity of the wave modes
c_g	$\frac{\mathrm{m}}{\mathrm{s}}$	group velocity
c_ℓ	$-$	model parameter
d	m	camber
e'	V	voltage fluctuation
f	$\frac{1}{\mathrm{s}}$	frequency
f_c	$\frac{1}{\mathrm{s}}$	center frequency
f_L	$-$	model function
f_ℓ	$-$	model function
f_p	$\frac{1}{\mathrm{s}}$	pseudo frequency
f_s	$\frac{1}{\mathrm{s}}$	sampling rate
$f_{\Delta(m,n)}$	$\frac{1}{\mathrm{s}}$	difference frequency
k	$\frac{1}{\mathrm{m}}$	wavenumber
k_C	$\frac{1}{\mathrm{m}}$	conversion wavenumber
k_FD	$\frac{1}{\mathrm{m}}$	free-stream disturbance wavenumber
k_TS	$\frac{1}{\mathrm{m}}$	Tollmien-Schlichting wavenumber
k_x	$\frac{1}{\mathrm{m}}$	Tollmien-Schlichting eigenvalue
$k_{x,i}$	$\frac{1}{\mathrm{m}}$	disturbance growth rate
$k_{x,r}$	$\frac{1}{\mathrm{m}}$	wavenumber
k_z	$\frac{1}{\mathrm{m}}$	spanwise wavenumber
$k_{z,m}$	$\frac{1}{\mathrm{m}}$	spanwise modulation wavenumber

$k_{z,\Delta(m,n)}$	$\frac{1}{\mathrm{m}}$	difference wavenumber
ℓ_K	m	Kolmogorov length scale
n	–	calibration constant
p	$\frac{\mathrm{kg}}{\mathrm{m\ s^2}}$	pressure
p_{cor}	$\frac{\mathrm{kg}}{\mathrm{m\ s^2}}$	pressure signal
p_{sat}	$\frac{\mathrm{kg}}{\mathrm{m\ s^2}}$	saturation pressure
$\vec{q}\,'(\vec{x},t)$	$\frac{\mathrm{m}}{\mathrm{s}}$, Pa	disturbances function
r	m	roughness
r_{h}	–	relative humidity
$\tilde{s}$	V	signal envelope
t	s	time
t	s	airfoil thickness
u_ℓ	$\frac{\mathrm{m}}{\mathrm{s}}$	Kolmogorov velocity
$\vec{u}$	$\frac{\mathrm{m}}{\mathrm{s}}$	boundary layer velocity
x	m	wall-tangential direction
$x_{\max}$	m	maximum arc length along the airfoil on each side
y	m	wall-normal direction
z	m	spanwise direction

Greek Letters

Symbol	Description	Unit

upper case

Γ	$\frac{\mathrm{m}^2}{\mathrm{s}}$	circulation
Λ	$\frac{\mathrm{kg\ m}}{\mathrm{s}^3\ \mathrm{K}}$	thermal conductivity of air
Υ	$^\circ$	yaw angle
$\bar{\Upsilon}$	$^\circ$	geometric slant angle of X-wire
$\bar{\Upsilon}_{eff}$	$^\circ$	effective yaw angle of X-wire
Φ_c	$-$	uncertainty of combined quantities
$\vec{\Omega}$	$\frac{\mathrm{m}^2}{\mathrm{s}}$	wall-normal vorticity
Ψ	$-$	Wavelet function
Ψ	$^\circ$	wave propagation angle

lower case

α	$^\circ$	angle of attack
γ	$-$	heat capacity ratio
γ_{12}	$-$	coherence between two signals
γ_{tot}	$-$	vortex distribution on the airfoil
δ	m	boundary-layer thickness
δ_1	m	displacement boundary-layer thickness
δ_2	m	momentum boundary-layer thickness
δ_e	m	boundary-layer edge
ϵ	$\frac{\mathrm{m}^2}{\mathrm{s}^3}$	energy dissipation rate

ε	$\frac{\mathrm{m}}{\mathrm{s}}$	shed vortex distribution
η	$-$	dimensionless wall normal coordinate
θ	$^\circ$	probe inclination
κ	$-$	reduced frequency
κ_δ	$-$	boundary layer frequency parameter
λ_x	m	wave length
μ	$\frac{\mathrm{kg}}{\mathrm{m\ s}}$	dynamic viscosity
ν	$\frac{\mathrm{m}^2}{\mathrm{s}}$	kinematic viscosity
ν_T^+	$-$	dimensionless eddy viscosity
ρ	$\frac{\mathrm{kg}}{\mathrm{m}^3}$	density
ϱ_{12}	$-$	cross-correlation of two signals
ρ_t	$\frac{\mathrm{kg}}{\mathrm{m}^3}$	stagnation density
ρ_∞	$\frac{\mathrm{kg}}{\mathrm{m}^3}$	free-stream density
τ	s	time shift parameter
τ_ℓ	s	Kolmogorov time scale
τ_m	s	time shift of correlation
τ_w	$\frac{\mathrm{kg}}{\mathrm{m\ s}^2}$	wall shear stress
ϕ	$^\circ$	phase profile
ϕ	$\frac{\mathrm{m}^2}{\mathrm{s}}$	velocity potential
ϕ_LE	$^\circ$	leading edge phase
ϕ_W	$^\circ$	phase difference between stream and wall
φ	$^\circ$	phase angle
χ	$-$	Riegels factor
$\psi(x, y, t)$	$\frac{\mathrm{m}^2}{\mathrm{s}}$	stream function
ω	$\frac{1}{\mathrm{s}}$	angular frequency

Abbreviations

Abbreviation	Description
ABL	Atmospheric Boundary Layer
AC	Alternating Current
AHRS	Attitude Heading Reference System
AOA	Angle of Attack
CAD	Computer-Aided Design
CFD	Computational Fluid Dynamics
CT	Constant Temperature
CTA	Constant Temperature Anemometry
DC	Direct Current
FFT	Fast Fourier Transforms
FPGA	Field Programmable Gate Array
GPS	Global Positioning System
IAG	Institute of Aerodynamics and Gas Dynamics
IMU	Inertial Measurement Unit
INS	Internal Navigation System
OS	Orr-Sommerfeld Equation
PC	Personal Computer
PDF	probability density function
PSD	Power Spectral Density
RANS	Reynolds Averaged Navier Stokes
RMS	Root Mean Square
SPL	Sound Pressure Level
SQ	Squire Equation

TS	Tollmien-Schlichting
TTL	Transistor-Transistor Logic
US	Unsteady Solution

A. Appendix

A.1. Thin Airfoil Theory Model

A description of the of the origin of the basic equations for the unsteady thin airfoil model is given by Schwarz (1940) and Bisplinghoff et al (1996). However, the solution of the necessary integrals is not provided. In the following only the foundations are repeated and emphasis is placed on the solution of the integrals for the present problem.

As mentioned in Chapter 2.3.1, substitution of equations (2.7), (2.8) and (2.12) into the law of Biot-Savart (2.13) yields an integro-differential equation for the unknown $\hat{\gamma}_{tot}(X)$. This equation can be inverted into an ordinary integral expression (Söhngen, 1939).

$$\hat{\gamma}_{tot}(X^+,\kappa) = \frac{2}{\pi}\sqrt{\frac{1-X^+}{1+X^+}}\left[\underbrace{\oint_{-1}^{1}\sqrt{\frac{1+\xi^+}{1-\xi^+}}\frac{\hat{W}_a}{X^+-\xi^+}\,\mathrm{d}\xi^+}_{:=I_b} + \frac{i\kappa\hat{\Theta}}{2}\underbrace{\int_1^\infty\sqrt{\frac{\zeta^++1}{\zeta^+-1}}\frac{\mathrm{e}^{-i\kappa\zeta^+}}{X^+-\zeta^+}\,\mathrm{d}\zeta^+}_{:=I_s}\right] \tag{A.1}$$

$$\hat{\Theta} = \frac{\hat{\Gamma}}{b}\mathrm{e}^{i\kappa} = \frac{4}{\pi i\kappa[H_1(\kappa)+iH_0(\kappa)]}\underbrace{\int_{-1}^{1}\sqrt{\frac{1+\xi^+}{1-\xi^+}}\hat{W}_a(\xi^+)\,\mathrm{d}\xi^+}_{:=I_a} \tag{A.2}$$

The circle denotes a Cauchy integral. $X^+ = X/b = -\cos(\vartheta)$, $\xi^+ = \xi/b = -\cos(\varphi)$ and $\zeta^+ = \zeta/b$ are dimensionless coordinates. The integrals I_a and I_b will be solved in the following derivation and substitution eventually yields the important equation (2.20). The semi-infinite integral I_s has no analytic

solution. This problem is avoided when considering only the amplitude distribution of the pressure difference for harmonic airfoil deformations. The pressure difference amplitude can entirely be expressed in terms of $\hat{\gamma}_{tot}$ (Bisplinghoff et al, 1996).

$$\Delta P(X^+,\kappa) = -\rho\bar{U}_\infty \left(\hat{\gamma}_{tot} - i\kappa \int_{-1}^{X^+} \hat{\gamma}_{tot}(\xi^+)\ \mathrm{d}\xi^+ \right) \tag{A.3}$$

As a result of the further integration of $\hat{\gamma}_{tot}$ the governing equation for the pressure amplitude only contains finite integrals (Schwarz, 1940).

$$\begin{aligned} \frac{\Delta\hat{P}(X^+,\kappa)}{\rho\bar{U}_\infty} =& \frac{2}{\pi}\Bigg\{ [1-\mathrm{C}(\kappa)] \sqrt{\frac{1-X^+}{1+X^+}} \int_{-1}^{1} \sqrt{\frac{1+\xi^+}{1-\xi^+}} \hat{W}_a(\xi^+)\mathrm{d}\xi^+ \\ &+ \sqrt{\frac{1-X^+}{1+X^+}} \oint_{-1}^{1} \sqrt{\frac{1+\xi^+}{1-\xi^+}} \frac{\hat{W}_a(\xi^+)}{X^+-\xi^+}\mathrm{d}\xi^+ \\ &- i\kappa \oint_{-1}^{1} \Lambda_1(X^+,\xi^+)\hat{W}_a(\xi^+)\mathrm{d}\xi^+ \Bigg\} \end{aligned} \tag{A.4}$$

Considering a sinusoidal gust excitation, the kinematic boundary condition $\hat{W}_a = W_a/\mathrm{e}^{i\omega t}$ of the harmonically deforming airfoil is described by the velocity amplitude

$$\hat{W}_a(\varphi) = -\hat{W}_g \mathrm{e}^{i\kappa\cos(\varphi)}. \tag{A.5}$$

Sears (1938) expressed the harmonic part conveniently in terms of a series of Bessel functions.

$$\mathrm{e}^{i\kappa\cos(\varphi)} = J_0(\kappa) + 2\sum_{n=1}^{\infty} i^n J_n(\kappa)\cos(n\varphi) \tag{A.6}$$

The Bessel functions are defined as follows (Bronstein et al, 2005):

$$J_n(\varphi) = \frac{i^{-n}}{\pi} \int_0^{\pi} \mathrm{e}^{iz\cos(\varphi)} \cos(n\varphi)\mathrm{d}\varphi \tag{A.7}$$

$$J_0(\varphi) = \frac{1}{\pi} \int_0^{\pi} \mathrm{e}^{iz\cos(\varphi)} \mathrm{d}\varphi \tag{A.8}$$

$$J_1(\varphi) = \frac{i}{\pi} \int_0^{\pi} \mathrm{e}^{iz\cos(\varphi)} \cos(\varphi)\mathrm{d}\varphi. \tag{A.9}$$

Substituting equation (A.5) into equation (A.4), the difference pressure amplitude reads

$$\Delta\hat{P}(X^+,\kappa) = -\frac{2\rho\bar{U}_\infty\hat{W}_g}{\pi}\Bigg\{ [1-\mathrm{C}(\kappa)]\sqrt{\frac{1-X^+}{1+X^+}}\underbrace{\int_{-1}^{1}\sqrt{\frac{1+\xi^+}{1-\xi^+}}\mathrm{e}^{-i\kappa\xi^+}\mathrm{d}\xi^+}_{:=I_a} + \sqrt{\frac{1-X^+}{1+X^+}}\underbrace{\oint_{-1}^{1}\sqrt{\frac{1+\xi^+}{1-\xi^+}}\frac{\mathrm{e}^{-i\kappa\xi^+}}{X^+-\xi^+}\mathrm{d}\xi^+}_{:=I_b} - i\kappa\underbrace{\oint_{-1}^{1}\Lambda_1(X^+,\xi^+)\mathrm{e}^{-i\kappa\xi^+}\mathrm{d}\xi^+}_{:=I_c}\Bigg\}. \tag{A.10}$$

$\mathrm{C}(\kappa)$ is the Theodorsen function, which is defined by a combination of Hankel functions of the second kind (Bisplinghoff et al, 1996).

$$\mathrm{C}(\kappa) = \frac{H_1(\kappa)}{H_1(\kappa)+iH_0(\kappa)} \tag{A.11}$$

Λ_1 is a function of the airfoil coordinates X^+ and ξ^+, which is only introduced later. For an analytic solution, the integrals I_a, I_b and I_c are considered separately and the airfoil coordinates are expressed by trigonometric functions.

$$\begin{aligned} I_a := \int_{-1}^{1}\sqrt{\frac{1+\xi^+}{1-\xi^+}}\mathrm{e}^{i\kappa\xi^+}\mathrm{d}\xi^+ &= \int_0^\pi \sqrt{\frac{1-\cos(\varphi)}{1+\cos(\varphi)}}\mathrm{e}^{-i\kappa\cos(\varphi)}\sin(\varphi)\mathrm{d}\varphi \\ &= \int_0^\pi \frac{1-\cos(\varphi)}{\sin(\varphi)}\mathrm{e}^{i\kappa\cos(\varphi)}\sin(\varphi)\mathrm{d}\varphi \\ &= \int_0^\pi (1-\cos(\varphi))\,\mathrm{e}^{i\kappa\cos(\varphi)}\mathrm{d}\varphi \\ &= \int_0^\pi \mathrm{e}^{i\kappa\cos(\varphi)}\mathrm{d}\varphi - \int_0^\pi \cos(\varphi)\mathrm{e}^{i\kappa\cos(\varphi)}\mathrm{d}\varphi \\ &= \pi\left[J_0(\kappa)-iJ_1(\kappa)\right]. \end{aligned} \tag{A.12}$$

The integral I_b is further split into four integrals. Their individual solution

requires the use of the Glauert integral

$$\oint_0^\pi \frac{\cos(n\varphi)}{\cos(\varphi)-\cos(\vartheta)}\mathrm{d}\varphi = \pi\frac{\sin(n\vartheta)}{\sin(\vartheta)}. \tag{A.13}$$

The necessary conversions and the solutions of the individual parts are listed in the following.

$$\begin{aligned} I_b :&= \oint_{-1}^{1} \sqrt{\frac{1+\xi^+}{1-\xi^+}}\frac{\mathrm{e}^{-i\kappa\xi^+}}{X^+-\xi^+}\mathrm{d}\xi^+ \\ &= \oint_0^\pi \sqrt{\frac{1-\cos(\varphi)}{1+\cos(\varphi)}}\frac{\mathrm{e}^{i\kappa\cos(\varphi)}}{-\cos(\vartheta)+\cos(\varphi)}\sin(\varphi)\mathrm{d}\varphi \\ &= \oint_0^\pi \frac{1-\cos(\varphi)}{\sin(\varphi)}\frac{\mathrm{e}^{i\kappa\cos(\varphi)}}{\cos(\varphi)-\cos(\vartheta)}\sin(\varphi)\mathrm{d}\varphi \\ &= \oint_0^\pi \frac{1-\cos(\varphi)}{\cos(\varphi)-\cos(\vartheta)}\mathrm{e}^{i\kappa\cos(\varphi)}\mathrm{d}\varphi \end{aligned} \tag{A.14}$$

.

The introduction of the series expansion (A.6) enables important simplifications since the Bessel functions are only dependent on κ and do not have to be considered for the integration.

$$\begin{aligned} I_b &= \oint_0^\pi \frac{1-\cos(\varphi)}{\cos(\varphi)-\cos(\vartheta)}\mathrm{e}^{i\kappa\cos(\varphi)}\mathrm{d}\varphi \\ &= \oint_0^\pi \left[\frac{1-\cos(\varphi)}{\cos(\varphi)-\cos(\vartheta)}\left(J_0(\kappa)+2\sum_{n=1}^{\infty} i^n J_n(\kappa)\cos(n\varphi)\right)\right]\mathrm{d}\varphi \\ &= \oint_0^\pi \Bigg[\underbrace{\frac{J_0(\kappa)}{\cos(\varphi)-\cos(\vartheta)}}_{:=I_{b,a}} + \underbrace{\frac{2\sum_{n=1}^{\infty} i^n J_n(\kappa)\cos(n\varphi)}{\cos(\varphi)-\cos(\vartheta)}}_{:=I_{b,b}} \\ &\qquad - \underbrace{\frac{J_0(\kappa)\cos(\varphi)}{\cos(\varphi)-\cos(\vartheta)}}_{:=I_{b,c}} - \underbrace{\frac{2\cos(\varphi)\sum_{n=1}^{\infty} i^n J_n(\kappa)\cos(n\varphi)}{\cos(\varphi)-\cos(\vartheta)}}_{:=I_{b,d}}\Bigg]\mathrm{d}\varphi. \end{aligned} \tag{A.15}$$

The individual parts read as follows.

$$\begin{aligned} I_{b,a} &:= \oint_0^\pi \frac{J_0(\kappa)}{\cos(\varphi)-\cos(\vartheta)}\mathrm{d}\varphi \\ &= J_0(\kappa)\oint_0^\pi \frac{\cos(0\varphi)}{\cos(\varphi)-\cos(\vartheta)}\mathrm{d}\varphi \\ &= J_0(\kappa)\frac{\pi\sin(0\vartheta)}{\sin(\vartheta)} \\ &= 0 \end{aligned} \tag{A.16}$$

$$\begin{aligned} I_{b,b} &:= \oint_0^\pi \frac{2\sum_{n=1}^\infty i^n J_n(\kappa)\cos(n\varphi)}{\cos(\varphi)-\cos(\vartheta)}\mathrm{d}\varphi \\ &= 2\sum_{n=1}^\infty i^n J_n(\kappa)\oint_0^\pi \frac{\cos(n\varphi)}{\cos(\varphi)-\cos(\vartheta)}\mathrm{d}\varphi \\ &= 2\sum_{n=1}^\infty i^n J_n(\kappa)\frac{\pi\sin(n\vartheta)}{\sin(\vartheta)} \end{aligned} \tag{A.17}$$

$$\begin{aligned} I_{b,c} &:= \oint_0^\pi \frac{J_0(\kappa)\cos(\varphi)}{\cos(\varphi)-\cos(\vartheta)}\mathrm{d}\varphi \\ &= J_0(\kappa)\oint_0^\pi \frac{\cos(\varphi)}{\cos(\varphi)-\cos(\vartheta)}\mathrm{d}\varphi \\ &= J_0(\kappa)\frac{\pi\sin(1\vartheta)}{\sin(\vartheta)} \\ &= \pi J_0(\kappa) \end{aligned} \tag{A.18}$$

For the last part the following two identities are needed.

$$\begin{aligned} \sin\left[(n-1)\ \vartheta\right]+\sin\left[(n+1)\ \vartheta\right] &= 2\sin(n\vartheta)\cos(\vartheta) \\ \cos\left[(n-1)\ \varphi\right]+\cos\left[(n+1)\ \varphi\right] &= 2\cos(n\varphi)\cos(\varphi) \end{aligned} \tag{A.19}$$

$$
\begin{aligned}
I_{b,d} &:= \oint_0^{\pi} \frac{2\cos(\varphi)\sum_{n=1}^{\infty} i^n J_n(\kappa)\cos(n\varphi)}{\cos(\varphi)-\cos(\vartheta)}\mathrm{d}\varphi \\
&= \sum_{n=1}^{\infty} i^n J_n(\kappa) \oint_0^{\pi} \frac{\{\cos\left((n-1)\,\varphi\right)+\cos\left[(n+1)\;\varphi\right]\}}{\cos(\varphi)-\cos(\vartheta)}\mathrm{d}\varphi \\
&= \sum_{n=1}^{\infty} i^n J_n(\kappa) \left\{ \oint_0^{\pi} \frac{\cos\left[(n-1)\;\varphi\right]}{\cos(\varphi)-\cos(\vartheta)}\mathrm{d}\varphi + \oint_0^{\pi} \frac{\cos\left[(n+1)\;\varphi\right]}{\cos(\varphi)-\cos(\vartheta)}\mathrm{d}\varphi \right\} \\
&= \sum_{n=1}^{\infty} i^n J_n(\kappa) \left\{ \frac{\pi\sin\left[(n-1)\;\vartheta\right]}{\sin(\vartheta)} + \frac{\pi\sin\left[(n+1)\;\vartheta\right]}{\sin(\vartheta)} \right\} \\
&= \pi \sum_{n=1}^{\infty} i^n J_n(\kappa) \left\{ \frac{\sin\left[(n-1)\;\vartheta\right]+\sin\left[(n+1)\;\vartheta\right]}{\sin(\vartheta)} \right\} \\
&= 2\pi \sum_{n=1}^{\infty} i^n J_n(\kappa) \left\{ \frac{\sin(n\vartheta)\cos(\vartheta)}{\sin(\vartheta)} \right\}.
\end{aligned}
\tag{A.20}
$$

Summation of the individual solutions yields

$$
\begin{aligned}
I_b &:= \oint_0^{\pi} \frac{1-\cos(\varphi)}{\cos(\varphi)-\cos(\vartheta)} \mathrm{e}^{i\kappa\cos(\varphi)}\mathrm{d}\varphi \\
&= I_{b,a} + I_{b,b} - I_{b,c} - I_{b,d} \\
&= -\pi J_0(\kappa) + 2\pi \frac{1-\cos(\vartheta)}{\sin(\vartheta)} \sum_{n=1}^{\infty} i^n J_n(\kappa)\sin(n\vartheta).
\end{aligned}
\tag{A.21}
$$

To solve for the integral I_c, the series approach of equation (A.6) and the function Λ_1 are introduced.

$$
\begin{aligned}
I_c &:= \oint_{-1}^{1} \Lambda_1(X^+,\xi^+)\mathrm{e}^{-i\kappa\xi^+}\mathrm{d}\xi^+ \\
&= \oint_0^{\pi} \Lambda_1(\vartheta,\varphi)\mathrm{e}^{i\kappa\cos(\varphi)}\sin(\varphi)\mathrm{d}\varphi \\
&= \oint_0^{\pi} \frac{1}{2}\ln\left[\frac{1-\cos(\varphi+\vartheta)}{1-\cos(\varphi-\vartheta)}\right]\mathrm{e}^{i\kappa\cos(\varphi)}\sin(\varphi)\mathrm{d}\varphi.
\end{aligned}
$$

$$
\begin{aligned}
I_c &:= -\frac{i}{\kappa}\oint_0^{\pi}\left(J_0(\kappa)+2\sum_{n=1}^{\infty} i^n J_n(\kappa)\cos(n\varphi)\right)\frac{\sin(\vartheta)}{\cos(\varphi)-\cos(\vartheta)}\mathrm{d}\varphi \\
&= -\frac{i\sin(\vartheta)}{\kappa}\left\{\underbrace{J_0(\kappa)\oint_0^{\pi}\frac{1}{\cos(\varphi)-\cos(\vartheta)}\mathrm{d}\varphi}_{=I_{b,a}\,(\mathrm{A.16})}\right. \\
&\qquad\left.+\underbrace{2\sum_{n=1}^{\infty} i^n J_n(\kappa)\oint_0^{\pi}\frac{\cos(n\varphi)}{\cos(\varphi)-\cos(\vartheta)}\mathrm{d}\varphi}_{=I_{b,b}\,(\mathrm{A.17})}\right\} \\
&= -2\pi\frac{i}{\kappa}\sum_{n=1}^{\infty} i^n J_n(\kappa)\sin(n\vartheta).
\end{aligned}
\tag{A.22}
$$

Substituting the results of I_a, I_b and I_c into equation (A.10), the final expression for the pressure difference amplitude is

$$
\begin{aligned}
\Delta\hat{P}(\vartheta,\kappa) &= -\frac{2\rho\bar{U}_\infty\hat{W}_g}{\pi}\left\{[1-\mathrm{C}(\kappa)]\sqrt{\frac{1+\cos(\vartheta)}{1-\cos(\vartheta)}}I_a\right. \\
&\qquad\left.+\sqrt{\frac{1+\cos(\vartheta)}{1-\cos(\vartheta)}}I_b - i\kappa I_c\right\} \\
&= 2\rho\bar{U}_\infty\hat{W}_g\left(\frac{1+\cos(\vartheta)}{\sin(\vartheta)}\right)\{\mathrm{C}(\kappa)\,[J_0(\kappa)-iJ_1(\kappa)]+iJ_1(\kappa)\} \\
&= 2\rho\bar{U}_\infty\hat{W}_g\left(\frac{1+\cos(\vartheta)}{\sin(\vartheta)}\right)\mathrm{S}(\kappa).
\end{aligned}
\tag{A.23}
$$

The steady part of the model is completely described by Schlichting and Truckenbrodt (1967). Therefore, the equations employed for the calculation are presented without further comments. Note the different definition of the coordinate system in Figure 2.3. All dimensionless quantities are now based

on the chord length L_c instead of the semi-chord b.

$$
\begin{aligned}
\frac{\bar{U}_{\mathrm{S1}}(X^+)}{\bar{U}_\infty} &= \frac{\gamma_1(X^+)}{2\bar{U}_\infty} = \pm\frac{\bar{\alpha}}{\chi(X^+)}\sqrt{\frac{1-X^+}{X^+}} \\
\frac{\bar{U}_{\mathrm{S2}}(X^+)}{\bar{U}_\infty} &= \frac{\gamma_2(X^+)}{2\bar{U}_\infty} = \pm\frac{1}{\pi}\sqrt{\frac{1-X^+}{X^+}}\int_0^1 \frac{dZ^{(s)}(\xi^+)}{d\xi^+}\sqrt{\frac{\xi^+}{1-\xi^+}}\frac{d\xi^+}{X^+-\xi^+} \\
\frac{\bar{U}_{\mathrm{S3}}(X^+)}{\bar{U}_\infty} &= \frac{1}{\chi(X^+)}\frac{1}{\pi}\int_0^1 \frac{dZ^{(t)}(\xi^+)}{d\xi^+}\frac{d\xi^+}{X^+-\xi^+} \\
\frac{\bar{U}_{\mathrm{S4}}(X^+)}{\bar{U}_\infty} &= \pm\frac{\bar{\alpha}}{\chi(X^+)}\frac{1}{\pi}\sqrt{\frac{1-X^+}{X^+}}\int_0^1 \left(\frac{dZ^{(t)}(\xi^+)}{d\xi^+} - \frac{Z^{(t)}(\xi^+)}{2\xi^+\,(1-\xi^+)}\right)\frac{d\xi^+}{X^+-\xi^+} \\
\frac{1}{\chi(X^+)} &= \frac{1}{\sqrt{1+\left(\frac{dZ^{(t)}(X^+)}{dX^+}\right)^2}} := \text{Riegels factor}
\end{aligned}
\tag{A.24}
$$

Approximating the dimensionless camber ($Z^{(s)}$) and thickness ($Z^{(t)}$) distributions by Fourier series and using $\xi = (1+\cos(\varphi))/2$, analytic solutions are found for the components $\bar{U}_{\mathrm{S1}}$ to $\bar{U}_{\mathrm{S3}}$. Only for the component $\bar{U}_{\mathrm{S4}}$ a quadrature is needed (Riegels, 1949). According to Schlichting and Truckenbrodt (1967) this part can also be considered as an additional camber and an angle of attack contribution, which enable analytical expressions. When combining the solutions of the steady and the unsteady model part, the different definition of the coordinate systems is to be considered.

A.2. Airfoil Geometry Data

The characteristic airfoil geometry of the wing glove (MW-166-39-44-43) and the wing (E580) of the motorized glider are given in Table A.1. Furthermore the complete coordinates of the wing-glove airfoil are listed.

Table A.1.: Airfoil geometry parameters normalized by the chord length.

Airfoil	Wing (E580)	Glove (MW-166-39-44-43)
Chord length	1.09 m	1.35 m
Maximum Thickness	0.161 ($X/L_c = 0.36$)	0.166 ($X/L_c = 0.39$)
Maximum Camber	0.041 ($X/L_c = 0.61$)	0.044 ($X/L_c = 0.43$)
Leading edge radius	0.010	0.013

Coordinates of the MW-166-39-44-43 Airfoil

X/L_c	Z/L_c	X/L_c	Z/L_c	X/L_c	Z/L_c
1.000175	0.000468	0.776323	0.073952	0.529019	0.121791
0.997305	0.002293	0.767413	0.076411	0.520140	0.122609
0.992710	0.004689	0.758505	0.078830	0.511261	0.123364
0.987587	0.006912	0.749606	0.081209	0.502378	0.124053
0.981902	0.009151	0.740727	0.083542	0.493489	0.124678
0.975657	0.011478	0.731869	0.085824	0.484595	0.125240
0.968858	0.013911	0.723031	0.088054	0.475696	0.125737
0.961530	0.016454	0.714212	0.090228	0.466791	0.126171
0.953738	0.019102	0.705410	0.092344	0.457879	0.126542
0.945572	0.021837	0.696628	0.094400	0.448964	0.126850
0.937126	0.024638	0.687869	0.096390	0.440049	0.127096
0.928507	0.027473	0.679109	0.098311	0.431136	0.127278
0.919755	0.030317	0.670321	0.100173	0.422223	0.127396
0.910888	0.033176	0.661510	0.101986	0.413308	0.127450
0.901967	0.036035	0.652706	0.103743	0.404393	0.127442
0.893003	0.038883	0.643906	0.105436	0.395485	0.127370
0.883996	0.041728	0.635098	0.107069	0.386581	0.127234
0.874977	0.044564	0.626289	0.108640	0.377679	0.127033
0.865964	0.047380	0.617479	0.110149	0.368788	0.126771
0.856958	0.050172	0.608662	0.111595	0.359912	0.126443
0.847957	0.052940	0.599838	0.112979	0.351046	0.126049
0.838969	0.055680	0.591008	0.114300	0.342198	0.125590
0.829992	0.058390	0.582171	0.115559	0.333367	0.125063
0.821018	0.061070	0.573326	0.116755	0.324554	0.124469
0.812054	0.063720	0.564476	0.117889	0.315763	0.123805
0.803106	0.066335	0.555620	0.118959	0.306992	0.123072
0.794170	0.068912	0.546758	0.119967	0.298244	0.122269
0.785240	0.071452	0.537893	0.120911	0.289529	0.121396

X/L_c	Z/L_c	X/L_c	Z/L_c	X/L_c	Z/L_c
0.280841	0.120447	0.018031	0.028809	0.021787	-0.016468
0.272180	0.119425	0.015856	0.026690	0.024452	-0.017305
0.263553	0.118328	0.013900	0.024685	0.027396	-0.018167
0.254956	0.117154	0.012141	0.022787	0.030661	-0.019059
0.246395	0.115903	0.010558	0.020985	0.034296	-0.019988
0.237876	0.114575	0.009132	0.019271	0.038346	-0.020961
0.229400	0.113167	0.007849	0.017636	0.042858	-0.021974
0.220971	0.111679	0.006694	0.016072	0.047871	-0.023023
0.212593	0.110109	0.005656	0.014572	0.053413	-0.024101
0.204270	0.108456	0.004727	0.013129	0.059486	-0.025195
0.196005	0.106716	0.003896	0.011739	0.066071	-0.026290
0.187796	0.104887	0.003154	0.010397	0.073130	-0.027371
0.179644	0.102969	0.002497	0.009099	0.080605	-0.028428
0.171558	0.100963	0.001923	0.007841	0.088416	-0.029449
0.163544	0.098867	0.001425	0.006620	0.096486	-0.030416
0.155607	0.096681	0.001000	0.005434	0.104777	-0.031323
0.147753	0.094403	0.000647	0.004281	0.113251	-0.032169
0.139989	0.092032	0.000367	0.003158	0.121869	-0.032959
0.132318	0.089566	0.000162	0.002064	0.130593	-0.033689
0.124747	0.087005	0.000039	0.000999	0.139412	-0.034361
0.117282	0.084349	0.000000	-0.000033	0.148311	-0.034979
0.109932	0.081598	0.000046	-0.001058	0.157275	-0.035544
0.102706	0.078754	0.000187	-0.002102	0.166294	-0.036059
0.095615	0.075822	0.000436	-0.003150	0.175363	-0.036525
0.088681	0.072809	0.000809	-0.004188	0.184482	-0.036946
0.081921	0.069721	0.001323	-0.005199	0.193646	-0.037325
0.075355	0.066569	0.001991	-0.006160	0.202849	-0.037666
0.069012	0.063368	0.002805	-0.007061	0.212087	-0.037970
0.062923	0.060136	0.003741	-0.007911	0.221359	-0.038240
0.057117	0.056892	0.004783	-0.008728	0.230662	-0.038479
0.051620	0.053657	0.005924	-0.009519	0.239989	-0.038688
0.046460	0.050462	0.007168	-0.010292	0.249339	-0.038868
0.041658	0.047332	0.008517	-0.011053	0.258711	-0.039023
0.037226	0.044295	0.009977	-0.011808	0.268100	-0.039152
0.033169	0.041375	0.011558	-0.012560	0.277505	-0.039257
0.029483	0.038587	0.013271	-0.013316	0.286927	-0.039340

X/L_c	Z/L_c	X/L_c	Z/L_c	X/L_c	Z/L_c
0.296361	-0.039402	0.562005	-0.034118	0.816689	-0.011601
0.305803	-0.039443	0.571498	-0.033700	0.825395	-0.009913
0.315258	-0.039464	0.580988	-0.033268	0.834153	-0.008167
0.324725	-0.039467	0.590470	-0.032820	0.842930	-0.006413
0.334194	-0.039452	0.599944	-0.032357	0.851670	-0.004692
0.343667	-0.039418	0.609407	-0.031877	0.860247	-0.003033
0.353149	-0.039367	0.618856	-0.031380	0.868585	-0.001488
0.362635	-0.039299	0.628293	-0.030865	0.876711	-0.000079
0.372123	-0.039215	0.637709	-0.030332	0.884621	0.001179
0.381611	-0.039115	0.647102	-0.029778	0.892333	0.002261
0.391101	-0.038997	0.656471	-0.029202	0.899912	0.003158
0.400593	-0.038863	0.665811	-0.028603	0.907428	0.003876
0.410086	-0.038714	0.675119	-0.027977	0.914903	0.004431
0.419577	-0.038548	0.684394	-0.027323	0.922331	0.004828
0.429065	-0.038366	0.693626	-0.026640	0.929715	0.005068
0.438554	-0.038166	0.702812	-0.025923	0.937039	0.005153
0.448045	-0.037950	0.711948	-0.025170	0.944290	0.005080
0.457534	-0.037718	0.721029	-0.024378	0.951461	0.004854
0.467024	-0.037469	0.730048	-0.023543	0.958518	0.004481
0.476516	-0.037203	0.739001	-0.022661	0.965435	0.003963
0.486012	-0.036921	0.747883	-0.021728	0.972181	0.003313
0.495511	-0.036624	0.756689	-0.020741	0.978694	0.002549
0.505009	-0.036312	0.765413	-0.019694	0.984935	0.001688
0.514507	-0.035983	0.774048	-0.018582	0.990837	0.000781
0.524008	-0.035640	0.782593	-0.017394	0.996351	-0.000031
0.533507	-0.035282	0.791070	-0.016112	0.999824	-0.000468
0.543006	-0.034909	0.799540	-0.014717		
0.552508	-0.034520	0.808069	-0.013209		